Garnet Ceramic Electrolytes for Next - Generation Lithium Batteries

A thesis submitted in part fulfilment of the requirements for the degree of Doctor of Philosophy at Imperial College London

Rowena H. Brugge

Department of Materials
Imperial College London
2018

I hereby declare that this thesis and the work reported herein is solely my own work. Information derived from the published and unpublished work of others has been acknowledged in the text and sources given.

R. H. Brugge
London, 2018

The copyright of this thesis rests with the author and is made available under a Creative Commons Attribution Non-Commercial No Derivatives licence. Researchers are free to copy, distribute or transmit the thesis on the condition that they attribute it, that they do not use it for commercial purposes and that they do not alter, transform or build upon it. For any reuse or redistribution, researchers must make clear to others the licence terms of this work.



Abstract

All-solid-state lithium batteries are of great interest scientifically as a next-generation of electrochemical energy storage devices, owing to their superior safety features and their potential to enable new chemistries to improve performance. The properties of the solid state electrolyte are integral to the overall cell capability – to date the most promising group of materials are the garnet-structured oxides, based on $Li_7La_3Zr_2O_{12}$ (LLZO), with high room temperature ionic conductivity and a wide electrochemical stability window. There are several aspects in the development of this relatively new material which are yet to be fully understood – these are the focus of this thesis.

In this work, processing cubic doped LLZO as a bulk ceramic was investigated and served as a basis for understanding its stability and electrochemical performance; it was optimised to obtain highly dense microstructures under atmosphere-controlled conditions to prevent reaction with moisture. Chemical inhomogeneities in the pellets, especially at the grain boundaries, as investigated by secondary ion mass spectrometry (SIMS) and low energy ion scattering, were shown to be important in determining the transport properties of the electrolyte - in particular the propensity for dendrite formation during cell cycling. It was shown that aluminium-rich grain boundaries in aluminium-doped LLZO favour the formation of inter-granular lithium dendrites (with a 60 % lower critical current density for cell failure) over gallium-doped LLZO.

The use of germanium (Ge^{4+}) as a dopant was studied, and shown to stabilise the cubic LLZO phase through substitution of 0.10 moles of Ge at the lithium sub-lattice (at the tetrahedral 24*d* sites), giving conductivities of the order $10^{-4}\,S\,cm^{-1}$ and redox stability over a 4.5 V range with lithium electrodes. Chemical and electrochemical characterisation of the moisture reactivity of gallium-doped LLZO was also carried out, showing a chemically-altered proton-rich region extending to 1.35 µm following 30 minutes immersion in H_2O at 100 °C and highly reactive grain boundaries. These chemical changes led to a threefold increase in the resistance of both the electrolyte and the interface with lithium electrodes. Chemical and tracer diffusivity of protons were estimated from the diffusion profiles of H^+ and D^+ obtained by SIMS depth-profiling.

A new methodology for measuring macroscopic lithium tracer diffusion in LLZO was introduced, using SIMS depth-profiling and isotopic labelling, in which a number of experimental parameters were varied to optimise the technique. The preliminary results for lithium diffusivity in doped LLZO obtained from this method were compared with values from other methods (impedance and nuclear magnetic resonance) and used to comment on the mechanism for lithium diffusion in the materials.

Acknowledgements

The utmost thanks are due to Dr Ainara Aguadero and Professor John Kilner for their supervision, the former having encouraged me at every stage of the journey and provided me with countless opportunities for development, for which I am most grateful. Their approach to scientific enquiry kept the joy of research alive during this thesis.

I wish also to acknowledge Professor Stephen Skinner for his guidance and support throughout my time at Imperial; his ability to lend a different perspective has been truly helpful.

The creation and growth of the lithium/battery group in the later stages of my PhD research has been a welcome source of discussion and entertainment, long may it continue. Particular thanks go to Dr Andrea Cavallaro for his wealth of knowledge and insight as well as assistance with LEIS measurements and to Dr Federico Pesci for his advice and for helping us all to embrace the lighter side of life.

Many thanks go to all the Electroceramicists, who have been such a convivial and diverse group of people who I have had the luck to work alongside and especially to Celeste van den Bosch – for the voice of calm when hope seemed lost at times.

I am grateful for the surface analysis staff in the Materials basement, especially Richard Sweeney and Dr Sarah Fearn for lively interactions and a relaxed approach to academic research. Life as a PhD student was a little easier thanks to their outlook. In particular I wish also to thank Dr Richard Chater for his patience and teaching, and invaluable feedback and input on ion beams, diffusion and scientific questions.

For multiple experimental techniques and discussions, collaborators and colleagues Dr Lauren Marbella and Steffen Emge at Cambridge, Drs Anna Regoutz, Ola Hekselman and Na Ni at Imperial and Dr Emanuela Liberti at Oxford/Diamond have given up much of their time, for which I am thankful.

My friends from home and Oxford have patiently stood by me and kept me going through the rough and smooth with words of encouragement, and Dimitri's mantra to dream big will remain with me as I embark on the next stage of life's journey. Thank you all.

Finally, I would like to thank my family for their enduring support and for believing in me always.

Contents

List of Figures **13**

List of Tables **17**

Nomenclature and Abbreviations **19**

1 Introduction **23**
1.1 Motivation and Rationale 23
1.2 Lithium Ion Batteries 25
1.3 All-Solid-State Batteries 28
1.4 In this Thesis 29

2 Theoretical Considerations **31**
2.1 Defect Chemistry and Ionic Transport 31
2.1.1 Defects in Crystals 31
2.1.2 Conductivity 34
2.2 Fundamentals of Diffusion 36
2.2.1 Fick's Laws 36
2.2.2 Correlated Motion and Long Range Diffusion 38
2.2.3 Solutions to the Diffusion Equation 39
2.2.4 Experimental Methods to Determine Lithium Diffusion 42
2.3 Electrochemistry of Lithium Batteries 46
2.3.1 Basics of a Battery and Electrochemical Stability 46
2.3.2 Energy Density and Capacity 47
2.3.3 Voltage 48
2.3.4 Power 49
2.4 Summary 50

3 Literature Review **51**
3.1 All-Solid-State Batteries and Solid State Electrolytes 51
3.1.1 Ceramic Crystalline Electrolytes 54
3.2 Garnet-Type Electrolytes 56
3.2.1 Background 56
3.2.2 Lithium-Rich Garnets 58
3.2.3 Structure and Transport 59

3.2.4 Doping . . . 62
3.3 Degradation of Garnets with H_2O and CO_2 . . . 68
3.4 Interface of Garnets with Lithium Metal Electrodes and Cell Cyclability . 73
3.5 Summary . . . 77

4 Experimental Methods **79**
4.1 Synthesis and Processing . . . 79
4.1.1 Sol-Gel Method . . . 79
4.1.2 Thermal Treatment . . . 80
4.1.3 Pellet Finishing . . . 82
4.1.4 Density Measurement . . . 83
4.2 Diffraction Techniques . . . 83
4.2.1 X-ray Diffraction . . . 84
4.2.2 Neutron Diffraction . . . 87
4.2.3 Structural Refinement . . . 88
4.3 Surface Characterisation . . . 89
4.3.1 X-ray Photoelectron Spectroscopy . . . 89
4.3.2 Low Energy Ion Scattering . . . 91
4.4 Electron Microscopy . . . 92
4.4.1 Scanning Electron Microscopy . . . 93
4.4.2 (Scanning) Transmission Electron Microscopy . . . 94
4.5 Inductively Coupled Plasma - Optical Emission Spectroscopy . . . 95
4.6 Nuclear Magnetic Resonance . . . 96
4.7 Electrochemical Testing . . . 99
4.7.1 Electrochemical Impedance Spectroscopy . . . 99
4.7.2 Cyclic Voltammetry . . . 102
4.7.3 Charge/Discharge Cycling . . . 103
4.8 Secondary Ion Mass Spectrometry . . . 103
4.8.1 Time of Flight SIMS . . . 106
4.8.2 Focussed Ion Beam SIMS . . . 107

5 Synthesis and Doping of $Li_7La_3Zr_2O_{12}$ **111**
5.1 Garnet Synthesis . . . 111
5.1.1 Thermal Treatment: Atmosphere and Temperature . . . 112
5.1.2 Crucible Effects . . . 117
5.2 Germanium Doping . . . 118
5.2.1 Optimising the Germanium Concentration . . . 121
5.2.2 Conductivity Measurements . . . 123
5.2.3 Microstructural Analysis . . . 129
5.2.4 Site Preference of Germanium . . . 130
5.2.5 Oxidation State of Germanium . . . 133
5.2.6 Redox Stability Measured by Cyclic Voltammetry . . . 133
5.3 Summary . . . 133

5.4 Suggested Future Work . . . 135

6 Moisture-Induced Degradation in $Li_7La_3Zr_2O_{12}$ 137
6.1 H_2O Reactivity of LLZO Powder . . . 138
6.1.1 Powder Characterisation . . . 138
6.1.2 Nuclear Magnetic Resonance . . . 141
6.2 Proton Exchange and Diffusion in LLZO Pellets . . . 142
6.2.1 Experimental Method . . . 143
6.2.2 Sample Characterisation . . . 143
6.2.3 Focussed Ion Beam - Secondary Ion Mass Spectrometry . . . 144
6.2.4 H_2O Reaction and Chemical Diffusion . . . 145
6.2.5 D_2O Reaction and Tracer Diffusion . . . 154
6.3 Effect of Protonation on Lithium Ionic Transport . . . 158
6.3.1 Impedance Method . . . 158
6.3.2 Impedance Results . . . 161
6.4 Surface Corrosion Layer Formation . . . 166
6.4.1 Low Energy Ion Scattering . . . 166
6.4.2 X-ray Photoelectron Spectroscopy . . . 168
6.5 Summary . . . 170
6.6 Suggested Future Work . . . 172

7 Lithium Isotopic Exchange, Diffusion and Transport in $Li_7La_3Zr_2O_{12}$ 175
7.1 Lithium Isotopic Exchange Techniques . . . 175
7.1.1 Solid State Diffusion Method . . . 176
7.2 Method Development . . . 177
7.2.1 Secondary Ion Energy Spectrum . . . 177
7.2.2 Verification of Isotopic Exchange . . . 179
7.2.3 Mass Interferences and Surface Chemistry . . . 183
7.2.4 Charging Effects . . . 184
7.2.5 Thin Film Lithium-6 Sources . . . 187
7.2.6 Summary of Solid State Diffusion Method . . . 191
7.3 Nuclear Magnetic Resonance Results . . . 192
7.3.1 ^{7}Li Pulsed Field Gradient (PFG) NMR . . . 192
7.3.2 ^{7}Li Spin Lattice Relaxation ($T1$) NMR . . . 194
7.4 Summary . . . 195
7.5 Suggested Future Work . . . 196

8 Symmetric Cell Cycling and Failure in $Li_7La_3Zr_2O_{12}$ / Lithium Metal Cells 199
8.1 Characterisation of Pristine Pellets . . . 199
8.1.1 Secondary Ion Mass Spectrometry Mapping . . . 202
8.2 Galvanostatic Cycling with Lithium Electrodes . . . 204
8.3 Post-Mortem Analysis . . . 206
8.3.1 Secondary Ion Mass Spectrometry . . . 206

8.3.2 X-ray Photoelectron Spectroscopy . . . 214
8.3.3 Nuclear Magnetic Resonance . . . 216
8.4 Discussion and Summary . . . 217
8.5 Suggested Future Work . . . 218

9 Conclusions and Further Work **221**
9.1 Conclusions . . . 221
9.2 Suggested Further Work . . . 224

Bibliography **227**

Appendices **253**
A.1 Synthesis and Doping of LLZO . . . 253
A.2 ^{1}H Pulsed Field Gradient NMR . . . 255
A.3 EIS Analysis of Pellets with Changing Thickness . . . 256
A.4 Calculating the Resistivity of Protonated H-Ga0.15-LLZO . . . 257
A.5 ^{7}Li NMR . . . 258
A.5.1 ^{7}Li Pulsed Field Gradient NMR . . . 258
A.5.2 ^{7}Li Spin Lattice Relaxation ($T1$) NMR . . . 258
A.5.3 XRD Patterns of Powders used for NMR Measurements . . . 259
A.6 Effects of Surface Roughness on FIB-SIMS Analysis of LLZO Pellets . . . 259
A.7 Symmetric Cell Cycling Characterisation . . . 262

Dissemination **265**

List of Figures

1.1 Global land-ocean temperature index and North Sea crude oil production 24
1.2 Schematic of commercial lithium ion battery 26
1.3 Relative energies of electrolyte and electrodes in a battery 28

2.1 Effect of an electric field on the migration of charged species in a crystal . 35
2.2 Diffusion profile with constant surface concentration and zero initial concentration 40
2.3 Semi-infinite diffusion profiles of solid-gas and solid-solid diffusion couples 41
2.4 SEI layers in energy level diagram showing relative energies of electrodes and electrolyte 48
2.5 Schematic of density of states of Li_xC_6 and $Li_{1-x}CoO_2$ electrode materials . 49

3.1 Arrhenius plot of various solid and liquid electrolytes 53
3.2 NASICON structure 54
3.3 Tetragonal $BaTiO_3$ structure 55
3.4 The ideal garnet crystal structure with formula $A_3B_2(CO_4)_3$ 57
3.5 Lithium polyhedra occupancy in the garnet structure 58
3.6 Effect of lithium content and site occupancy on conductivity in LLZO . . . 59
3.7 Energy barriers for lithium diffusion in garnets 61
3.8 $Ia\bar{3}d$ and $I\bar{4}3d$ cubic space groups of doped LLZO 66
3.9 Li and H sites in $I\bar{4}3d$ and $Ia\bar{3}d$ cubic H-LLZO 71

4.1 Li_2O-Al_2O_3 phase equilibrium diagram 82
4.2 The generation and diffraction of X-rays by a crystal 85
4.3 Neutron scattering amplitudes of the elements 88
4.4 Energy level diagram of an atom 90
4.5 LEIS schematic 92
4.6 Electron-sample interactions in electron microscopy 93
4.7 Schematic of a TEM column in TEM and STEM modes 95
4.8 NMR signal production and acquisition 97
4.9 Illustrative Nyquist diagram 100
4.10 Coin cell configurations 102
4.11 Cyclic voltammetry sweep and voltammogram 103
4.12 SIMS collision event schematic 104

4.13 TOF-SIMS ion beam modes 107

5.1 Powder X-ray diffraction patterns of Ga0.15-LLZO following different atmosphere and temperature treatments 113
5.2 Ga0.15-LLZO powder SEM images 114
5.3 STEM bright field and annular dark field images of Ga0.15-LLZO 115
5.4 Atomic positions in LLZO viewed along the (001) zone axis 115
5.5 LLZO pellet images 116
5.6 Pellet XRD patterns of undoped LLZO, thermally treated in ZrO_2 and Al_2O_3 crucibles 118
5.7 Images and SIMS mass spectra of a liquid phase front in LLZO pellets . . 119
5.8 LEIS depth profiles of Al- and Ga-LLZO pellets with and without contact with alumina crucible during sintering 120
5.9 XRD patterns of Ge-doped LLZO pellets 122
5.10 Nyquist plots of Ge0.15-, Ge0.10-, Ge0.05- and undoped LLZO pellets with symmetrical Au electrodes 124
5.11 Nyquist plots of Ge-LLZO and undoped LLZO electrolytes with Au symmetrical electrodes, fitted to a single R//CPE element 125
5.12 Nyquist plots of Ge-LLZO and undoped LLZO electrolytes with Au symmetrical electrodes, fitted to two R//CPE elements 127
5.13 Nyquist plots of a Ge0.10-LLZO symmetric cell with Li electrodes 129
5.14 Images of Ge0.10-LLZO pellets thermally etched at 900 °C 131
5.15 TOF-SIMS maps of the surface of a Ge0.10-LLZO pellet 131
5.16 Neutron powder diffraction pattern of Ge0.10-LLZO 132
5.17 XPS Al 2p and Ge 2p core spectra of Al0.15-LLZO and Ge0.10-LLZO pellets 134
5.18 Cyclic voltammogram of a Li/Ge0.10-LLZO/Li cell 134

6.1 Powder XRD patterns before and after H_2O reaction of Ga0.15-LLZO . . . 139
6.2 Rietveld refinements of powder XRD patterns of Ga0.15-LLZO 140
6.3 ^1H NMR spectra of protonated powder Ga0.15-LLZO samples 141
6.4 ^1H and ^7Li PFG NMR on 100 °C protonated Ga0.15-LLZO powder 142
6.5 Pristine Ga0.15-LLZO pellet characterisation by XRD and SEM 144
6.6 Pristine Ga0.15-LLZO FIB-SIMS depth profiles 146
6.7 Secondary electron and positive ion images of H_2O-immersed Ga0.15-LLZO pellets 147
6.8 Negative secondary ion mass spectra of pristine and H_2O/30 Ga0.15-LLZO 147
6.9 FIB-SIMS depth profiles of H_2O/30 Ga0.15-LLZO 149
6.10 XRD pattern on H_2O/30 Ga0.15-LLZO pellet 150
6.11 FIB-SIMS negative ion depth profiles of H_2O/5 and H_2O/15 Ga0.15-LLZO 150
6.12 Length of protonated H-Ga0.15-LLZO region, chemical diffusion length of H^+ and calculated H and Li content in H-Ga0.15-LLZO for 100 °C H_2O/30, H_2O/15 and H_2O/5 Ga0.15-LLZO 151
6.13 Negative secondary ion mass spectrum of H_2O/30/D_2O/6 Ga0.15-LLZO 154

6.14 FIB-SIMS depth profiles of $H_2O/30/D_2O/6$ Ga0.15-LLZO 155
6.15 Normalised isotopic fractions of OD^- in $H_2O/30/D_2O/6$ Ga0.15-LLZO . . 156
6.16 Isotopic fractions of OD^- in $H_2O/15/D_2O/3$ and $H_2O/5/D_2O/1$ Ga0.15-LLZO, fitted to Crank solution for tracer diffusion 157
6.17 Schematic of possible ionic transport arrangements within a Ga0.15-LLZO grain following 100 °C H_2O and D_2O immersion 159
6.18 Nyquist plots and Arrhenius plots for Ga0.15-LLZO air-exposed sample with symmetrical Au electrodes 161
6.19 Nyquist plots of pristine Ga0.15-LLZO with symmetrical Li electrodes . . 162
6.20 Nyquist plots of pristine, air-exposed and 100 °C H_2O-immersed pellets with symmetrical Li and sputtered Au electrodes 163
6.21 Schematic illustrating the arrangement of pure LLZO and H-LLZO regions in a pellet following H^+/Li^+ exchange 165
6.22 Optical microscope images of a LLZO-$La_2Zr_2O_7$ mixed phase pellet after air exposure and after polishing away the surface 166
6.23 LEIS depth profiles of LLZO pellets following different atmospheric treatments 167
6.24 Sub-surface LEIS spectra of Al0.15-LLZO and Ga0.15-LLZO after air exposure, and spectra and depth profiles of Ge0.10-LLZO after air exposure and glove box storage 168
6.25 LEIS depth profile and secondary ion image of a Ga0.15-LLZO air-exposed pellet containing Li_2ZrO_3 grains 169
6.26 XPS Li 1s, O 1s and C 1s core spectra for air-exposed and pristine Ge0.10-LLZO samples 170

7.1 The solid state lithium diffusion method 178
7.2 Secondary ion energy spectrum at $m/z = 7$ on ^{6}Li metal 179
7.3 FIB-SIMS depth profile through a ^{6}Li metal/LLZO interface 181
7.4 ^{6}Li isotopic fractions in a ^{6}Li metal/LLZO exchange couple, measured with increasing distance from the ^{6}Li metal source 182
7.5 FIB-SIMS positive ion mass spectrum of LLZO pellet surface 183
7.6 Schematic of possible Li diffusion pathways in a LLZO grain following proton-lithium exchange 184
7.7 Effect of a tungsten needle contact on collected SIMS depth profiles and mass spectra of LLZO pellet 186
7.8 SIMS depth profiles on Al and Li thin films deposited on Al0.15-LLZO and Si(001) wafer 188
7.9 SIMS depth profiles on LiF and Li thin films deposited on Al0.15-LLZO . 189
7.10 SIMS depth profiles on LiF and Li thin films deposited on Al0.15-LLZO, after ^{6}Li exchange 191
7.11 Variable temperature PFG NMR data for Ga-, Ge-doped and undoped LLZO powders 193

8.1 secondary electron images of thermally etched Ga-LLZO and Al-LLZO . . 200
8.2 Room temperature EIS Nyquist plot of Al-LLZO and Ga-LLZO symmetric cells with Li electrodes 201
8.3 TOF-SIMS and FIB-SIMS maps of pristine Al-LLZO surface 202
8.4 TOF-SIMS maps of pristine Al-LLZO and Ga-LLZO surfaces 203
8.5 Galvanostatic cycling of symmetrical cells 205
8.6 Measured resistance as a function of current density during galvanostatic cycling of Al-LLZO and Ga-LLZO cells 206
8.7 Nyquist plot of Al-LLZO and Ga-LLZO cells post-cycling and image of dissassembled Ga-LLZO coin cell 207
8.8 Images of dendritic features in LLZO following cycling 208
8.9 Al-LLZO in-grain SIMS depth profiles pre- and post-cycling, and surface mapping after cycling 210
8.10 Ga-LLZO in-grain SIMS depth profiles pre- and post-cycling, and surface mapping after cycling 211
8.11 SIMS depth profile chemical analysis of features post-cycling 212
8.12 FIB-SIMS maps of Al-LLZO inter-granular dendritic feature after cycling . 213
8.13 XPS Li 1s, O 1s, Al 2p and C 1s core spectra of Al-LLZO pristine and cycled pellets 215
8.14 ^{7}Li NMR and MRI of dendritic Al-LLZO and Ga-LLZO pellets 217

A.1 XPS Zr 3d, La 3d, Li 1s and O 1s core spectra for Ge0.10-LLZO samples produced under oxygen and vacuum atmospheres 253
A.2 XRD patterns of Ge0.30- and Ge0.50-LLZO pellets 254
A.3 XRD pattern of Ge0.10-LLZO, doping at the Zr site 254
A.4 XRD pattern of Ge0.10-LLZO powder, used for neutron diffraction 255
A.5 ^{1}H PFG NMR on 100 °C protonated Ga0.15-LLZO powder 255
A.6 ^{7}Li PFG NMR at room temperature on Ga0.15-LLZO powder 258
A.7 $T1$ ^{7}Li NMR data for Ga- and Ge-doped LLZO powders 258
A.8 XRD patterns of powders used for ^{7}Li NMR diffusivity measurements . . 259
A.9 LLZO pellets with different roughness: secondary electron and white light interferometry microscope images 260
A.10 Effect of surface roughness on collected SIMS depth profiles and mass spectra of LLZO pellet 261
A.11 FIB-SIMS map of Ga-LLZO pristine pellet 262
A.12 X-ray powder diffraction patterns of Ga0.15-LLZO and Al0.15-LLZO before cell cycling 263
A.13 X-ray powder diffraction patterns of Ga0.15-LLZO and Al0.15-LLZO following cell cycling and failure 263
A.14 Li-Ga phase equilibrium diagram 264

List of Tables

1.1 Graphite-$LiCoO_2$ cell reactions 26

2.1 Experimental methods for determining diffusivity in solids 43

3.1 Reported conductivities in the literature for Li site doping in LLZO 63
3.2 Table of crystal radii of cations in LLZO 67
3.3 First principles defect site energies in LLZO for a range of cation dopants . 69

4.1 Table of capacitance values 101

5.1 Table of particle sizes of Ga0.15-LLZO powders 114
5.2 Table of crystal radii of Li, Al and Ge cations 121
5.3 ICP-OES measured atomic concentrations for Ge-LLZO with different nominal compositions 123
5.4 Equivalent circuit model fits for a single R//CPE element for Ge-LLZO and undoped LLZO electrolytes with Au symmetric electrodes 126
5.5 Equivalent circuit model fits for a two R//CPE element fit for Ge-LLZO and undoped LLZO electrolytes with Au symmetric electrodes 128
5.6 Equivalent circuit model fits for a symmetric Li/Ge0.10-LLZO/Li cell . . . 130
5.7 Neutron powder diffraction data of Ge0.10-LLZO determined by Rietveld refinement 132

6.1 Normalised peak intensities of ^{1}H NMR chemical shifts of protonated Ga0.15-LLZO 142
6.2 Table of calculated values for the 100 °C H_2O Ga0.15-LLZO pellets 152
6.3 Measured and calculated transport properties of Li^+ and H^+ in pristine Ga0.15-LLZO and H_2O/30 H-Ga0.15-LLZO 153
6.4 Equivalent circuit model fits at 25 °C of impedance spectra parameters for pristine, air-exposed, H_2O/15 and H_2O/30 Ga0.15-LLZO cells with Li and Au symmetric electrodes 160
6.5 Quantification of XPS Li, La and Zr ratios in Ge0.10-LLZO samples 169

7.1 Measured ^{6}Li isotopic fractions $C(^{6}Li)$ on ^{6}Li metal at different SIMS detector voltage offsets 179
7.2 Estimated diffusion length and diffusivity for the first ^{6}Li isotopic exchange experiment 180

7.3 Estimated Li diffusivity from ^{6}Li/LiF/Li/Al0.15-LLZO isotopic exchange experiments 190
7.4 EIS-predicted and PFG NMR experimental room temperature diffusivities D(Li) 194
7.5 Activation energies from EIS, PFG and $T1$ relaxation NMR measurements of LLZO samples 194

8.1 Equivalent circuit model fits at 25 °C of impedance spectra for pristine Ga-LLZO and Al-LLZO pellet cells with Li symmetric electrodes 201
8.2 Quantification of XPS La and Al ratios, in cycled and pristine Al-LLZO samples. 216

A.1 Calculated ^{1}H diffusion coefficients in H-Ga0.15-LLZO from ^{1}H PFG NMR data 256
A.2 EIS analysis of a Ga0.15-LLZO pellet with various thicknesses 256
A.3 Ratios of thickness, impedance and normalised impedance values of a Ga0.15-LLZO pellet with various thicknesses 257
A.4 Resistance calculations for H-Ga0.15-LLZO region 257

Nomenclature and Abbreviations

δ	chemical shift
ϵ_0	vacuum permittivity
ϵ_r	relative permittivity
η	applied potential
λ	wavelength
μ	chemical potential; mobility
$\bar{\mu}$	electrochemical potential
ρ	density, or specific gravity; resistivity
σ	conductivity
τ	transport number
χ^2	goodness of fit
ω	angular frequency
ω_0	Larmor frequency
A	area
B_0	magnetic field strength
C	capacitance
C(x)	isotopic fraction of species x
D	diffusivity (general)
D^*	tracer diffusivity
D_C	chemical diffusivity
D_J	self-diffusivity
D^σ	conductivity-derived diffusivity (from Nernst-Einstein)

d	lattice spacing
E^0	standard cell potential
E_a	activation energy
E_B	binding energy
E_F	Fermi energy
E_g	electrochemical potential window
E_K	kinetic energy
F	Faraday constant
h	Planck constant
H_R	Haven ratio
j	flux density
k	Boltzmann constant
k^*	surface exchange coefficient
M	magnetic moment
M_w	molecular mass
m/z	mass-to-charge ratio
N_A	Avogadro's number
P	power
Q	capacity
q	charge
R	resistance
T	temperature
$T1$	NMR spin-lattice relaxation time
$T2$	NMR spin-spin relaxation time
V	voltage
V_0	equilibrium voltage
V_OC	open circuit voltage
Z	impedance
ΔG	change in Gibbs free energy
ΔH	change in enthalpy
ΔS	change in entropy

ABF	annular bright field
AC	alternating current
ADF	annular dark field
Al-LLZO	aluminium-doped $Li_7La_3Zr_2O_{12}$ (unspecified concentration)
Al0.15-LLZO	$Li_{6.55}Al_{0.15}La_3Zr_2O_{12}$
ASR	area specific resistance
BAM	burst alignment mode
BF	bright field
C	capacitor
CPE	constant phase element
CT	charge transfer
CV	cyclic voltammetry
DC	direct current
DF	dark field
DFT	density functional theory
EC	ethylene carbonate
EDX	energy dispersive X-ray spectroscopy
EELS	electron energy loss spectroscopy
EIS	electrochemical impedance spectroscopy
FCC	face-centred-cubic
FEG	field emission gun
FIB-(SIMS)	focussed ion beam-(secondary ion mass spectrometry)
Ga-LLZO	gallium-doped $Li_7La_3Zr_2O_{12}$ (unspecified concentration)
Ga0.15-LLZO	$Li_{6.55}Ga_{0.15}La_3Zr_2O_{12}$
GB	grain boundary
Ge-LLZO	germanium-doped $Li_7La_3Zr_2O_{12}$ (unspecified concentration)
Ge0.10-LLZO	$Li_{6.6}Ge_{0.10}La_3Zr_2O_{12}$
HAADF	high angle annular dark field
HCBM	high current bunched mode
H-LLZO	protonated $Li_7La_3Zr_2O_{12}$ (unspecified concentration)
HOMO	highest occupied molecular orbital
ICP-OES	inductively coupled plasma - optical emission spectroscopy
LATP	$Li_{1.3}Al_{0.3}Ti_{1.7}(PO_4)_3$
LCO	$LiCoO_2$
LEIS	low energy ion scattering
LiPON	$Li_xPO_yN_z$
LISICON	$Li_{3.5}Zn_{0.5}GeO_4$
LLTO	$Li_{0.5}La_{0.5}TiO_3$

LLZO	$Li_7La_3Zr_2O_{12}$
LMIG	liquid metal ion gun
LUMO	lowest unoccupied molecular orbital
MAS NMR	magic angle spinning nuclear magnetic resonance
MRI	magnetic resonance imaging
μ^+SR	muon spin relaxation
NASICON	$NaA_2^{IV}(PO_4)_3$ (A^{IV} = Ge, Ti or Zr)
ND	neutron diffraction
NMR	nuclear magnetic resonance
NRA	nuclear reaction analysis
Oh	octahedrally-coordinated lattice site
PC	propylene carbonate
PEO	polyethylene oxide
PFG NMR	pulsed field gradient nuclear magnetic resonance
PVD	physical vapour deposition
QENS	quasi-elastic neutron scattering
R	resistor
RC	resistor-capacitor in parallel
RF	radio frequency
RT	room temperature
SE	secondary electron
SEI	solid-electrolyte interphase
SEM	scanning electron microscopy
SI	secondary ion
SIMS	secondary ion mass spectrometry
SOC	state of charge
SRIM	stopping and range of ions in materials
(S)TEM	(scanning) transmission electron microscopy
Td	tetrahedrally-coordinated lattice site
TGA	thermogravimetric analysis
TOF-(SIMS)	time of flight-(secondary ion mass spectrometry)
UHV	ultra high vacuum
XANES	X-ray absorption near-edge spectroscopy
XPS	X-ray photoelectron spectroscopy
XRD	X-ray diffraction
YAG	$Y_3Al_2Al_3O_{12}$
YIG	$Y_3Fe_2Fe_3O_{12}$

Chapter 1

Introduction

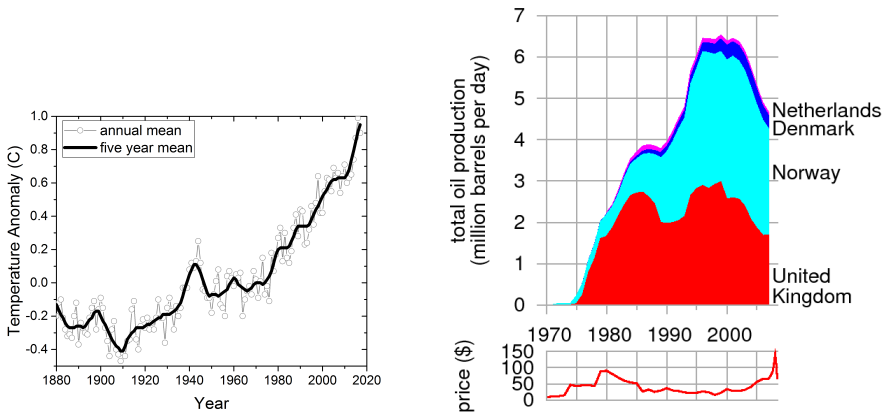
This introductory chapter serves to set the context for the scientific work reported in this thesis and the applications which are, and are expected to be, made possible through the research being conducted by the scientific community in this field. In this chapter, the rationale for research within the field of energy storage materials, especially next-generation lithium batteries in the form of all-solid-state batteries, is discussed. These future energy storage devices are required for enabling a low-carbon, sustainable economy in order to mitigate anthropogenic global climate change and pollution whilst meeting future energy demands.

1.1 Motivation and Rationale

Energy policy today is more pertinent and complex than at any time before in human history. The demand for energy is increasing as a result of a growing population and global development, and it is expected that energy consumption will increase by over half by 2030 [1].

Much of our global energy generation relies on the combustion of fossil fuels, with over 80 % of global energy supply provided by coal, oil and gas combined in 2015 [2]. The burning of these fuels results in emission of CO_2 and other greenhouse gases, which are known factors in their contribution to global warming and climate change [3], of which energy-related emissions account for at least two-thirds of total emissions [2]. The effects of climate change are expected to have a significant impact on the future of man's existence on earth, and already we are feeling its effects: the latest studies from NASA's Goddard Institute for Space Studies (see Figure 1.1a) shows that 2016 was the warmest year globally since records began in 1880, and apart from 1998, the ten warmest years on record have all occurred since the year 2000 [4]. The consequences of global warming are likely to involve increasing incidences of extreme weather events across the world, including droughts in some areas, floods and turbulent weather in others [5], and already these types of events are becoming increasingly frequent and more radical in nature [6]. What is more, the social cost and impact of climate change is expected to affect the poorest people in the world the soonest and hardest of all [7].

The use of fossil fuels also has implications on energy security - they are a finite



(a) (b)

Figure 1.1: (a) Global land-ocean temperature index, illustrating the change in global surface temperature relative to 1951-1980 average temperatures. Data from NASA's Goddard Institute for Space Studies (GISS) [4]; (b) total crude oil production from the North Sea, and oil price in dollars per barrel [3].

resource and, as accessible, more affordable reserves run out, so their supply looks uncertain. For many nations, including the UK, where access to fossil fuels is diminishing (Figure 1.1b), being able to produce and store energy without relying on fuel supply from other nations subject to geopolitical instability, thus avoiding supply disruption and an 'energy gap' [3], is a very real need.

In order to mitigate the advancement of global warming and move away from fossil fuels, we need to utilise alternative, sustainable sources of energy, in particular renewable energies such as solar and wind. However, the successful implementation of these energy sources relies on extensive development of renewable energy technologies to lower their associated costs and improve their energy production capabilities. In addition, because these alternative energy supplies (including nuclear) are not able to be turned on and off as and when the demand is there, a future sustainable energy economy requires a way of storing this energy, coupling the variable supply to the changeable demand, and also allowing energy to be released into the grid as electricity during peak hours when it is more valuable [8].

A number of electrical energy storage systems currently exist, storing the energy as mechanical, chemical and thermal energy. Currently the most widely used technology in worldwide energy storage is pumped hydro, accounting for over 99 % of total storage capacity, followed by compressed air [9]. Pumped hydro has a high efficiency (greater than 80 %) and low cost per unit stored energy [9], but can be costly to setup and is geographically-dependent, with a finite number of available sites. Compressed air energy storage is still in development and currently has limited market uptake.

Electrochemical energy systems are able to provide a much higher energy density than these physical systems; however the cost-performance balance is too high for many of these. Current lithium ion battery technologies are the most promising for small (a few kW h) and medium (a few 100 kW h) systems, where performance and autonomy (the maximum amount of time the system can continuously release energy, defined by the

ratio of energy capacity to maximum discharge power) are important [8], but in order for scale up of these technologies to happen, costs need to be reduced and performance improvements made.

In addition to stationary storage for large-scale energy systems, the electrification of transport is a step towards ending fossil fuel use (provided the energy to generate the electricity is renewables-generated), and for this application the lithium ion battery is a strong candidate, and is already being adopted in commercial electric and hybrid electric vehicles [10]. However, existing lithium ion batteries have a number of shortcomings for these applications, relating to their safety features, driving range, cost and relatively low power density. The consumer electronics market has, however, driven down the cost of lithium ion batteries, with recent estimates placing the cost of producing lithium ion cells from \$145 $(\text{kWh})^{-1}$ and the cost of a battery pack as low as \$190 $(\text{kWh})^{-1}$. The goal of most automotive manufacturers and the US Department of Energy is \$125 $(\text{kWh})^{-1}$ for a battery pack by 2022, based on a \$3.50 per gallon oil price [10, 11]. Despite these advances, new emerging chemistries based on lithium ion need further development in order to achieve the desired energy output, safety and reliability for implementation in a next-generation of energy storage devices.

1.2 Lithium Ion Batteries

As discussed in the previous section, lithium ion batteries have the potential to contribute significantly to storing energy cheaply and efficiently, ready to be used as electricity. However, in order to be used in large scale applications such as grid storage (and to enable grid peak-shaving, reducing electrical power consumption during periods of maximum demand) and in electric vehicles, considerable progress is needed to increase the energy density and safety whilst lowering cost.

The term 'battery' is used to describe a transducer composed of one or more interconnected electrochemical cells containing positive and negative electrodes (mixed ionic-electronic conductors) separated by an ion-conducting electrolyte, used for the generation of electric current from stored chemical energy. Of those which are commercially available, secondary lithium ion batteries (first released in 1991 by Sony) allow reversible charge and discharge cycling and provide the greatest energy densities. They are based on intercalation chemistry at the anode and cathode (Figure 1.2).

During discharge, the anode (chemical potential μ_a) is oxidised as electrons flow through an external circuit, causing the cathode (chemical potential μ_c) to be reduced. At the same time, Li^+ ions are transported from the anode through the electrolyte and intercalated into the cathode. The electrolyte enables the separation of ionic and electronic transport in the system and in an ideal case will have a transport number (defined as the fraction of the total current carried by a given ion in an electrolyte) for lithium, τ_{Li}, equal to one. The equilibrium voltage V_0 is the difference in chemical potentials of the lithium atoms in the two electrode materials (redox pair) in the absence of an applied current, given in Equation 1.1, where F is the Faraday constant (the charge on one mole of electrons)

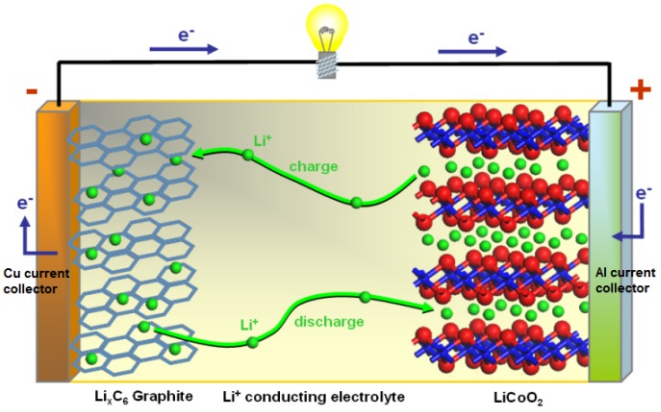


Figure 1.2: Schematic of a commercially available lithium ion battery consisting of a graphite anode and a layered $LiCoO_2$ cathode on discharge, and a conducting organic electrolyte. Adapted from a figure by Johnson Matthey Battery Systems [12].

and n is the number of electrons transferred per mole, such that nF is the total charge transferred during the reaction.

$$\frac{\mu_a - \mu_c}{nF} = V_0 \tag{1.1}$$

In the absence of an applied voltage, the chemical potential (μ) and electrochemical potential ($\bar{\mu}$) are equivalent; however to reverse the reaction (charge the cell), a potential (ϕ) is applied and the electrochemical potential is described by Equation 1.2, where z is the ionic charge.

$$\bar{\mu} = \mu + zF\phi \tag{1.2}$$

In the Sony cell comprising graphite and perovskite $LiCoO_2$ electrodes, the overall electrochemical reaction is given by the half-cell potentials at the anode and cathode in Table 1.1 [13], where φ^0 is the standard redox potential of the electrodes and E^0 is the standard cell potential.

Table 1.1: Electrochemical reactions at the anode, cathode, and in the overall cell for the commercial graphite-$LiCoO_2$ cell, and their corresponding potentials, vs. the standard hydrogen electrode [13].

$Li_xC \rightleftharpoons C + xLi^+ + xe^-$	$\varphi^0 = -2.90\,V$	Anode
$Li_{1-x}CoO_2 + xLi^+ + xe^- \rightleftharpoons LiCoO_2$	$\varphi^0 = 1.20\,V$	Cathode
$Li_xC + Li_{1-x}CoO_2 \rightleftharpoons C + LiCoO_2$	$E^0 = 4.10\,V$	Total

During charging above $x = 0.5$, the delithiated $Li_{1-x}CoO_2$ cathode structure can undergo surface reactions and is unstable, leading to evolution of oxygen and decomposition of the material. This is the result of changes in the electronic and magnetic state of CoO_6 octahedra caused by overlapping Co d-orbital and O p-orbital bands following lithiation. As lithium is extracted during charge, Co^{3+} is oxidised to

Co^{4+} and electron holes are created and trapped as the peroxide $(O_2)^{2-}$, which eventually combine and result in oxygen gas evolution. The operating voltage during discharge decreases from the theoretical maximum of 4.1 V to a cut-off minimum value of about 3 V, with an average value of about 3.6 V over the discharge cycle [14]. The fact that not all of the lithium can be reversibly intercalated limits the practical capacity of the cell to about half of the theoretical value calculated from Faraday's laws (Equation 1.3) to $130\,\mathrm{A\,h\,kg^{-1}}$ [15].

As illustrated by the limitations of the $LiCoO_2$-based battery, one of the biggest challenges faced by researchers in the development of battery technologies is to improve the cell performance in terms of enhancing the amount of energy stored in the cell by increasing the energy density of lithium batteries. The energy density (in $\mathrm{W\,h\,g^{-1}}$ or $\mathrm{W\,h\,cm^{-3}}$) of a battery is determined by the product of the equilibrium voltage V_0 of the cell and the capacity Q of reversible charge transfer between the anode and cathode per unit weight ($\mathrm{A\,h\,g^{-1}}$) or unit volume ($\mathrm{A\,h\,cm^{-3}}$). The capacity is given by Equation 1.3 and is defined as the amount of charge per unit weight (or unit volume) that is transported outside the cell during discharge at a constant current I_{dis} over time. M_{w} in Equation 1.3 is the molecular mass of the active electrode material, and gives a gravimetric capacity in $\mathrm{A\,h\,g^{-1}}$, where the scaling factor 3600 converts Coulombs (A s) to the conventional unit, A h.

$$Q = \frac{nF}{3600 M_{\mathrm{w}}} \tag{1.3}$$

Hence Q and V_0 need to be maximised in order to increase energy density, by selecting chemical redox couples with lightweight elements and dense particle morphologies, and large differences in reduction potentials (giving the cell a large electrochemical window). Various high voltage cathodes (greater than 4 V vs. Li^+/Li) are being developed along with the use of lithium metal as an anode material. Lithium has the most negative available redox potential of −3.04 V relative to the standard hydrogen electrode [16], and is the lightest metal in the periodic table, with a specific gravity, ρ, of $0.53\,\mathrm{g\,cm^{-3}}$. It has a high theoretical gravimetric capacity of $3.86\,\mathrm{A\,h\,g^{-1}}$, and can act as its own current collector, thus facilitating design of high energy density storage systems [13, 17, 18]. However, during continuous plating/replating cycles, the metal has a tendency to form dendrites with the consequent risk of short-circuit and thermal runaway when used with a liquid electrolyte, as well as reacting with the liquid until a stable solid-electrolyte interphase (SEI) forms as a protective barrier to further reaction. Furthermore, commercially available liquid electrolytes are not electrochemically stable against Li.

Thus a high voltage approach requires the development of new and stable electrolytes which can withstand electrochemical reaction with the electrodes under these conditions. To achieve thermodynamic stability during cell operation, a large electrochemical stability window (E_{g}) is required in which the electrochemical potential of the anode ($\bar{\mu}_{\mathrm{a}}$) and cathode ($\bar{\mu}_{\mathrm{c}}$) must sit within the lowest unoccupied and highest occupied molecular orbitals (LUMO and HOMO, respectively) of the electrolyte (Figure 1.3), thus avoiding the need for a protective SEI layer.

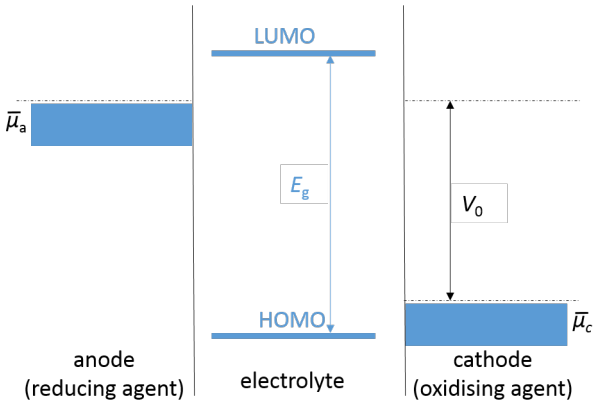


Figure 1.3: Relative energies of the anode and cathode electrochemical potentials, $\bar{\mu}_a$ and $\bar{\mu}_c$, the equilibrium voltage V_0 and the electrolyte window E_g, to achieve thermodynamic stability of the electrode and electrolyte.

1.3 All-Solid-State Batteries

All-solid-state lithium batteries contain anode, cathode and electrolyte in solid state form, and are a potential technology for the next generation of energy storage solutions for grid-level, automobile and consumer electronics. By using a solid state electrolyte in place of a traditional liquid, many of the limitations of conventional lithium ion batteries (particularly in the case of electric vehicles where energy density and safety are critical) can be addressed. Their wide electrochemical window offers the possibility of making use of higher voltage cathodes and metallic anodes, translating into devices enabling larger energy densities for increased driving range between charges in transportation applications. Importantly, by removing the highly flammable organic electrolyte, serious safety issues can be avoided, particularly in the large-format battery packs used in electric vehicles where explosions and fires have attracted much media attention in recent years. Higher operating temperatures, longer cycle life [19] and longer shelf life [20] are all expected to be possible with solid electrolytes owing to their greater stability over their liquid analogues.

There are two general classes of solid state electrolyte materials: lithium conducting inorganic ceramics or glasses, and organic polymers. Currently, polymeric lithium conductors are market leading; however, most are hybrid systems, coupling a polymer with a plasticising organic solvent, leading to safety concerns, leakage and corrosion, as well as barriers to miniaturisation [21]. A promising alternative is to use a ceramic electrolyte. This could be integrated into the cell to form an all-solid-state battery or as a lithium-conducting ceramic membrane acting as a mediator between the cathode-electrolyte and anode-electrolyte compartments.

A viable electrolyte must have an ionic conductivity of at least $1\,\mathrm{mS\,cm^{-1}}$ at room temperature [22]. The biggest challenge for solid state lithium battery development is to achieve high power densities (units of $\mathrm{W\,g^{-1}}$ or $\mathrm{W\,cm^{-3}}$), a property which is limited by both slow lithium transport through the solid electrolyte (lithium ion conductivity) and the interfacial compatibility and kinetics at the electrolyte-electrode interface. For

this reason, understanding and optimising the lithium ion kinetics in the bulk and at the interfaces of solid state battery electrolytes and electrodes is essential for the development of next-generation batteries [23–26].

1.4 In this Thesis

The aim of this work is to investigate the transport properties and reactivity of one particular family of ceramic lithium-conducting electrolytes, the garnet-structured oxides. These materials, based on the formula $Li_7La_3Zr_2O_{12}$ (LLZO), are widely viewed as one of the most promising families of electrolyte materials for use in solid state lithium ion conducting batteries, owing to their large electrochemical window, good lithium ion conductivity and chemical stability against lithium metal. These materials are reviewed extensively in Chapter 3. The properties of these materials are investigated through a number of experimental studies, using the experimental methods described in Chapter 4. Firstly, the factors which contribute to optimal ionic conductivity during synthesis (relating to doping strategies and synthesis conditions) are studied in Chapter 5, intended to build on and make sense of existing research. Next, the stability of LLZO in air and water is investigated in Chapter 6, and the associated degradation processes are characterised, chemically and electrochemically, to develop a good understanding of moisture reactivity and its effect on the performance of LLZO in an electrical device, as well as the associated handling and operating implications. In Chapter 7, an experimental method for determining macroscopic diffusion of lithium in LLZO is introduced, using a stable lithium isotope technique. It is shown to be a promising complimentary technique for observing true long-range diffusion of lithium ions in lithium conductors, given further development. Finally, Chapter 8 deals with the lithium dendrite problem in solid state cell setups using garnet electrolyte with a lithium metal electrode, which occurs during cell cycling above a composition-dependent variable threshold current density and results in cell failure. Chemical analysis is used to attempt to explain the mechanism for dendrite formation and propagation.

Chapter 2

Theoretical Considerations

This chapter serves to give an outline of the basic theory underlying ionic transport in ceramics, and the role of defects in enabling this. The theory of diffusion and its application to ionic conductors is explored, and is extended to include a discussion of the measurement of ionic diffusion in ceramic materials (in particular the diffusion of lithium) by various experimental techniques. Isotopic tracer diffusion is placed under special focus, as it is included in this thesis as a technique for measuring proton (H^+) and lithium ion (Li^+) mass transport. Finally, the fundamentals of electrochemistry in lithium ion batteries is explained and related to the main challenges facing their development, and applied to an all-solid-state battery framework.

2.1 Defect Chemistry and Ionic Transport

In electrochemical energy storage systems such as lithium batteries, the lithium defects are mobile and the other defects are generally considered frozen owing to the operation temperature (nominally room temperature) being lower than the melting points of the electrode and electrolyte materials [27]; however, there are some exceptions to this [28]. Defect chemistry needs to be considered to understand the equilibrium behaviour and charge/discharge properties of the system.

2.1.1 Defects in Crystals

A defect is a deviation from an idealised crystal structure, and such imperfections determine a multitude of properties such as electrical, diffusional, mechanical and optical characteristics. Defects are classified into two main categories depending on their dimensionality, namely point defects and extended defects. Point defects (zero-dimensional) occur where atoms are missing (vacancies) or occupy the interstices between normal sites (interstitials); substituted atoms are also classed as point defects. Extended defects can include one-dimensional line defects, such as dislocations, and two-dimensional planar defects, which describe a discontinuity in the crystal structure, such as a grain boundaries. Three-dimensional defects also exist, and are aggregates of atoms or vacancies [29, 30]. Here the discussion will be limited to point defects occurring

in oxides.

The introduction of defects in a crystal must obey charge neutrality, which means that defects often appear in pairs of opposite effective charge. Effective charge describes the electrical charge a defect carries relative to its surrounding lattice, and as such the net excess charge given to the crystal when the defect is introduced. It can be described by Kröger-Vink notation [31], where a defect carrying an effective single positive charge bears a superscript dot ($^{\bullet}$), and a defect carrying an effective negative charge bears a superscript prime ($'$).[1]

Electronic defects can also be used to charge-compensate ionic defects. For example, an oxygen vacancy $V_{\mathrm{O}}^{\bullet\bullet}$ may be neutralised by a divalent cation vacancy V''_{cation} (a Schottky Pair, see below), but it may also be compensated by being associated with two electrons, 2e′. Likewise, a divalent cation vacancy might be compensated by association with two positive holes (absence of an electron).

Intrinsic Defects

Intrinsic defects are thermally generated in a perfect crystal through disorder and, at all temperatures above absolute zero, a statistical description akin to Boltzmann's distribution can be used to quantify the expected defect concentration. This is because the change in the Gibbs free energy ΔG of the system given by Equation 2.1 is thermodynamically favourable if the non-configurational[2] entropy change ΔS is greater than the defect formation enthalpy ΔH, which holds for defect formation at a given temperature T above 0 K as disorder is generated in the system.

$$\Delta G = \Delta H - T\Delta S \tag{2.1}$$

The equilibration concentrations of defects (where the Gibbs free energy is at a minimum) in a simple binary oxide MO are given by Equations 2.2 and 2.3 [30]:

$$n_{\mathrm{S}} \approx N \exp\left\{-\frac{\Delta H_{\mathrm{S}}}{2kT}\right\} \tag{2.2}$$

$$n_{\mathrm{F}} \approx (NN')^{1/2} \exp\left\{-\frac{\Delta H_{\mathrm{F}}}{2kT}\right\} \tag{2.3}$$

where n_{S} and n_{F} are Schottky and Frenkel defect concentrations, respectively (see below for a description of these types of disorder); ΔH_{S} and ΔH_{F} are the enthalpy changes accompanying the formation of the associated defects; N is the concentration of anions or cations and N' is the concentration of available interstitial sites; k is Boltzmann's constant.

Typically, $\Delta H_{\mathrm{S}} \sim 2$ eV, such that at 1000 K, $n_{\mathrm{S}}/N \sim 10^{-6}$ i.e. 1 ppm defect concentration [32, 33]. Higher defect concentrations can be retained at room temperature if cooling is

[1] In Kröger-Vink notation the main body of the notation identifies the species (e.g. a Zr for a Zr ion or V for a vacancy) and the subscript denotes the lattice site which the species is occupying in the host lattice (i is used for an interstitial). Superscript × denotes zero effective charge.

[2] Non-configurational entropy is associated with changes in lattice strain and vibrational frequencies accompanying the defect; configurational entropy is due to the possible arrangement of the defects and is accounted for in the expression.

rapid compared to the rate at which the defect is eliminated.

The two most common causes of crystalline point defects are Frenkel- and Schottky-disorder. A Frenkel defect is a misplaced ion, so a crystal with Frenkel disorder contains vacancy-interstitial pairs caused by ion migration to an interstitial position. Frenkel defects depend on the existence in a lattice of empty spaces that can accommodate displaced ions. An example of a Frenkel defect is a Zr^{4+} ion occupying interstitial sites in the ZrO_2 fluorite structure, described by Equation 2.4 in Kröger Vink notation, where V''''_{Zr} is a zirconium vacancy, $Zr_i^{\bullet\bullet\bullet\bullet}$ is the Zr interstitial and 'null' indicates the creation of defects from a perfect lattice.

$$\text{null} \rightleftharpoons V''''_{Zr} + Zr_i^{\bullet\bullet\bullet\bullet} \tag{2.4}$$

Anti-Frenkel defects are so called because instead of a cation interstitial, an anion occupies the interstitial site, creating a vacancy with positive effective charge, for example the fluoride interstial F'_i in the fluorite CaF_2 structure (Equation 2.5).

$$\text{null} \rightleftharpoons V_F^{\bullet} + F'_i \tag{2.5}$$

Schottky defects consist of both cation and anion vacancies in stoichiometric amounts to maintain charge neutrality. This involves the creation of new lattice sites in the stoichiometric ratio, i.e. the crystal gets larger, which is measurable in metals. In ZrO_2, this may be written as:

$$\text{null} \rightleftharpoons V''''_{Zr} + 2V_O^{\bullet\bullet} \tag{2.6}$$

Extrinsic Defects

Extrinsic defects may be created in a solid solution as substitutional or interstitial species, which can be introduced by the addition of non-native species (dopants) or by synthesising the material with non-stoichiometry, for example through control of the precursor concentrations or through atmospheric control (i.e. altering the partial pressure of oxygen).

Any substituent ion with a higher positive charge than the ion it replaces, such as Ga^{3+} on a Li^+ site in LLZO, is termed a 'donor'. The defect $Ga_{Li}^{\bullet\bullet}$ is compensated for by two V'_{Li} species, in the case of doping in LLZO (Equation 2.7).

$$Ga_2O_3 \xrightleftharpoons{\text{LLZO}} 2Ga_{Li}^{\bullet\bullet} + 4V'_{Li} + 3O_O^{\times} \tag{2.7}$$

An ion of lower charge than the one it replaces is called an 'acceptor', e.g. Ga^{3+} on a Ti^{4+} site in $BaTiO_3$. Ga'_{Ti} will have an effective negative charge, which can be compensated for by a positively charged oxygen vacancy or an interstitial positively charged cation or a 'hole' in the conduction band.

Changes in lattice parameter of crystals may be determined experimentally by X-ray diffraction (XRD), and it might be expected that changes in volume caused by introduction of dopants might be a straightforward way to estimate defect concentrations by invoking

Vegard's Law, which describes a linear relationship between dopant concentration and change in lattice volume in an ideal solid solution [34]. In the supervalent-doped $Li_7La_3Zr_2O_{12}$ garnet structure, in which donor dopants are charge compensated for by Li vacancies in order to maximise the conductivity (for more discussion see Chapter 3, Section 3.2.4), determining the optimal dopant concentration has remained a problem, however. This is due to the difficulty of establishing the actual (instead of nominal) stoichiometry of intentionally doped atoms in the bulk material and also that it is still not entirely clear what level of lattice expansion/contraction best promotes Li diffusion, despite the lattice parameter being relatively straightforward to measure using high resolution X-ray or neutron diffraction [35].

2.1.2 Conductivity

Long range charge transport in ceramics may be ionic, electronic or a mixture of both in nature. In ideal electrolytes, purely ionic transport occurs, and the charge carriers are anions or cations. In electrodes, the charge carriers are electrons and ions. The total conductivity, σ, in a ceramic is given by the sum of the partial conductivities associated with each charge carrier:

$$\sigma = \sum_i \sigma_i \tag{2.8}$$

Each partial conductivity, σ_i, is given by

$$\sigma_i = n_i q_i \mu_i \tag{2.9}$$

where n_i is the charge carrier density, q_i is the effective charge on the carrier, and μ_i is the mobility. Both carrier density and mobility depend on composition, temperature and atmosphere. Most often, a single charge carrier dominates due to large differences in mobility and carrier density for different species in a ceramic, for example in electrolytes with negligible electronic conductivity. The transport number, τ_i, determines the partial conductivity of a charge carrier in terms of the total conductivity (Equation 2.10) [32]. This description is based on the assumption of dilute solution theory where each of the mobile species do not interact with each other.

$$\tau_i = \frac{\sigma_i}{\sigma} \tag{2.10}$$

Ionic conduction depends on the presence of vacant sites into which ions can move, and in the absence of an applied field, thermal vibrations proportional to T may cause ions and vacancies to exchange sites [30]. This so-called self-diffusion is linked to the conductivity, which is the ionic drift caused by an electric field by the Nernst-Einstein relation [32]:

$$D_i = \frac{\sigma_i kT}{n_i q_i^2} \tag{2.11}$$

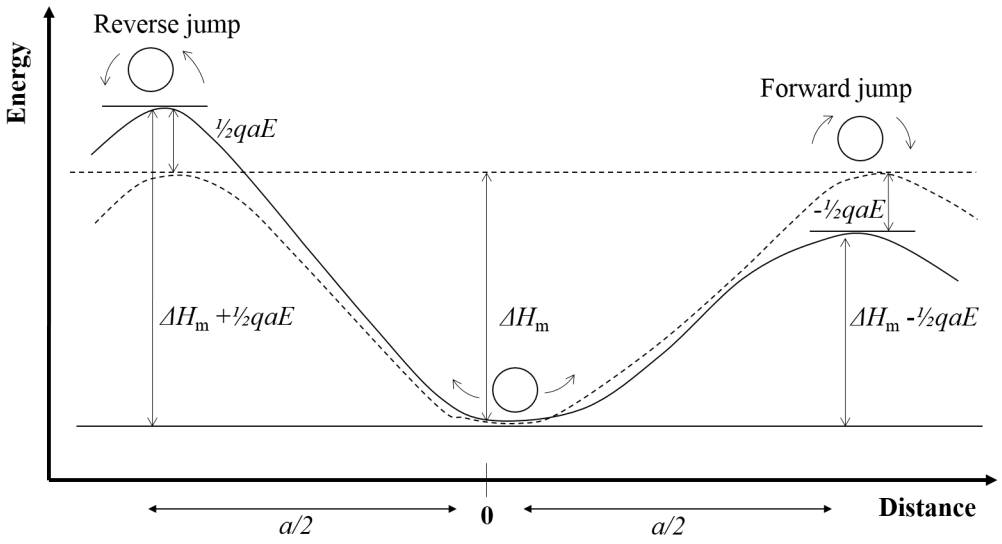


Figure 2.1: Schematic illustration of the effect of an electric field on the migration of charged species in a homogeneous crystal. The dashed line represents the energy profile in the absence of an electric field E, where ΔH_m is the activation energy, and the solid line indicates the behaviour under application of field. On applying a field, in the forward direction the activation energy may be considered to be lowered by $\frac{1}{2}aqE$ and increased by the same amount in the reverse direction, where a is the separation between forward and reverse jump positions and q is charge of the mobile species. Figure adapted from Norby [32].

where D_i is the self-diffusion coefficient for an ionic species i, assuming random-walk diffusion of the particle in the absence of a chemical potential gradient [36]; n_i is the charge carrier density (which is derived from N/unit cell volume, where N is the number of charge carriers in the unit cell). Again, this description is valid for dilute solutions only.

Current flow in ionic conductors occurs by ion hopping of, e.g. Li^+, ions between crystal lattice sites with a superimposed drift by an applied electric field E (Figure 2.1). Ion hopping is thermally activated, and there exists an energy barrier, or activation energy, ΔH_m associated with this process, which must be overcome for the hop to take place (assuming the destination site is vacant). There is no net transport of charge without an externally applied electric field, as the ion hopping occurs at random and the activation energy is the same in all equivalent directions in a homogeneous crystal (illustrated by the dashed line in Figure 2.1), being a function of the three-dimensional angle of the hop.

On applying an electric field, the activation energies are changed, and there is a difference in the energy levels in the forward and backward directions. In the forward direction of the field (downhill) the activation energy is reduced to $\Delta H_\mathrm{m} - \frac{1}{2}aqE$ and in the reverse (uphill) direction increased to $\Delta H_\mathrm{m} + \frac{1}{2}aqE$. The $\frac{1}{2}aqE$ term corresponds to the work done by the applied field E moving a charge q by distance $\frac{a}{2}$ in the direction of the field. Thus hopping events are more probable in the direction of the applied field.

The net flux density of a hopping charge carrier in an electrical field, and thus the conductivity, is proportional to the self-diffusion coefficient, as seen in Equation 2.11. This Nernst-Einstein relation is derived assuming random diffusion, thus it is meaningful for

relating electrical and diffusional transport of atoms and ions. In evaluating the activation energy associated with the diffusion coefficient from conductivity measurements, it is necessary to plot $\ln(\sigma_i T)$ against $1/T$, from the expression of conductivity in terms of the exponent of the activation energy. It is also important to note that in the derivation of Nernst-Einstein it is implicitly assumed that the ions and electrons move independently of each other, e.g. that there is no interaction between ionic and electronic flows [32].

2.2 Fundamentals of Diffusion

As already seen, solid state diffusion is the mechanism by which ionic transport occurs in ceramic materials. In the literature, many different terms are used to describe diffusional behaviour under differing experimental conditions. This section will discuss the fundamental equations underpinning these different types of diffusion and their solutions as applied to the system under study as laid out by Fick (1855) [37] and Crank (1956) [38].

2.2.1 Fick's Laws

The transfer of matter due to random molecular motion is quantitatively described by Fick's first law, which uses the hypothesis that the rate of flow of a diffusing substance through an isotropic medium (given by the flux j, flow rate per unit area) is proportional to the concentration gradient ($\frac{\mathrm{d}C}{\mathrm{d}x}$) measured normal to the section (Equation 2.12)

$$j = -D\frac{\mathrm{d}C}{\mathrm{d}x} \tag{2.12}$$

where C is the concentration of the diffusing species and x is the space coordinate measured normal to the section, and the proportionality constant D is the diffusion coefficient (units of length^2 time^{-1}). The negative sign arises because diffusion occurs in the direction opposite to that of increasing concentration.

Fick's first law assumes a fixed concentration gradient across the plane through which the flux occurs. However, in many cases the concentration and concentration gradient changes with time. Such cases are covered by Fick's second law. The change in concentration per unit time at any position is proportional to the gradient in flux at that position, given in Equation 2.13:

$$\frac{\partial C}{\partial t} = -\frac{\partial j}{\partial x} \tag{2.13}$$

When combined Fick's first law, which is valid at any one time and position, gives Equation 2.14.

$$\frac{\partial C}{\partial t} = \frac{\partial}{\partial x}\left(D\frac{\partial C}{\partial x}\right) \tag{2.14}$$

And as D is not a function of location, and is independent of concentration, this becomes:

$$\frac{\partial C}{\partial t} = D\frac{\partial^2 C}{\partial x^2} \tag{2.15}$$

Equation 2.15 is a linear second-order partial differential equation for the concentration field $C(x,t)$. It may be solved explicitly under certain boundary conditions that may be closely approximated experimentally (Crank [38]), as described in Section 2.2.3.

Atoms in a crystal vibrate due to thermal motion, with a given Debye frequency. Using a non-correlated, random-walk model of ionic transport, we can obtain an expression for three-dimensional movement of particles (flux density j) making jumps across a distance a with an average jump frequency, ν, under a concentration gradient $\frac{\mathrm{d}C}{\mathrm{d}x}$, given by Equation 2.16.

$$j = -\frac{1}{6}a^2\nu\frac{\mathrm{d}C}{\mathrm{d}x} \tag{2.16}$$

Combining with Fick's first law (Equation 2.12), we obtain an expression for the self-diffusion coefficient D in the three-dimensional case:

$$D = \frac{a^2\nu}{6} \tag{2.17}$$

Also, considering a large number of jumps n occurring in time t, such that $\nu = n/t$, then inserting into Equation 2.17, we get:

$$na^2 = 6Dt \tag{2.18}$$

Although the number of jumps is very large, the mean displacement of each atom is relatively small, as it mostly moves back and forth around the same position and only a small fraction of the vibrations leads to a jump. As it is not possible to observe the individual jumps, it is necessary to obtain an expression to link the individual atomic jumps for a large number of atoms and the diffusion phenomena that we can observe macroscopically. Equation 2.18 is equal to the square of the displacement of a randomly diffusing atom, R^2, which is a version of the Einstein-Smoluchowski relation (Equation 2.19). The mean displacement is given by the square root of R^2, leaving:

$$R = \sqrt{6Dt} \tag{2.19}$$

where R is the radius of the sphere that a diffusing atom, on average, will distance itself from its starting point, after time t.

Changing this to a single-dimensional displacement (i.e. x-direction only), $R^2 = 3x^2$, where x^2 is the mean square displacement in each orthogonal direction. This leads to an expression for the mean diffusion length x in one dimension in a three-dimensional cubic crystal as:

$$x = \sqrt{2Dt} \tag{2.20}$$

The expressions given in this section assume random diffusion, and in most cases

diffusion (as measured experimentally by tracer atoms to give the tracer diffusivity, D^*, see Section 2.2.4) is not completely random, but is correlated to some extent with previous jumps.

2.2.2 Correlated Motion and Long Range Diffusion

In the preceding discussion relating diffusion coefficients to random motion of ions in a crystal, the diffusion coefficients take the form of the self-diffusivity, which will be defined here onwards as D_J, describing the random-jump motion of the atoms in the absence of correlation effects [39]. Correlated motion arises due to electrostatic interactions (i.e. Li^+-Li^+ repulsions in the case of some Li ion conductors), lattice-ion interactions, and other external effects, such as chemical gradients and applied electric fields. To account for the differences in macroscopic (long-range diffusive processes) and microscopic (local, atomic scale) measures of diffusion, correlation factors are used and defined by the ratio of the two diffusion coefficients. For example, the tracer diffusion coefficient, D^*, for correlated diffusion of an atom in a crystal is related to the self-diffusivity D_J through a correlation factor f, given in Equation 2.21 (assuming no significant isotope effects) [40, 41].

$$D^* = fD_J \tag{2.21}$$

The correlation factor is governed by the crystal structure and the diffusion mechanism. $f = 1$ for random, uncorrelated motion, and $0 < f < 1$ for correlated motion (where there is an increased likelihood of backward hopping following any given jump). Tracer diffusion can be measured using isotopic tracer methods (more detail follows in Section 2.2.4).

Likewise the thermodynamic factor Θ deviates from 1 to compensate for the the driving force underlying diffusion in the presence of a chemical potential (Equation 2.22):

$$D_C = \Theta D_J \tag{2.22}$$

Here D_C is the chemical diffusion coefficient, described by Fick's laws and defined as the macroscopic response of the diffusing system in the presence of a concentration gradient (i.e. in the case of proton diffusion during H_2O exchange on the LLZO pellets in Chapter 6 (Section 6.2), or, to a lesser extent, ^{6}Li diffusing into LLZO from a ^{6}Li metal source without a pre-equilibrium anneal in Chapter 7).

Correlation effects also arise under the presence of an applied electric field: the Nernst-Einstein relation in Equation 2.11 makes the assumption that the availability of mobile defects is unchanged by an external electric field; hence the diffusion measured is equal to the self-diffusion. However in reality this is often not true, and another correlation factor f_c needs to be used to describe this non-ideality:

$$D^\sigma = f_c D_J \tag{2.23}$$

D^σ is the electrochemical impedance spectroscopy (EIS)-derived diffusivity using

the Nernst-Einstein relation, as already discussed. The Haven ratio, H_R, is the ratio of D^*/D^σ (Equation 2.24) and quantifies whether an observed conductivity is due to a single charge carrier or several carriers [41, 42]. For single ions diffusing via random jumps, $H_R = f = f_c = 1$ and $D^* = D_J = D^\sigma$. A large Haven ratio (> 2) indicates highly correlated ionic motion, and is observed in many fast-ion conductors [43].

$$H_R = \frac{D^*}{D^\sigma} = \frac{f}{f_c} \tag{2.24}$$

2.2.3 Solutions to the Diffusion Equation

The tracer method allows measurements of diffusion in homogenous materials- that is, without imposing chemical gradients (disregarding the difference in atomic weight between atoms in the crystal and of the tracer, known as the isotope effect). A common technique is to deposit a film of stable minor isotope on a plane surface of a sample and determine the activity of the diffusing species as a function of distance from the plane surface. If the thickness of the sample is much larger than the penetration depth of the tracer, the solid can be considered semi-infinite. Furthermore, if the diffusion is homogenous (e.g. taking place by lattice diffusion, as opposed to grain boundary transport), the concentration of the diffusing tracers normal to the plane is through a solution of Fick's second law with appropriate boundary conditions. If the concentration of the diffusing species at the surface (C_s) is constant (which is unlikely for a film source described above), the diffusion can be given by Equation 2.25 [32, 38]:[3]

$$\frac{C - C_0}{C_s - C_0} = 1 - \operatorname{erf} \frac{x}{2\sqrt{D^* t}} = \operatorname{erfc} \frac{x}{2\sqrt{D^* t}} \tag{2.25}$$

where $C = C(x, t)$ is the concentration of the diffusing species at penetration distance x at time t, $C_s = C(0, t)$ is the constant surface concentration, and $C_0 = C(x, 0)$ is the initial concentration in the solid. The diffusion profile for this setup is illustrated in Figure 2.2, in the case where $C_0 = 0$. The penetration and amount of diffusing species in the solid are proportional to $\sqrt{t}$.

In the well-established oxygen isotopic exchange tracer diffusion method for bulk oxygen ion conductors [45, 46], a sample is allowed to exchange with an enriched isotope source of known concentration (involving an 'exchange anneal' with, e.g., ^{18}O gas) and the isotopic fraction is measured as a function of distance from the source. The flux of the isotopes across the surface, $-D^*(\frac{\partial C}{\partial x})|_{x=0}$ is directly proportional to the difference in the ^{18}O concentration between the surface, C_s, and the gas, C_g, for a given time t. The constant of proportionality is known as the exchange coefficient, k^*.

This particular system (Case 1), is illustrated in Figure 2.3a and is modelled as one-dimensional, semi-infinite diffusion under the following system and conditions for surface exchange boundary and uniform initial conditions:

[3] The mathematical function erf z, known as the error function, is given by $\operatorname{erf} z = \frac{2}{\sqrt{\pi}} \int_0^z \exp(-\eta^2) d\eta$, and has the properties $\operatorname{erf}(-z) = -\operatorname{erf} z$, $\operatorname{erf}(0) = 0$; $\operatorname{erf}(\infty) = 1$; $1 - \operatorname{erf} z = \operatorname{erfc} z$.

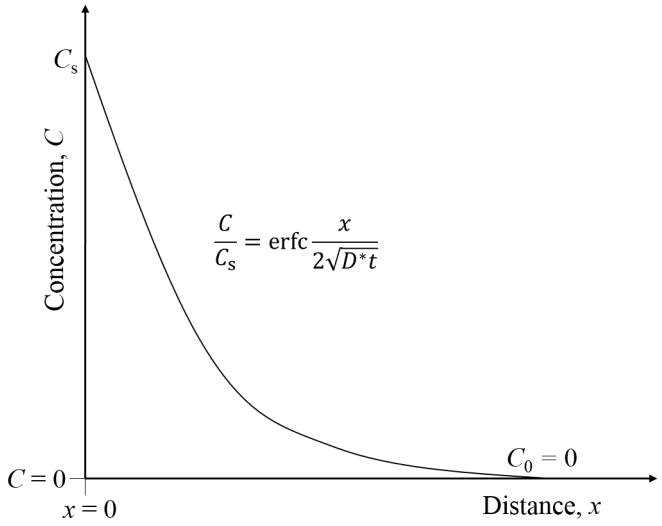


Figure 2.2: Graphical representation of a diffusion profile when the surface concentration $C_s = C(0, t)$ of the diffusing species remains constant with time, and the initial concentration of solid, C_0, is equal to zero (Equation 2.25).

$$\begin{cases} \frac{\partial C'}{\partial t} = D^* \frac{\partial^2 C'}{\partial x^2} & \forall (x, t) \in (0, \infty) \times [0, \infty); \\ C'|_{t=0} = 0 & \forall x \geq 0; \\ C'|_{x=0} = 1 + \frac{D^*}{k^*} \frac{\partial C'}{\partial x}|_{x=0} & \forall t > 0; \\ \lim_{x \to \infty} C'(x, t) = 0 & \forall t > 0. \end{cases}$$

C' is the normalised isotopic concentration at each point as defined by Equation 2.26:

$$C'(x, t) = \frac{C(x, t) - C_{bg}}{C_g - C_{bg}} \tag{2.26}$$

where C_{bg} is the background isotropic fraction throughout the sample initially (C_0 in Equation 2.25) and C_g is the isotopic fraction of the exchange gas (source of minor isotope).

The solution to this semi-infinite diffusion system, Case 1, is given by Equation 2.27:

$$C'(x, t) = \text{erfc}\, \frac{x}{2\sqrt{D^*t}} - \exp\left\{\frac{k^* x}{D^*} + \frac{k^{*2} t}{D^*}\right\} \text{erfc}\left\{\frac{x}{2\sqrt{D^*t}} + k^* \sqrt{\frac{t}{D^*}}\right\} \tag{2.27}$$

The above solution can be expressed more concisely by two non-dimensional parameters, x' and h':

$$C'(x', h') = \text{erfc}\, x' - \exp(2x'h' + h'^2)\, \text{erfc}(x' + h') \tag{2.28}$$

where

$$x' = \frac{x}{2\sqrt{D^*t}} \tag{2.29}$$

$$h' = k^* \sqrt{\frac{t}{D^*}} \tag{2.30}$$

The normalised depth x' is the distance from the exchange surface, scaled with respect

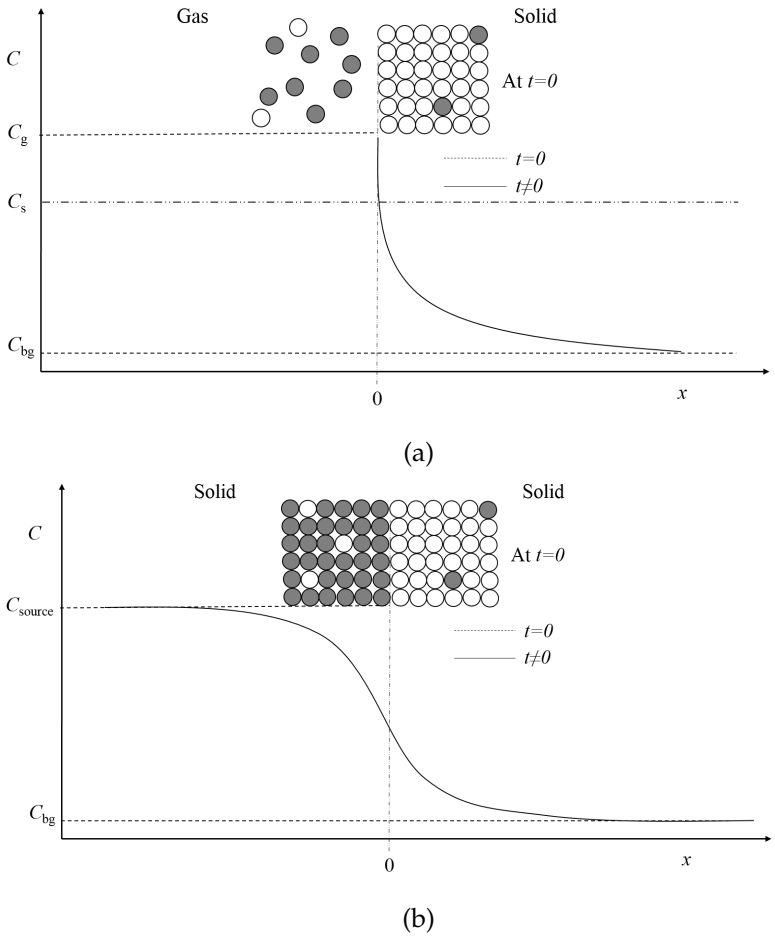


Figure 2.3: Diffusion profiles (a) Case 1: gas-solid couple boundary conditions for one-dimensional semi-infinite diffusion, with constant gas concentration C_g and surface concentration C_s; (b) Case 2: solid-solid couple in which the source ($x < 0$) concentration C_{source} changes with time.

to a characteristic diffusion length, $2\sqrt{Dt}$, and used to more easily compare experiments with different exchange durations. h' describes the relative influence of the surface (k^*) and bulk (D^*) processes. In Chapter 6 of this thesis, where proton diffusivity in LLZO pellets is evaluated by using a D_2O source of D^+ following an initial exchange in H_2O, the diffusion is approximated to the Crank solution illustrated here (Case 1). The dimensionless parameter, x', is used to find D from the length x at which background concentration is reached in the profiles (i.e. $C'(x,t)$ approaches zero). This is approximated to the value at $x' = 2$, i.e. $x = 4\sqrt{(Dt)}$, taken from Figure 3.4 of Crank [38].

In the case of a source of tracer ions whose concentration C_{source} changes as a function of exchange time, such as a thin film enriched crystal deposited on a chemically identical (but not isotopically enriched) bulk crystal, Case 2, illustrated in Figure 2.3b, applies. The following boundary conditions are used:

$$\begin{cases} \frac{\partial C'}{\partial t} = D^* \frac{\partial^2 C'}{\partial x^2} & \forall (x,t) \in (0,\infty) \times [0,\infty); \\ C'|_{t=0} = 1 & x < 0; \\ C'|_{t=0} = 0 & x \geq 0. \end{cases}$$

The amount of diffusing species remains constant and equal to the amount originally present in the source. The solution for Case 2 is given by:

$$C'(x,t) = \frac{1}{2} \operatorname{erfc} x' \tag{2.31}$$

Where C' is here defined as:

$$C'(x,t) = \frac{C(x,t) - C_{\text{bg}}}{C_{\text{source}} - C_{\text{bg}}} \tag{2.32}$$

In this work, a lithium-6 metal source in contact with LLZO (see Chapter 7) is used as a diffusion couple for estimating the lithium diffusivity in LLZO. This special case cannot be strictly modelled on either Case 1 (Crank solution for semi-infinite diffusion) or Case 2 described above for the following reasons: the lithium diffusivity D^* differs in both parts of the couple (so cannot be modelled as Case 2), there exists an interfacial resistance (i.e. k, again contrary to Case 2) and it occurs in a finite domain (thus cannot be applied to semi-infinite diffusion). However, owing to limitations in the experimental data and for the purpose of obtaining an approximation of D, the diffusion is modelled on Crank's solution. Thus, the dimensionless parameter $x' = 2$ is used to find D from the length x at which background concentration is reached in the profiles ($x = 4\sqrt{(Dt)}$).

2.2.4 Experimental Methods to Determine Lithium Diffusion

There are several experimental methods which exist for studying diffusion in solids, each with a different range of diffusivities which are able to be measured and which can be grouped into two categories: direct and indirect methods. Direct methods are based on Fick's laws and are sensitive to long-range diffusion (and thus are macroscopic). Indirect methods usually study phenomena which are influenced by the diffusion jumps of atoms, often sensitive to single or a few atomic jumps only. Examples of both types of methods are summarised in Table 2.1.

Microscopic (Indirect Methods)

Microscopic methods such as nuclear magnetic resonance (NMR) and EIS usually study phenomena which are influenced by the diffusional jumps of atoms in solids. Some of these methods are sensitive to a few atomic jumps only. In these cases local hopping is measured, e.g. hopping in traps for instance around impurity atoms. This can be different from the long range transport especially if the traps are deep. Quantities such as relaxation times, chemical shifts and linewidths are measured to determine the mean residence time of the diffusing atoms, τ, and the Einstein-Smoluchowski relation (seen in Equation 2.19) is used to deduce the diffusivity D in the simple case of uncorrelated

Table 2.1: Summary of indirect and direct methods for experimentally determining diffusivity in solids [47].

Direct Methods	**Indirect Methods**
Tracer diffusion (stable isotopic exchange method and radiotracer method) + profiling (i.e. SIMS)	Nuclear magnetic resonance spectroscopy (NMR)
Chemical diffusion + profiling	Impedance spectroscopy (EIS)
Nuclear reaction analysis (NRA)	Mossbauer spectroscopy
Neutron radiography	Quasi-elastic neutron scatterimg (QENS)
Pulsed field gradient NMR (PFG NMR)	Positive muon-spin relaxation (μ^+SR)

motion.

Impedance spectroscopy is the most-used method for temperature-dependent characterisation and resolution of the components of direct current (DC) conductivity, and uses the Nernst-Einstein relation to convert conductivity, σ, to charge diffusivities, D^σ. However, the technique is not *a priori* lithium selective, but is a medium/long range probe for ionic motion (so in a sense, is an indirect, semi-macroscopic technique). This technique is described in more detail in Chapter 4, Section 4.7.1.

NMR relaxation methods, however, are explicitly selective on Li motion and probe local jump frequencies on short length-scales (see Chapter 4, Section 4.6 for more details of the technique) [48]. These have to be converted into diffusivities using model assumptions (including accounting for correlation factors and the Haven ratio, Section 2.2.2), but can access self-diffusion coefficients across a large range ($D \sim 10^{-10}$ to 10^{-20} $m^2\,s^{-1}$) [47]. Direct diffusion measurement is also possible with the use of field gradient (FG) NMR, which is described under the section 'Macroscopic (Direct Methods)'.

Diffusion-induced NMR relaxation rates are governed by a motional correlation function which describes the dynamics of ions present. This function tells us about the mean correlation rate of the dynamic process under study, deviations from random motion (correlation effects), and the dimensionality of the ion hopping process [49]. To compare Li jump rates deduced from spin-lattice relaxation NMR measurements with EIS data, we use the Nernst-Einstein and Einstein-Smoluchowski equations (Equations 2.11 and 2.19, respectively). The first connects the real part of the complex bulk conductivity, with the tracer diffusion coefficient, D^*, via the Haven ratio H_R. Combined with the Einstein-Smoluchowski expression for uncorrelated motion, the DC conductivity and jump rate can be related.

Quasi-elastic neutron scattering (QENS) provides a microscopic measure of the jump diffusion coefficient D_J by observation of the energy and angular dependence of the neutron scattering function and their comparison to theoretical models, but is limited to relatively fast diffusion processes; thus is restricted to transport measurement in high-temperature Li ion conductors [50].

Positive muon-spin relaxation (μ^+SR) spectroscopy is a recent addition to the toolkit for investigating Li transport [51, 52]. Upon decay of a muon, the direction of the emitted positron is preferentially aligned with the parent muon's magnetic moment. Relaxation processes with nearby lithium nuclei are used to determine the rate of ionic hopping in an analogous way to NMR relaxometry, where μ^+SR probes time-space whereas NMR probes frequency-space. The technique has a limited time window owing to the muon decay process and is too sensitive to detect D(Li) above about 10^{-12} m^2 s^{-1}, and the low-energy muon beam has 200 nm probing depth and 1 to 10 nm resolution [50]. In addition, as with NMR and QENS, only powder samples can be measured and so no microstructural effects on diffusivity are probed with these techniques, i.e. grain boundary effects.

As such, discrepancies exist between the measured activation energy of Li hopping as measured by QENS, NMR and μ^+SR compared to those determined from AC impedance measurements. This is due to additional factors influencing the Li diffusion on top of simply the intrinsic nature of the Li-conducting solid, such as grain boundaries, impurities and other defects [43, 50]. Additionally, even when comparing bulk with bulk, i.e. when the grain boundary component is fully resolved in impedance analysis, it must be remembered that the DC conductivity measures long range transport, whilst the other techniques measure local hopping.

Without prior knowledge of correlation factors, it is not possible to conclusively separate long- and short-range diffusion as probed by these microscopic techniques. Direct methods are needed to measure long-range diffusivity.

Macroscopic (Direct Methods)

Macroscopic methods such as pulsed field gradient (PFG) NMR and tracer diffusion enable long-range transport of ions to be probed directly, without the need for model assumptions.

The use of isotope tracers in the isotopic exchange method gives an undisputable method for following the movement of a diffusion front of isotopically labelled species through a material to determine the self-diffusion coefficient (ignoring isotope mass effects). The radiotracer method is a commonly-used state-of-the-art technique for metallic materials due to its high detection sensitivity [53]; however, no suitable radioactive tracers are available for the study of Li: ^{8}Li is the only radioactive isotope, with a half-life of just 0.84 s, preventing diffusion studies with this method. However, lithium has two stable isotopes, and the lower abundance ^{6}Li (7.5 %) can be used for lithium self-diffusion experiments using the stable isotope exchange method. This technique involves forming a diffusion couple with one half enriched in the minor stable isotope (^{6}Li), which is allowed to inter-diffuse. Analytical methods are used to study the resulting diffusion profile, following the isotopic fraction as a function of distance (or depth). The technique is termed the isotopic exchange and depth-profiling (IEDP) method. The analytical methods used include secondary ion mass spectrometry (SIMS), nuclear reaction analysis (NRA) and neutron radiography.

SIMS is used in this thesis for following the lithium isotope tracers, and is described

in detail in the Experimental Methods (Chapter 4, Section 4.8). It has been implemented previously to find the lithium self-diffusivity in some lithium-containing oxides and glasses [54–60].

NRA uses high energy, low mass ions such as protons to induce nuclear reactions with the tracer, which are used to follow elemental concentrations - for the detection of ^{6}Li, the nuclear reaction ^{6}Li(d,α)^{4}He can be used [53, 61]. Depth profiling is achieved by varying the energy of the incoming beam, and the method itself is non-destructive.

Neutron radiography makes use of the fact that lithium has a large neutron cross-section which differs by four orders of magnitude between ^{6}Li and ^{7}Li isotopes. Using a ^{7}Li enriched source, a measure of macroscopic lithium diffusion is obtained by observing the time-evolution of spatially resolved neutron transmission rates in the sample [62–64]. However, limits on spatial resolution of the neutron detectors require long diffusion path lengths in order to resolve the diffusion process [65].

Designing and developing an experimental setup to measure tracer diffusion using the IEDP method is the biggest challenge for the accurate determination of tracer diffusion in fast lithium conducting materials (especially, as in the case of the garnet electrolytes, when the room temperature diffusivity is high, $D(\mathrm{Li}) \sim 10^{-13}\,\mathrm{m^2\,s^{-1}}$).

PFG NMR permits direct diffusivity measurement on powder samples without referring to a microscopic model, and has been used to measure diffusivity in some lithium garnets [66, 67]. Field gradient experiments probe macroscopic transport by analysing changes in spin evolution as nuclei migrate through the gradient field. Slow longitudinal relaxation rates permit long diffusion times, allowing sensitivity towards slower diffusion rates [65]. More detail on the technique is given in Chapter 4, Section 4.6 but the reader is directed to the comprehensive book by Sørland for a full overview [68]. Chapter 7 compares such measurements with EIS-derived values and preliminary results for tracer diffusivities.

Mathematical/Modelling Methods

Ab initio statistical mechanics calculations provide insight into both the thermodynamics and kinetics of transport in lithium ion conductors. By combining calculations of activation barriers and pathways for various jump mechanisms with electronic structure calculations and kinetic Monte-Carlo simulations, thermodynamic and kinetic properties can be measured at thermodynamic equilibrium for a range of lithium conductors. Molecular dynamics simulations generate information at the microscopic level, such as atomic positions and velocities, and converting this information to macroscopic observables requires statistical mechanics. Such studies have been used to understand the motion of lithium in LLZO [69–72]. These methods are advantageous in that a large number of material properties can be calculated for a range of materials under different conditions at a faster rate than achievable experimentally.

By combining information on all three classes of diffusivity measurement methods, important information about the nature of Li ion transport can be deduced; in particular,

by comparing NMR, EIS and tracer diffusivity measurements with computational models, mechanistic information on the nature of lithium transport (such as correlation effects), may be obtained.

2.3 Electrochemistry of Lithium Batteries

The main challenges in the development of rechargeable lithium batteries were touched upon in Chapter 1, and are highlighted in the following section. The underlying electrochemical theory is related to these critical properties, which are given below:

1. Safety
   The development of safer lithium batteries requires the development of a non-flammable electrolyte with either a larger electrochemical window between its lowest unoccupied molecular orbital (LUMO) and its highest occupied molecular orbital (HOMO), or the ability to form a solid-electrolyte interphase (SEI) which is able to form rapidly and safely, preventing plating of Li on, e.g. a carbon-based anode during charging. *Electrochemical stability* is key here.

2. Energy density (units $\mathrm{W\,h\,g^{-1}}$)
   The energy density is the product of the *voltage* and *capacity* of reversible Li insertion/extraction to/from the electrodes. These in turn will depend on the match of electrode electrochemical potentials $\bar{\mu}$ and the HOMO/LUMO of the electrolyte, as well as the number of Li ions which can be reversibly transferred.

3. Power (energy transferred per unit time, units W)
   Power and *power density* (power delivered per unit weight of the cell, units $\mathrm{W\,g^{-1}}$) are important properties which are determined by the *charge/discharge rate* of the battery and as such require *high Li conductivities* ($\sigma_{\mathrm{Li}} > 10^{-4}\,\mathrm{S\,cm^{-1}}$ at ambient temperature) in the electrolyte and across the electrolyte-electrode interface.

4. Long service life
   To enable a long service life, the components of the battery must be *chemically compatible/stable*.

5. Environmentally benign, low cost
   These factors are important for commercialisation and a low environmental impact but will not be explored further here.

2.3.1 Basics of a Battery and Electrochemical Stability

As described in Chapter 1, the equilibrium potential, V_0, is described by the difference in electrochemical potentials $\bar{\mu}$ of the two electrodes (the redox couple, comprising the oxidised species '*Ox*' (at the anode during discharge) and reduced species '*Red*' (at the cathode during discharge)) and predicted by the Nernst equation, represented in Equation 2.33 for an n-electron process.

$$V_0 = \frac{\bar{\mu}_{Ox} - \bar{\mu}_{Red}}{nF} = \frac{\Delta\mu^0}{F} + \frac{RT}{nF} \ln\left\{\frac{[Ox]}{[Red]}\right\} \tag{2.33}$$

where $\Delta\mu^0$ is the change in chemical potential for the reaction (a constant at fixed temperature and pressure), R is the gas constant, F is the Faraday constant representing the charge on one mole of electrons and T is the temperature.

During charge, Li is moved from the positive electrode, a level of lower chemical potential, to the negative electrode (higher chemical potential), and vice versa on discharge. The potential is a measure of how much a component is unfavourable in a given phase (i.e. a high lithium chemical potential μ_{Li} is unfavourable). Hence thermodynamic stability (and thus safety) requires locating the electrode potentials within the window of the electrolyte such that $\bar{\mu}_{\mathrm{a}} <$ LUMO and $\bar{\mu}_{\mathrm{c}} >$ HOMO, to prevent reduction or oxidation of the electrolyte [73]. Under these constraints, Equation 2.34 holds:

$$nFV_0 = \bar{\mu}_{\mathrm{a}} - \bar{\mu}_{\mathrm{c}} \leq E_{\mathrm{g}} \tag{2.34}$$

where E_{g} is the HOMO-LUMO energy separation of the electrolyte (known as the electrolyte window). In practice, this means that whatever the potentials of the selected electrodes in a cell, the chosen electrolyte must have a large enough electrochemical window to enable electrochemical stability. The challenge is thus finding an electrolyte with a wide window to enable the largest range of potentials at the electrodes to support a high theoretical voltage cell.

However, a passivating SEI layer at the electrode/electrolyte boundary can lend kinetic stability to a larger V_0 provided $V_0 - E_{\mathrm{g}}$ is not too large, as shown in Figure 2.4. Examples are Li metal or carbon-based anodes with non-aqueous electrolytes where $\bar{\mu}_{\mathrm{a}} >$ LUMO (and which, in the case of the SEI layer breaking up, results in the formation of Li dendrites). The SEI needs to have fast Li^+ transport and must not block electron transfer between the current collector and the active electrode material in order to be effective.

2.3.2 Energy Density and Capacity

The energy density of a battery cell is equal to QV_0, where Q is the capacity of reversible charge transfer per unit weight ($\mathrm{A\,h\,g^{-1}}$) between the electrodes. nF corresponds to the charge transferred (associated with the number of electrons, n), and by maximising the number of lithium atoms transferred at the electrodes, this in turn is maximised. For example, in the $Li_{1-x}CoO_2$ electrode material, the number of Li transferred per transition metal cation is 0.5 (i.e. $n = 0.5$). In graphitic carbon, 1 Li is transferred per 6 C atoms ($n = 1$). This can be determined experimentally by measuring the capacity of each electrode in a half-cell with a Li metal anode.

In practice, Q, and hence the energy density, decreases with the rate of charge/discharge (i.e. the magnitude of electronic current in the external circuit, which has to be matched with the internal ionic current in the cell). This is because the electronic current density is much larger than the ionic current density of the electrodes and electrolyte, including the rate of ion transfer across the interface. Thus at high current

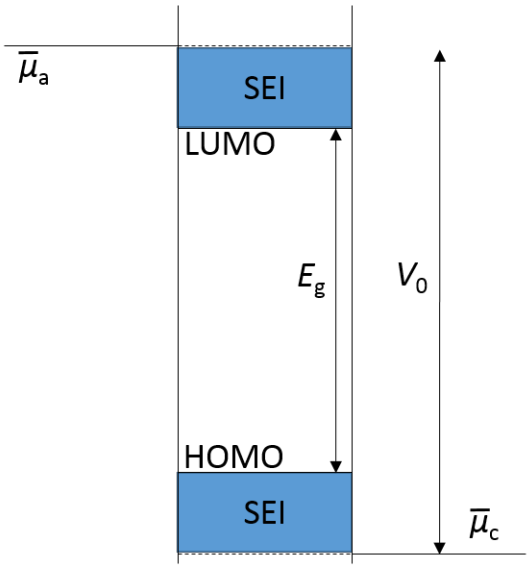


Figure 2.4: Schematic open-circuit energy diagram showing the formation of passivating SEI layers which enable $\bar{\mu}_a >$ LUMO and $\bar{\mu}_c <$ HOMO. E_g is the HOMO-LUMO energy separation of the electrolyte, V_0 is the equilibrium voltage and $\bar{\mu}_a$ and $\bar{\mu}_c$ are the anode and cathode electrochemical potentials, respectively.

densities (high charge/discharge rates), the ionic motion within an electrode and/or across the interfaces with the electrolyte is too slow for charge distribution to reach equilibrium, leading to a decrease in reversible capacity. This in turn has implications on the power output of a cell.

Experimental Capacity

The experimental (practical) capacity can be found by cycling the electrode at a constant current (galvanostatic cycling). This enables quantification of the fraction of exchangeable ions and electrons within the host structure in the electrochemical reaction (the state of charge or SOC, defined as the battery capacity as a percentage of maximum capacity), which can be used to deduce the experimental capacity of the electroactive material (in $\mathrm{A\,h\,g^{-1}}$) under the experimental conditions.

2.3.3 Voltage

As mentioned previously, to increase the energy density of a cell, we need to increase the cell voltage V_0. In an ideal case, $V_0 \geq 4\,\mathrm{V}$ vs. $\mathrm{Li^+/Li}$ [73]. Using a solid state electrolyte is one way to enable this, as it could provide a large electrochemical window, E_g (see Figure 2.4), thus enabling larger voltages to be accessed, if a suitable electrode couple can be found (as $nFV_0 = \bar{\mu}_a - \bar{\mu}_c$).

Figure 2.5 shows a density of states diagram for graphitic $\mathrm{Li_xC_6}$ and $\mathrm{Li_{1\text{-}x}CoO_2}$ electrodes. The value of $\bar{\mu}_a$ and $\bar{\mu}_c$ which will determine V_0, depend on the Fermi energy, E_F, in the itinerant-electron band (as in a carbon electrode), or the energy of a redox couple of a transition metal cation (e.g. $\mathrm{Co^{3+}/Co^{4+}}$ in $\mathrm{Li_{1\text{-}x}CoO_2}$). The redox couple energy also depends on the formal valence state of the cation, the level of covalent

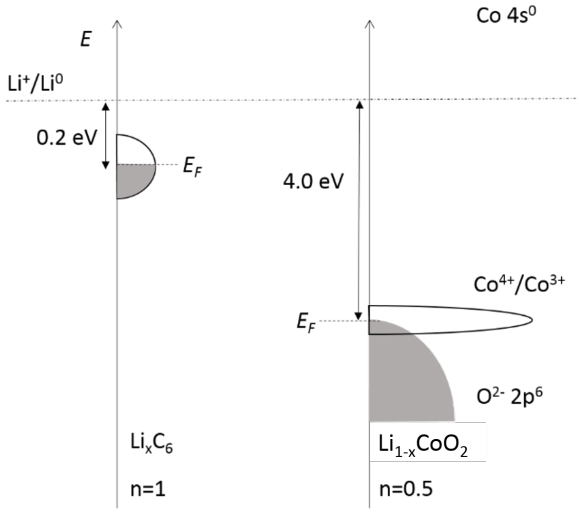


Figure 2.5: Schematic of density of states showing the relative positions of the Fermi energy E_F in an itinerant electron band for Li_xC_6 and the Co^{3+}/Co^{4+} redox couple for $Li_{1-x}CoO_2$, where n is the number of electrons transferred per mole of electrode compound, adapted from Goodenough [73].

nearest-neighbour bonding (i.e. whether with O or S), which in turn is influenced by the presence and nature of the countercations and the crystal structure. In addition, the position of a redox couple relative to the bottom of a broad conduction band or top of an anion p band may determine the intrinsic voltage limit of the electrode (for example, in the case of $Li_{1-x}CoO_2$, the Co redox couple is 'pinned' at the top of the O 2p band, limiting its intrinsic upper voltage to 4.0 V vs. Li^+/Li) [73].

The equilibrium voltage V_0 is the theoretical cell voltage. Often, before current is applied, the electrochemical cell has an open circuit voltage V_{OC} that differs from V_0. $V_{OC} - V_0$ is usually due to surface species yielding an apparent voltage which is not representative of the bulk material. Additionally, during cycling, the voltage profile may move above and below V_0 due to polarisation and resistances from all parts of the cell, this difference between V_0 and discharge V_{dis} or charge V_c, given in Equation 2.35, is the overpotential, η, which is largely ascribed to the impedance for cation transfer within the cell; I_{dis} is the discharge electronic current [74].

$$V_{dis} = V_0 - \eta_{dis} I_{dis} \tag{2.35}$$

2.3.4 Power

Power is a measure of how quickly batteries can deliver stored energy (and given with respect to cell weight or volume when quoted as power density, units of $W\,g^{-1}$). As seen from the Nernst equation in Equation 2.33, the equilibrium voltage V_0 is determined solely by the electrode materials; however, the current generated is influenced by the electrolyte and electrode kinetics. Internal resistances (R_{int}) present in the components of the cell will limit the current and thus the actual power output, P, seen in Equation 2.36.

$$P = P_{(R_{\text{int}} \to 0)} - I^2 R_{\text{int}} \tag{2.36}$$

In a rechargeable cell, electric power is stored as chemical energy and released during the reaction of cathode and anode, when the electronic current is conducted through an external circuit to deliver power, $P_{\text{dis}} = I_{\text{dis}} V_{\text{dis}}$. Increasing the Li ion kinetics in terms of the mobility in the electrolyte (Li conductivity, σ_{Li}) and at the interface with the electrodes, will enable high power batteries to be realised by allowing high currents to be accessed. This is especially critical in the development of all-solid-state batteries, where the electrolyte component is an inorganic solid and typically has lower conductivities than conventional liquid electrolytes. The improvement to conductivity has been pursued extensively in the search for a highly Li-conducting inorganic electrolyte; however, the interface kinetics in solid state batteries are as yet not well understood, but are critical for enabling a high performance all-solid-state battery (see Chapter 3, Section 3.4).

2.4 Summary

In this chapter the fundamentals of defect formation in crystalline oxides have been introduced. Charge and mass transport in ionically conducting materials have been discussed and described in terms of the effect of external electric fields acting on them. This has been extended to a discussion of diffusion, using the Fickian model to describe, and using the solutions of Crank to model, diffusivities. An overview of the various experimental methods in the literature for probing both microscopic and macroscopic diffusion of Li has been given, including a discussion of the effect of correlated motion on measured diffusivities. In particular the use of tracer isotope methods has been discussed as it is of particular interest in this work where it has been developed for use in Li conducting inorganic electrolytes. Finally, an introduction to the basics of electrochemistry in Li ion batteries has been included, highlighting the areas which need to be looked at in order to move to a next-generation of devices.

Chapter 3

Literature Review

The Introduction (Chapter 1) and Theoretical Considerations (Chapter 2) have provided the context for the importance of developing better batteries in order to enable both high-performance portable energy storage systems (including in automotive applications), as well as grid-level systems required for storing electricity generated from intermittent renewable sources. The fundamental requirements for their development have been introduced, highlighting the factors which will need to be improved in order to meet these requirements, and the limitations with current battery technologies.

This chapter will serve to provide a more detailed overview of state-of-the-art all-solid-state batteries, which have the potential to overcome the performance issues associated with current battery technology base on liquid electrolytes. In particular, the focus will be directed on solid state electrolytes, with a literature review of the garnet-structured $Li_7La_3Zr_2O_{12}$ (LLZO) material, as it is the most promising lithium-conducting ceramic and the material of choice for this thesis. The review will include an overview of the structure and transport properties of LLZO, and attempts made to modify these characteristics through doping strategies. Next, a summary of reported degradation behaviour of the material caused by lithium-proton exchange processes during exposure to moisture will be given. Finally, the interfacial stability with lithium metal electrodes and cell charge/discharge cyclability will be reviewed.

3.1 All-Solid-State Batteries and Solid State Electrolytes

Current state-of-the-art lithium ion batteries will soon reach a physicochemical limit for their energy density [75], but the demand for higher power and energy densities will continue to increase. All-solid-state batteries in which the traditional liquid electrolyte is replaced by a solid electrolyte have the potential to address this need for increased energy and power density by enabling the use of new chemistries, in addition to addressing concerns over stability and safety which exist for current technologies. Despite growing interest in solid state batteries, many challenges remain in both manufacturing and fundamental understanding.

Solid state electrolytes offer beneficial features over organic liquid electrolytes, which have been described in Chapter 1 . For successful implementation in lithium batteries, an

electrolyte material must be chosen which fulfils the following requirements [19, 21, 73]:

1. A large electrolyte window, E_g
2. A Li-ion conductivity, $\sigma_{Li} > 10^{-3}\,S\,cm^{-1}$ over the temperature range of battery operation
3. An electronic conductivity, $\sigma_e < 10^{-10}\,S\,cm^{-1}$
4. Retention of the electrode/electrolyte interface during cycling when the electrode changes volume
5. A transference number, $\tau_{Li} = \sigma_{Li}/\sigma_{total} \approx 1$, where σ_{total} includes conductivities by other ions in the electrolyte as well as σ_{Li} and σ_e
6. Chemical stability over ambient temperature ranges and temperatures in the battery under high power
7. Chemical stability with respect to the electrodes, including the ability to form rapidly a passivating solid electrolyte interface (SEI) layer if necessary, where kinetic stability is required because the electrode potential lies outside the electrolyte window
8. Safe materials, i.e. preferably non-flammable and non-explosive if short-circuited
9. Low toxicity and low cost
10. Scalable (important for commercialisation).

Solid electrolytes currently fulfil many of these requirements, in particular points 1-3, 5 and 6-8 in the case of inorganic electrolytes; however, there is still a way to go before all-solid-state batteries can be realised commercially. There are three general classes of solid electrolyte materials for lithium batteries: lithium conducting glasses, organic polymers and inorganic ceramics, which are described below.

Thin film, amorphous LiPON electrolytes with the composition $Li_xPO_yN_z$, where $x = 2y + 3z - 5$, were pioneered at Oak Ridge National Laboratory and are used in all-solid-state microbatteries with intercalation oxide-based cathodes and Li metal anodes [23, 76]. The thin films are physically deposited by, e.g., sputtering. Despite the good chemical stability with electrode materials, the room temperature conductivity σ_{Li} is relatively low ($10^{-6}\,S\,cm^{-1}$) and large-scale production is expensive; hence the application is limited to thin-film devices. Similar to the diffusion process in a crystal structure, ionic transport in glassy materials starts with ions at local sites being excited to neighbouring sites and then collectively diffusing on a macroscopic scale [77].

Lithium-conducting polymer electrolytes (dry-polymer-in-salt), such as polyethylene oxide (PEO), use a polymer host together with a lithium salt to act as a solid solvent. These systems are stable with respect to Li metal, flexible, easy to produce a large-area membrane and have a low shear modulus; however, the ionic conductivity is relatively low at room temperature ($10^{-4}\,S\,cm^{-1}$) and the electrolytes have limited thermal stability and a oxidation voltage of less than 4 V. Composite polymer systems use a ceramic filler

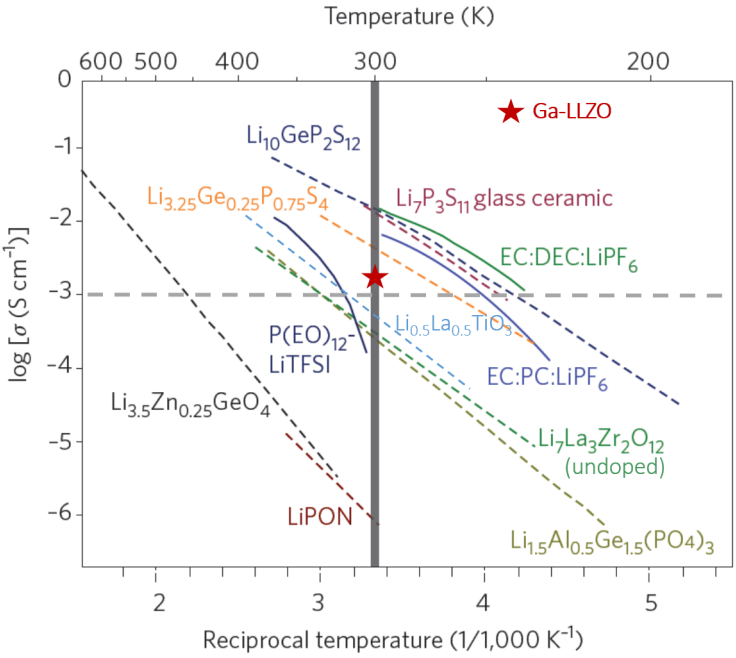


Figure 3.1: Arrhenius plot illustrating temperature dependence of ionic conductivities σ for various solid and liquid electrolytes, from Janek [75]. Solid lines indicate organic electrolytes; dashed lines indicate inorganic electrolytes. The grey vertical line marks room temperature and the horizontal line indicates the target conductivity of 1 mS cm^{-1}. Ga-doped forms of $Li_7La_3Zr_2O_{12}$ (LLZO) have been reported with conductivities exceeding this at room temperature (indicated by the star).

to improve the conductivity by reducing the glass transition temperature [77]. In polymer electrolytes, microscopic ion transport is related to the segmental motion of polymer chains above the glass transition temperature. The segmental motion of the chains can create free volumes for the hopping of lithium ions that coordinate with the polar groups. The number of free ions depends on the dissociation ability of the lithium salt in the polymer [78].

An Arrhenius plot of a range of electrolytes is given in Figure 3.1. A viable electrolyte must have an ionic conductivity of 1 mS cm^{-1} at room temperature [22] (corresponding to $\log_{10}\sigma = -3$ on the plot); current organic liquid electrolyte ethylene carbonate (EC) - propylene carbonate (PC) containing 1 M $LiPF_6$ has a lithium conductivity of 10^{-2} S cm^{-1}. The best conductivity at room temperature to date is that of the $Li_{10}GeP_2S_{12}$ solid electrolyte (σ_{Li} = 12 mS cm^{-1}) reported by Kamaya *et al.* [79], outperforming even liquid electrolytes. However, in-situ X-ray photoelectron spectroscopy studies on the material by Wenzel [80] have shown the material decomposes on contact with metallic lithium into Li_3P, Li_2S and a Li-Ge alloy. This was also predicted by first principles studies by the Ceder group [81]. This highlights a big challenge for solid state electrolyte development in achieving high conductivities whilst maintaining their inherent stability and safety features.

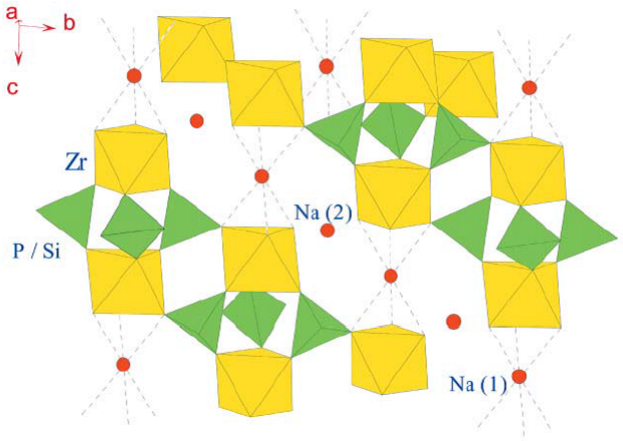


Figure 3.2: Structure of $Na_3Zr_2PSi_2O_{12}$ (NASICON). The red circles denote Na(1) and Na(2) occupying interconnected channels within the skeleton framework of ZrO_6 octahedra and P/SiO_4 tetrahedra. Figure from Sebastian *et al.* [85].

3.1.1 Ceramic Crystalline Electrolytes

Inorganic ceramic crystalline electrolytes conduct ions through both ion and vacancy transport, and the kinetics can be described by an Arrhenius-type relationship (see Chapter 2, Section 2.1.2). Examples of these materials are NASICON-, LISICON-, thio-LISICON-, perovskite- and garnet-type lithium ion conductors.

Nasicon, Lisicon and Thio-Lisicon

The NASICON 'NA SuperIonic CONductor', $NaA^{IV}_2(PO_4)_3$ (A^{IV} = Ge, Ti or Zr) structure, was identified by Kierkegaard in 1968 [82] and then studied in 1976 by Goodenough and Hong [83] in their search for a three-dimensional (3D) network structure based on the anisotropic conduction pathways of β-alumina. It consists of a covalent skeleton $[A_2P_3O_{12}]^-$ of AO_6 octahedra and PO_4 tetrahedra, which form 3D interconnected channels and two types of interstitial positions (1) and (2) where conductor cations (i.e. Na^+) are distributed (see Figure 3.2). The conductor cations move from one site to another through bottlenecks, the size of which depends on the nature of the skeleton ions and on the carrier concentration in both type of sites [21]. For example, partial substitution of P(V) by Si(IV) gives a solid solution with an increased number of Na^+ for charge balance [84].

Lithium-ion conductors based on the NASICON structure have been incorporated into lithium-ion batteries; for example $Li_{1.3}Al_{0.3}Ti_{1.7}(PO_4)_3$ (LATP) where a trivalent Al is substituted for the Ti^{4+}, was reported to have the optimum Li ionic conductivity of these type of compounds (bulk $\sigma_{Li} = 3\,mS\,cm^{-1}$ at 298 K). Aono *et al.* [86] attributed this enhancement to the presence of trivalent cations in the Ti site which results in better densification of the pellet and an increase in Li content, which they claim reduces the grain boundary activation energy for lithium migration. Despite the good conductivities found for these materials, the major problem is their reactivity with lithium metal owing to the reducible Ti(IV) species which leads to mixed (both ionic and electronic) conductivity,

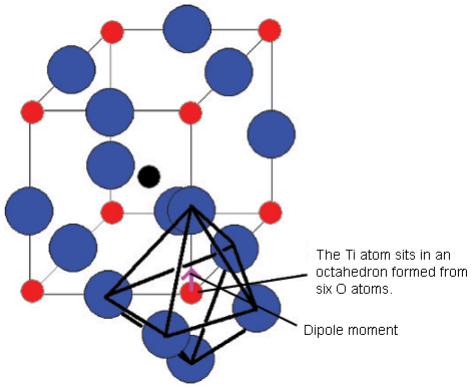


Figure 3.3: Tetragonal structure of $BaTiO_3$, showing elongation along the *c*-axis (vertical) and the arrangement of TiO_6 octahedra. Figure from DoITPoMS, University of Cambridge [92].

making them unsuitable for use in Li-metal batteries.

LISICON, for example $Li_{3.5}Zn_{0.5}GeO_4$ in Figure 3.1, has a framework similar to the orthorhombic γ-Li_3PO_4 and was pioneered by Hong [87], who deduced the structure of the material $Li_{14}Zn(GeO_4)_4$ and identified its superionic conductivity. Its conductivity was explored and characterised further by Bruce and West [88, 89]; however, despite promising lithium conductivity and a high electrochemical window, the material also undergoes reduction in contact with Li metal (Ge^{4+} is reduced to Ge^0 and Ge^{2+}) [24, 90]. The reactivity with Li metal is reduced on replacing the O^{2-} anion with the larger, more polarisable S^{2-}, creating a thio-LISICON analogue, for example $Li_{3.5}Ge_{0.25}P_{0.75}S_4$ in Figure 3.1, with a room temperature lithium conductivity of 2.2 mS cm^{-1} [91]. However, the material is sensitive to moisture (that is, it generates gaseous H_2S) and is chemically unstable. The stability can be improved by the addition of metal oxides, and the presence of oxygen atoms in the Li_2S–P_2S_5 system reduces the interfacial resistance between the cathode (metal oxide) and the sulfide electrolyte [77].

A-Site Deficient Perovskites

Historically, perovskite titanates (ABO_3, B= Ti), received attention due to their functional properties, such as ferroelectricity and dielectricity, caused by displacement of Ti atoms towards one of the octahedrally-coordinated oxygens; for example in $BaTiO_3$ (Figure 3.3), the cubic phase transforms to a tetragonal structure (elongation along the *c* axis) below 120 °C to give a noncentrosymmetric phase which has a permanent dipole, causing a change from dielectric to ferroelectric behaviour.

The cubic $Li_{0.5}La_{0.5}TiO_3$ (LLTO) was first made by Brous *et al.* [93]. Later observations of increased capacitance with increasing temperature, dielectric loss and relaxation were considered to be due to Li motion by Inaguma [94], which led to investigations into its conductivity properties, and it was found that the structural stability originates from the larger La ions, whilst the high conductivity (bulk σ_{Li} ~1 mS cm^{-1} at room temperature) arises from the mobile Li ions.

The A-site deficient compound is formed from the parent structure $Ba^{2+}Ti^{4+}O_3$ as

a starting point, substituting La^{3+} into the A-site (Ba^{2+}) to give $La^{3+}_{2/3}TiO_3$ (where one third of the A-sites are vacant owing to charge neutrality). Small amounts of Li are then substituted into the A-site, according to the formula $Li_{3x}La_{2/3-x}TiO_3$. Ion migration occurs through a network of A-site vacancies and Li ions; by increasing the La/Li ratio to > 1, A-site vacancies are created, and a maximum conductivity has been observed for the ratio La/Li = 1.4 [95].

As for the mechanism for conductivity, it is believed to proceed via the A-site vacancies and involves rotating/tilting of TiO_6 octahedra corresponding to the opening/closing of bottlenecks with a positive volume of activation, i.e. a dilation of the bottleneck occurs as Li jumps from A-site to vacancy. The size of the bottleneck can be modified by dopants, thus changing the activation energy and the conductivity. Emery *et al.* [96] used a combination of electrochemical impedance spectroscopy (EIS) and ^{7}Li nuclear magnetic resonance (NMR) techniques to understand the conductivity in LLTO. They found that the motion of lithium is highly correlated, explaining the large difference in activation energies measured by the two different techniques.

These materials have a large grain boundary resistance, with inconsistencies in the reported conductivity possibly arising from differences in grain size and thus grain boundary contributions to the total conductivity. It is thus important to understand the microstructure when dealing with these and similar materials, and to be able to carefully control the synthesis conditions as they have a large impact on electronic properties.

In addition, despite high conductivity values, a major problem with the possible use of this material as an electrolyte in lithium batteries is, as in LATP, the reduction of Ti(IV) to Ti(III) at relatively low potentials (~2 V), with the onset of electronic conductivity and short-circuiting being possible [85]. The drive for a conductive yet stable material, based on a structure with similar constituents to LLTO, has led to the development of garnet lithium conducting oxide materials, which are the focus of this thesis and are discussed below.

3.2 Garnet-Type Electrolytes

In the previous discussion of inorganic crystalline electrolytes it has been shown that, in general, most of the discovered materials have either high ionic conductivity (for example LLTO), or high electrochemical stability (i.e. LISICON), but not both. Garnet-type electrolytes based on the formula $Li_7La_3Zr_2O_{12}$ on the other hand, possess high lithium ion conductivity ($>1\,mS\,cm^{-1}$) and good thermal, chemical and electrochemical stability against reactions with prospective electrode materials, making them a promising family of solid electrolyte for all-solid-state lithium ion rechargeable batteries.

3.2.1 Background

Traditional garnets have the formula $A_3B_2C_3O_{12}$, and consist of AO_8 dodecahedral cages, BO_6 octahedral cages and CO_4 tetrahedral cages. In the mineral form, they exist as orthosilicates with C=Si, for example the gemstone grossular garnet, $Ca_3Al_2Si_3O_{12}$. These

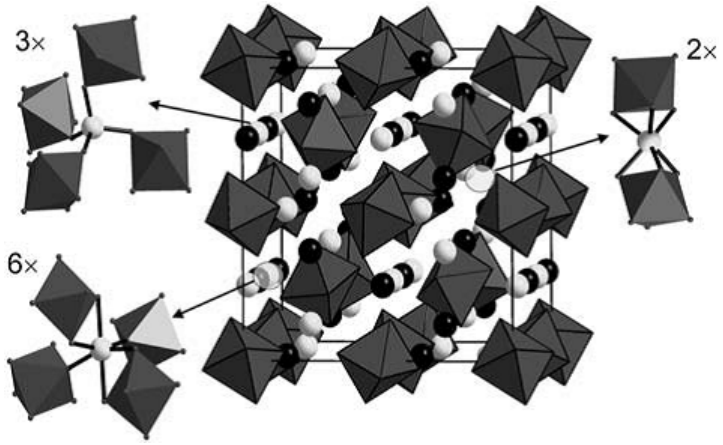


Figure 3.4: The idealised garnet crystal structure with formula $A_3B_2(CO_4)_3$ showing isolated BO_6 octahedra (corresponding to ZrO_6 in LLZO) and black and grey spheres of A and C cations, respectively. The three tetrahedral C-sites can be occupied by Li in conventional Li garnets, but on filling with more Li, the six octahedral and two trigonal prismatic interstitial sites are also available to be occupied, as indicated. Figure from Cussen [98].

materials were first synthesized and studied as magnetic rare-earth functional garnets (e.g. 'YIG' and 'YAG', $Y_3Fe_2Fe_3O_{12}$ and $Y_3Al_2Al_3O_{12}$, respectively) which received scientific interest due to their useful technologically-related physical and chemical properties such as in laser applications (YAG is a host material for solid state lasers) [97]. An ideal garnet has a face-centred-cubic (FCC) lattice with the space group $Ia\bar{3}d$. The crystal structure is shown in Figure 3.4.

Thangadurai *et al.* [99] first discovered lithium conduction in garnet-type materials in 2003 for the Li 'stuffed' structure $Li_5La_3M_2O_{12}$ (M = Nb, Ta), which they reported to have a bulk conductivity of the order $10^{-6}\,S\,cm^{-1}$ at room temperature. This sparked interest in these materials as lithium conducting candidates for lithium battery electrolytes.

Lithium garnets which fulfil the ideal $A_3B_2(CO_4)_3$ structure were first synthesised by O'Callaghan [100] in an attempt to understand the structural properties of the lithium garnet family and to draw conclusions between lithium content and conductivity. The difficulty with studying these materials is their complex crystal structure combined with the negligible scattering of X-rays by lithium when using X-ray diffraction (XRD) techniques, making the determination of structural data rather difficult. Using neutron diffraction (ND) studies on $Li_3Ln_3Te_2O_{12}$ (Ln = Y, Pr, Nd, Sm-Lu), O'Callaghan found an increase in lattice constant with increasing Ln ionic radius, and that Li is located only in tetrahedral (Td, Wyckoff notation 24*d*) C-sites in the cubic space group $Ia\bar{3}d$. O'Callaghan [100] found a fairly low Li conductivity of $10^{-5}\,S\,cm^{-1}$ at 600 °C, with a high activation energy (>1 eV). This implied that the lithium in the tetrahedral 24*d* sites is less mobile and must not be responsible for high conductivity found in higher-doped Li garnets. It was suggested that to improve conductivity, the amount of Li in the octahedral (Oh, Wyckoff symbols 48*g* and 96*h* for ordinary and distorted octahedra, respectively) lattice sites in these systems needed to be optimised.

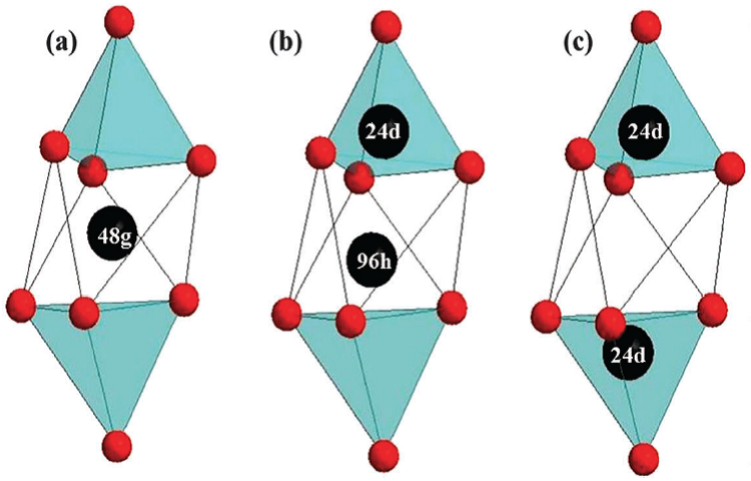


Figure 3.5: Lithium polyhedra occupancy in the garnet structure $Li_{5+x}La_{3-x}A_xM_{2-y}B_yO_{12}$ where A= divalent, M= tri/tetravalent and B= pentavalent cations. Three possible arrangements of Li ions is shown in (a) to (c), see text for an explanation of these arrangements. Figure from O'Callaghan and Cussen [101].

3.2.2 Lithium-Rich Garnets

This need to optimise the lithium content in order to improve the conductivity led to the development and study of a wide range of lithium-rich, or 'stuffed', garnets, which contain more lithium than can be accommodated at the tetrahedral C-sites, and in which the excess lithium begins to populate the octahedral 48g interstitial sites. These garnets have 5-7 Li atoms per formula unit.

The Li_5-phase $Li_5La_3M_2O_{12}$ (M = Nb, Ta, Sb) was also studied by ND by O'Callaghan and Cussen [101, 102] and found to exist in the same cubic structural form as the Li_3 phase but with lithium in both partially-filled tetrahedral (24d) and distorted octahedral (96h) sites. This was also found to be the case for Li_6-phases, such as $Li_6ALa_2M_2O_{12}$ (A= Mg, Ca, Sr, Ba), produced by substituting La^{3+} with divalent ions to increase the Li concentration, except that the Li_6 phases have a higher concentration of vacancies on tetrahedral 24d sites [103, 104]. The formation of vacancies allows for clustering of Li to avoid electrostatic repulsion caused by small Li-Li distances [101].

Each octahedron (96h, 48g) is connected to two tetrahedra (24d) while each tetrahedron is connected to four octahedra by face-sharing, as shown in Figure 3.5. The figure also shows the electrostatic repulsive effect of Li ions in close proximity: when tetrahedral geometry is adopted (24d), the neighbouring Li is located either in another tetrahedron, with a vacant octahedron separating the two ions (Figure 3.5c) or in an adjacent octahedron but in a distorted position (96h), away from the face of the occupied tetrahedron (Figure 3.5b). When a central octahedral site is occupied (Figure 3.5a), it is believed that the adjacent tetrahedral cannot be occupied by another lithium due to unfavourable Coulombic effects. Hence any adjoining 24d – 96h – 24d unit must always have at least one vacant site, and A-site 24d vacancies must occur when the amount of Li per formula unit exceeds three [69]. From this setup it is clear that there are a number of unoccupied

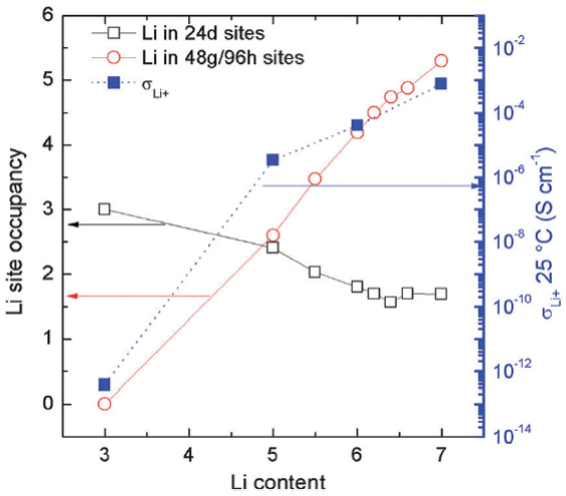


Figure 3.6: Effect of lithium content on room temperature conductivity (σ) and Li site occupancy in lithium-rich garnets. Adapted from Thangadurai *et al.* [107].

sites (vacancies) into which Li ions may migrate and cause Li sublattice rearrangement as part of a cooperative conduction mechanism. This led to the prediction by Xie *et al.* that the upper theoretical limit for Li content which can be accommodated by the structure is 7.5 Li per formula unit [105], involving half-occupancy of 24*d* C sites, fully octahedral site occupancy, and an ordering of the C-site vacancies.

As previously mentioned, the increase in occupancy of octahedral Li sites is related to an increase in conductivity (see Figure 3.6). It was originally believed that the highest conductivities corresponded to a lithium content of 7 atoms per formula unit. In 2007 Murugan [106] synthesised the conductive compound $Li_7La_3Zr_2O_{12}$ (LLZO); however, in trying to replicate these results, Awaka [103] found only a less-conducting tetragonal polymorph with space group $I4_1/acd$, which is the thermodynamically stable form of pure LLZO. The nominal stoichiometry of 'fast ion conducting' pure $Li_7La_3Zr_2O_{12}$ is thus a misnomer. The reason for the reduced conductivity in the tetragonal form arises from the fully ordered distribution of lithium atoms and vacancies (with all octahedral sites occupied), and in fact the cubic form is only stabilised due to addition of Al into the lattice (inadvertently at first through the use of alumina crucibles at elevated temperatures), such that the cubic 'Li_7' garnets are actually of the form Li_{7-x}, with the necessary presence of Li vacancies for cubic stabilisation. In fact, around 6.5 Li per formula unit, short-range ordering of the Li sites occurs, which means that just below this Li content, the highest conductivity in the material is obtained [105]; this Li_{7-x} form of the material is what is meant when referring to 'cubic LLZO'.

3.2.3 Structure and Transport

The high conductivity of the cubic LLZO material has resulted in a number of studies looking at the mechanism for Li transport, using a mix of NMR techniques, simulation studies and neutron diffraction data to understand the link between structure and transport of Li in the lattice.

Solid state NMR techniques have been used in several studies of garnets to follow the conduction mechanism. Structural information is obtained through high resolution ^{6,7}Li magic angle spinning (MAS) NMR, using the interpretation of chemical shifts to find the lithium occupancy of sites with different chemical environments. Information about lithium diffusion is found from lineshape analysis of static NMR spectra as a function of temperature or relaxometry experiments. It should be noted that unambiguous assignment of lithium sites is difficult as the range of chemical shifts (δ) is narrow for these materials. O'Callaghan *et al.* [108] used ^{6}Li NMR to investigate the family of $Li_{3+x}Nd_3Te_{2-x}Sb_xO_{12}$ and found that the lithium motion is between octahedral sites only, with no involvement of the tetrahedra. They believed the energy barrier to migration from tetrahedron to octahedron is too high to be viable in these systems (Figure 3.7a). Cussen [98] is in agreement with this hypothesis, stating that the lithium motion in LLZO is a cooperative mechanism through the edge-sharing octahedra only. However, Bottke *et al.* found that in $Li_{6.5}La_3Zr_{1.75}Mo_{0.25}O_{12}$ both 24*d* and 96*h* neighbouring sites are involved in Li diffusion, implying jump processes along octahedral-tetrahedral-octahedral (Oh-Td-Oh) pathways [48].

Xu *et al.* [109] used density functional theory (DFT) simulations and found the conduction pathway to be highly dependent on the lithium content. They used a Vienna *ab initio* simulation package to model Li conductivity by finding the minimum energy path of Li ion migration at 0 K. They found that in Li_7-LLZO, the high occupancy of octahedral sites mean that the vacant octahedral sites (10 % of total octahedral sites) must be involved in the diffusion pathway. They suggest that migration must occur between two octahedral sites located either side of a tetrahedral site (Figure 3.7c).

These two migration pathways have different energy barriers, with 'route A' (octahedral-octahedral jump, Figure 3.7b), having the higher activation energy (0.8 eV calculated), and 'route B' (octahedral-tetrahedral-octahedral path, Figure 3.7c) involving several energy minima, but with an activation energy calculated to be 0.26 eV for the energy maxima for crossing the tetrahedron-octahedron border. It would therefore be expected that the bottleneck pathway for movement between octahedral lithium sites via a neighbouring tetrahedron ('route B') is the favourable pathway. However, it is known that DFT tends to overestimate activation energies and as this study is purely computational performed at 0 K, care must be taken in its interpretation.

These findings are in agreement by the work of Jalem and co-workers, who investigated the diffusion coefficient and site occupancy of Li ions within the three-dimensional network structure of cubic LLZO using *ab initio* molecular dynamics [110]. They found the mechanism for Li self-diffusion to be a concerted migration through two jump events: (i) cooperative motion through the Oh-Td-Oh Li arrangement, and (ii) a direct edge-pass jump (Oh-Oh), due to the unstable residence of Li ion at the tetrahedral site.

Work by Han *et al.* [111], using a maximum entropy method analysis of neutron diffraction data to obtain the nuclear density distribution of LLZO with temperature, is in agreement with Xu and Jalem; they describe a lithium diffusion pathway of 'Li(24*d*)–Li(96*h*)–Li(48*g*)–Li(96*h*)–Li(24*d*) chain segments'. Additionally, work by Wang

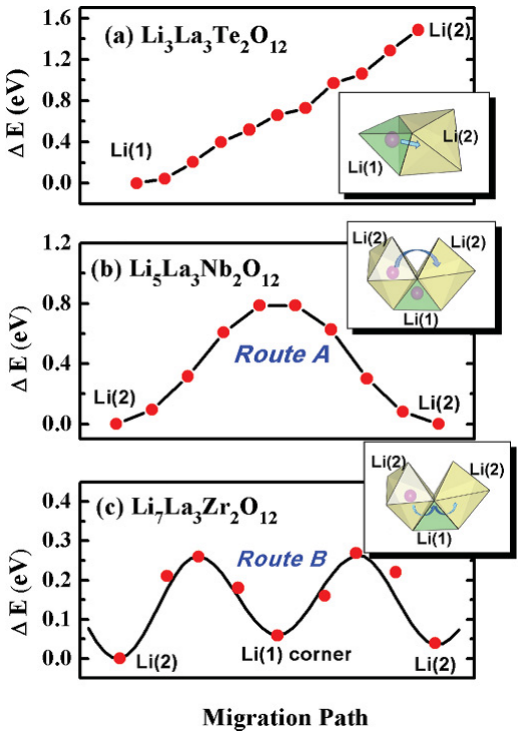


Figure 3.7: Energy barriers for lithium diffusion across different geometries in the lithium garnet family, calculated by Xu *et al.* [109] (a) Li_3 material: energy cost to move Li from tetrahedral (Li(1)) site to neighbouring octahedral site (Li(2)); (b) and (c) possible migration pathways for LLZO: (b) is an octahedral-octahedral jump (also seen for Li_5 materials), where (c) is an octahedral-tetrahedral-octahedral movement were the bottleneck is at the tetrahedral site.

et al. [112] used ^{6}Li magic angle spinning and ^{7}Li pulsed field gradient NMR to show that the lithium mobility at the 24*d* sites dominates the total ionic conductivity of the samples, acting as a bottleneck for diffusion.

Recently, a new acentric symmetry for LLZO ($I\bar{4}3d$ space group) has been discovered by Wagner, Rettenwander *et al.* [113–115] for $Li_{7-3x}Fe_xLa_3Zr_2O_{12}$ (for $0.09 < x < 0.30$), $Li_{7-3x}Ga_xLa_3Zr_2O_{12}$ (with x> 0.07) and $Li_{6.4}Al_{0.2-x}Ga_xLa_3Zr_2O_{12}$ (where the phase transition occurred for an Al:Ga substitution ratio of 0.05:0.15). In the co-doped material, the symmetry change was shown to be accompanied by a reduction in the Li ion transport activation energy to 0.26 eV. This space group had only been reported before for the protonated material $Li_{6-x}H_xCaLa_2Nb_2O_{12}$ [116], was confirmed by transmission electron microscopy (TEM) and attributed to the unequal Li^+ and H^+ distributions in the network (see Section 3.3). In the work on the doped LLZO materials, it was seen that an increase in Li conductivity increases with an increase in the Ga/Al content ratio, accompanied by a lower area specific resistance and smaller grain size. The formation of the $I\bar{4}3d$ space group is attributed to the site preference of Ga^{3+}, which causes a splitting of the 24*d* position into two different sites, namely Li1 (12*a*) and Li2 (12*b*). The behaviour of Fe is shown to be very similar to Ga in this respect. This change in structure leads to a change in lithium diffusion mechanism and faster Li ion dynamics probed by NMR relaxometry [113]. These results are interesting because they show that LLZO materials with the $I\bar{4}3d$ space group show superior Li-ion conductivity compared to that of conventional LLZO garnets with the $Ia\bar{3}d$ space group, a discovery which has only recently been made.

These studies illustrate that a delicate interplay exists between crystal structure, lithium content, site occupancy, and total conductivity in the LLZO system.

3.2.4 Doping

As described in Section 3.2.2, the undoped, pure LLZO structure exists as a tetragonal polymorph ($I4_1/acd$ space group), which has poor ionic conductivity at room temperature ($\sim 10^{-6}$ S cm^{-1}) due to the ordering of the lithium lattice (full octahedral site occupancy). This space group is the thermodynamically stable form of LLZO, existing at room temperature due to a volume-preserving tetragonal distortion that relieves internal structural strain [117]. Increasing the temperature to around 650 °C results in a phase transition to the cubic $Ia\bar{3}d$ phase [117–119], which has a disordered Li sublattice (with all Li symmetry sites partially occupied). The cubic phase is the technologically useful form as it has approximately two orders of magnitude greater conductivity than the tetragonal phase, and thus stabilising the cubic phase at room temperature is desired. This is possible through the use of cation supervalent dopants.

Supervalent doping with e.g. Al^{3+} at the Li sublattice introduces Li vacancies (V'_{Li}) due to charge balance (Equation 3.1, in Kröger Vink notation). With enough of these vacancies, the ordering of the Li sublattice is disrupted, and the resultant disorder, in combination with lattice relaxation, produces the cubic phase [35, 117].

$$Al_2O_3 \xrightleftharpoons{LLZO} 2Al^{\bullet\bullet}_{Li} + 4V'_{Li} + 3O^{\times}_{O} \tag{3.1}$$

These same vacancies are also responsible for opening up previously blocked Li^+ hopping paths leading to an enhanced conductivity. This observation has led to a number of studies focussed on improving the conductivity through doping strategies; these include substitution of donor dopants at the Zr (16*a*) and La (24*c*) sites (i.e. with higher-valent Ta(V) [69, 119–124] and Ce(IV) [125]), which were selected so as to prevent the obstruction of lithium ionic pathways for conduction which might be expected when doping at the Li sites [126]. Examples of these substitutions are given in Equation 3.2 and 3.3.

$$Ta_2O_5 \xrightleftharpoons{LLZO} 2Ta^{\bullet}_{Zr} + 2V'_{Li} + 5O^{\times}_{O} \tag{3.2}$$

$$CeO_2 \xrightleftharpoons{LLZO} Ce^{\bullet}_{La} + V'_{Li} + 2O^{\times}_{O} \tag{3.3}$$

The effect of dopant type and content on bulk ionic conductivity is summarised nicely by Thangadurai [107, 127] in graphical and tabular form. A point of note is the lack of clear distinction in the literature on the bulk and the grain boundary conductivity of measured pellet samples. 'Total' conductivity is often quoted, and it is often not specified if this refers to the bulk or the bulk plus grain boundary contributions. In most cases they are not easy to separate and thus there is a lot of spread in the results. However, some of the highest reported conductivities to-date using supervalent dopants substituted at the Li sublattice are summarised in Table 3.1.

Table 3.1: Reported conductivities in the literature for doped LLZO with cations substituted at the Li sublattice (chemistries reported are as nominally intended).

Dopant and substituted cation site	**Dopant amount (atoms per formula unit)**	**Total conductivity at room temperature (S cm^{-1})**	**Activation energy (eV)**	**References**
Al^{3+} (site unspecified)	0.15-0.40	2.0-9.9x10^{-4}	0.30-0.37	[121, 128–130]
Ga^{3+} (site unspecified)	0.30	5.4x10^{-4}	0.32	[131]
Ge^{4+} on La or Li (unspecified)	0.12	7.6-8.3x10^{-4}	-	[132, 133]
Al^{3+} on 24*d* Li	0.20-0.30	4.0-5.2x10^{-4}	0.20-0.55	[51, 134–136]
Ga^{3+} on 24*d* Li	0.15-0.25	1.2-1.5x10^{-3}	0.25-0.30	[113, 137, 138]
Ga^{3+} on 24*d* Li and Sc^{3+} on Zr	0.15 (0.10 Sc)	1.8x10^{-3}	0.29	[139]
Fe^{3+} on 12*a* Td Li ($I\bar{4}3d$ space group)	0.25	1.4x10^{-3}	0.28	[114]

Amongst the highest room temperature ionic conductivities in LLZO have been

achieved by doping on the Li sublattice (with Ga^{3+} and more recently Fe^{3+}) [113, 114, 137, 138], sometimes in combination with a co-dopant at the Zr site [139], suggesting a threshold value of dopant concentration that can be accommodated without disruption to fast lithium diffusion. Following the discovery that dopants enable cubic stabilisation and an increase in conductivity (in particular the role of Al^{3+} which had unwittingly been introduced from alumina crucibles during synthesis in Murugan's paper [106]), an understanding of their exact site occupancies and content for optimum conductivity has been investigated.

Aluminium Doping

The nature of the aluminium substitution is still subject to some debate; solid state NMR studies by Hubaurd and Buschmann suggest Al occupies the 24*d* lithium site [134, 140], Geiger's interpretation of NMR ^{27}Al resonances point to occupancy of both 24*d* and octahedral positions [141], whilst neutron diffraction studies by Li *et al.* suggest that Al resides in 48*g* octahedral sites [142]. Neutron diffraction by Gu *et al.* and Wang *et al.* modelled Al in the 24*d* site [112, 120]. Rettenwander tried to consolidate the two interpretations with the use of DFT calculations by suggesting Al^{3+} could have a number of slightly different local 4-fold coordinations around the crystallographic 24*d* and 96*h* sites in cubic LLZO, leading to broad ^{27}Al NMR resonances which are not straightforward to interpret. He suggested that the 48*g* site may be partially occupied, but that the calculated Al NMR chemical shift value for such coordination has not been observed in experimental NMR spectra [143]. Meanwhile, Düvel used ^{7}Li NMR to predict that Al will also enter La and Zr sites with increased Al content [144]. Limitations associated with both NMR and ND experimental techniques for the localisation of atomic positions affect the confidence with which researchers can assign dopant lattice sites; despite being a local technique, interpretation of NMR line shapes is non-trivial (especially when broad resonances are observed), and neutron diffraction is a non-local technique which only provides an average structural description.

Rangasamy investigated the effect of Al and Li concentration on the formation of cubic LLZO, and found that at least 0.204 moles of Al is required to stabilise the cubic phase. The solubility of Al in the cubic phase is suggested to peak at 0.389 moles [145].

From an experimental viewpoint, it is important to note the difficulty in separating the effect of Al on cubic stabilisation and increased conductivity from other Al-associated observations, such as its behaviour as a sintering aid [128] arising from the formation of a Li_2O-Al_2O_3 melt during high temperature sintering (see the phase diagram in Figure 4.1 of Chapter 4). This effect leads to a reduced precision in controlling the Al doping content in the garnet lattice, as Al can segregate at the grain boundaries [140, 146], and Al from the crucible can create a gradient of concentrations through the sample. The picture is further complicated as many literature reports do not make the distinction between nominal and actual aluminium content in their samples, or they are unable to separate Al present in the bulk material and in grain boundaries using bulk techniques such as inductively coupled plasma (ICP) spectroscopy.

Gallium Doping

Following the success of aluminium doping on the transport properties of Al-doped LLZO (Al-LLZO), attention has since been directed at using other dopant cations on Li sites. Because gallium is located directly below aluminum in the periodic table, and hence should show similar crystal-chemical behaviour, it was selected as a dopant at the Li sublattice, and has been shown to stabilise the cubic phase and provide even better conductivities (up to 1.46 mS cm^{-1} reported by Wu *et al.* [138]).

El Shinawi [131] obtained cubic garnets with room temperature conductivities of up to 5.4×10^{-4} S cm^{-1} with a doping level of 0.3 Ga atoms per formula unit ($Ga_{0.3}$). Below $Ga_{0.3}$, the tetragonal phase was obtained, and above $Ga_{0.4}$, impurity phases including $LiGaO_2$ were observed, indicating the excess Ga was not incorporated into the garnet lattice. They proposed that a similar mechanism to that of aluminium substitution was occurring.

Later work by Bernuy-Lopez *et al.* [137] reported conductivities of 1.3 mS cm^{-1}, the highest values at the time. This was achieved with a doping level of 0.15 atoms of Ga per formula unit, as measured by ICP. It could well be the case that El Shinawi had real Ga concentrations lower than reported, as the values quoted are those expected from the stoichiometry of reagents, but here not directly measured. Bernuy-Lopez *et al.* used ^{71}Ga NMR to find that the Ga was present in the 24*d* (tetrahedral) sites of the LLZO lattice. They hypothesised that 0.15 moles of Ga provides the optimum concentration of Li ion charge carriers and Li vacancies in the conduction pathway. The reduction in conductivity at higher doping levels ($Ga_{0.3}$) is attributed to blocking effects of Ga in the 24*d* position.

Additionally, the processing of the material in the latter report was more tightly controlled, with a dry oxygen furnace for heat treatment, to obtain denser samples and to prevent moisture reaction which is detrimental to conductivity (this is discussed later in Section 3.3). This further illustrates that care must be taken in interpreting the conductivity values, as factors such as microstructure, purity and measurement setup will influence the conductivity measured by impedance spectroscopy. The effect of microstructure and density is important as this will alter the grain contact and affect the volume fraction of the grain boundary phase, which has a different conductivity to the bulk material [135, 147].

To explain why Ga doping produced a higher conductivity material than Al-LLZO, the size and site preferences of the cations was used as an explanation. A table of the cation crystal radii under different coordination environments is given in Table 3.2. The larger Ga^{3+} is expected to prefer the 96*h* octahedral site over the 24*d* site [126], which might be expected to be less of a hindrance for Li transport, as the 24*d* site is a junction for Li ion diffusion. However, the crystallographic position of Ga in the lattice has, like Al, proven difficult to ascertain, with ^{71}Ga NMR studies giving different results. As mentioned previously, Bernuy-Lopez [137] reported the Ga^{3+} to be in the 24*d* site, whereas Rettenwander first reports a preference for the Ga at 96*h* sites [148], and in a later report, using stronger magnetic fields, suggests that neither Al or Ga have a difference in preferences for 24*d* or 96*h* sites in the $Ia\bar{3}d$ symmetry [149]. These differences in opinion

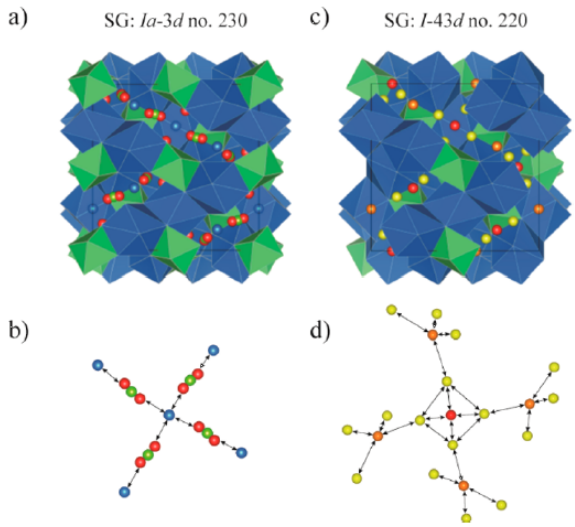


Figure 3.8: $Ia\bar{3}d$ and $I\bar{4}3d$ cubic space groups of LLZO. (a) Crystal structure of $Ia\bar{3}d$ LLZO, showing blue LaO_8 dodecahedra (24*c*), green ZrO_6 octahedra (16*a*) and lithium distributed over three sites: 24*d* tetrahedral coordination (red spheres), 48*g* octahedral coordination (green spheres), and distorted 96*h* octahedral coordination (blue spheres); (b) gives the Li-ion diffusion pathway. (c) Crystal structure of $I\bar{4}3d$ LLZO, with the lithium distributed over three sites: two tetrahedrally-coordinated 12*a* (red spheres) and 12*b* (orange spheres), and 48*e* octahedral coordination (yellow spheres); (d) gives the Li-ion diffusion pathway. Figure from Wagner [115].

arise from difficulties in interpretation of NMR lineshapes, and also likely a dependence on the synthesis conditions.

In a recent study by Wagner [115], in which the Ga-doped LLZO (Ga-LLZO) (and also Fe-doped LLZO) is seen to crystallise in the $I\bar{4}3d$ structure (Figure 3.8c) for greater than 0.15 Ga atoms per formula unit (a.p.f.u.), XRD and ND data refinements suggest the Ga has a site preference for the 12*a* tetrahedral Li site, which drives the symmetry reduction change and is tentatively used to explain the higher electrochemical performance of Ga-LLZO when compared to Al-LLZO. While the small Al^{3+} keeps $Ia\bar{3}d$ symmetry, the larger Ga^{3+} and even larger Fe^{3+} show the change in symmetry, indicating a strong influence of steric size effects on inducing the symmetry change. Indeed, Ga^{3+} and Fe^{3+} have been shown to prefer the larger and more distorted (12*a*) tetrahedral site [114].

Rettenwander [113] and co-workers then explored this comparison between Al- and Ga-doped LLZO further by measuring activation energies for a series of co-doped materials with the formula $Li_{6.4}Al_{0.2-x}Ga_xLa_3Zr_2O_{12}$ ($0 \leq x \leq 0.2$, with increments of $x = 0.05$). They found the lowest overall activation energy for the $Al_{0.00}Ga_{0.20}$ end-member (~0.26 eV), lower than previously reported (0.3 to 0.37 eV) but similar to computed values (0.24 to 0.3 eV). Two distinct drops in activation energy were found for the compositions $Al_{0.15}Ga_{0.05}$ and $Al_{0.05}Ga_{0.15}$. Using DFT calculations, the first drop was attributed to the presence of Ga^{3+} raising the site energy of its tetrahedral neighbour by 10 meV more than Al^{3+}; this acts to smooth the energy landscape for Li migration, effectively lowering the energy difference between Oh and Td Li sites. The second drop was explained by the change of phase to $I\bar{4}3d$ symmetry at $Al_{0.05}Ga_{0.15}$, which is expected to have more facile

Li diffusion than the $Ia\bar{3}d$ structure.

Not all lithium ions can contribute to conduction simultaneously, because only a small number of vacancies are available - Ahmad estimated that the concentration of charge carriers in LLZO is $\sim 12.3\,\%$ of the total lithium ions [150]. Thus, it is suggested that activating more lithium ions to participate in conduction may improve the conductivity [138], as well as enlarging the lithium ion migration pathway and using the strong Coulombic interactions between cation dopants and the lithium ions to activate the Li for conduction [138].

A Li conductivity limit has been given by Jalem *et al.* [72] on the basis of force field simulations, of $\sigma_{\text{bulk}} = 1.7\,\text{mS}\,\text{cm}^{-1}$ [151] for Ga-doped LLZO. Many researchers believe there is a sweet spot for the Li content in LLZO for optimum conductivity between 6.4-6.6 Li a.p.f.u. [50, 105, 117, 152, 153], which corresponds to the lowest number of lithium vacancies required to stabilise the cubic phase. Hence for a trivalent Ga or Al substitution on a Li site, 0.13-0.2 a.p.f.u. of dopant cations are needed. This value provides the guideline for balancing maximum Li content whilst optimising the vacancy content to achieve high conductivity.

Table 3.2: Table of crystal radii of cations in LLZO, showing their valence and crystal radius in 4- and 6-fold coordinated (CN) sites; data from Shannon's *Revised Effective Ionic Radii* [154].

Ion	**Valence**	**4 CN crystal radius (Å)**	**6 CN crystal radius (Å)**
Li	+1	0.73	0.90
Zr	+4	0.73	0.86
La	+3	-	1.172
Al	+3	0.53	0.675
Ge	+4 (+2)	0.53	0.67 (0.87)
Zn	+2	0.74	0.88
Ga	+3	0.61	0.76
Fe	+3 (+2)	0.63 (0.77)	0.69 (0.75)
P	+5 (+3)	0.31	0.52 (0.90)
Si	+4	0.40	0.54

Higher Supervalent Dopants

Using higher valent cation dopants means theoretically a lower content of dopant is required to obtain the same Li ion and vacancy concentration compared to the case of a lower valent dopant, based on charge compensation arguments, which could be advantageous if a blocking effect of the cation is reduced. Some studies on higher valent dopants at the Li sublattice have been made, exploring this theme further.

Huang *et al.* [133] reported Ge-doped LLZO which stabilised in the cubic phase with a room temperature conductivity of $8.3 \times 10^{-4}\,\mathrm{S\,cm^{-1}}$ for 0.12 Ge a.p.f.u. (where it is not clarified if this is a bulk or total conductivity). Higher nominal dopant concentrations gave GeO_2 impurity phases in the XRD patterns, expected to be located at the grain boundaries, and the corresponding impedance spectra showed separation of grain boundary and bulk semicircle responses at these higher concentrations. Using the argument of the optimal Li content of 6.4-6.6 a.p.f.u., and assuming substitution at the Li sublattice, it would be expected that 0.1-0.15 Ge a.p.f.u. would give the best lithium conductivity. They also observed grain growth as a function of Ge content, likening its similarity to Al as a sintering aid. The similarity in ionic radii between Al^{3+} and Ge^{4+} can be seen in Table 3.2; thus it might be expected that the two cations will have similar crystallographic preferences in the lattice. Despite using zirconia crucibles to sinter the pellets, the starting materials were heated on alumina crucibles, and no quantitative chemical analysis was carried out, so it is not possible to rule out Al contamination and its lattice stabilisation effects. The study used X-ray absorption near-edge spectroscopy (XANES) to attempt to localise the Ge dopant position, and determined the Ge^{4+} to occupy either the La (24*c*) sites or 96*h* Li sites in the $Ia\bar{3}d$ crystal structure, by comparing experimental Ge K edge spectra with theoretical spectra. This preliminary study shows that it might be possible to stabilise the cubic LLZO using Ge^{4+} doping, but further work is needed to characterise the material.

Huang [132] also attempted doping with Si^{4+}, but found it resulted in a reduction of ionic conductivity, and energy dispersive X-ray (EDX) analysis showed that the Si was concentrated at the grain boundaries. This might be explained by its crystal radius (Table 3.2), being much smaller than Li^+, Ga^{3+}, Al^{3+} and Ge^{4+}, making it energetically unfavourable to exist within the LLZO lattice.

No other higher valent dopants substituting at the Li position have been explored experimentally; however, a theoretical paper by Miara *et al.* [155] has used first principles methods to predict the defect energy and site preference of a large number of candidate dopants (128 in total). Using a cut-off of 2 eV for the energy for defect formation, and selecting the lowest energy for each element, their work predicts that Al^{3+}, Ga^{3+}, Zn^{2+} and Fe^{3+} reside at the Li site, with Ge^{4+} preferring the Zr site, with the defect energies given in Table 3.3. This is contrary to the work of Huang in their prediction of the Ge substitution preference; however, limitations of both XANES and first principles methods used in these papers for determining dopant site occupancy must be considered. Miara *et al.* [155] also predict that neither Si^{4+} nor P^{5+} can be used to substitute at any position in LLZO owing to the high calculated energy for defect formation in placing these cations in the garnet lattice, reflecting Huang's findings with experimental silicon doping.

3.3 Degradation of Garnets with H_2O and CO_2

The existence of hydrogarnets, obtained from proton-exchange of anhydrous garnets (e.g. $Ca_3Al_2(OH)_{12}$ from $Ca_3Al_2Si_3O_{12}$) has been known for some time [156]. Despite this,

Table 3.3: First principles defect site energies in LLZO for a range of cations and oxidation states, data from Miara *et al.* [155]. Bold values represent feasible dopant positions.

Element and oxidation state	***E*(defect) for Li site (eV)**	***E*(defect) for Zr site (eV)**
Al^{3+}	**1.356**	-
Fe^{3+}	**1.324**	-
Ga^{3+}	**1.158**	-
Ge^{4+}	5.536	**1.106**
Ge^{2+}	-	2.874
P^{3+}	4.78	3.549
P^{5+}	5.916	4.342
Si^{4+}	3.591	2.354
Zn^{2+}	**1.319**	1.653

Li-stuffed garnets were initially thought to be stable to moisture [106], but are now known to be sensitive to moisture and undergo facile proton exchange with lithium [157–159]. This leads to a protonated garnet phase (H-LLZO), and the release of LiOH which goes on to react with CO_2 if present (e.g. in air), to form Li_2CO_3. Direct reaction with CO_2 is also possible, proceeding via the creation of oxygen vacancies to balance loss of Li ions. Both reactions have been shown to stabilise the cubic phase material by creating a disordered Li network [119].

Several groups have used EIS and diffraction studies to evaluate the chemical stability and proton exchange of Li-stuffed garnets in water and air. In 2010, Nyman [160] reported an alternative approach to stabilising the cubic $Ia\bar{3}d$ phase starting from tetragonal $Li_5La_3Ta_2O_{12}$ and $Li_5La_3Nb_2O_{12}$ compositions; placing the powders in liquid H_2O, they reported a pH increase to 10-11 caused by the proton-lithium (H^+/Li^+) exchange in the material and a concomitant increase in the conductivity resulting from the phase change.

Galven *et al.* looked at $Li_7La_3Sn_2O_{12}$ and $Li_5La_3Nb_2O_{12}$ powders in benzoic acid in ethanol solution, which were left to reflux for 1 week [161, 162]. Both compositions underwent proton-lithium exchange, accompanied by a phase transitions from tetragonal to cubic $Ia\bar{3}d$ symmetry in $Li_7La_3Sn_2O_{12}$, and a change of symmetry from cubic $Ia\bar{3}d$ to the noncentrosymmetric space group, $I2_13$ in the $Li_5La_3Nb_2O_{12}$ material. The filtrate from the reflux was analysed with flame photometry to assess the extent of protonation; this came to 70 % and 82 % for the Sn- and Nb-doped materials, respectively. They hypothesised that H^+/Li^+ exchange occurs readily for garnet stoichiometries with greater than 3 Li atoms per formula unit, and that the exchange propensity is independent of lithium ion conductivity and lattice parameter. They also noted that following partial exchange, the lattice parameter increased depending on the extent of exchange, and that this is attributed to the replacement of strong Li-O bonds with weaker O-H—O bonds. Additionally, they

observed no marked change in conductivity which, combined with NMR relaxometry, they inconclusively put down to both the Li^+ and H^+ having similar mobilities.

Truong *et al.* [163] studied $Li_5La_3Nb_2O_{12}$ and $Li_{5+x}Ba_xLa_{3-x}Ta_2O_{12}$ powders in water at room temperature and noted an improved stability against protonation of the Ta-doped material compared to the Nb analogue, which attributed to the greater strength and covalency of the Ta-O bond over the Nb-O bond.

Larraz *et al.* [118] investigated the tetragonal-cubic transition temperature in LLZO, and the apparent lowering of this temperature when the sample is hydrated (i.e. stored in air, and/or heating steps performed in air). They found using in-situ XRD and thermogravimetric analysis (TGA), that the pure, reversible transition occurs at 645 °C on heating and 625 °C on cooling, and that a low-temperature (100 to 200 °C) transition to a cubic phase is caused by the insertion of water molecules in the structure or a H^+/Li^+ exchange mechanism, which, when heated at higher temperatures, results in loss of H_2O and adsorbed CO_2 and reverts to the tetragonal form. This might be used to explain the larger unit cells of many reported 'low-temperature' syntheses of cubic-LLZO.

In addition to tetragonal-cubic transitions, structural distortions starting from a cubic $Ia\bar{3}d$ garnet have also been reported following proton exchange. Galven and co-workers [116] studied $Li_6CaLa_2Nb_2O_{12}$ under acetic acid reflux and found it formed a noncentrosymmetric structure with the $I\bar{4}3d$ space group, with a 81.7 % exchange of Li. They used neutron diffraction to tentatively assign site preference for the protons and Li; Li^+ was found to exist in 12*b* sites (corresponding to half of the 24*d* tetrahedral sites in the $Ia\bar{3}d$ space group), with H^+ in two 48*e* sites (formed by the splitting of the distorted 96*h* octahedra in the $Ia\bar{3}d$ space group).

A paper by Orera [159] has a detailed analysis of the conditions determining the proton-lithium exchange and obtained crystal phases from tetragonal LLZO, showing that the symmetry and thus configuration of protons and lithium depends on the proton content and exchange temperature, which themselves are not independent of one another. They report that temperatures above 150 °C are required to facilitate homogeneous exchange (by increasing the mobility of the Li^+ and H^+ ions). Air-annealing at 150 °C for several days resulted in a highly-protonated noncentrosymmetric $I\bar{4}3d$ garnet, as described by Galven [116]. Figure 3.9 shows the proposed distribution of H and Li sites in both structures; in the $I\bar{4}3d$ structure, Li has a preferred occupancy of the 12*b* site, and the protons sit in octahedral cages, bound to oxygen atoms surrounding the less-occupied 12*a* site, forming O_4H_4 units around these sites. These units are also found in hydrogarnets, where all the tetrahedral sites are empty. At 350 °C, air-annealing lead to a lower degree of protonation, and the centrosymmetric $Ia\bar{3}d$ space group was adopted, with H and Li split across Oh sites. The lower protonation at this higher temperature is thought to be due to reinsertion of Li into the lattice from Li_2CO_3 formed in air; water reflux at 90 °C saw much higher degrees of protonation, close to those seen with 150 °C air anneal. The paper did not include conductivity measurements; however, the milder exchanges where less lithium is exchanged are expected to be more conductive, owing to the presence of mobile octahedral Li.

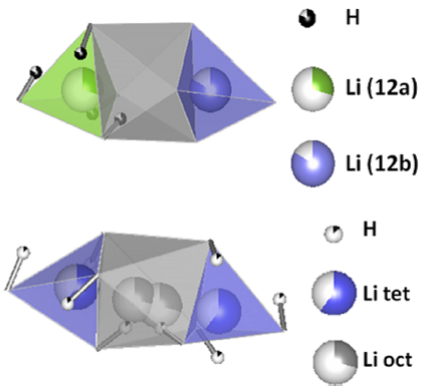


Figure 3.9: Schematic representation of the Li and H sites in the refinement of H-LLZO; crystallising in the $I\bar{4}3d$ space group (top), after 150 °C air annealing; and the $Ia\bar{3}d$ space group (bottom), after 350 °C air-annealing. Figure from Orera *et al.* [159].

Ma *et al.* [164], on the other hand, did not observe any phase transformation for cubic LLZO exposed to aqueous solutions and suggested that LLZO with the space group $Ia\bar{3}d$ is relatively stable, even at very high H^+/Li^+ exchange rates of 63.6 %, which involve almost entirely 96*h* Li sites. A particular focus of this study was on the presence of any other space groups such as $I2_13$ or $I\bar{4}3d$, which the study clearly denies. As the phase transition to $I\bar{4}3d$ seems to be triggered by a splitting of the 24*d* position in $Ia\bar{3}d$ [115], which is not affected by the H^+/Li^+ exchange, it is difficult to see how a phase transition can be caused by a H^+/Li^+ exchange at the 96*h* position only; so possibly other processes such as the heating to 350 °C might have caused the phase transition to $I\bar{4}3d$ reported by Orera [159].

Meanwhile, Shimonishi [165] followed the stability of cubic $Li_{7-x}La_3Zr_2O_{12}$ in LiCl, LiOH and HCl aqueous solutions, immersing pellets of the material in the solutions at 50 °C for 1 week before vacuum drying at 220 °C. The study reported no change in the XRD patterns, unaltered bulk conductivities, but a change in the surface morphology and decrease in grain boundary conductivity for the LiOH- and HCl-immersed samples, as well as for samples immersed in liquid H_2O. They report these observations to be due to a segregation of highly resistive decomposition products at the grain boundaries and surface of the pellets, but were unable to characterise these further as they were not detected in the XRD patterns.

Yow [124] performed proton exchange on cubic Ta-doped LLZO pellets in H_2O at room temperature and found by TGA analysis that the extent of exchange was 5.4 % after 1 day and 8.8 % after 7 days immersion, using a core-shell model described previously for $Li_{0.34}La_{0.55}TiO_3$ perovskites [166] to describe the exchange process, which is density dependent. The study predicted that, for a 100 % dense pellet, with a linear composition gradient between a protonated region (taken as the stoichiometry of the powdered sample under the same exchange conditions) and an unprotonated core, the region of proton-exchanged garnet would extend to 0.25 mm after 1 week room-temperature H_2O immersion. The study measured the activation energy of the conductivity in the pellets with immersion time, which increased from 0.39 eV after 1 day to 0.70 eV after 7 days, and

used molecular dynamics simulations to hypothesise that for a high degree of protonation (~50 %), the garnet is a mixed proton, lithium conductor at high temperature (~1200 K), but a proton-conductor at low temperature (500 K).

Crystallographic studies on the protonated cubic LLZO phases were later carried out by Larraz *et al.* [157], using MAS NMR on air-exposed and washed powders to remove soluble LiOH and Li_2CO_3 impurities and to detect chemical shifts associated with lattice proton and lithium ions only; they have shown that the distorted octahedral sites preferentially exchange with the protons, which is in agreement with work by Orera [159], Galven [116], Ma [164] and Li *et al.* [167] They also predict a low proton conductivity owing to weak hydrogen bonding and protons being tightly bound to oxygen anions in the lattice. Ma [164] showed that the stable exchange (up to 64 % of Li) in cubic LLZO in H_2O can be reversed by immersing the protonated garnet in LiOH solution.

The implication of proton-lithium exchange and air reactivity on processing and transport properties of the LLZO pellets has also been investigated. Bernuy-Lopez [137] followed strict moisture-controlled synthesis of Ga-LLZO, handling and processing the material under an argon atmosphere in a glove box, and performing heat treatments of pellets and powders under pure, flowing oxygen. The study found the densification of the pellet was improved as a result, giving high measured conductivities (and also with implications for suppressing Li dendrite growth). MAS NMR was used to probe the existence of protons of the material, before and after air exposure; proton shifts were observed for both LiOH species and protons inside the lattice in a 1:1 ratio following air exposure, highlighting the fast exchange in the material and the importance for controlled atmosphere processing of the powders [166].

The Doeff group [168] investigated the air-reactivity of pellets of Al-LLZO and the impact on interfacial resistance with Li metal electrodes. By controlling the particle size of the powders, they were able to obtain small- (~20 µm diameter) and large- (~150 µm diameter) grained pellets which showed differences in behaviour when exposed to air. Although both pellet types formed Li_2CO_3 at the surface, thus increasing the interfacial resistance with Li metal, the larger-grained material reacted much more dramatically, giving an order of magnitude higher resistance after 24 hours air exposure than the small-grained sample. This was attributed to the difference in Al and Li distribution on the surface of the pellets; the larger-grained sample had more Li and less Al in the grains, due to a more pronounced liquid-phase sintering process which favoured the formation of Al-rich grain boundaries, depleting it in the bulk. The increased Li content, and thus reactivity in the large-grain samples was shown to favour a two-step reaction in air, reacting first with H_2O to form LiOH, followed by reaction with CO_2 to form Li_2CO_3. However, in the Al-rich small-grained surface, the direct reaction with CO_2 to form the carbonate is favoured, but being the kinetically slower reaction, Li_2CO_3 forms to a lesser extent at the surface in the same exposure time. This report used X-ray photoelectron spectroscopy (XPS) to study the surface only of the pellets, and does not comment on the insertion of H^+ into the lattice, or the likely extent of proton exchange in the two types of samples. They were not able to separate grain and grain boundary processes

in their impedance measurements, and as such did not evaluate the change in transport properties of these features following air exposure.

Sharafi *et al.* [169] also reported on the interfacial properties with lithium metal electrodes due to the formation of the $LiOH/Li_2CO_3$ degradation products on the surface of the ceramic. The study found that the air reactivity depends on the relative humidity, with a higher relative humidity favouring faster Li_2CO_3 formation. They used electron energy loss spectroscopy (EELS) analysis to determine the reaction progresses through the two-step process described above, and found a Li-deficient layer below the top Li_2CO_3 layer, supporting the idea of the reaction progressing via a lithium exchange mechanism.

To summarise this review section on air and moisture degradation of Li-stuffed garnets, much work has focussed on the ability of proton-lithium exchange to stabilise the cubic $Ia\bar{3}d$ garnet phase in powder samples in acidic media. It is generally agreed that the octahedral Li exchange preferentially with protons, being the more mobile site. Various noncentrosymmetric modifications have been discussed as a result of the exchange process, which are dependent on several experimental factors. However, there is a need to evaluate the macroscopic implications of H^+/Li^+ exchange - very few studies look at the conductivity of exchanged materials - despite some reports of dynamic exchange between octahedral and tetrahedral Li sites in the protonated compounds [157], their long-range conduction has not been evaluated.

3.4 Interface of Garnets with Lithium Metal Electrodes and Cell Cyclability

The wide electrochemical stability window of LLZO garnets is in principle such that they are compatible with Li metal as an electrode; this in combination with the mechanical hardness of the ceramic (hardness/yield strength of ~6.3 GPa for LLZO compared to 0.655 GPa for metallic lithium) [170] was expected to prevent the formation of Li dendrites [171] commonly formed with liquid or polymer electrolytes. However, reports of short-circuiting due to dendrite-like creation have been reported in LLZO/Li metal cells, highlighting the need to understand the stability of the system, especially under electric polarisation [129, 172]. Kotobuki observed short-circuiting behaviour above an applied current of density of just 10 $\mu A\,cm^{-2}$ in a symmetric Li metal cell with an undoped, cubic LLZO [172], putting the behaviour down to high interfacial resistance between the metal and LLZO, caused by an inhomogeneous current distribution between the two. In general, this high interfacial resistance dominates the total cell resistance, especially when using very thin ceramic electrolyte membranes, and so is the limiting factor in cell performance (preventing the accessibility of high current densities and thus fast discharge/charge cycles).

The origins of high interfacial resistance are multiple: poor electrode/electrolyte contact, slow charge transfer and low charge carrier mobility in the interfacial region can each increase interfacial resistance [173]. Several strategies for improving the contact at the interface have been successful at reducing the interfacial resistance - including the use

of heat and pressure for improving Li metal wettability, and chemical and microstructural modifications of the LLZO pellet interface. Some of these strategies are described below.

Prior to their work described in the previous section [168], Cheng *et al.* [173] showed a simple polishing procedure and care of handling could remove corrosion products (LiOH, Li_2CO_3) formed on the surface during air exposure, resulting in an eight-fold reduction in the area specific resistance (ASR, defined as the interfacial or charge-transfer resistance of each electrode, normalised by area) of the Li/Al-LLZO interface. Sharafi *et al.* [174] extended this work by using contact angle measurements to quantify the Li wettability on LLZO, following wet and dry polishing procedures, and heat treatments. They report a low ASR ($2\,\Omega\,cm^2$) to be due to a combination of surface corrosion layer removal, and good wettability achieved by fine polishing (0.5 µm roughness) and heat treatment.

Cheng [147] also investigated the effect of microstructure and found that the interfacial resistance and cycling performance in Li/LLZO/Li cells are strongly correlated with the grain size and can be reduced by engineering of the microstructure and grain boundaries. Smaller grains (bimodal distribution of both 20 to 40 µm and less than 10 µm diameters) resulted in a lower ASR and higher critical current before short-circuiting than large-grained LLZO (100 to 200 µm). X-ray Laue microdiffraction showed no difference between the two microstructures, confirming that the better performance observed for small-grained samples can be attributed to the larger relative amount of surface layer grain boundaries, rather than grain orientation and grain boundary misorientation effects. This implied a beneficial effect of presumably low resistance grain boundaries on the interface with lithium metal. However, no further comment was made on this observation, in terms of the interaction of grains and grain boundaries with Li metal electrodes.

Chemical modifications/interlayers have also been used as an alternative approach to improving the contact at the electrode/electrolyte interface and/or to reduce the decomposition of the LLZO during cycling, which could lead to dendrites and cell failure. The idea is to create an interlayer which can enhance the interfacial charge and charge carrier (Li^+) transport properties. Luo *et al.* [175] used an amorphous Si layer on LLZO which becomes lithiated on contact with lithium metal, to improve the lithium wettability and thus enhance the Li mobility, leading to a smaller ASR ($127\,\Omega\,cm^2$) and charge/discharge cycling with up to $0.2\,mA\,cm^{-2}$ current densities. Han *et al.* [176] used an Al_2O_3 layer to reduce the ASR to the lowest reported value yet ($1\,\Omega\,cm^2$) and provide cyclability at $0.2\,mA\,cm^{-2}$, using the same arguments as Luo *et al.*, but the interface resistance was not directly measured using EIS; instead, the ASR was extrapolated from direct current cycling data. Neither paper reports on the mechanism or specific surface chemistry of how the surface modifications improve the cell performance, particularly on how the modification leads to increased critical current density for short-circuit. Ge-Li alloying (previously seen with $Li_{10}GeP_2S_{12}$ and Li metal) [80] has also been exploited by Luo *et al.* [175], using an evaporated Ge layer (20 nm) between Li metal and Ca- and Nb-co-doped LLZO, heating to 200 °C for 10 minutes to accelerate the Ge-Li reaction. This strategy is designed to provide continuous intimate contact between the Li metal and LLZO pellet surface.

An approach proposed by Goodenough and co-workers [177] introduced a cross-linked polymer in between garnet and Li metal, which effectively improved their contact and delivered stable electrochemical cycling performance. Despite the advantages of this technique on the interface transport properties, the use of such thick interlayers may limit the volumetric energy density of batteries.

Zhu *et al.* [178] used first-principles calculations to investigate the intrinsic electrochemical stability of LLZO, finding it to be within the narrow range of 0.05 to 2.91 V (vs. Li^+/Li). The phase equilibria at the reduction potential (0.05 V) consist of Zr_3O, La_2O_3 and Li_2O, and Li_2O_2, La_2O_3 and $Li_6Zr_2O_7$ at the oxidation potential (2.91 V). The much larger electrochemical stability reported elsewhere in cyclic voltammetry experiments [172, 179] is put down to an interfacial passivation mechanism, kinetically inhibiting the reaction with Li metal.

Difficulty in producing a clean, representative interface with Li metal makes the ability to perform microscopy characterisation difficult (largely due to the unstable and reactive Li metal). Ma *et al.* [180] studied in-situ formation of the interface using scanning transmission electron microscopy, using Li metal coating a tungsten tip to make contact with LLZO, and studied the interface formation as a function of time. They used spatially-resolved EELS performed immediately upon contact between Li and cubic Al-LLZO and studied the O K-edge in the EELS linescan to provide information on the localised atomic bonding configuration in LLZO. They found a reconfiguration of the O structure up to 6 nm away from Li metal contact (i.e. less than 5 unit cells). They also saw an increase in Li content from 6.25 to 6.95 a.p.f.u. They propose that Li^+ from Li metal must enter LLZO to maintain charge balance following reduction of LLZO by Li metal, and that formation of tetragonal LLZO is likely. Tetragonal-LLZO stopped growing instantaneously after formation, serving as a passivation layer preventing the cubic LLZO from being reduced completely by Li; i.e. it forms a self-limiting SEI layer with very small resistance as it is so thin. Note that this is a microscopic study and doesn't account for resistance increases due to mechanical contact issues (or contamination of surface) on a larger scale. Note also that no applied currents were used in this study; however, studying systems away from equilibrium, for example in-situ studies during cycling, are important for furthering our understanding of these systems.

The short-circuiting behaviour of LLZO with a lithium electrode is reported to arise from the formation of lithium dendrites in the cell. The mechanism of dendrite formation is disputed; however, several theories exist which concern both mechanical and electrochemical properties. It is generally agreed that the Monroe-Newman model [181, 182] describing conventional 'dendrites' in polymer systems in terms of shear modulus is not valid in ceramic electrolytes. Additionally, as the transference number for Li^+ is near unity in LLZO, diffusion is not expected to limit the current density as it does in liquid electrolytes. The influence of grain boundaries and their lithium ion diffusion kinetics is frequently put forward as the crux of the mechanism; however, difficulties in measuring the impedance and chemical composition of grain boundaries has made for a challenging problem to understand and solve.

Long *et al.* [123] argue that short-circuiting and dendrites are caused by current-focussing along low-conductivity aluminium-rich grain boundaries, which is used to explain the observations by Cheng [147], and suggested that Al-doped garnets will have lithium aluminates that are unstable against contact with lithium metal. They also show that even in hot-pressed Al-free garnets of 99 % ceramic density, dendrites form along grain boundaries as a consequence of current-focusing due to their poor local ionic conductivities and difficulty in creating an optimal Li-metal/ceramic contact. They found the Al-free LLZO grain boundaries were smaller and composed mainly of Li_2O, and could find inside traces of metallic lithium following short-circuit, using TEM and EELS analysis, and NMR Knight Shift measurements. When using a sputtered gold buffer layer, current densities as high as $0.5\,mA\,cm^{-2}$ were stable. The use of a gold buffer layer promotes the formation of an gold-lithium alloy at room temperature, helping provide a homogenous distribution of current at the surface during cycling. At higher current densities, it was proposed that short-circuiting occurs as a result of inhomogeneous deposition and dissolution of Li due to different conductivities of the grain and grain boundary (inferred from low temperature impedance measurements).

Virkar [183] proposes a model for degradation of lithium-conducting membranes under charging conditions, where the chemical potential of lithium μ_{Li} in the electrolyte may exceed that corresponding to pure lithium, μ^0_{Li}. This is expected to lead to precipitation of lithium and/or reaction with the electrolyte, and corresponding capacity fade. Raj and Wolfenstine [184] propose that a local electro-chemo-mechanical potential of Li develops from high local ionic resistivity of grain boundaries or from physical irregularities in the shape of the Li metal interface. This potential is reduced by the back-stress generated from the formation of the precipitate which opposes the nucleation of the dendrite, and is increased by the local electrical resistance of grain boundaries or by the concentration of current at a protrusion in the lithium metal surface. The growth of such a feature is estimated to occur if the interfacial charge transfer resistance is greater than $14\,\Omega\,cm^2$. The authors of the paper have proposed several current limit diagrams, showing the interplay between current density, ionic conductivity of the electrolyte and fracture stress of the ceramic on determining dendrite formation. These models agree with experiments in terms of the critical current density for dendrite nucleation.

PhD thesis work by Manalastas [185] suggested that local pressurisation caused by mechanical stress of lithium point-contacts produces fracture lines in the ceramic which lead to the mechanical propagation of metallic lithium, following the model proposed by Raj. This mechanism was expected to be dominant at low temperatures where local current densities are inhomogeneous as a result of poor Li metal-LLZO contact, and as a result of prolonged lithium plating/stripping. This was experimentally demonstrated following a 5 V polarisation, and it is unclear whether this leads to local heating of the metal, accelerating the process.

Porz *et al.* [186] observed the propagation of Li dendrites from electroplated lithium metal on single- and poly-crystalline Ta-doped LLZO, coupling galvanostatic cycling with in-situ microscopy. They suggest an initial growth mechanism based on the propagation

of surface flaws, showing that the current density for initial crack propagation is not correlated to surface roughness; rather that lithium metal plating occurs in the presence of any type of surface flaw or defect, using capillary action to help fill them. Once the flaw is completely filled, mechanical stresses within the lithium metal and electrolyte are expected to rise as the plating continues. Above a critical current density, the Li plating overpotentials, and corresponding mechanical stresses, reach values sufficiently large to extend surface defects, which subsequently can also form more complex networks.

Finally, in another take on the origin of metallic lithium formation in LLZO, Aguesse *et al.* [187] observed isolated lithium metal agglomerates, in addition to propogated dendrite networks, in Ga-LLZO after cell cycling with Li metal electrodes, but were unable to say whether these resulted from interconnected pores in the ceramic (not visible from scanning electron microscopy analysis). They speculate that these might form by the reduction of Li^+ ions in the LLZO by recombination with an electron from the oxygen network, or from residual electronic conductivity, creating electron transfer from the electrode to the Li ion.

3.5 Summary

The development of solid state electrolytes for lithium batteries is an important part of enabling a low-carbon energy future. This chapter has reviewed a range of literature on the most promising ceramic lithium conductor, the garnet-type oxide. It has covered development in the understanding of the structure of lithium-stuffed garnets, and its relationship to lithium transport in the material. Strategies involving doping with supervalent cations to enhance the ionic conductivity have been discussed, in addition to the degradation reactions with H_2O and CO_2, and the role of proton-lithium exchange on stability and ionic transport. Finally, the properties relating to the lithium metal electrode/electrolyte interface have been discussed, in terms of the interfacial resistance and implications on cell performance, in addition to the behaviour under cell cycling and the propagation of lithium dendrites.

Based on this review of the key properties of lithium-rich garnets, there are a number of open questions to be addressed in this thesis:

1. Is it possible to correlate the concentration and site occupancy of supervalent dopants on the lithium sublattice with the transport properties (i.e. ionic conductivity) of LLZO? How does the conductivity depend on the number of lithium vacancies generated by doping, the dopant content and position, and the number of lithium ions in the lattice?

2. What is the effect of doping and synthesis conditions on the microstructure, and subsequently, the effect on the ionic transport?

3. Can we macroscopically measure the diffusion of lithium, to complement existing microscopic studies, long-range pulsed field gradient (PFG) NMR-probed diffusion, and computational predictions?

4. To what extent does the proton-lithium exchange reaction and associated degradation products effect the macroscopic transport properties of LLZO? What is the effect of deep proton exchange on pellets of LLZO, both chemical and electrochemical, and how does the diffusion of H^+ proceed during this process?

5. What is the effect of different dopants on the cell performance of LLZO with lithium electrodes? Can we use chemical analysis to understand the critical currents for dendrite formation in LLZO and correlate to compositional properties?

Chapter 4

Experimental Methods

This chapter contains an overview of the principle experimental techniques used in this work. Firstly a description of the methodology for synthesis and processing of ceramic garnet-structured lithium-conducting electrolytes is given, followed by details of the diffraction techniques used for identifying crystallography, namely X-ray and neutron powder diffraction. Next, the electrochemical characterisation techniques (impedance spectroscopy, cyclic voltammetry and charge/discharge cycling) used are discussed, before an outline is given of additional characterisation techniques drawn on in this thesis- including X-ray photoelectron spectroscopy (XPS), electron microscopy, low energy ion scattering (LEIS) and nuclear magnetic resonance (NMR). As secondary ion mass spectrometry (SIMS) is relied heavily upon in the analysis of these materials, especially in the interpretation of ion exchange experiments, a detailed discussion of its theory and application is included.

4.1 Synthesis and Processing

Ceramic synthesis is usually classified under two primary experimental routes: solution and solid state methods. In this thesis, the sol-gel form of the solution route was exclusively used in the synthesis of garnet electrolyte materials. The garnet compositions explored in this work are based on the formula $Li_{7-nx}M_xLa_3Zr_2O_{12}$ (M-LLZO), where M is a cation of charge n. In particular, compositions where M = Ga^{3+} and Al^{3+} are the primary focus, as they are widely reported in the literature due to Ga-doped LLZO being a highly conductive material, and as Al is a common impurity introduced into the structure through the use of alumina crucibles. Undoped LLZO, which formally adopts the tetragonal, less-conducting structure, is also explored, in addition to Ge-doped LLZO (Chapter 5) as a new garnet composition (see Chapter 3 for more discussion of the role of dopants).

4.1.1 Sol-Gel Method

The samples in this work were prepared using a modified Pechini-type [188] citrate/nitrate route based on the process reported by Aguadero *et al* [137]. The traditional sol-gel

method is a solution-based method for ceramic synthesis which utilises the ability of alpha-hydroxycarboxylic acids (such as citric acid) to form chelates with selected metal ions, which then undergo polyesterification when heated with a hydroxyalcohol. This has the advantage over conventional solid state methods of homogenously combining the components of the desired ceramic composition on a molecular level, ensuring mixing at the correct stoichiometry without the need for extensive mechanical mixing of the powder precursors. It can allow very small quantities of materials to be introduced homogenously into a solid state matrix and also allows greater control of particle size when combined with subsequent heating steps [189].

In this modified route, the sol-gel or resin formed upon heating (dehydration) consists of the dissolved stoichiometric mixture of cation compounds in ethanol (sometimes added to aid the dissolution of the pentanedionate compound), citric acid (added in excess as a complexing agent to ensure molecular scale mixing is maintained on evaporation), and nitric acid. It can be decomposed at moderate temperature (here 600 °C) in a muffle furnace to remove the organic material and leaving the mixed metal oxide.

In this work, a beaker or porcelain bowl was filled with stoichiometric amounts of lithium nitrate $LiNO_3$ (99 %) lanthanum (III) nitrate hexahydrate $La(NO_3)_36H_2O$ (99.9 %), zirconium (IV) 2,4- pentanedionate $ZrC_{20}H_{28}O_8$ and dopant atoms in the form of gallium (III) oxide Ga_2O_3 (99.99 %), aluminium (III) nitrate nonahydrate $Al(NO_3)_39H_2O$ (98 %) or germanium (IV) oxide GeO_2 (99.98 %) (all from Alfa Aesar). An additional amount of lithium nitrate was added to allow for lithium losses at elevated temperatures (nominally 10 wt% excess). Citric acid (10 wt%, equivalent to 0.542 molar, approx. 200 ml) and a small amount of nitric acid to aid dissolution (68 wt%, approx. 5 to 10 ml, VWR Chemicals) were added and the solution left to stir with a magnetic stirrer on a hotplate until a gel formed. The gel was combusted in a furnace for 12 hours at 600 °C (heating rate: 2 °C min^{-1}, cooling rate: 10 °C min^{-1}) in order to remove all water and organic compounds. The temperature was then held at 100 °C to prevent condensation of water and transferred to an argon-filled glove box via a vacuum antechamber.

4.1.2 Thermal Treatment

The resulting dry powder from the thermal decomposition step was hand-milled in an agate pestle and mortar to a fine powder inside the glove box (<0.3 ppm H_2O), followed by calcination at 800 °C for 12 hours in dry flowing oxygen (99.9999 %; 0.5 ppm H_2O) or in an argon-supplied furnace coupled to the glove box (5 mbar pressure). This temperature was chosen as it is above the typically reported phase-transition temperature between the tetragonal and cubic garnet phases for the vacancy-free LLZO material [117–119]. This step is thus designed to allow facile cation diffusion and favour the formation of the thermodynamically stable oxide product. The use of an oxygen atmosphere with a defined oxygen partial pressure is designed to control the site preferences and oxidation states of the ions, and is preferred over other atmospheres for defining the material obtained at this step.

In the garnet $Li_7La_3Zr_2O_{12}$ (LLZO) material, the formation of a cubic LLZO phase

depends on the thermal treatment temperature [190, 191], time and atmosphere [118, 137], heating and cooling rate [191], dopant [35, 120, 155] and lithium stoichiometry [98, 153]. As in any system containing multiple chemical components, there exists a phase equilibrium which balances decomposition and reorganisation of phases, and can be described as a function of temperature. Sufficient time for the completion of the garnet-phase formation reaction and equilibration of Li across tetrahedral (Td) and octahedral (Oh) sites is also necessary during thermal treatment. The lithium distribution across these sites changes as the temperature increases above the phase transition temperature, starting from the ordered lithium distribution found in the tetragonal garnet and into a random distribution in between Oh and Td positions in the cubic phase with increasing temperature [191].

In this work a third step was carried out to produce a dense ceramic pellet. The calcined powder was milled and pressed into pellets (typically 10 or 13 mm diameter green body) in the glove box using a uniaxial press under an applied weight of 2 to 3 tonnes, depending on diameter. The pellet was finally sintered at one of a number of high temperatures (1100 °C to 1200 °C) for 6 hours, ensuring a bed of the same powder (mother powder) encased the pellet in the crucible. Three types of atmospheres were used for the sinter steps: tubular furnace with dry oxygen flow (99.9999 %; 0.5 ppm H_2O); vacuum furnace coupled to glove box (10^{-4} mbar); and argon-supplied furnace coupled to glove box (5 mbar). The result is a dense pellet which is ground and polished depending on the desired finish for experiments (Section 4.1.3). Al_2O_3 crucibles were used as the typical vessel for powder and pellet thermal treatments, using a loose fitting lid for argon or vacuum-atmosphere glove box housed ovens (owing to the pump-down process used before the heating program and to minimise powder escaping into the furnace). In special cases, ZrO_2 crucibles were used to avoid aluminium contamination.

Heating to above 1100 °C with a holding step is used to sinter the pellets. This temperature step allows the growth of grains and pellet densification. It is also the cause of the sometimes unintentional introduction of Al^{3+} into the garnet lattice from the alumina crucible (as in the case of Murugan *et al*. [106] when they first reported superionic conductivity in LLZO), through the action of a liquid eutectic at 1055 °C from the Li_2O-Al_2O_3 system [192, 193] (Figure 4.1). The liquid melt is thought to aid the sintering process (known as liquid phase sintering) [194], as well as leading to diffusion of Al into the grains [195, 196]. The formation of this melt leads to loss of precision in controlling the Al doping content, and also the occurrence of directional mass transport and grain growth. Samples sintered at these high temperatures contain a graded distribution of Al throughout their volume. We have seen this directional distribution of cations using LEIS and SIMS analysis, with both Ga-doped and Al-doped pellets ($Li_{7-3x}M_xLa_3Zr_2O_{12}$, with M = Ga, Al and x = 0.10 to 0.15), where there is clear diffusion of Al (leading to enrichment) from the crucible into the nearest pellet face and across the pellet edges after high temperature treatment (Chapter 5, Section 5.1.2).

Special care was taken to avoid the exposure of the powders and pellets to moisture, by handling and processing all steps in the glove box. It is important to control the moisture

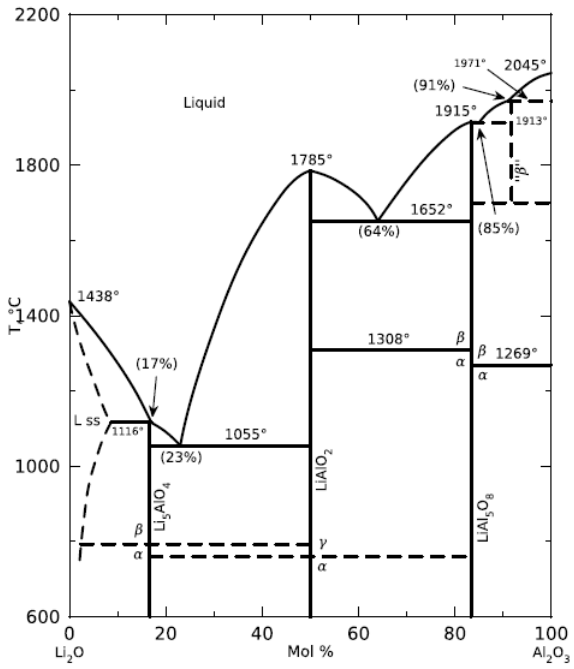


Figure 4.1: Li_2O-Al_2O_3 phase equilibrium diagram (where T is the temperature, Mol% is the molar fraction of Al_2O_3 in %) determined by Cook and Plante [192], showing a liquid eutectic at 1055 °C at 23% Al_2O_3.

levels during synthesis to avoid reaction of LLZO with water leading to proton-lithium exchange processes and associated changes in transport properties (see Chapter 3, Section 3.3 and Chapter 6 for further discussion).

4.1.3 Pellet Finishing

The mother powder used to cover the pellet during sintering creates partly-fused powders on the surface of the sintered pellets, which is removable by abrading the pellets. Polishing was carried out within the argon glove box using 800, 1200, 2400 and 4000-grit SiC polishing papers (Struers), and also with diamond powders up to 0.1 µm in diameter, if a finer finish was needed for certain analyses. The details of polishing will be described on a case-by-case basis in each of the results chapters.

Where the microstructure needed to be revealed, careful fine polishing to 0.1 µm with diamond paste was sufficient to view in an optical microscope. Thermal etching was a faster method which was also used to reveal the microstructure to a greater extent. This involved heating the pellet on a platinum foil in argon to 900 °C for 30 minutes. The thermal etching process undoes mechanical damage caused by polishing by allowing the grains to recrystallize, thus revealing the grains and grain boundaries at the surface of the pellet, and leaving a relief effect [197].

4.1.4 Density Measurement

The density of the pellets was measured either geometrically, using the mass and calculated volume from geometrical measurements with callipers, or by the Archimedes method [198] with dry ethanol (water was not used to avoid reactions of the LLZO pellet caused by proton-lithium exchange processes).

The theoretical density (ρ_{theory}) of the material is given by Equation 4.1, where n is the number of formula units per unit cell (8 in the case of LLZO), M_{w} is the molecular mass, V is the unit cell volume (calculated from diffraction measurements of lattice parameters) and N_{A} is Avogadro's number.

$$\rho_{\text{theory}} = \frac{nM_{\text{w}}}{N_{\text{A}}V} \tag{4.1}$$

The Archimedes method is based on the expression for the specific gravity of a solid, ρ, (Equation 4.2), where $W(\text{a})$ is the weight of the sample in air, $W(\text{fl})$ the weight in liquid and $\rho(\text{fl})$ is the density of the liquid.

$$\rho = \frac{W(\text{a})\rho(\text{fl})}{W(\text{a}) - W(\text{fl})} \tag{4.2}$$

The buoyancy is given by $W(\text{a}) - W(\text{fl})$ and, to allow for buoyancy in air, the following corrections are made, where $\rho(\text{a})$ is the density of air ($0.0012\,\text{g}\,\text{cm}^{-3}$) under standard conditions and $\rho(\text{fl})$ is $0.789\,34\,\text{g}\,\text{cm}^{-3}$ for ethanol at 20 °C [199], giving Equation 4.3:

$$\rho = \frac{W(\text{a})\{\rho(\text{fl}) - \rho(\text{a})\}}{\rho(\text{fl})|W(\text{a}) - W(\text{fl})|} + \rho(\text{a}) \tag{4.3}$$

The Archimedes method was carried out by measuring the weight of the sample in air followed by measuring the weight in dry ethanol. Prior to weighing, the pellet was immersed in boiling ethanol until no more bubbles were seen to leave the sample, thus removing any air bubbles inside the pellet which might contribute to an increased buoyancy. The temperature of the ethanol during the measurement was recorded to ensure an accurate value of density of the fluid.

4.2 Diffraction Techniques

The crystal structure and phase purity of the powders and pellets obtained were measured by X-ray diffraction. Crystal structure subtleties regarding space group identification and lithium distribution and quantification, as well as dopant localisation, were made using neutron powder diffraction. Le Bail and Rietveld pattern refinement of the diffraction data using the FullProf program [200] were employed for phase determination and for refining the space groups, atomic positions, occupancy, lattice parameters and isotropic thermal displacement of the atoms.

4.2.1 X-ray Diffraction

X-ray diffraction (XRD) is a fast, non-destructive, analytical technique used for phase identification of crystalline materials and can be used to measure the average spacing between layers or rows of atoms - hence providing information on the unit cell dimensions. Diffraction is defined as the interference between waves resulting from an object in their path. This can be applied to X-rays using the phenomenon that they are scattered by electrons in atoms (Thomson scattering, the elastic scattering of electromagnetic radiation by a free charged particle) [201], resulting in diffraction for a periodic array of scattering centres separated by distances similar in wavelength to the radiation ($\approx 100\,\text{pm}$), e.g. lattice planes in a crystal.

The X-rays are generated by bombarding a metal with high energy electrons. The electrons decelerate as they plunge into the metal, generating radiation with a continuous range of wavelengths (Bremsstrahlung). A few high intensity peaks are superimposed on this continuum, which are created by the collision of incoming electrons with the atoms' inner shells (Figure 4.2a). An electron is expelled from an inner shell as a result, causing an electron of higher energy to drop into the vacancy created and emitting the excess energy as an X-ray photon (Figure 4.2b) [84]. K_α radiation is thus created by an electron transition to the innermost K shell (1s orbital, principal quantum number 1) from a 2p orbital of the second outermost L shell, and occurs as a doublet owing to spin-orbital interactions.

The diffraction of these X-rays by a crystal follows the condition that reflection from successive parallel planes be coherent if the path difference between parallel reflected beams is an integral number (n) of wavelengths (λ). Bragg's Rule (Equation 4.4) [202] gives the condition for a diffracted beam, where d is the interplanar spacing and θ is the angle of incidence with respect to the scattering planes.

$$2d \sin\theta = n\lambda \tag{4.4}$$

From the reflections observed when a monochromatic beam of X-rays falls on a crystalline solid, it is possible to determine the size and symmetry of the unit cell as only those rays which satisfy the Bragg condition constructively interfere (Figure 4.2c) and produce a characteristic diffraction pattern for the material.

The angle at which reflection can occur for a family of parallel lattice planes, described by Miller indices (h,k,l), is determined only by the lattice symmetry and unit cell parameters through the Bragg relationship, where the interplanar spacing d_{hkl} is related algebraically to the unit cell parameters, as seen in Equations 4.5 and 4.6 for the special case of a cubic unit cell in which the cell parameters obey $a = b = c$ [203].

$$\frac{1}{d_{hkl}^2} = \frac{h^2 + k^2 + l^2}{a^2} \tag{4.5}$$

$$a^2 = \frac{\lambda^2}{4\sin^2\theta}\left\{h^2 + k^2 + l^2\right\} \tag{4.6}$$

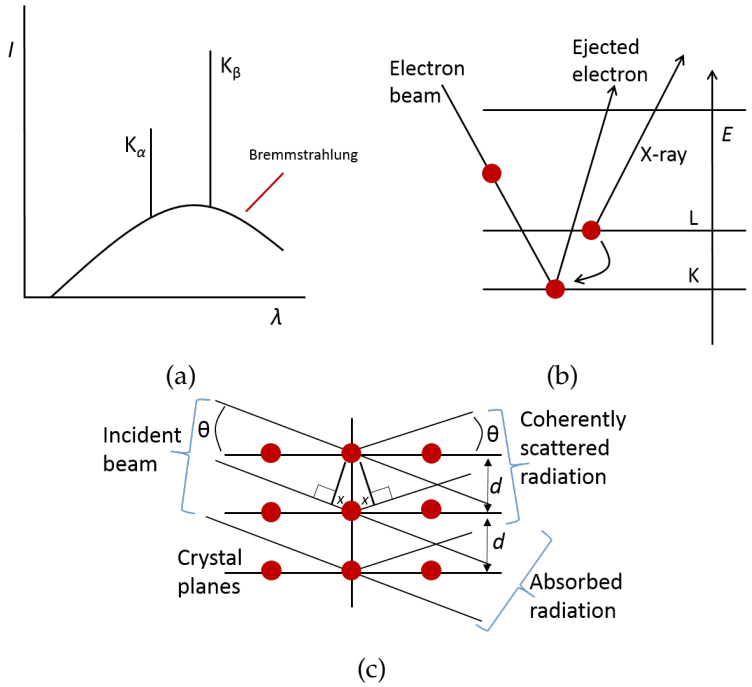


Figure 4.2: (a) The continuous range of X-ray wavelengths (λ) produced as high energy electrons bombard a metal, overlaid with sharp, intense peaks (intensity I) from collision with inner shells of atoms (termed K_α and K_β radiation); (b) the production of X-ray photons from ionisation of external electrons and ejection of inner shell electrons, where E is the energy of the electrons in the atom, and K and L are the electron shell labels; (c) diffraction of X-rays by atoms in a crystal lattice with interplanar spacing d, showing the schematics of Bragg's Law (Equation 4.4), where $d \sin\theta = x$, and $2x$ is the path difference, equal to an integer number of wavelengths for constructive interference. θ is the angle of incidence for the incoming X-ray beam.

The Bragg rule gives the geometrical condition for a reflection to occur. The observed intensity of the reflection is a function of several factors, which depend on a mixture of the experimental setup and the composition and physical properties of the crystalline solid sample. The relative intensity for a powder diffractogram is given by Equation 4.7 [204], where I_{hkl} is the intensity of the $\{hkl\}$ reflections and Lp_{hkl} is the Lorentz polarisation factor, which allows for the partial polarisation of the reflected beam and the geometry of the measurement (tabulated values). The multiplicity factor, J_{hkl}, describes the relative proportion of planes contributing to the same reflection. W_{hkl} is the temperature (atomic displacement) factor which describes how the thermal vibrations of atoms at normal temperatures cause them to occupy a larger volume than when at rest, and will reduce the scattering. The effect is more noticeable at high angles. The $\exp(-2W)$ term models atomic displacement, giving an indication of atomic disorder on a site. The absorption factor, A_{hkl}, is a function of the Bragg angle and can be elastic ($\Delta\lambda = 0$) or inelastic ($\Delta\lambda \neq 0$, i.e. fluorescence).

$$I_{hkl} \propto Lp_{hkl} J_{hkl} F_{hkl}^2 \exp(-2W_{hkl}) A_{hkl} \tag{4.7}$$

The structure factor, F_{hkl}, describes the amount of scattering from hkl planes in the direction θ defined by Bragg's law (Equation 4.8) [203], where the unit cell in the crystal contains N atoms of which the j^{th} atom has an atomic scattering factor $f_j(hkl)$ and the fractional unit cell coordinates x_j, y_j, z_j. The atomic scattering factor measures the amount of scattering in direction θ from a single atom of the type located at x_j, y_j, z_j.

$$F_{hkl} = \sum_{j=1}^{N} f_j(hkl) \exp 2\pi i(hx_j + ky_j + lz_j) \tag{4.8}$$

In practice, powder diffraction patterns are produced by measuring the number of counts along a 2θ scan by varying the position of the X-ray source relative to the detector. Bragg-Brentano geometry is used, i.e. the geometry of the goniometer is such that reflections from the sample result in the diffracted beam being refocused at the detector when the sample is rotated at half the speed of the detector ($\theta/2\theta$). The generation of X-rays from a copper target results in characteristic X-rays of Cu-$K_{\alpha 1}$ ($\lambda = 1.5405$ Å), Cu-$K_{\alpha 2}$ ($\lambda = 1.5444$ Å) and Cu-K_β, hence the instrument is fitted with a monochromator which removes the Cu-K_β component. The preferred orientation of crystallites in the specimen will affect the relative intensities observed, making sample preparation important in ensuring random orientation of crystallites (milling the powder finely prior to diffraction measurement).

X-ray diffraction is used on both powders and pellet samples in this work to characterise the materials in terms of crystallographic phase formation and to determine the lattice parameters of each phase. Where precise control of the atmosphere is required (i.e. in the proton exchange work, Chapter 6), a sample holder using Kapton (polyimide) tape is used to protect samples from the air by mounting the powder or pellet sample in the glove box. Patterns were typically obtained between 10 and 90 °2θ, using a step size of 0.034 °2θ on a Bruker D2 Phaser instrument for fast acquisition for a quick phase

purity check, and on a Panalytical Empyrean instrument for higher quality data used for refinements, with the angle range 10 to 80 °2θ, a step size of 0.001 °2θ, and time per step of 40 s step^{-1}. Both use Cu-K$_\alpha$ radiation. Le-Bail [205] and Rietveld [206–208] refinements using the FullProf program [200] were made to determine lattice parameters and atomic site occupancies, respectively.

4.2.2 Neutron Diffraction

Because X-rays are scattered according to electron density, there is an atomic number (Z)-dependence on the observed X-ray diffraction pattern, meaning that heavy elements will contribute disproportionately to the XRD pattern. As such, light atoms such as O, Li, and H (important in the study of the materials of interest in this work) are difficult to locate in the presence of heavier atoms as their X-ray scattering ability is negligible. Unlike X-rays, neutrons (of appropriate wavelength, in this case, 1.5940 Å) are scattered by nuclei; the nuclear scattering length is no longer a function of Z and has a much narrower range than the atomic scattering factor in XRD (see Figure 4.3 for a plot of neutron scattering cross-sections as a function of atomic weight). Light elements can thus contribute a lot to a neutron diffraction pattern so that their atomic coordinates can be accurately determined. Additionally, atoms of similar atomic number which are difficult to distinguish using XRD may have very different scattering lengths in neutron diffraction. Hence neutron diffraction can contain some important information on lithium, as its scattering ability is large and negative (its bound coherent scattering length is −1.9 fm) [209] (Figure 4.3), allowing ease of localisation and quantification compared to XRD. Because the scattering is caused by nuclei instead of electrons, there is no need to use an atomic form factor to describe the shape of the electron cloud of the atom, and hence the scattering power of the atom does not fall away with the scattering angle. So there can be strong, well-defined diffraction peaks even at high angles. However to enable good counting statistics, large sample volumes are required, and the experiments require reactor or spallation sources for the neutrons.

In this work, neutron powder diffraction was carried out at the research reactor at Institut Laue-Langevin (ILL), France, which uses a steady neutron flux (1.5 x 10^{15} neutrons s^{-1} cm^{-2}) [211] as a result of nuclear fission with a uranium source. Powder samples of Ge-LLZO were sent under an argon atmosphere and measured to localise the Ge and Li atoms in the lattice, using the D2B high-resolution two-axis diffractometer with a high take-off angle (135°) Ge monochromator and constant wavelength (λ =1.594 Å). The sample (a cylinder of the powder) was diffracted by a high resolution monochromatic incident beam, and the Bragg reflections were measured by a bank of 128 ^{3}He detectors, which are moved such that the counts are averaged over several detectors. For the measurements, the angular range used is 0.05 to 159.95 (°2θ) and the step scan increment = 0.05 (°2θ).The neutron scattering lengths for Li, Al, Ge and Zr are -1.90, 3.45, 8.19 and 7.16, respectively [209].

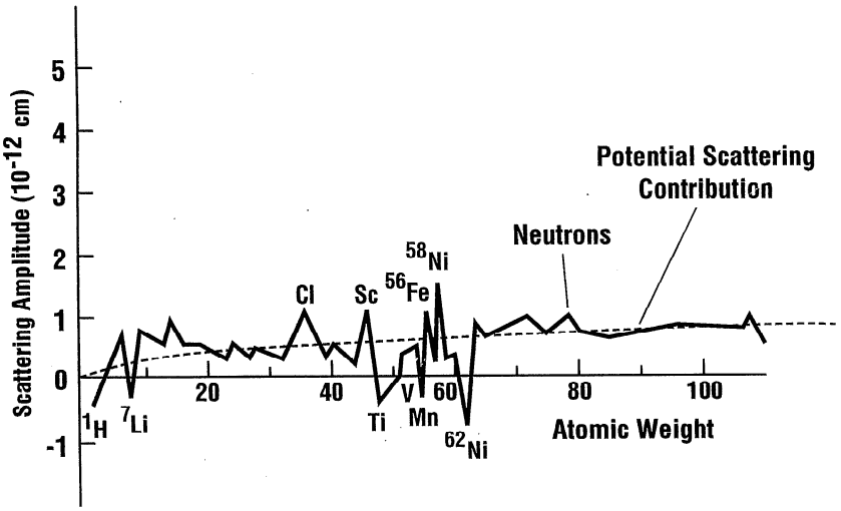


Figure 4.3: Plot of neutron scattering amplitudes as a function of atomic weight (adapted from Bacon) [210].

4.2.3 Structural Refinement

Refinement is utilised to obtain structural information from powder XRD and neutron diffraction patterns. Structural solution methods (such as Rietveld [206]) rely on the generation of approximate phases from the reflections obtained to develop a structural model, as direct calculation of electron density is not possible. The observed amplitudes of reflections are compared to the calculated amplitudes given by model-based structure factors and refined further.

It is common to begin with the le Bail [205] method of refinement, which enables pattern fitting by first determining the unit cell parameter and the space group. This is followed by fitting refineable parameters using a least squares method to minimise the difference between the calculated and observed profiles. In the le Bail method, peak intensities cannot be fitted using the least squares method - instead, an arbitrary starting peak intensity is used, which after each least squares fit is recalculated as the new set peak intensity. Having performed le Bail, Rietveld refinement can then be performed. Rietveld introduces additional structure factors which enable the peak intensities to be fitted from the structural model.

In this work, patterns were fitted using Fullprof software [200] with le Bail and Rietveld refinements. A pseudo-Voigt [212, 213] peak shape function was used to fit the data. The quality of refinement was assessed visually and through the goodness of fit parameter, χ, which is defined by Equation 4.9 [207] and provides an indication of the agreement between the model and the experimental data,

$$\chi = \sqrt{\frac{R_{\mathrm{wp}}}{R_{\mathrm{exp}}}} \tag{4.9}$$

where R_{wp} is the weighted profile and R_{exp} is the expected residual profile. As the fit improves, χ^2 tends to 1.

4.3 Surface Characterisation

Two of the surface-sensitive techniques used in this thesis are described here, X-ray photoelectron spectroscopy (XPS) and low energy ion scattering (LEIS), which have surface sensitivities ranging from the top atomic layer (LEIS) to several nanometres (XPS). Another surface analysis technique, secondary ion mass spectrometry (SIMS), will have its own section dedicated to it (Section 4.8), at the end of this chapter, as it is used more extensively in this thesis and merits a more detailed discussion.

4.3.1 X-ray Photoelectron Spectroscopy

X-ray photoelectron spectroscopy is a quantitative spectroscopic technique which measures the elemental composition of a surface (typically 0.5 to 10 nm sampling depth) [214] and the electronic state of its elements. In XPS, an X-ray source generates monochromatic radiation which irradiates the sample, causing it to emit photoelectrons. Both core and valence electrons can be ionized by X-ray radiation; it is the core electrons whose binding energy (E_B) is characteristic of their element, thus allowing the elemental surface composition of the sample to be determined. XPS requires a high vacuum environment ($< 10^{-9}$ mbar), so as to avoid interference of the photoelectrons in gas-phase collisions. E_B is found by measuring the kinetic energy, E_K, of the sample's emitted photoelectrons, according to Equation 4.10,

$$E_K = h\nu - \Phi - E_B \tag{4.10}$$

where Φ is the workfunction of the sample, the minimum work needed to extract electrons from the Fermi level (see, for example, Figure 4.4) across a surface carrying no net charge, and $h\nu$ is the incident photon energy.

Koopmans' theorem [215] states that the binding energy of an electron is the difference between the initial ($E_{initial}$) and final (E_{final}) states of the atom during photoemission. If there is no relaxation (electronic rearrangement) following photoemission, then E_B can be said to be equal to minus one times the orbital energy. From E_B, the elements in the surface layers are identified and information about the oxidation state and bonding of the atoms can be extracted by observing small changes in E_B (caused by a change in chemical environment).

XPS is a surface sensitive technique, in that only those electrons close to the surface of the sample are able to escape elastically and contribute to the peak intensity. Those emitted deep in the bulk of the sample are inelastically scattered, so cannot overcome the work function and contribute to the spectral background. The sampling depth is defined as the depth from which 95 % of all photoelectrons are scattered by the time they reach the surface (3λ, where λ = the inelastic mean free path of an electron in a solid). Most λ are in the range 1 to 3.5 nm for Al K_α radiation, hence the sampling depth is 3 to 10 nm [216].

XPS can also be used for the quantitative elemental analysis of a sample. Assuming a uniform elemental composition within the XPS sampling depth, the XPS peak area I_i

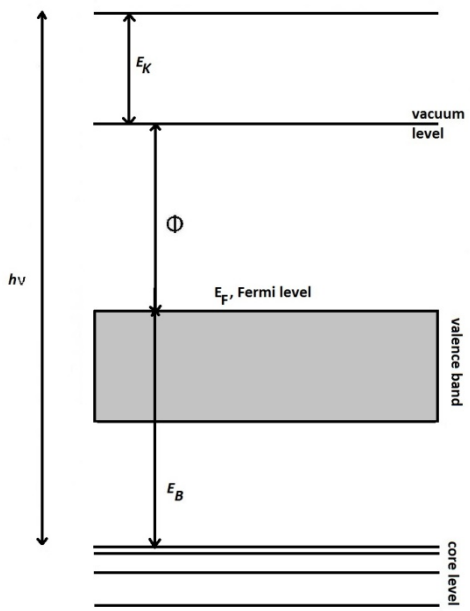


Figure 4.4: Energy level diagram of an atom showing the relationship between the photon energy ($h\nu$), the work function (Φ), the electron's binding energy (E_B) and the kinetic energy of the photoelectron (E_K).

associated with an element i is proportional to its concentration N_i. However, the peak area also reflects the photoionisation cross-section σ_i, the electron mean free path λ_i and instrument detection efficiency factors (combined into one constant factor K) associated with the XPS peak involved (Equation 4.11) [216]. In modern analysis software packages all three factors are accounted for, and use a library of tabulated sensitivity factors that have been determined from a combination of theoretical calculations of cross-sections and reference measurements. The sensitivity factors cover both cross-section and instrument factors.

$$I_i = N_i \sigma_i \lambda_i K \tag{4.11}$$

In this work the technique is used to understand surface chemistry of LLZO pellets (with a probing depth estimated to be 3 to 10 nm, considering the inelastic mean free path of electrons in inorganic materials) [168, 216] to investigate the oxidation state of Ge in Ge-doped LLZO (Chapter 5, Section 5.2.5) and after different atmosphere treatments to follow the moisture reactivity (Chapter 6, Section 6.4.2), as well as surface chemistry changes in LLZO following cell cycling. Samples were polished and cleaned with isopropyl alcohol and acetone in the argon-filled glove box prior to transfer in a vacuum suitcase to the instrument, and mounted with conductive carbon tape. Measurements were taken using a 200 µm by 200 µm beam, using a flood gun for charge compensation. The spectra were recorded on a Thermo Scientific K-Alpha+ spectrometer with a chamber pressure of 2x10^{-9} mbar and an Al K_α X-ray source (incident photon energy $h\nu$ = 1486.6 eV) with a double focussing 180° hemispherical analyser and 2D detector. Data were collected

at pass energies of 200 eV for survey, and 20 eV for core level spectra. The binding energy of the obtained XPS spectra was calibrated with respect to the C 1s peak of adventitious carbon at 284.8 eV. XPS spectra were quantitatively analysed using the Avantage software package by deconvoluting Voigt-type line-shapes, preceded by subtracting a Shirley-type background [217] (for Zr 3d spectra) and linear background (for Al 2p and Li 1s spectra). The software uses the Tanuma-Powell-Penn [218] approach to account for the inelastic mean free path. Measurements and analyses were made by Dr Anna Regoutz at Imperial College London.

4.3.2 Low Energy Ion Scattering

Low energy ion scattering is a surface analysis technique which gives the atomic composition of the outer atoms of the surface of a specimen, as well as enabling high resolution depth-profiling of a material [219]. The strength of LEIS analysis lies with the fact that it is truly surface sensitive, in that it can be used to analyse the uppermost monolayer of a material [220, 221]. In addition, LEIS is able to provide isotopic information and is generally considered to be free from matrix effects as the elemental yields are independent of the chemical environment of the surface atom, and it is also less sensitive to surface roughness than its sister technique, SIMS [222] (Section 4.8). In LEIS, noble gas ions of a known mass and energy are fired at the surface of the specimen; the energy of these incident ions are 0.5 to 10 keV in the low energy regime. These ions are backscattered by the surface atoms and produce an energy spectrum, with peaks resulting from binary collisions of an ion with an outer atom of the sample. The energy of the peak is determined by the conservation of energy and momentum, as described by Equation 4.12 [219]:

$$E_\mathrm{f} = E_i \left\{ \frac{\cos\theta + \sqrt{(r^2 - sin^2\theta)}}{1+r} \right\}^2 \tag{4.12}$$

for $r = m_\mathrm{at}/m_\mathrm{ion} \geq 1$ and $\theta \geq 90°$.
m_ion is the mass of the ion with incident energy E_i which is backscattered over an angle θ by a surface atom of mass m_at, and the backscattered energy of the ion is E_f. Figure 4.5 shows a schematic of the process, which shows the incident ion beam directed at the surface at an angle α with respect to the surface normal. Projectiles are scattered from surface atoms almost exclusively by binary collisions, with an energy $E_\mathrm{f} = kE_0$. Ions that have penetrated the target further up to a depth Δx will leave the surface with an energy $E_1 \ll kE_0$. [220]

The energy distribution of the backscattered ions is therefore a mass spectrum of the atoms in the outer surface of the specimen, and the backscattering can only occur for atoms of a higher mass than the mass of the noble gas ion. It is thus theoretically possible to detect lithium, using $^3He^+$ and $^4He^+$; however, under the conditions used here there is a lack of sensitivity towards lithium detection owing to an undesirable background at low scattering energies caused by sputtering ejection of light atoms or adsorbed species on the surface. As such, lithium was not followed under the measurement time constraints in this thesis. However, Téllez *et al*. [222] have recently reported the ability to detect lithium

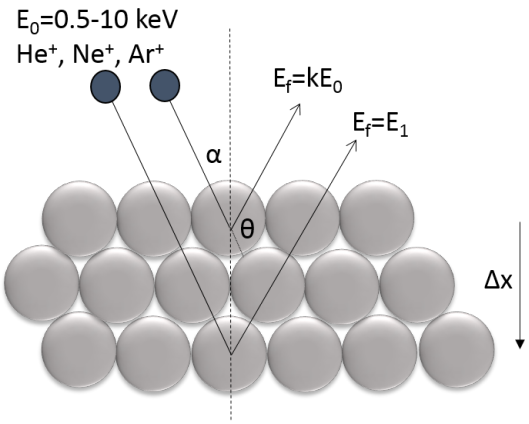


Figure 4.5: Schematic of experimental conditions in LEIS, adapted from Brongersma [220]. See text for an explanation of the symbols.

in $Li_{3x}La_{2/3-x}\square_{1/3-2x}TiO_3$ (an ABO_3 perovskite, where $\square$ is an A-site vacancy) using an ion beam pulsing approach, which requires long analysis times. LEIS probes the outer atomic layer of a sample under the normal operating mode, as the probability of projectile ions neutralising during a scattering event is high and thus the likelihood of a projectile scattering off deeper layers is dramatically reduced in comparison to the surface layer; using a sputter beam such as Ar^+ can enable successive atomic layers to be analysed.

In this thesis LEIS is used to probe the surface chemistry of LLZO pellets after different atmosphere treatments in Chapter 6 (Section 4.3.2), using sputtering to follow the formation of a corrosion layer following air and moisture exposure. Measurements were made on a Qtac100 instrument (ION-TOF GmbH) with a 3 keV $^4He^+$ primary analysis ion beam with 5 nA current, and a secondary 0.5 keV Ar^+ sputter ion beam operating with a current of 100 nA for depth-profiling. To maintain surface accuracy when using the primary beam, the total dose of each analysis spectra was kept below the static limit of $7x10^{14}$ ions cm^{-2} for the ^4He projectiles. The Ar^+ dose used was $3.4x10^{15}$ ions cm^{-2} to enable sputtering processes. Measurements and analysis were made by Dr Andrea Cavallaro at Imperial College London.

4.4 Electron Microscopy

Electron microscopy is a method of microscopy which uses a beam of accelerated electrons as a source of illumination to create an image of a specimen [223]. The wave-particle duality of the electron allows it to be used in place of visible light in an imaging setup. High resolutions can be achieved as it uses a beam of high energy electrons to probe the surface, for example an electron with energy $\sim$ 20 keV is equivalent to a wavelength of $\sim$ 0.012 nm (which is significantly lower than that of visible light, 400 to 700 nm). Thus, compared to an optical microscope, significantly smaller details of a sample may be resolved as described by the Rayleigh criterion, which states that resolution is λ-limited [224].

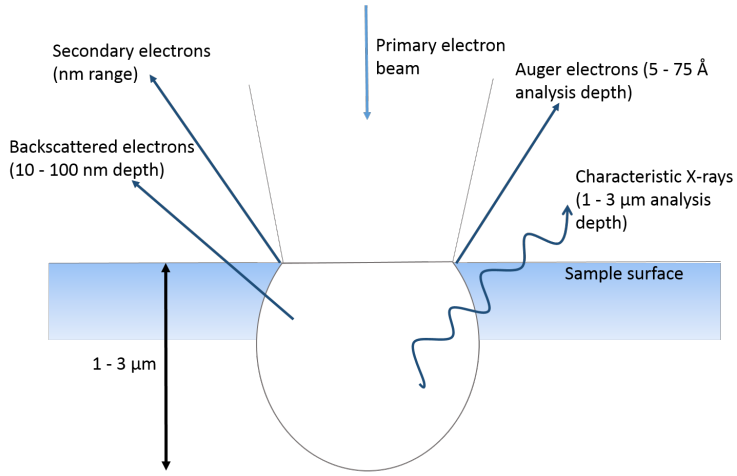


Figure 4.6: Representation of some of the electron interactions occurring upon interaction of a primary electron beam with a sample under analysis in an electron microscopy setup. Image adapted from the SURF group, University of Brussels [226].

4.4.1 Scanning Electron Microscopy

Scanning electron microscopy (SEM) is an electron-sample interaction technique in which data are collected over a selected area of the sample surface to generate a 2-dimensional image of the sample. SEM carries some advantages over techniques such as transmission electron microscopy in its ease of sample preparation and its ability to image larger samples due to the use of a scanning electron beam [225].

A scanning electron microscope setup consists of an applied voltage between a conductive sample and a filament, under a high vacuum (10^{-4} to 10^{-10} mbar). A beam of emitted electrons interacts with the sample surface producing a variety of signals, illustrated in Figure 4.6.

Secondary electrons are produced when weakly bound electrons from the sample's conduction band interact with the incident electrons, providing enough energy for their ejection. They are emitted only very near the surface of the sample (typically 5 to 50 nm) and have energies less than 50 eV [227]. As the angle of incidence increases, the incident beam electrons travel greater distances in the region of the sample close to the surface. As a result more secondary electrons are generated within the escape depth in these areas, leading to a higher apparent electron emission. Edges and ridges of the sample thus emit more secondary electrons and so appear brighter in the image, giving topographical information on the sample.

Backscattered electrons are produced when electrons from the incident beam are deflected in the sample. They are produced over a greater depth range, and are higher in energy than secondary electrons. Backscattered images reveal compositional information, as atoms with greater atomic numbers will produce a larger number of backscattered electrons, thus giving a brighter area in the image [223].

The probe volume in the sample will depend on the density and Z-number of the material and is proportional to the accelerating voltage of the electrons, as well as the spot size used (as determined by the aperture and condenser lenses).

4.4.2 (Scanning) Transmission Electron Microscopy

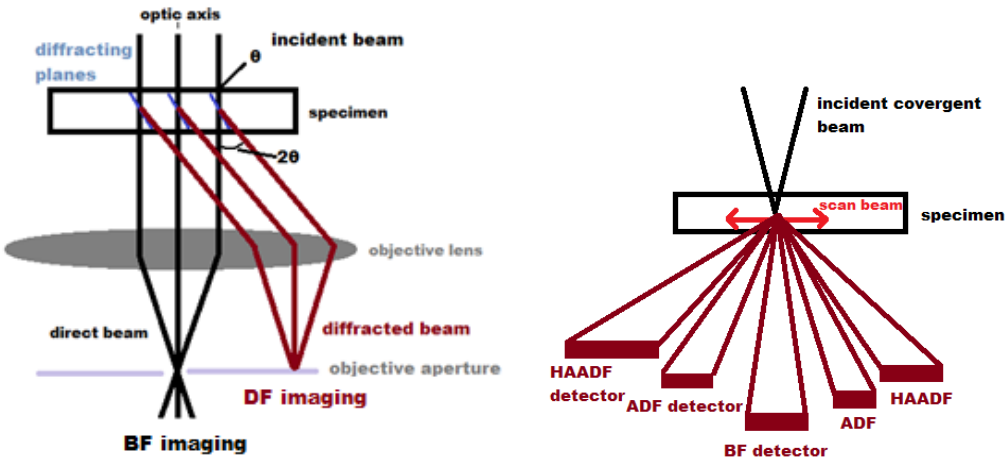
Transmission electron microscopy (TEM) uses a beam of highly accelerated electrons (200 to 300 keV) which are transmitted through a specimen to form an image, hence the specimen needs to be thin enough (less than 50 nm) so as to allow electrons to pass through it without losing a significant amount of energy. Fine details, such as single columns of atoms, can be captured, and the interpretation of image contrast created by the interaction of the electron beam as it transmits through the specimen is used to understand a number of properties relating to the material. The TEM can be operated in two modes: TEM and scanning-TEM (STEM) modes. The reader is directed to the textbooks on the subject by Goodhew, Humpries and Beanland [228] and Williams, Carter and Barry [229] for a more in-depth discussion on the technique.

The main difference between TEM and STEM is that rather than a parallel beam of electrons incident on the sample in TEM mode (Figure 4.7a), STEM uses a converged beam focussed at a spot on the specimen surface. To create an image, the beam is raster scanned (like SEM) and the signal from each point is recorded on an annular detector. Hence no objective lens is needed for imaging the sample, and theoretically the magnification achievable is unlimited. Multiple detector types are accessible in STEM, illustrated in Figure 4.7b, and the method is often able to acquire signals in parallel [229, 230].

In conventional TEM mode, an objective aperture is used to select both bright field (BF) and dark field (DF) imaging modes; in bright field imaging, the objective aperture selects the direct beam only; in dark field imaging, the objective aperture selects the diffracted beam only (see Figure 4.7a). Since BF imaging excludes the scattered electrons, regions in the sample that enhance electron scattering will appear dark. In DF imaging mode, because only elastically scattered parts of the beam are allowed to form the image, strongly scattering regions will appear bright. In STEM mode, an annular detector, such as an annular DF (ADF) or a high-angle annular DF (HAADF) detector (see Figure 4.7b), is used to select highly scattered electrons.

Images that form by coherently scattered electrons (such as BF images) are difficult to interpret, because scattered beams can interfere with direct beams (constructively) and with themselves. Hence the need for structure solving with computer modelling. In this sense, STEM images are easier to interpret than TEM images as only the heavier ions scattering strongly and incoherently are detected when using an annular detector. For example, in high-angle annular dark-field (HAADF) STEM, Z-contrast atomic resolution imaging is possible, where the intensity is directly proportional to Z^2. In BF we can also image light elements but because the contrast is purely coherent image interpretation is more challenging. Annular bright field (ABF) imaging mode in STEM, on the other hand, is a special imaging mode, where the contrast is formed both coherently and incoherently. Thus it has the advantage of being able to image light elements alongside heavy elements in a STEM configuration.

Additionally, the use of an aberration corrector enables electron probes to be focused to sub-ångström diameters, allowing images with sub-ångström resolution to be acquired. This recent development has made it possible to identify individual atomic columns with



(a) TEM (b) STEM

Figure 4.7: Schematic of a TEM column in TEM mode (a) and in STEM mode (b), showing the arrangement of detectors.

unprecedented clarity.

In this work, analyses were carried out on the powder specimens dispersed in ethanol and dropped onto lacey carbon grids on the image-corrected FEI TITAN 80/300 at Imperial College London (measurements made by Dr Na Ni) in TEM mode for initial feasibility tests, and on the double corrected Jeol ARM300F microscope (measurements by Dr Emanuela Liberti at Diamond and Oxford University) in STEM mode operated under 300 keV accelerating voltage, with the proposal numbers EM16932 and EM18050. The convergence semi-angle used in STEM was approximately 25 mrad. The ABF and ADF detectors had an inner convergence semi-angle of 10 mrad and 70 mrad, respectively and an outer collection semi-angle of 25 mrad and 200 mrad, respectively. To avoid damage to the sample from the beam and to record the structure before degradation, a different area on the particle was used for tilting and a time series of low exposure scans were recorded that were corrected and averaged for drift.

Data analysis was carried out by registering the images using a non-rigid algorithm as implemented in both the Smart Align software [231], and an in-house non-rigid algorithm developed by Dr Colin Ophus (Berkeley). Following image averaging, template matching was performed [232].

4.5 Inductively Coupled Plasma - Optical Emission Spectroscopy

Inductively coupled plasma - optical emission spectroscopy (ICP-OES) is a quantitative technique for determining the chemical composition of a material. The technique can resolve concentrations as low as parts per billion, under favourable conditions. The instrument comprises a plasma torch, consisting of a quartz tube surrounded by flowing argon gas, covered by an induction coil. As a high frequency current is applied to the coil, a spark forms which ignites the argon gas to produce a plasma. The sample, dissolved in strong acid, is injected into the plasma, and its constituent atoms undergo

electronic transitions. These transitions give off electromagnetic radiation of characteristic wavelength, which is collected and separated to obtain an intensity scale for selected wavelengths. The concentration of the elements in the sample is calculated through comparison with known calibration standards.

In this work, ICP-OES was used as a quantitative compositional technique on the bulk material in powder form, to confirm the stoichiometry of elements in the garnet and verify the actual concentration of dopants, as well as the presence of any impurities. A Thermo Scientific iCAP 6300 Duo ICP spectrometer was used to measure samples dissolved in 5 wt% nitric acid, aided by heating and stirring, with the elemental concentrations targeted at 1 to 20 ppm to ensure maximum sensitivity of the technique. Ga, Zr, Al, Ge, La and Li calibration standards from Sigma Aldrich were diluted in the same concentration of nitric acid to produce a set of calibration standards of 1 ppm, 5 ppm, 10 ppm and 20 ppm. Samples and calibration standards were measured gravimetrically, directly weighing into volumetric flasks before diluting with the 5 wt% nitric acid solution.

4.6 Nuclear Magnetic Resonance

Nuclear magnetic resonance spectroscopy relies on the phenomenon which occurs when the nuclei of certain atoms (with non-zero spin, i.e. nuclei with an odd number of either protons or neutrons) are placed within a magnetic field, with the result that they absorb and re-emit electromagnetic radiation. The energy of the radiation is at a specific resonance frequency which is dependent on the strength of the applied magnetic field experienced by the nucleus and the Larmor frequency of the given nucleus. The principle of NMR involves two steps; the first is the alignment (polarisation) of the magnetic nuclear spins in an applied fixed magnetic field, B_0; the second is a perturbation of this alignment through the introduction of a radio frequency (RF) pulse (illustrated in Figure 4.8). Because of the dependence of the perturbation frequency on the local magnetic field at the nucleus, NMR spectroscopy is used to probe the local chemical environment of a nucleus under study.

The randomly orientated nuclear spins become aligned under the influence of the external magnetic field, resulting in the creation of a net magnetic moment M along the same direction (defined as the z-direction), as illustrated in Figures 4.8a and b. The build-up of magnetisation is driven by spin-lattice relaxation processes ($T1$ relaxation) and eventually reaches a maximum (thermal equilibrium, Figure 4.8c). The nuclear spins precess under the influence of the magnetic field with a frequency ω_0 (the Larmor frequency) which is characteristic for every nuclei, and which is related to the energy difference between the nuclear spin states (Zeeman levels). Internal NMR interactions cause perturbations to these distinct energy levels and therefore lead to a distribution of frequencies. Next, the thermal equilibrium of the magnetisation is manipulated by RF pulses and induces a voltage, which decays as a result of relaxation processes, and is detected as free induction decay. A Fourier transformation of the voltage-time signal results in an NMR signal of frequency against intensity (Figure 4.8d) [233].

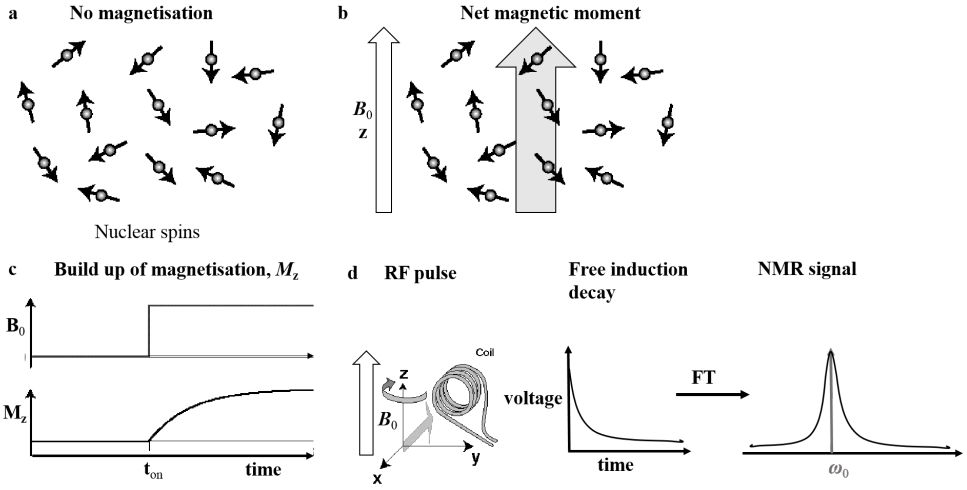


Figure 4.8: Basic schematic for NMR signal production and acquisition. (a) No magnetisation exists for randomly orientated spins; (b) magnetisation (M_z) builds up as a magnetic field B_0 is applied along the z-direction and a net magnetic moment results; (c) spin-lattice relaxation determines the rate of magnetisation build-up; (d) a radio frequency (RF) pulse results in a voltage being produced which decays and is detected as free induction decay, while a Fourier transform (FT) of the decay produces a NMR signal. Adapted from Pecher [233] and Levitt [234].

Solid state NMR is a useful characterisation method for analysing ionic motion at the atomic level, allowing the local structure and ion dynamics of specific nuclei to be detected. Unlike solution NMR, solid state NMR spectra are broad owing to the observation of all anisotropic, orientation-dependent interactions, which although an asset in terms of the wealth of information available, can also be disadvantageous as the chemical shift resolution is compromised. Magic angle spinning (MAS) however, enables the effect of anisotropy to be removed [235, 236]. This involves physical rotation of the sample which mimics the averaging processes seen in solution, and results in an averaging of the orientation-dependent anisotropic interactions which include dipolar coupling (through-space interaction of nuclear spin with local magnetic fields generated by other neighbouring spins), chemical shielding (anisotropic interaction of unsymmetrical electron distribution around a nucleus) and first order quadrupolar (nuclei with spin > 1/2) interactions. MAS NMR can thus provide detailed information about the distribution of certain ions (in particular ^{6}Li, ^{7}Li and ^{27}Al in the case of garnet LLZO electrolytes studied here) with high resolution and sensitivity.

In addition, NMR techniques can be used to probe the ion dynamics (such as Li ion) at different length/timescales. Pulsed field gradient (PFG) NMR can be used to collect self-diffusion coefficients on a macroscopic scale (in the range 10^{-14} m^2 s^{-1} to 10^{-9} m^2 s^{-1}) by varying the pulse gradient strength, duration, and pulse interval time (also known as diffusion time) [65, 66, 237]. Relaxation experiments, such as measuring the spin-lattice relaxation rate ($R1$), provide Li-ion dynamics information on different timescales. $R1$ is sensitive to jump rates in the range of the Larmor frequency ω_0. In this thesis, both PFG macroscopic diffusivity and $R1$ microscopic measurements are used to follow the lithium diffusive motion, and temperature-dependent measurements are used to calculate the

activation energy E_a [66, 96].

Relaxation is the process by which spins in a system return to their equilibrium state following a pulse, through interaction with the environment. At equilibrium, the energy level populations are equal to those described in the Boltzmann distribution, giving rise to an equilibrium magnetisation; after a radio frequency pulse is applied the net magnetisation is flipped from equilibrium and its components parallel and perpendicular to the magnetic field decay independently. Both spin-lattice ($R1$) and spin-spin ($R2$) relaxation rates can be found, by measuring the corresponding relaxation times, $T1$ and $T2$, respectively. $T1$ depends on the rate of molecular motion and the physical interactions that cause a fluctuating field at the nucleus and the rate, $R1$, is a measure of the transition probability of the spins between distinct Zeeman levels [238]. $T1$ corresponds to the energy transfer between the spin-system and the 'lattice' (where the term 'lattice' represents all degrees of freedom of the material other than the spin-system). $T2$ describes the relaxation of the nuclear spins to a state of quasi-thermal equilibrium among themselves but not with the lattice [47].

Nuclear magnetic resonance measurements were carried out in Professor Clare Grey's group at Cambridge University by Dr Lauren Marbella and Steffen Emge. ^{7}Li PFG NMR measurements were conducted to extract the lithium diffusion coefficients and activation energies for the garnet samples, as well as variable temperature $T1$ (spin-lattice) relaxation experiments to measure the activation energies for Li ion hopping. ^{1}H NMR spectra and PFG NMR measurements were also obtained for the protonated powdered LLZO (Chapter 6), and ^{7}Li NMR and magnetic resonance imaging was conducted on cycled pellets of Ga- and Al-doped LLZO for dendrite chemical analysis.

Powder samples of different LLZO compositions were sent in Ar-filled, sealed containers which were later transferred under Ar to 5 mm NMR glass tubes modified with a J. Young valve, making the total volume of the powders in the container around 200 to 400 µl. ^{7}Li NMR diffusion spectra were recorded on a Bruker Avance III 300 MHz spectrometer using a Diff50 probehead equipped with an extended variable temperature (EVT) 5 mm single-tuned ^{7}Li saddle coil insert. Spectra were recorded with a stimulated echo PFG sequence at elevated temperatures due to the increase in $T2$ observed at high temperature. (N.B. No attempt was made to calibrate the temperature for this experimental setup because a single-tuned ^{7}Li coil was used and no reliable ^{7}Li reference is routinely used for temperature calibration. The Bruker manual states that for static measurements, the temperature calibration should be within ± 7 °C of the set value.) The increase in $T2$ allowed the use of longer gradient pulses, δ, that were necessary to measure the relatively slow diffusion coefficients present in the solid electrolytes. The gradient strength, g, was varied from 0.87 to 2300 G cm^{-1}. The response of the NMR signal intensity, I, to variation in g, is described by the Stejskal–Tanner equation:

$$\frac{I}{I_0} = \exp\left\{ -g^2\gamma^2\delta^2(\Delta - \frac{\delta}{3})D \right\} \tag{4.13}$$

where I_0 is the intensity in the absence of gradients, γ is the gyromagnetic ratio ($\gamma_{^7\mathrm{Li}}$ = 103.962 × 10^6 s^{-1} T^{-1}), δ is the effective gradient pulse duration, Δ is the diffusion time,

and D is the diffusion coefficient. Typical δ values ranged from 0.8 ms to 1.5 ms and Δ values ranged from 50 to 150 ms.

4.7 Electrochemical Testing

4.7.1 Electrochemical Impedance Spectroscopy

Impedance spectroscopy is a useful tool for the characterisation of electroceramic materials as it enables the electrical properties to be measured and separated into their component parts, for example grain boundary and bulk grain contributions to the total conductivity. These features will have a resistance contribution in series to the total direct current (DC) resistance. However they may have differing electrical relaxation (time constants) under an alternating current (AC) electric field. Impedance spectroscopy involves measuring the impedance of a sample over a wide range of frequencies and characterising the different parts of the material according to their electrical relaxation time. Impedance has both resistive and a capacitive/inductive (reactive) components which can be determined by applying an AC voltage across the sample and placing a resistor in series and measuring the in- and out-of-phase components of the voltage and dividing by the magnitude of the current [239]. The relationship between the AC voltage V of amplitude V_0 and angular frequency $\omega = 2\pi f$ is described by Equation 4.14.

$$V = V_0 \exp\{i\omega t\} \tag{4.14}$$

The current I induced can be described according to Ohm's law by Equation 4.15, which shows current is in phase with the voltage. It follows from the definition of impedance ($Z = V/I$) that the impedance of a resistor is its resistance R.

$$I = \frac{V_0}{R_0} \exp\{i\omega t\} \tag{4.15}$$

When applied across a capacitor with capacitance C, the voltage causes the circuit element to continually charge and discharge (with charge Q) (Equation 4.16).

$$Q = CV_0 \exp\{i\omega t\} \tag{4.16}$$

Differentiating with respect to time t gives the current (Equation 4.17), which oscillates at the same frequency as the voltage but lags the voltage by $\pi/2$.

$$I = \frac{dQ}{dt} = i\omega CV_0 \exp\{i\omega t\} \tag{4.17}$$

It follows that the impedance of a capacitor is given by Equation 4.18:

$$Z = -\frac{i}{\omega C} \tag{4.18}$$

Hence impedance has real and imaginary components and varies with frequency. These can be plotted on a Nyquist diagram (Figure 4.9) in which the x-axis shows the real

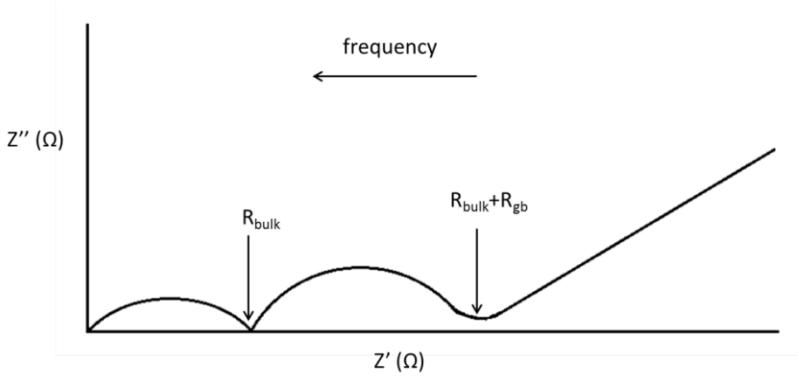


Figure 4.9: Nyquist plot showing two R-C element pseudo-semicircles representing bulk and grain boundary components of impedance in a circuit, with restances R_{bulk} and R_{gb}, respectively; plus a low frequency line representative of charge build-up at a blocking electrode.

component and the y-axis shows the imaginary component of impedance.

Different regions of the sample which have an associated process will each have a distinctive resistor-capacitor (RC) element in a parallel arrangement, each of which has a characteristic relaxation time $\tau = RC$ seen as a pseudo-semicircle on the Nyquist plot, each with a characteristic frequency f_{max} (Equation 4.19) corresponding to the semicircle maximum Z'' (with arc peak angular frequency $\omega_{\text{max}} = \tau^{-1}$).

$$f_{\text{max}} = \frac{1}{2\pi RC} \tag{4.19}$$

The semicircles are usually easily resolved as the capacitances associated with each phenomena are different (Table 4.1). Some merging of these semicircles may occur, as seen in the coalescing grain and grain boundary responses for the lithium garnets in this work. Often the impedance arcs are depressed or distorted and can be modelled better by replacing the capacitor C with a constant-phase element (CPE) [240], which has an impedance given by Equation 4.20:

$$Z_{\text{CPE}} = \frac{1}{Q(i\omega)^n} \tag{4.20}$$

where n describes the non-ideality of the device which is unity for an ideal capacitor with capacitance Q [241] . The effective capacitance of the CPE is given by Equation 4.21.

$$C = (R^{1-n}Q)^{1/n} \tag{4.21}$$

The components of the equivalent circuit can be assigned to the appropriate process by consideration of their capacitance value. Table 4.1 from Irvine *et al.* [239] details typical capacitance values for a range of processes.

The low frequency spike shown in Figure 4.9 represents charge build-up at blocking metal electrodes (for example, Au blocking electrodes in the case of the lithium-conducting ceramics studied here). Ideally, the response from the electrode is solely in the imaginary regime caused by a double layer capacitance of Li ions and electrons at the

Table 4.1: Capacitance (C) values and their possible interpretation [239].

Capacitance, F	**Phenomenon Responsible**
10^{12}	Bulk
10^{11}	Minor, second phase
10^{11}-10^{8}	Grain boundary
10^{10}-10^{9}	Bulk ferroelectric
10^{9}-10^{7}	Surface layer
10^{7}-10^{5}	Sample-electrode interface
10^{4}	Electrochemical reactions

interface with the electrolyte. When the electroactive species is not fully blocked at the interface, Warburg-type behaviour is seen when there is ion diffusion kinetics towards the electrodes. In an ideal case this will give an inclined spike of angle 45° when there is infinite diffusion of the mobile species into the electrode material, with $|Z'| = |Z''|$.

AC impedance was performed on the samples using both Li and Au (Li-blocking) metallic symmetric electrodes. To prepare the Au electrode cells, Au was sputter-deposited onto the pellets using a magnetron sputter coater (Q150T, Quorum Technologies Ltd, UK) with a sputtering current of 20 mA for 2 minutes, resulting in an Au layer of roughly 50 nm thickness. During this process, a circular mask of diameter 0.6 mm was applied to both sides of the pellets to control the geometry of the Au coating (with a fixed area of 0.28 cm^2). The subsequent cells were measured either in a coin cell setup (described below) for inert-atmosphere measurements, or in a custom-made sample holder placed in a tube furnace under static air, using Pt contacts attached to the wires. Measurements were taken in static air using this setup at room temperature and as a function of temperature, using a thermocouple placed next to the sample for temperature measurement.

For the Li symmetric cell measurements, polished (and in some cases, thermally etched) pellets were assembled into coin cells (of dimension type 2032) with lithium metal foil discs (6.3 mm diameter, 1.35 mm thick) in the argon-filled glove box, as illustrated in Figure 4.10, and crimped to close using a manual coin cell crimper (Hohsen Corp.). For 'cold-pressed' Li electrodes, the Li foil was first cleaned with a steel blade to remove surface impurities, then used to sandwich the LLZO pellet by manually pressing together. Stainless steel spacers and springs were used to ensure the total thickness of the stack was <3.2 mm to ensure a good electrode-electrolyte contact and to maintain constant compression between the active components. For 'hot-pressed' Li electrodes, which were used in the cycling experiments (Chapter 8), the Li foil was adhered to each side of the pellet by heating on a hotplate on the steel cap for 30 minutes at 150 °C, weighing down with a steel weight. This was repeated on each side of the pellet before coin cell assembly. For variable temperature measurements using the Li symmetric electrode coin cells, a

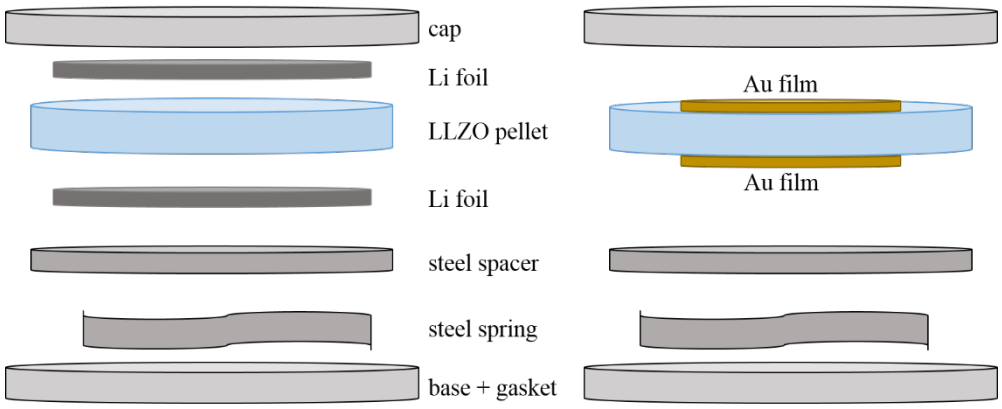


Figure 4.10: Schematic of coin cell setup with Li (left) and Au (right) symmetric electrodes.

Linkam Scientific THMS600 temperature-controlled stage, which uses liquid nitrogen to cool the cell down to 100 °C, was used. The cell was kept at the temperature of interest for two hours prior to measurement.

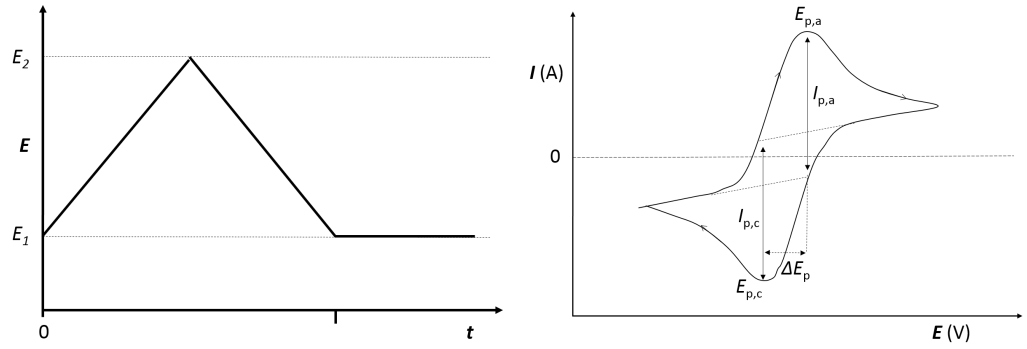
Impedance spectroscopy was performed on a Solatron 1260 Impedance Analyser instrument from 13 MHz to 0.1 Hz with a signal amplitude of 100 mV, measuring 20 points per decade with a 10 s integration time, unless otherwise specified. The impedance was measured with a 2-contact rig and plotted in Nyquist-type plots with the response fitted to equivalent circuits using Z-view software [242].

4.7.2 Cyclic Voltammetry

Cyclic voltammetry (CV) is a potentiodynamic technique, in that it measures the current produced in response to the potential applied to a working electrode. In a CV experiment the working electrode potential is increased linearly with time. When a set potential is reached, the potential is reversed (Figure 4.11a). This can happen multiple times during a single experiment.

The current at the working electrode is plotted against the applied voltage to give a cyclic voltammogram, as the potential of the working electrode is swept from E_1 to E_2 (Figure 4.11b). Where there is no electrochemical response, the current produced as the potential changes is non-Faradaic, i.e. capacitive. At potentials near or at the overpotential (η) required for reaction, the current is Faradaic (caused by charge transfer at the electrode). This current illustrates the changing rate constant for electron transfer and the mass transport properties of the electroactive species, producing characteristic redox curves.

In this thesis, cyclic voltammetry is used on Ge0.10-LLZO pellet samples to confirm their redox stability across a large applied voltage range using Li metal as reference, counter and working electrodes. An Ivium Stat potentiometer was used for the measurements, over a voltage range of –0.5 to 4 V vs. Li^+/Li, with a scan rate of 10 mV s^{-1}.



(a) (b)

Figure 4.11: (a) Cyclic voltammetry (CV) sweep diagram of potential, E, with time, t. Potential is swept between E_1 and E_2; (b) cyclic voltammogram of a fully reversible redox couple showing peak potential E_p, peak current I_p, and peak separation potential ΔE_p. The arrows on the trace show the direction in which the potential is swept. The subscripts a and c denote anodic (oxidative) and cathodic (reductive) processes, respectively.

4.7.3 Charge/Discharge Cycling

The electrochemical properties of cells are commonly studied using the charge/discharge galvanostatic method, i.e. electrochemical cycling at a constant current applied per gram of active material or, as in the case of ceramic electrolytes with Li metal electrodes, with respect to the total surface area of the electrode. In general, the resulting galvanostatic profile displays the evolution of the cell voltage as a function of the chemical composition (and structural phase transformations) of the electrode material [233].

In this work, charge/discharge cycling is performed on symmetric Li/LLZO/Li cells to measure the voltage as a function of applied current and to determine the onset current density for cell failure, or dendrite formation (Chapter 8). Cell cycling on symmetric Li electrode coin cells was carried out using a 580 Battery Test System (Alvatek) and BCycle software at room temperature. Cells were prepared using the 'hot-pressed' Li procedure described above in Section 4.7.1. Cells were cycled with increasing current densities from 0.01 mA cm^{-2} to 2 mA cm^{-2} with steps of 0.01 mA cm^{-2}, held for 30 minutes for each charge and discharge step, with a 5 minutes rest period between charge/discharge cycles, until the cell showed short-circuit behaviour. Cycled pellets were prepared for post-mortem analysis on the surface and cross-sections of the cycled pellets by disassembling the coin cells in the glove box (using a Hohsen disassembler) and peeling away the adhered Li metal (taking care not to damage the surface morphology of the pellet). For cross-section fracture surface analysis, the cycled pellets were cleaved in half by manually snapping the pellet before mounting on a specially-designed SIMS holder for viewing the cross-section.

4.8 Secondary Ion Mass Spectrometry

Secondary ion mass spectrometry is used in this work as a highly sensitive, mass-specific chemical technique to analyse the surfaces and near-surface regions of the garnet pellets

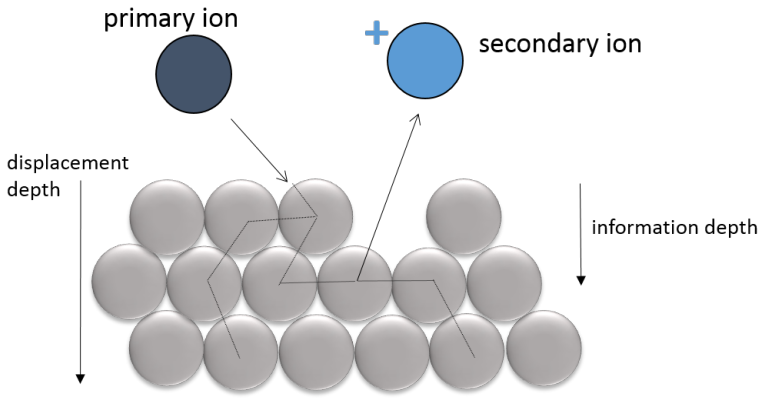


Figure 4.12: Representation of a SIMS collision event, leading to the formation of a secondary ion ejected by the solid and capable of capture by the SIMS detector, adapted from Fearn [244].

following a range of chemical and atmospheric treatments. It is exploited, in particular, in this work owing to its ability to distinguish between different stable isotopes of the same element and so is a technique for concentration depth-profiling of isotopically-enriched or labelled atomic species in a material. This work was pioneered by Kilner *et al*. [45, 46, 243] in the field of oxygen ion conducting materials for high temperature solid oxide fuel cells, oxygen membranes and oxygen sensors, and used to experimentally determine macroscopic oxygen diffusivities using a ^{18}O tracer. In addition to its ability to detect and differentiate between isotopes, its ability to detect light elements (such as H and Li) and its high lateral and depth resolution, including selected area analysis with the help of secondary ion imaging (in the focussed ion beam-SIMS, Section 4.8.2), makes it a powerful analysis tool. For these reasons SIMS was used extensively in this thesis for moisture reactivity and corrosion characterisation experiments (Chapter 6), lithium isotopic labelling (Chapter 7) and dendritic analysis in cycled cells (Chapter 8).

SIMS essentially involves the bombardment of a surface with a beam of primary ions, which results in sputtered atoms and molecules forming, some of which will be ionised as they leave the target surface. These so-called secondary ions are extracted in the SIMS instrument and mass analysed prior to reaching the ion counting detector.

During a SIMS measurement, ions which have been accelerated to high energies (typically 10 to 40 keV) are fired at a surface, and some of their kinetic energy is transferred to the lattice by billiard-ball type collisions, producing a collision cascade within the solid (up to a so-called displacement depth). Some of the particles will intermix within the sample, but some atoms or groups of atoms will receive enough energy for them to overcome the surface binding forces and become ejected from the sample, as illustrated schematically in highly simplified form in Figure 4.12. These particles will have a much lower energy than the incoming primary ions owing to dissipation of energy during the collision process, but will be greater in number than the incident primary ions. The information depth associated with the depth of the origin of these particles is quoted to be several atomic layers (i.e. $\sim$ 0.25 to 1.25 nm) [245]; however, due to the multiple collision processes that occur during sputtering, this may be greater in some cases. The distance

between the incident primary ion and the location of ejection of the secondary ion may be up to 10 nm in an inorganic sample [244].

SIMS operation is divided into two operating modes: dynamic and static. In static SIMS a low primary ion beam dose is used to minimise the interaction of the primary ion beam with the top layer of atoms in the sample, such that <1 % of the surface is removed [246], and the analysis is essentially non-destructive. This has been shown to be true when the dose is $< 10^{15}$ particles cm^{-2} in inorganic materials [244], or <1 nA cm^{-2} [247]. In dynamic SIMS, the dose of the primary ion beam (>1 µA cm^{-2}) [247] is much higher. By monitoring secondary ion signals as a function of time we are able to yield a distribution of species with depth. It is possible to combine the two techniques through the use of a sputtering beam during a nominally static regime to allow collection of depth-dependent data.

Ionisation occurs at or very close to the emission of the particles from the surface, hence the ionisation process is strongly influenced by the chemical state of the surface, and this is known as the SIMS matrix effect. The emission of secondary ions can be described by the basic SIMS equation, Equation 4.22. Here I_n is the secondary ion intensity of species n (i.e. the measured counts), I_p is the primary ion beam current, Y is sputter yield (which depends on beam conditions and target material), α_n is the ionisation probability (which depends on the beam conditions - the energy of the primary ion beam and angle of incidence, and also on the local chemistry and species n identity), and C_n is the concentration. T is an instrumental transmission factor (it describes the efficiency of ion extraction and transport to the mass spectrometer).

$$I_n = I_\mathrm{p} Y \alpha_n T C_n \tag{4.22}$$

Equation 4.22 shows that the measured secondary ion counts, I_n, is proportional to the concentration C_n, however quantification problems arise due to α_n, which is the chemistry-dependent 'matrix-effect' described above; hence normally quantification of SIMS measurements require a standard reference sample of the same matrix material with known concentrations of the element of interest, used to calibrate measurements.

Isotope measurements of a single element mean the process can be simplified as α_n is the same for both isotopes, assuming a negligible isotopic effect arising from difference in mass (being less pronounced for heavier versus lighter elements), and all other terms in the SIMS equation are identical. Hence we can assume the same constant of proportionality for both isotopes when relating secondary ion intensity (I) to concentration. Additionally, the proportionality constants will cancel on taking the isotopic fraction, $C(x)$, which in the case of lithium-6 (^{6}Li), is given by Equation 4.23:

$$C(^6\mathrm{Li}) = \frac{I(^6\mathrm{Li})}{I(^6\mathrm{Li}) + I(^7\mathrm{Li})} \tag{4.23}$$

The ionised particles are mass resolved by a mass analyser, the three most common types being the quadrupole, the magnetic sector and the time-of-flight detector. Each of these have a different associated sensitivity and mass resolution, and are selected

depending on whether dynamic or static SIMS measurements are being made; for example, in dynamic SIMS a high sensitivity for a particular element may be required. In this work, a quadrupole detector was used in the dynamic-mode 'focussed ion beam' (FIB) SIMS instrument, and a time of flight (TOF) detector was used in the TOF-SIMS instrument, under static SIMS mode. More details on these two instruments are given in the following sections.

4.8.1 Time of Flight SIMS

In this work a dual-beam TOF-SIMS V instrument (ION-TOF GmbH, Münster, Germany) was used for selected analyses, with protected-atmosphere sample transfer using a vacuum suitcase transfer module. A liquid metal ion gun (LMIG) of Bi^+ ions or Bi^{3+} cluster ions is used as the primary ion beam source, which works by forming Bi ions through a field emission process using a very high extraction field to give a very high brightness ion beam, which has a small relative energy spread and hence a good focus quality (and correspondingly high lateral resolution). This is coupled with a high current, low energy sputter gun in dual beam mode to enable depth-profiling by alternating sputter and analysis steps, using an electron impact source i.e. O_2^+ ion, Ar_n^+ clusters, or a surface ionisation source i.e. Cs^+. Electron impact sources are formed from ionisation of the gas by electron impact. The O_2^+ ion beam enhances the positive secondary ion yield by a surface chemical effect. Surface ionisation sources are formed from the thermal ionisation of atoms. Cs^+ ions readily lose their 6s valence electron, so are good for the detection of electronegative species. The sputter is used over a much greater area than the analysis in order to avoid crater edge effects. In most cases here, the sputtered crater width is set to 500 µm by 500 µm, with the analysis rastering over an area of 200 µm by 200 µm.

The first step in the analysis by TOF-SIMS is to send a short-duration primary ion pulse (to enable high mass resolution) to the sample. In bunched or high current bunched mode (HCBM)[1], a $\sim$ 20 ns pulse is sent through a condenser in order to bunch the ions together and form a packet of about 0.6 ns. In burst or 'pulsing-enabled burst alignment mode' (BAM)[1] a longer pulse (i.e. 100 ns) is modulated with a MHz signal in order to cut several $\sim$ 1 ns pulses (bursts) out of a larger ion packet [248]. Figure 4.13 illustrates these two modes. In this instrument setup, saturation of the TOF detector can occur, but using a pulsed burst mode, rather than bunched mode, prevents saturation of the detector whilst enabling high count rates to be maintained for minor isotopes which is important to minimise error due to counting statistics in the measurement of isotopic ratios. Burst mode also delivers higher lateral resolution, which is important when carrying out linescan analyses. The disadvantage with using bunched mode is that the mass resolving power R, which is defined as the ability to separate two adjacent peaks' full width half maximum, and equal to $m/\Delta m$, is around 3500, which may be too low for some analyses. For high mass resolution but lower lateral resolution, HCBM mode is better suited.

The pulsed ion beam defines the start time for detection of the secondary ions, which

[1]ION-TOF nomenclature for the two ion beam modes in TOF-SIMS

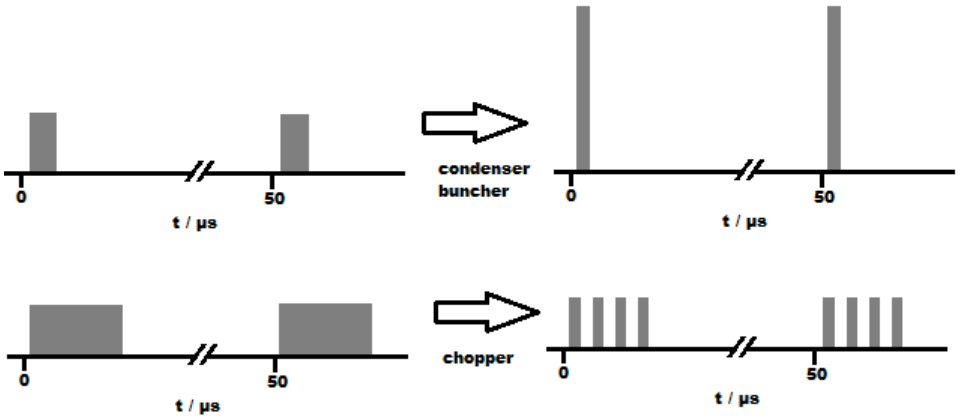


Figure 4.13: Schematic of the two operational modes of the Ga^+ LMIG in the TOF-SIMS instrument; bunched mode (top) and burst mode (bottom).

are extracted normal to the surface by a 2 keV electrical potential and are accelerated to the same kinetic energy E_K. As $E_K = \frac{1}{2}mv^2$, the velocity v of the ions is now inversely dependent on the square root of their mass m. The ions are separated according to their velocity in a flight tube of known length without the use of an electric or magnetic field. The arrival times of the ions at the detector will thus depend on their mass, so a mass spectrum can be formed. The detector is a single-ion counting system, so the possibility of several ions arriving at the same time and not being recorded is accounted for by Poisson statistics, which is especially important in high intensity isotope signals where accurate isotopic ratios are required.

Under bombardment by primary ions, electronically insulating samples can become charged, leading to a change of ion extraction energies - local field effects causing disturbance of secondary ion trajectories - and migration of mobile ions in the sample. To prevent this, a charge compensation system is used in which a low-energy electron source (20 V electrons) is combined with a pulsed secondary ion extraction field [249].

In this thesis, TOF-SIMS was used for large-area analysis of samples, in particular for ion mapping of multiple secondary ion species.

4.8.2 Focussed Ion Beam SIMS

In this work, a quadrupole mass analyser-based FIB-SIMS system was used, an FEI FIB200-SIMS instrument (ThermoFisher Scientific) fitted with a second, HIDEN EQS 1000 SIMS detector, enabling dual-polarity detection simultaneous acquisition [250]. This system is operated under dynamic conditions, using a liquid metal ion gun (LMIG) consisting of a Ga^+ primary ion source and a two-lens column operating at 30 keV. The source consists of a tungsten needle coated in gallium, which under the high extraction voltage (12 kV) results in ionisation of Ga and a finely focussed primary beam (~ 10 nm diameter under optimal conditions with 20 pA current). The chamber pressure during operation was typically $5x10^{-7}$mbar.

In dynamic SIMS, the objective is to establish steady state conditions of erosion rate

and surface chemistry, which with a Ga^+ primary ion beam is said to be reached at a dose of $\sim 10^{15} - 10^{16}$ ions cm^{-2}. Under the steady state condition, as the target is bombarded by primary ions, some of these ions are retained in the target after implantation, whilst the exposed surface is being simultaneously sputtered away. Steady state is obtained when primary ion implantation and removal processes are equally matched; at this point the concentration of primary ions in the base of the sputter crater is at a maximum. Prior to this dose, but above the static regime dose, a pre steady state regime is said to exist in which the surface chemistry, erosion rate and ion yields of the crater base may change drastically as irradiation proceeds.

The quadrupole mass analyser separates incoming ions on the basis of their mass-to-charge (m/z) ratio using an oscillating electromagnetic field across the ion trajectory [251]. It contains four parallel rods under constant DC bias with opposite pairs of rods carrying an additional oscillating radio frequency AC component. The ratio of these two voltage amplitudes selects the mass of the ion that can travel between the entrance and exit apertures at either ends of the 4 rods of the analyser. The fluctuation of the field causes most ions to travel on an unstable oscillating path, but a single m/z ratio ion at a time will follow a stable trajectory, reaching the detector. This depends on the selection of a very narrow range of secondary ion energies (< 1 eV) input into the mass analyser. In this work, the minimum increment is 0.05 u for the quadrupole SIMS detectors where the full width, half-maximum value for a typical $^{16}O^-$ peak is 0.37 u in the FEI detector.

As sputtering removes atoms/molecules present at the outer surface of a solid, measurement of the secondary ion signal as a function of sputtering time provides a depth distribution of the signal measured. Profiles over depths ranging from several nm to ~ 10 µm can be collected [252].

In this work, the primary ion beam is from a gallium ion source and is incident at 30° to the normal of the ceramic surface (to ensure efficient secondary ion collection, given by T in Equation 4.22) operated with a range of currents. This means that primary Ga^+ ions are implanted into the sample with a range of ~ 15 nm and a distribution half-width of ~ 7 nm estimated by the model SRIM (stopping and range of ions in materials) [253] and detected as Ga^+ secondary ions. The current of the Ga^+ primary ion beam is varied in this work depending on the data collection technique used - a larger current for depth-profiling (100 pA to 1 nA) of deep craters is used, whereas near-surface features are followed with a lower current (< 500 pA) to enable higher depth resolution (< 10 nm). The crater depths were calibrated using the secondary electron image recorded with the sample tilted at 45°. Imaging is carried out with a typically 30 pA primary ion beam current, to minimise surface damage, in both secondary electron and ion imaging modes. The ability to image in these modes to a high resolution (~ 5 nm) enables selected area analysis of the sample; for example, in the LLZO pellet samples we are able to selectively depth-profile within grains, enabling the separation of grain and grain boundary chemical information. FIB-SIMS depth-profiling was used in tracer diffusion experiments (Chapters 6 and 7) to extract diffusion lengths up to 5 µm depth. The eucentric height (where the sample tilt

axis is through the sample surface at the centre of the imaged area) is used to ensure the gallium primary ion beam condition (i.e. beam current density) is maintained and produces reproducible results between analyses.

Chapter 5

Synthesis and Doping of $Li_7La_3Zr_2O_{12}$

As discussed in Chapter 3, a thorough characterisation of $Li_7La_3Zr_2O_{12}$ (LLZO) ceramic materials is somewhat lacking in the literature. Despite some comprehensive structural studies on phase formation and crystallography of the powdered material, the formation of technologically-useful ceramic pellets or membranes is hindered by a limited understanding regarding the processing and associated microstructural effects, which have a knock-on effect on electrochemical characterisation and implications for device performance. These effects can originate from synthesis and processing conditions, but also include the role of added dopants used to stabilise the cubic phase.

The issues addressed in this chapter are twofold: Firstly, the synthesis and processing parameters used in this thesis are introduced; these have been designed to be optimised for the production of garnet ceramics, and are intended to build on existing research. Here the focus is on Ga-doped and Al-doped LLZO compositions, which are introduced in this chapter and which are characterised in more detail in later chapters. These are selected for study as technologically relevant and interesting compositions as solid electrolytes: Ga-doped LLZO has been reported to possess the highest room temperature Li ion conductivity for the garnet materials to date ($> 1\,mS\,cm^{-1}$) [113, 137–139], and Al is a common impurity introduced through alumina crucibles used as a vessel for sintering the pellets. Secondly, a new dopant is investigated (Ge^{4+}), in an attempt to evaluate its feasibility to be used in LLZO, and to answer questions on the role of dopants on the structural and transport properties of both the LLZO grains and the pellet as a whole (including grain boundaries, interfaces, impurities and sinterability).

5.1 Garnet Synthesis

The two doped cubic garnet compositions on which much of the experimental work in this thesis is based are Ga0.15-LLZO and Al0.15-LLZO (with the nominal stoichiometries $Li_{6.55}Ga_{0.15}La_3Zr_2O_{12}$ and $Li_{6.55}Al_{0.15}La_3Zr_2O_{12}$, respectively). The doping content of 0.15 atoms per formula unit (a.p.f.u.) was chosen based on the argument that an optimal lithium content of 6.4 to 6.6 Li a.p.f.u. is necessary for the best ionic conductivity in these

materials [50, 105, 117, 152, 153], and based on the work of Bernuy-Lopez *et al.* [137] in which the highest conductivities for LLZO at the time were reported for a controlled synthesis method using a measured Ga content of 0.15 a.p.f.u. The nominal Al content for Al-LLZO samples was chosen to match this concentration, as both dopant cations are expected to substitute in the same position of the Li sublattice (see Chapter 3 for a discussion of dopants in LLZO).

Some optimisation of the synthesis and processing parameters were made, in order to obtain dense, phase-pure and conductive ceramic pellets. A discussion is included below.

5.1.1 Thermal Treatment: Atmosphere and Temperature

Work described by Bernuy-Lopez *et al.* [137], involving synthesis of Ga0.15-LLZO by sintering in flowing dry oxygen, highlighted the importance of controlling the atmosphere to obtain highly dense pellets and to prevent proton-lithium exchange processes occurring as a result of atmospheric moisture reactivity. We thus took this method and developed it further, making use of a new custom-made glove box setup which was coupled to a high temperature furnace, in which all processing steps were carried out (see Chapter 4 Sections 4.1.1 and 4.1.2 for specific details on the synthesis and thermal treatment).

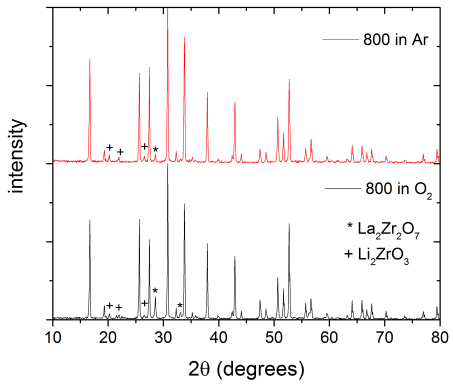
Several combinations of atmosphere treatments for the calcination and sintering steps were tested, using combinations of dry flowing oxygen, air, vacuum and argon atmospheres (the latter two being carried out in the glove box furnace, which does not have the capability for air or oxygen atmosphere operation).

Figure 5.1 summarises the resultant powder X-ray diffraction (XRD) patterns on Ga0.15-LLZO starting from the same batch of combusted powder (made from the sol-gel technique using 10 % excess Li in the starting materials and combusted at 600 °C) for different calcination and sintering atmospheres and temperatures. Heating for 12 hours at 800 °C in O_2 followed by 6 hours at 1150 °C under argon gave the purest cubic phase powder; however, some commonly-found Li_2ZrO_3 impurity remained in these experiments (with diffraction peaks labelled with a + symbol in Figure 5.1).

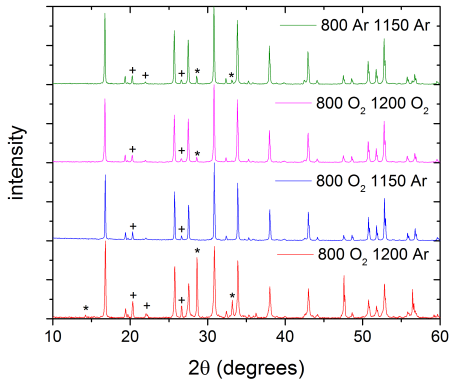
The two impurity phases, Li_2ZrO_3 and $La_2Zr_2O_7$, seen in Figure 5.1 were frequently encountered during the course of this PhD synthesis work, highlighting the meta-stable and complex nature of LLZO, which is very sensitive to changes in stoichiometry. The control of the starting materials for obtaining the desired garnet phase and avoiding the formation of secondary phases was found to be critical.

Particle Size

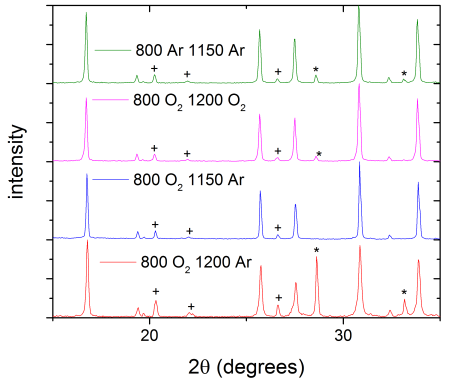
Particle size analysis was carried out using dynamic light scattering on powder samples of Ga0.15-LLZO in suspension and also with scanning electron microscopy (SEM) imaging following different atmosphere, time and temperature treatments. The corresponding particle sizes are given in Table 5.1, and images are given in Figure 5.2. In general, a bi- or tri-modal particle size distribution is seen. Cheng *et al.* [147] used bimodal particle size distribution to produce dense pellets of Al-LLZO with grain sizes 20 to 40 µm across. It is thus not unsurprising that our final choice of thermal treatment of the LLZO powders



(a)

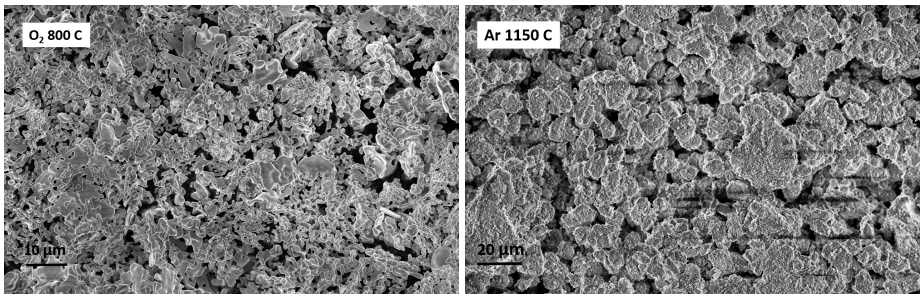


(b)



(c)

Figure 5.1: Powder X-ray diffraction patterns of Ga0.15-LLZO following different atmosphere and temperature treatments. (a) Following an initial calcination heat treatment step (800 °C for 12 hours) and (b and c) following calcination for 6 hours at 800 °C and sintering at higher temperature, where (c) is an expanded view of (b) in the range 15 deg $< 2\theta <$ 35 deg. * indicates $La_2Zr_2O_7$ impurity peaks; + indicates Li_2ZrO_3.



(a) (b)

Figure 5.2: Ga0.15-LLZO powder SEM images after thermal treatment in (a) O_2 at 800 °C for 12 hours and (b) argon at 1150 °C for 6 hours.

(12 hours at 800 °C in O_2 before sintering the pellets in argon at 1150 °C) gave a bimodal distribution of grains which were densely packed (see Chapters 6 and 8 for micrographs of the sintered pellets).

Table 5.1: Average particle sizes of Ga0.15-LLZO powders undergoing different heat and atmosphere treatments as measured by dynamic light scattering.

Thermal treatment	800 °C O_2, 6 hours	800 °C O_2, 12 hours	1150 °C argon, 6 hours
Particle sizes (µm)	0.7, 3, 20	0.7, 20	0.7, 20

High Resolution Scanning Transmission Electron Microscopy

Scanning transmission electron microscopy (STEM) was carried out on powder Ga0.15-LLZO samples as a characterisation tool in which atomic columns can be imaged directly, confirming the crystal structure and as a means to check for the presence of defects or secondary phases. It was initially hoped that using high resolution aberration-corrected STEM that Li atoms, dopants and also protons (in the proton-exchanged samples in Chapter 6) might be imaged; however, as discussed here, this was found not to be possible under the present conditions.

For the STEM measurements, finely milled powder was suspended in dry ethanol to make a just-translucent suspension and sonicated to disperse, then 10 drops of the suspensions were dropped onto lacey carbon film copper mesh grids, before mounting in a double tilt Be holder. Bright field (BF) and annular dark field (ADF) images were taken simultaneously along the [001] zone axis to resolve the columns of oxygen atoms. Due to problems of damage to the sample from the beam, a low beam current of 0.6 pA and $5x10^6$ magnification was used, following a high current (several hundreds of nA) beam shower to remove hydrocarbon contamination under the beam caused by residual carbon from ethanol. Additionally, fast acquisition of frames (2 µs/frame), to make a three-dimensional stack of 12 frames, was undertaken, and the average of these frames was used (see Chapter 4, Section 4.4.2 for further details).

The Ga0.15-LLZO powder STEM images show the expected atomic arrangement for

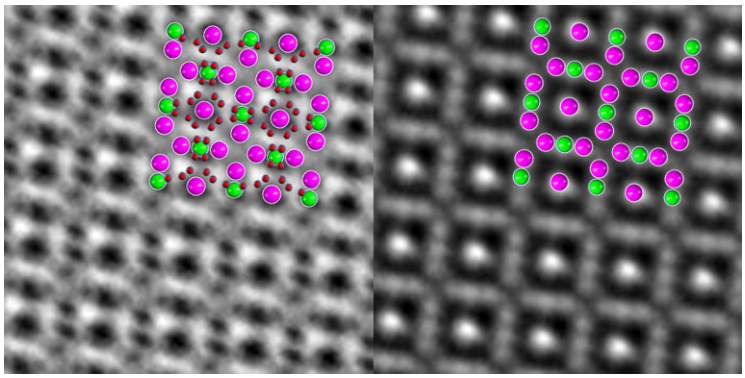


Figure 5.3: STEM bright field (BF) (left) and annular dark field (ADF) (right) images taken at 300 kV with a current of 0.6 pA of Ga0.15-LLZO powder, along the [001] zone axis. Purple atoms are La, green are Zr and red are O. Images were averaged and template matched [232] (see Chapter 4, Section 4.4.2 for further details).

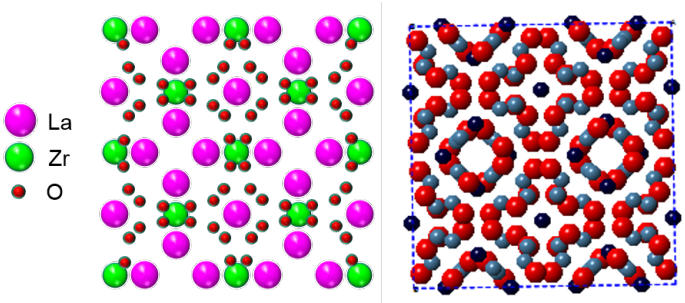


Figure 5.4: Atomic positions of (a) La, Zr and pure oxygen columns only and (b) the Li atoms (24*d* in navy blue, 96*h* in light blue) and O atoms (red), viewed along the [001] zone axis in cubic LLZO. Images were created in CrystalMaker software [254].

the cubic form of the garnet, with the columns of oxygen atoms in the BF image visible as bright spheres, and the regular arrangement of heavy Zr and La atoms in the ADF image (Figure 5.3). Figure 5.4 shows the expected arrangement of atoms along the [001] zone axis for cubic LLZO.

Lithium atoms are not visible in this setup owing to sensitivity of the sample under the beam which leads to radiolysis (bond breaking) of the LLZO powder when it is exposed for a period of time. However, the oxygen atoms (pure columns which do not experience shadowing from the heavier elements, shown in red in Figure 5.4) are visible as bright areas in the BF image. In general, the powders appeared defect-free, with long-range ordering of atoms.

The sample was also measured in STEM mode under a lower, 200 kV, accelerating voltage, with a current of 4 pA to test the effect of voltage on the type and extent of beam damage to the specimen. It was found that an equal extent of beam damage is caused with this lower voltage setting, with the sample amorphising under the beam when exposed for more than a minute, confirming radiolysis as the primary mechanism for beam damage (instead of knock-on effects caused by electrons displacing atoms which are dominant at much lower voltages).

It was also noted that leaving the specimens on the TEM grids in air for long periods



(a) (b)

Figure 5.5: Dense, translucent (a) Al0.15-LLZO and (b) Ga0.15-LLZO pellets.

of time (several hours), caused an amorphous region to form around the particles, which was visible under the TEM imaging mode, likely caused by formation of LiOH and Li_2CO_3 (see Chapter 6 for a full discussion of proton exchange and degradation processes in these materials).

Despite much work involved in optimising the technique for high resolution imaging of these materials, and the challenges associated with beam damage and sample sensitivity, a workable method for imaging the garnet has been developed, and will be carried forward for future work now that the limitations of the technique in studying LLZO are better understood.

Sintered Pellets

In addition to the favourable phase purity using 800 °C O_2 followed by 1150 °C Ar heat treatments, the densities of the sintered pellets under an argon atmosphere were found to be far superior to those sintered in air or flowing dry oxygen, with up to 35 % reduction in the relative density measured geometrically for an air sintered pellet compared to an argon sintered pellet, and up to 20 % reduced densities for oxygen-sintered pellets.

The current synthesis and processing parameters were thus selected in order to obtain phase pure, high density pellets, under highly moisture-controlled conditions – calcining in oxygen to obtain the correct stoichiometry, followed by the final sintering step under argon atmosphere. Transparent garnet pellets were thus obtained (as illustrated in Figure 5.5), using the selected synthesis and processing method. It was noted that occasionally, some pellets appeared blue in colour (Figure 5.5b), a phenomenon only observed when sintering in an argon (and also vacuum) atmosphere.

X-ray photoelectron spectroscopy (XPS) measurements of the samples thermally treated in flowing oxygen furnace (both calcine and sintering steps in O_2) showed that these samples underwent severe charging during measurement, causing the line shape to be distorted and preventing the peaks from being fitted, whereas pellets sintered under vacuum or argon did not show the same charging effects (see Appendix A.1 Figure A.1). It is possible that colour centres may be created in some of the pellet samples sintered under vacuum and argon atmospheres, which are more reducing in nature, producing some electronic conducting behaviour in the pellets which helps dissipate charge. To facilitate the creation of colour centres, oxygen vacancies ($V_O^{\bullet\bullet}$) might be formed which trap the electrons (e′), see Equation 5.1 [28, 160, 255].

$$V_O^{\bullet\bullet} + 2e' \rightleftharpoons V_O^{\times} \tag{5.1}$$

This could be consistent with the proposal that oxygen atoms leave the surface of LLZO as O_2 in combination with Li^+ loss under reducing conditions, resulting in the formation of oxygen and lithium vacancies [256]. Coloured Ta- and Nb-doped garnets have been reported previously [160], the colours seen to intensify as a function of thermal treatment time and put down to the formation of Li^+ and/or O^{2-} vacancies. The existence of oxygen vacancies in LLZO has been reported only once before, by Kubicek *et al.* [28], where a change in oxygen vacancy concentration was implied through oxygen isotopic exchange experiments. Further investigations into the presence of colour centres and oxygen vacancies is beyond the scope if this work but is an important aspect in the understanding of phase stability and ionic mobility in these materials.

5.1.2 Crucible Effects

In order to understand the effect of the crucible type during high temperature sintering, experiments were carried out in which ZrO_2 crucibles were used in all stages of the thermal treatment for a number of different undoped, Ga-doped and Ge-doped LLZO pellets. The resultant pellets were found to be brittle and failed to hold their form during even light abrasion with SiC paper. This supports the role of alumina crucibles in aiding a liquid sintering process through the formation of a Li_2O-Al_2O_3 eutectic. The relative density, measured by Archimedes' method in ethanol, using a ZrO_2 crucible in cubic Ga- and Ge-LLZO pellets was found to reduce from above 95 % as found with an Al_2O_3 crucible, to below 50 %. The effect of Al from the Al_2O_3 crucible is clearly seen in the nominally undoped pellet XRD patterns in Figure 5.6. It shows that in the sample made in an alumina crucible, the resultant XRD pattern is largely cubic ($Ia\bar{3}d$ space group), likely due to doping of the LLZO with Al^{3+} from the crucible. However, in the sample made in a ZrO_2 crucible the phase is tetragonal (space group $I4_1/acd$), with associated peak splitting illustrated by the three split peaks of the (024) diffraction plane, but the pattern is dominated by a large pyrochlore ($La_2Zr_2O_7$) set of peaks (indicated by *). This is expected to be due to Li loss from the top surface of the pellet during sintering, resulting in the formation of pyrochlore secondary phases at the surface. This was described in previous reports with Ta-LLZO [123], in which $La_2Zr_2O_7$ was found on the top surface of pellets when sintering was performed without the protection of a closed environment to keep the partial pressure of Li in the crucible constant. It is possible also that the presence of Al from the Al_2O_3 crucible may help prevent Li loss in the sample through the presence of the Al_2O_3-Li_2O eutectic, which traps the Li ions.

Secondary electron and optical images of undoped LLZO pellets sintered in alumina crucibles (Figure 5.7) show evidence of liquid phase sintering, seen as a front formed across the pellets from the edges. This was confirmed by the presence of a large amount of Al^+ secondary ions as detected by secondary ion mass spectrometry (SIMS) surface mass spectra at the edge of the pellet when compared to the central region of the pellet (Figure 5.7d).

Low energy ion scattering (LEIS) was utilised to investigate the migration of light cations through pellets of LLZO during the sintering process. Both Ga0.15-LLZO and

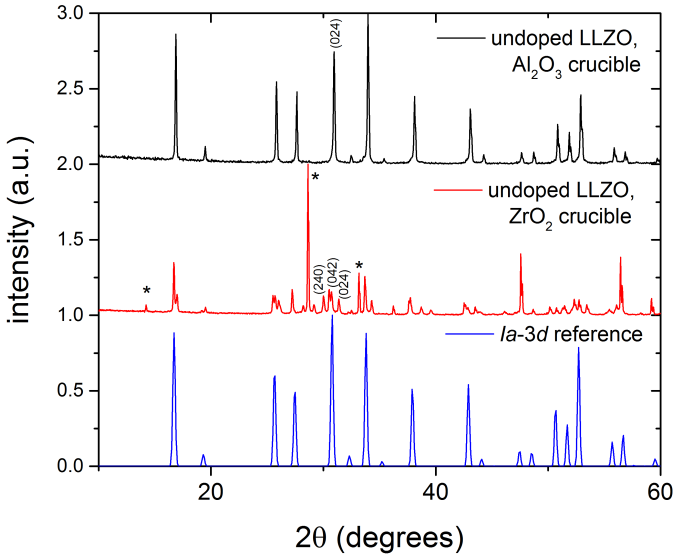


Figure 5.6: Pellet XRD patterns of nominally undoped LLZO, with thermal treatment in ZrO_2 (red line, middle) and Al_2O_3 (black line, top) crucibles. The sample sintered in an Al_2O_3 crucible shows almost pure cubic ($Ia\bar{3}d$ space group) symmetry (reference pattern shown at the bottom), whereas the ZrO_2-treated LLZO pattern takes the tetragonal phase with a large quantity of pyrochlore phase (peaks marked by *). (240),(042) and (024) indicate the diffraction peaks of the (024) plane which split in the tetragonal structure.

Al0.15-LLZO cold-pressed pellets were sintered in alumina crucibles. Both sides of the pellets were subsequently measured in LEIS depth-profiling mode to determine the relative differences in Al and Ga content. Figure 5.8 shows ^{4}He LEIS depth profiles over an analysis area of 750 µm by 750 µm. The dose per cycle was 7x10^{14} ions cm^{-2} for the ^{4}He analysis gun, and 3.4x10^{15} ions cm^{-2} for the Ar sputter gun, to ensure that most of the sputtering was carried out by the lower energy sputter gun to allow reasonable depth calibration and to minimise intermixing from the higher energy ^{4}He projectiles. LEIS measurements were taken by Dr Andrea Cavallaro at Imperial College London. It can be seen that in both Ga- and Al-LLZO pellets, the top side which was not in direct contact with the alumina crucible shows an overall net loss of Al and/or Ga relative to the under side that was in direct contact with the crucible. Even in the Ga-LLZO pellet, Al is present as it is introduced through the crucible and shows a directional distribution (being more plentiful on the side of pellet in contact with the crucible during sintering). These results highlight the ease of mobility of the lighter cations in LLZO during the thermal treatment processes, with implications on compositional control and Li^+ charge carrier concentration.

5.2 Germanium Doping

The possibility of doping with Ge^{4+} was also investigated, using a nominal concentration range of 0.05 to 0.15 Ge a.p.f.u. of LLZO, in order to achieve the optimal Li ion to vacancy

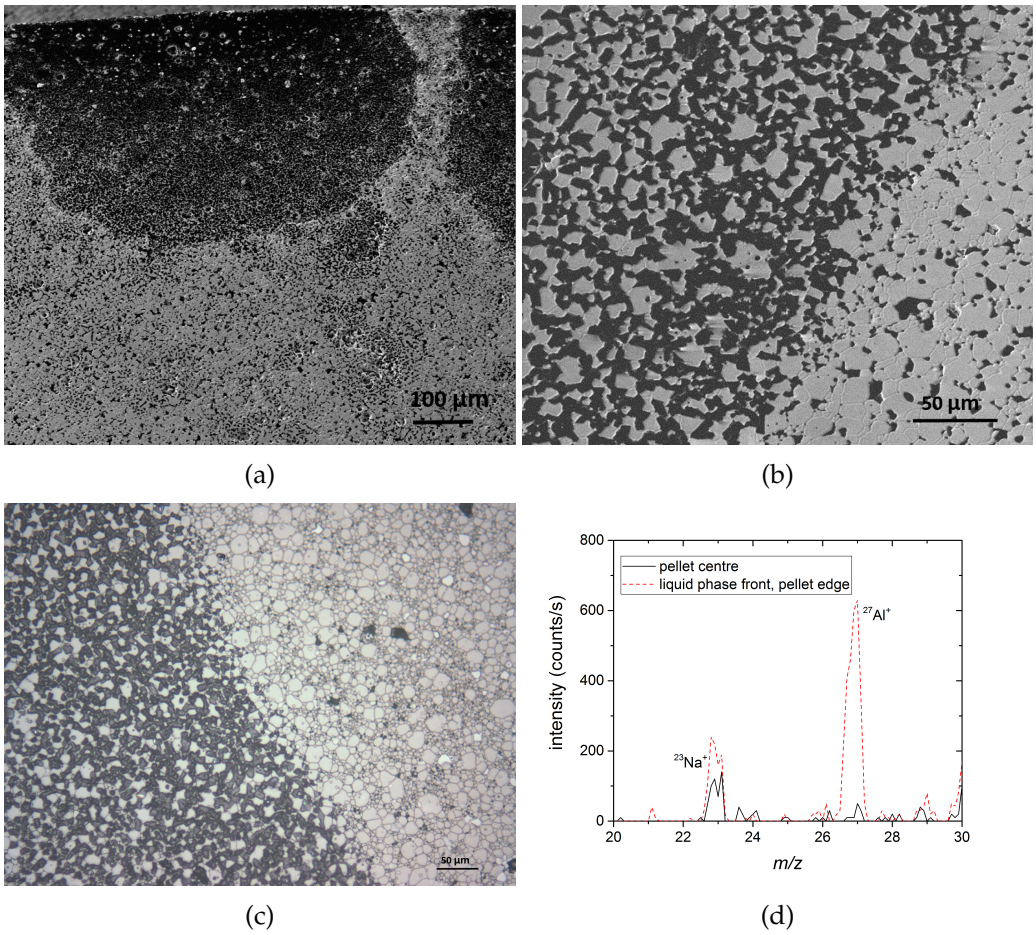


Figure 5.7: (a) Secondary electron, (b) secondary ion and (c) optical images of an undoped LLZO pellet surface showing a liquid phase front (dark contrast) from the edges of the pellet formed during sintering. (d) SIMS positive secondary ion surface mass spectra of the pellet centre (away from the liquid phase front, black solid line), and the pellet edge (red dashed line), taken over an area of 100 µm by 100 µm with a primary ion beam current of 300 pA.

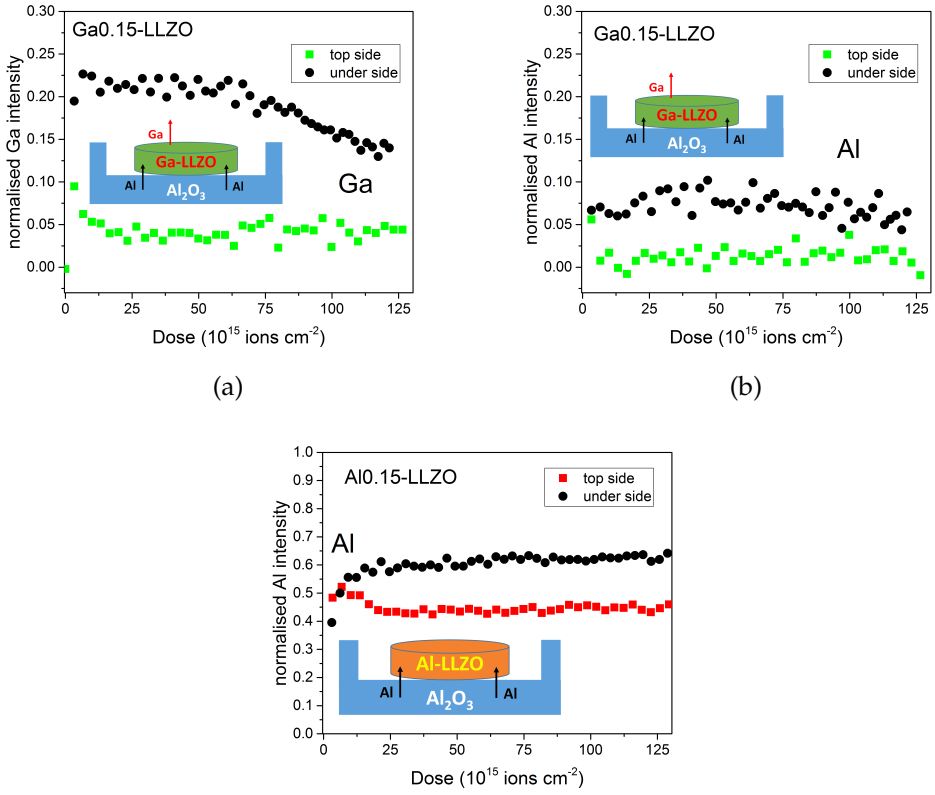


Figure 5.8: ^{4}He LEIS depth profiles with a 0.5 keV Ar sputter gun showing normalised Al and Ga intensities (with respect to the sum of all surface species) for (a and b) Ga0.15-LLZO and (c) Al0.15-LLZO pellets sintered in alumina crucibles, measured on both sides of the pellets. The sputter area is 1500 µm by 1500 µm and the analysis area is 750 µm by 750 µm.

concentration ratio for maximum conductivity (targeting a Li content of 6.4 to 6.6 a.p.f.u., as described in Chapter 3). The principle for using Ge^{4+} as a potential dopant is based on the idea that, following the success of the trivalent species Ga^{3+} and Al^{3+} which stabilise the cubic phase with a maximum conductivity at 0.15 a.p.f.u., a better ionic conductivity might be achieved with a higher valent cation which can be accommodated in the garnet structure whilst maintaining its oxidation state. It is suggested that this could be achieved because of the lower concentration of dopant species needed to maintain the optimum Li stoichiometry (charge balance dictates three Li vacancies created per mole of Ge added, instead of two with Al and Ga, as seen in Equations 5.2 and 5.3), thus reducing ion pathway blocking effects and improving conductivity. It was noted in Chapter 3 that the crystal radius of Ge^{4+} is almost identical to that of Al^{3+} in both tetrahedrally- and octahedrally-coordinated sites (see Table 5.2); as such, it might be expected that Ge^{4+} would have similar crystallographic preference to Al for the Li sites in the lattice.

$$GeO_2 \xrightleftharpoons{LLZO} Ge_{Li}^{\bullet\bullet\bullet} + 3V'_{Li} + 2O_O^{\times} \tag{5.2}$$

$$\frac{1}{2}Ga_2O_3 \xrightleftharpoons{LLZO} Ga_{Li}^{\bullet\bullet} + 2V'_{Li} + \frac{3}{2}O_O^{\times} \tag{5.3}$$

Table 5.2: Table of crystal radii of Li, Al and Ge cations, showing their valence and crystal radius in 4- and 6-fold coordinated (CN) sites; data from Shannon's *Revised Effective Ionic Radii* [154].

Ion	**Valence**	**4 CN crystal radius (Å)**	**6 CN crystal radius (Å)**
Li	+1	0.73	0.90
Al	+3	0.53	0.675
Ge	+4(+2)	0.53	0.67(0.87)

The aim of this work is to fully characterise the Ge-doped LLZO material, both structurally and electrochemically, and to assess its suitability for use as a solid state electrolyte, and to use it together with known properties of Al- and Ga-doped LLZO, to relate the lattice occupancy of the dopant to the observed conductivity trends for the series.

5.2.1 Optimising the Germanium Concentration

Preliminary work by Huang *et al.* showed that the cubic phase could be achieved with a Ge doping content of 1 wt%, and that Ge behaves as a sintering aid (favouring grain growth) [133]. 1 wt% corresponds to ~ 0.12 Ge a.p.f.u., consistent with previous estimates for optimum Li content. For this reason, compositions with a range of nominal Ge stoichiometry 0.05 to 0.15 a.p.f.u. were investigated to further characterise the phase stability and conductivity trends. Huang also observed that a high Ge content in the

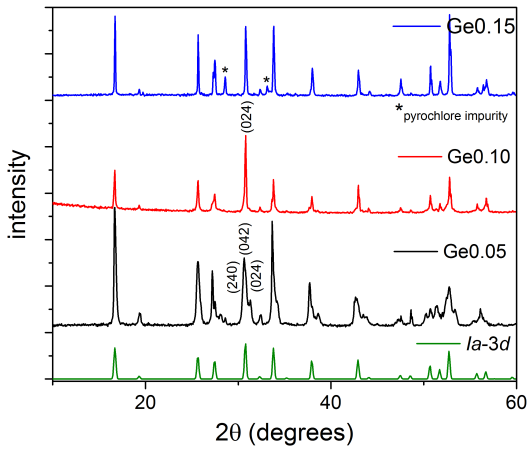


Figure 5.9: XRD patterns of Ge-doped LLZO pellets, showing the variation between different doping content compositions, and the theoretical reference pattern for cubic $Ia\bar{3}d$ (shown at the bottom). (240),(042) and (024) indicate the diffraction peaks of the (024) plane which split in the tetragonal structure.

starting materials may lead to accumulation in grain boundaries, especially in the form of GeO_2 which has a melting point of 1115 °C, below the sintering temperature used. It may also act as a sintering aid, improving the connection between grains.

X-ray Diffraction

Figure 5.9 shows XRD patterns of the Ge-doped LLZO pellets with different nominal Ge concentration. In agreement with the work of Huang [133], the sharpest cubic pattern is found for the Ge0.10-LLZO sample. At lower concentrations of Ge, lattice stabilisation is not as effective, resulting in a splitting and broadening of the diffraction peaks, indicative of tetragonal character. For example, the diffraction of the (024) plane in the cubic structure yields one single peak in the theoretical profile, but splits into three peaks in the tetragonal $I4_1/acd$ structure, seen in the Ge0.05-LLZO pattern. The pattern for Ge0.15-LLZO is cubic but shows pyrochlore impurity peaks (marked with *), likely to be due to a low initial amount of Li in combination with the high temperature sintering conditions - which might favour some volatilisation of Li, resulting in the formation of $La_2Zr_2O_7$. The compositions Ge0.30-LLZO and Ge0.50-LLZO were also tested, producing XRD patterns containing a large number of impurities, dominated by $La_2Zr_2O_7$ phase (see Appendix A.1, Figure A.2). For this reason, Ge0.10-LLZO was chosen as the target composition for further characterisation.

Inductively Coupled Plasma – Optical Emission Spectroscopy

Inductively Coupled Plasma – Optical Emission Spectroscopy (ICP-OES) was used to test the stoichiometry of Ge-doped LLZO, in particular to check the true content of Ge and test for the presence of Al from the crucibles. The surface of the pellet samples were abraded before analysis to remove surface layers, before preparing solutions as described

in Chapter 4, Section 4.5. It should be noted that the technique does not discriminate between grain and grain boundary compositions.

Table 5.3: ICP-OES measured atomic concentrations for Ge-LLZO pellets with different nominal compositions.

Composition (nominal)	**Li a.p.f.u.**	**Ge a.p.f.u.**	**Al a.p.f.u.**	**Zr a.p.f.u.**	**La (fixed) a.p.f.u.**	**Ge+Al a.p.f.u.**	**Theoretical Li a.p.f.u. (from Ge+Al content)**
Ge0.15-LLZO ($Li_{6.4}Ge_{0.15}La_3Zr_2O_{12}$)	6.31	0.12	0	2.01	3	0.12	6.52
Ge0.10-LLZO ($Li_{6.6}Ge_{0.10}La_3Zr_2O_{12}$)	6.84	0.05	0.03	2.05	3	0.08	6.71
Ge0.05-LLZO ($Li_{6.8}Ge_{0.05}La_3Zr_2O_{12}$)	6.92	0.02	0.13	2.05	3	0.15	6.53
Undoped LLZO (Al_2O_3 crucible)	8.17	0	0.16	2.01	3	0.16	6.52

Table 5.3 shows the measured atomic concentrations given as atoms per formula unit for the three Ge-LLZO pellet compositions, as well as an undoped LLZO sample which formed a cubic-tetragonal mixed phase and was sintered in an alumina crucible (its XRD pattern is shown in the Appendix A.5.3, Figure A.8a). It can be seen that Ge is present at levels slightly lower than expected from the nominal stoichiometries of the starting materials (final column), perhaps due to the high temperature conditions resulting in some Ge volatilisation. Additionally, the Al and Ge exhibit a cooperative effect, in that the aluminium content varies inversely with Ge content, which might be expected if they are competing for the same substitution sites in the lattice as a result of their similar radii, and are both acting to stabilise the cubic structure of the material. The Li content calculated from the total Ge+Al concentration, assuming substitution at the Li sublattice, is not the same as the measured content, implying that the dopants are not solely present in the LLZO lattice (but likely also to be found in the grain boundaries).

In the undoped LLZO, which was not fully stabilised in the cubic phase, the Li content is correspondingly high (8.17 a.p.f.u.), and the Al content therefore likely corresponds to an amount distributed across both grains and grain boundaries introduced from the crucible (as, despite its high concentration, the amount of Al measured in the pellet was not sufficient for cubic stabilisation of the garnet lattice).

5.2.2 Conductivity Measurements

Conductivity measurements of Ge-LLZO were made using electrochemical impedance spectroscopy (EIS) with sputtered Au blocking electrodes to create a symmetrical cell measured over the frequency range 13 MHz to 0.1 Hz (see Chapter 4 Section 4.7.1). The

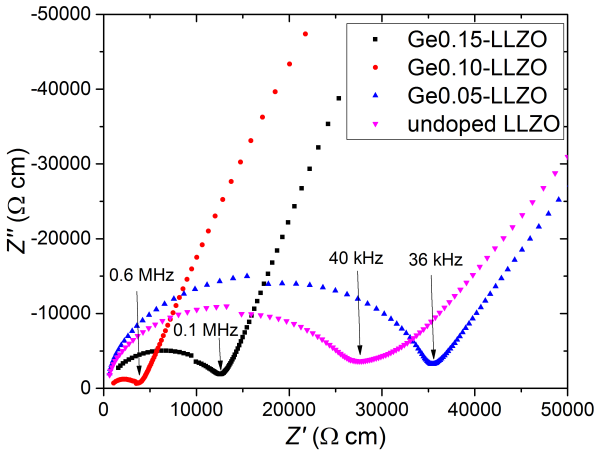


Figure 5.10: Nyquist plots of Ge0.15-, Ge0.10-, Ge0.05- and undoped LLZO pellets with symmetrical Au electrodes measured at room temperature across the frequency range 13 MHz to 0.1 Hz.

spectra (Figure 5.10) show a high frequency semicircle followed by a low frequency contribution coming from the highly resistive electrodes. The electrodes are not purely Li^+ blocking (i.e. they have an associated resistance), probably due to a degree of Au-Li alloying and secondary phases at the interface which may have formed during the air exposure to and from the sputtering process. The presence of an additional arc due to grain boundaries or interface effects is not clearly seen by eye in the spectra, and may be hidden in the electrode response. To quantify the spectra, combinations of a resistor in parallel with a constant phase element (denoted R//CPE) are used, with a high frequency inductance L (on the order 10^{-6} H) and an internal resistance R_{int} fixed at 5 Ω (measured with a blank, or 'shorted' cell) in series. First, fitting the high frequency semicircle to a single R1//CPE1 component (and the low frequency tail to R2//CPE2) gave a fit shown in Figure 5.11 and with the fitted data described in Table 5.4.

The conductivity σ corresponding to the high frequency component was calculated from the resistance R using Equation 5.4, where l is the electrolyte thickness and A is the electrode area.

$$\sigma = \frac{l}{RA} \tag{5.4}$$

The capacitance is calculated from the constant phase element fit, CPE, as discussed in Chapter 4, Section 4.7.1, where:

$$Z_{CPE} = \frac{1}{Q(i\omega)^n} \tag{5.5}$$

Here, ω is the angular frequency, n is the description of non-ideality (given as CPE-P in Z-View software [242]), Q is the non-ideal capacitance (given as CPE-T in Z-View software), and C is found from Equation 5.6 [257]:

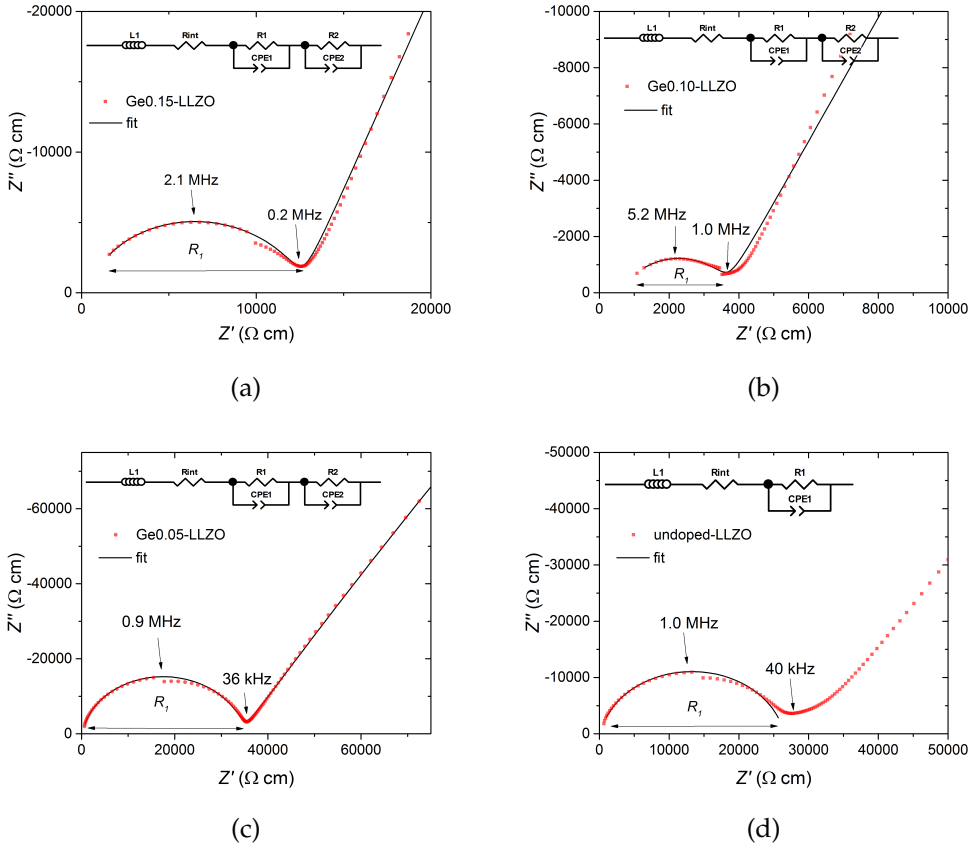


Figure 5.11: Nyquist plots for the room temperature impedance spectra of Ge-LLZO and undoped LLZO electrolytes with Au symmetrical electrodes, with a fitting of the high frequency arc using a single R1//CPE1 component (using the equivalent circuit shown, inset); the low frequency tail is not fitted in undoped-LLZO.

Table 5.4: Calculated values of conductivity σ, capacitance C and relative permittivity ϵ_r from the high-frequency component fit to a single R1//CPE1 element in the Nyquist plots (Figure 5.11), taken at 25 °C. l is the pellet thickness, A is the area of the electrode, n is the non-ideality factor for capacitance.

	Ge0.05-LLZO	**Ge0.10-LLZO**	**Ge0.15-LLZO**	**Undoped LLZO**
***R* [Ω]**	17236	1149	4747	16973
σ **[S cm^{-1}]**	2.9x10^{-5}	2.8x10^{-4}	8.1x10^{-5}	3.8x10^{-5}
CPE [F s^{n-1}]	3.5x10^{-11}	2.3x10^{-10}	1.3x10^{-10}	5.2x10^{-11}
n	0.92	0.86	0.87	0.89
***C* [F]**	2.0x10^{-11}	1.8x10^{-11}	1.4x10^{-11}	8.9x10^{-12}
***C* x *l*/*A* [F cm^{-1}]**	7.8x10^{-12}	5.9x10^{-12}	5.5x10^{-12}	5.7x10^{-12}
ϵ_r	88	66	62	64

$$C = (R^{1-n}Q)^{1/n} \tag{5.6}$$

The relative permittivity, ϵ_r , is calculated from the capacitance C by Equation 5.7, where ϵ_0 is the vacuum permittivity (8.854×10^{-14} F cm^{-1}) [258]:

$$\epsilon_r = \frac{Cl}{A\epsilon_0} \tag{5.7}$$

In the case of Ge0.10-LLZO, the high frequency component fitted to a single R1//CPE1 element gives a capacitance of 1.8×10^{-11} F, and an ϵ_r of 66. For the undoped sample, which contained 0.16 Al a.p.f.u. as measured by ICP, and stabilised in mixed cubic-tetragonal symmetry, has a corresponding C of 8.9×10^{-12} F, and an ϵ_r of 64. All the compositions tested had similar values of capacitance and relative permittivity. A realistic value for the bulk permittivity of an oxide is between 50-80 as reported in the literature [113, 259, 260], with a capacitance typically in the pF range [239]. As such, the calculated values for the high frequency arcs agree with a bulk process. However, a grain boundary contribution is expected to also exist; for this reason, the high frequency semicircle was then fitted with two R//CPE parallel circuits, R1//CPE1 and R2//CPE2, tentatively representing bulk and grain boundary contributions. Figure 5.12 and Table 5.5 summarise these fits.

The fitting of R2//CPE2 for Ge0.10- and Ge0.15-LLZO yield capacitances of 4.6×10^{-10} F and 4.2×10^{-10} F, respectively. In the undoped LLZO sample, the capacitance is 3.0×10^{-9} F. These three values sit within the range expected for a grain boundary process. In Ge0.05-LLZO, the R2//CPE2 fit gives $C = 8.0 \times 10^{-11}$ F, implying that the two high frequency processes are less well defined, creating difficulty in the fit. This might be because the bulk resistance is expected to be higher in this composition. A meaningful fit of the mid-frequency region of the spectra is non-trivial, making it difficult

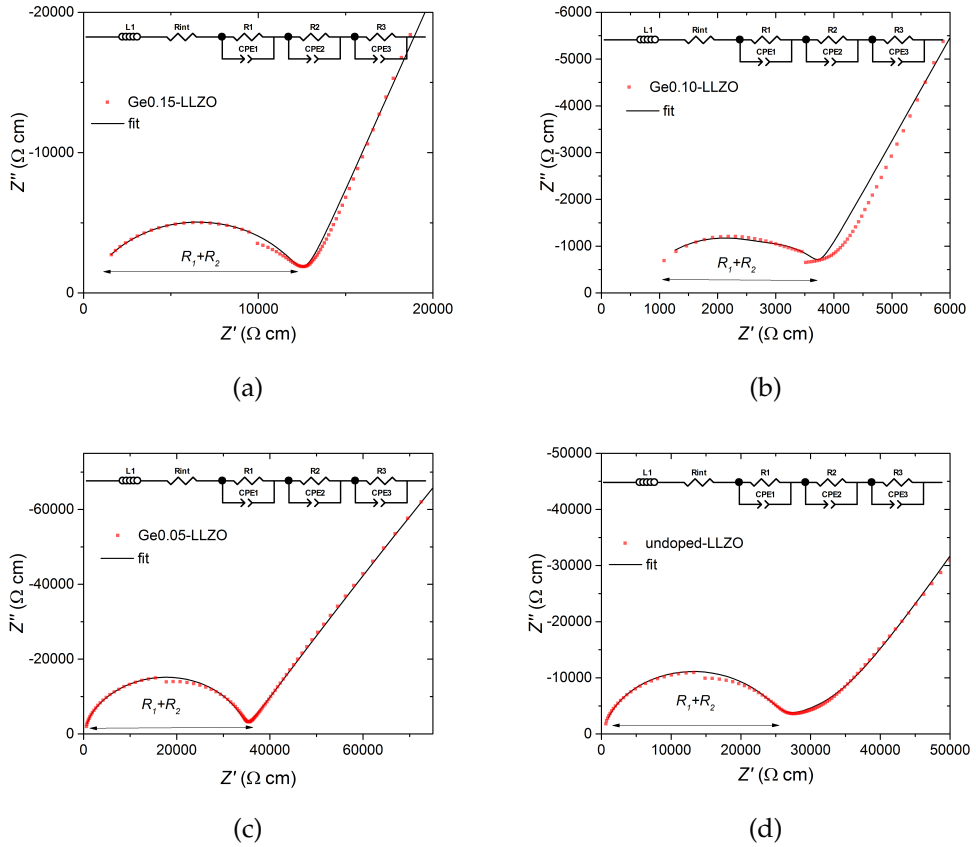


Figure 5.12: Nyquist plots for the room temperature impedance spectra of Ge-LLZO and undoped LLZO electrolytes with Au symmetrical electrodes, with a fitting of the high frequency arc using two R//CPE components (using the equivalent circuit shown, inset).

to confirm that its origin is from a high-resistance grain boundary. It may be that in the lower resistance R_1 (bulk) samples (i.e. Ge0.10-LLZO), the wiring inductance has a more significant effect on distorting the data, and the high-frequency end of the arcs are lost at room temperature, making fitting difficult, even with the introduction of an inductance element in the equivalent circuit. Nevertheless, the geometry-corrected C_1 and ϵ_{r1} values for Ge0.10-LLZO are in agreement with a bulk effect and the associated bulk conductivity, σ_1 (i.e. σ_{bulk}) is $3.4 \times 10^{-4}\,S\,cm^{-1}$, which an order of magnitude lower than the highest reported bulk conductivities for garnets ($> 1\,mS\,cm^{-1}$). It is also possible that the gold electrode response masks the mid-frequency component, making fitting difficult.

Later in this thesis (Chapter 6 Section 6.3), low temperature ($< 0\,°C$) EIS of Ga0.15-LLZO is measured, allowing better separation of high- and mid-frequency features for further analysis. Thickness experiments were carried out and confirmed the existence of the mid-frequency semicircle in Ga0.15-LLZO that changes as a function of thickness, suggesting a grain boundary (or charge double layer), rather than surface/interface, origin of the mid-frequency feature.

Owing to these complications of fitting the impedance data, the low-frequency component is preferentially treated as a single R//CPE element here, giving a total conductivity calculated from the resistance (Table 5.4).

Table 5.5: Calculated values of conductivity σ, capacitance C and relative permittivity ϵ_r from the high-frequency component fit to two R//CPE elements in the Nyquist plots (Figure 5.12), taken at 25 °C. l is the pellet thickness, A is the area of the electrode and n is the non-ideality factor for capacitance.

	Ge0.05-LLZO	**Ge0.10-LLZO**	**Ge0.15-LLZO**	**Undoped LLZO**
R_1 **[Ω]**	16723	937.3	4700	15786
σ_1 **[S cm^{-1}]**	3.0x10^{-5}	3.4x10^{-4}	8.1x10^{-5}	4.1x10^{-5}
CPE$_1$ [F s^{n-1}]	3.4x10^{-11}	2.3x10^{-11}	1.2x10^{-10}	3.9x10^{-11}
n_1	0.93	0.98	0.87	0.91
C_1 **[F]**	1.1x10^{-11}	1.7x10^{-11}	1.5x10^{-11}	9.0x10^{-12}
C_1 **x** l/A **[F cm^{-1}]**	5.3x10^{-12}	5.5x10^{-12}	5.6x10^{-12}	5.8x10^{-12}
ϵ_{r1}	60	62	63	65
R_2 **[Ω]**	509.5	198	45.8	6014
σ_2 **[S cm^{-1}]**	9.9x10^{-4}	1.6x10^{-3}	8.4x10^{-3}	1.1x10^{-4}
CPE$_2$ [F s^{n-1}]	1.4x10^{-11}	2.7x10^{-11}	1.5x10^{-13}	3.9x10^{-7}
n_2	1.1	1.2	1.4	0.55
C_2 **[F]**	8.0x10^{-11}	4.6x10^{-10}	4.2x10^{-10}	3.0x10^{-9}

Symmetric Li/Ge0.10-LLZO/Li Cell Impedance

The measurement of Li/Ge0.10-LLZO/Li symmetric cell impedance, using the same pellet as measured with gold electrodes, is shown in Figure 5.13 and the fit summarised in Table 5.6. The high- and mid-frequency components seen in the Au electrode cell, found at frequencies above 0.5 MHz, are just visible and are fitted to a single R1//CPE1 element, representing a combined bulk+grain boundary contribution, as discussed in the previous section. In addition, a low frequency semicircle is seen due to the interface with lithium electrodes is seen and fitted to R2//CPE2.

The obtained total conductivity from the high frequency arc fit is approximately one order of magnitude lower here than with Au electrodes. It is possible that poor Li contact results in changes to the apparent R_{bulk}, R_{GB} and interfacial resistance.

For example, the area specific resistance of the low frequency arc (R2//CPE2) with Li electrodes in Figures 5.13a and 5.13b is 0.8 MΩ cm^2, which is much larger than reported values for Li/LLZO interfaces. It is unclear whether this is caused solely by the poor contact with Li metal, or whether there are additional resistive contributions from i.e. grain boundaries (and possibly also space-charge layers), which are more resistive here than in Ga0.15-LLZO and Al0.15-LLZO (seen in Chapters 6 and 8).

Furthermore, the area-specific capacitance (C_2/A) for the large, low frequency R2//CPE2 component determined from Equation 5.6 and normalised with respect to

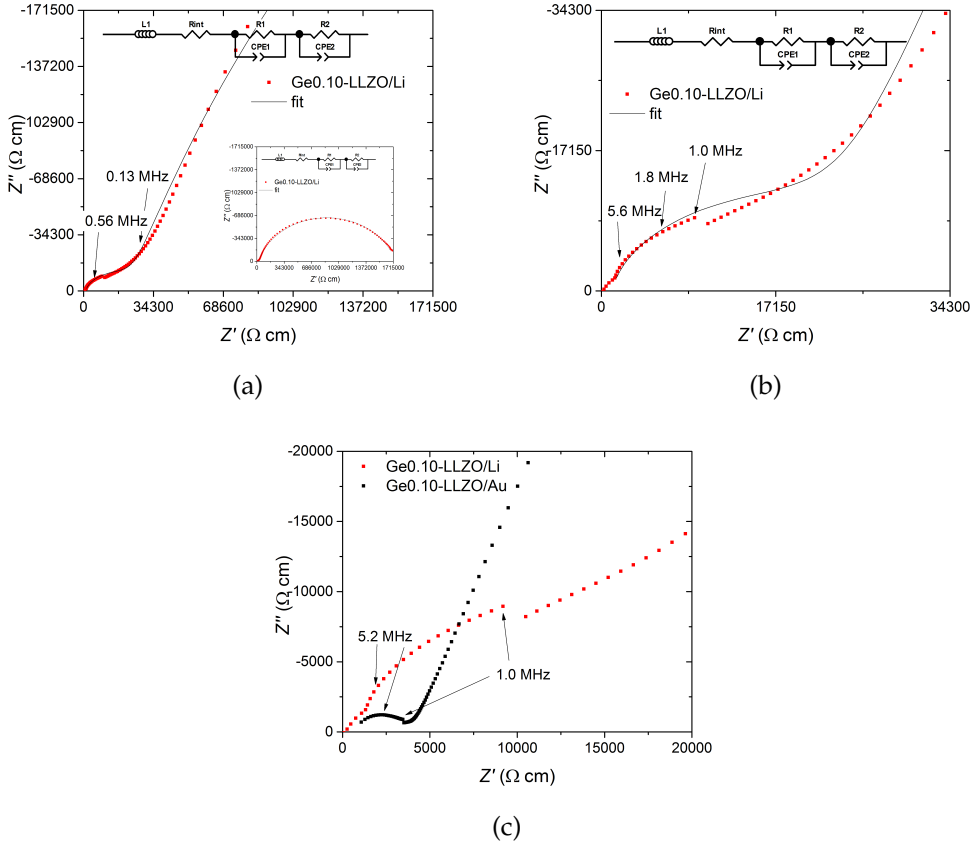


Figure 5.13: Nyquist plots of a symmetric cell of Ge0.10-LLZO sandwiched between (a and b) lithium electrodes with the fit line using two R//CPE elements (inset equivalent circuit), with an expanded frequency range view shown as an inset. (c) Comparison of Au and Li symmetrical electrode cells at high frequencies; measured between 20 MHz and 1 Hz frequency (13 MHz and 1 Hz for the Au electrode cell).

electrode area is 3.1×10^{-9} F cm^{-2}, which is low for a Li metal-electrolyte interface compared to the literature (typically below 10^{-8} F cm^{-2} [173]) and compared to Ga0.15-LLZO measured in Chapter 6 (which has a charge transfer capacitance of the order 10^{-5} F cm^{-2}). Further impedance measurements and analysis are needed to better understand these processes, and this work should be viewed as a preliminary analysis.

5.2.3 Microstructural Analysis

To attempt to understand better the impedance spectra seen with Ge-LLZO, the pellet morphology, phases and microstructure are investigated using imaging techniques. Optical and secondary electron images of Ge0.10-LLZO pellets, which have been thermally etched at 900 °C to reveal the microstructure, show large, well connected grains - in some cases larger than 100 µm in diameter - and bimodally distributed (Figure 5.14). These grains are much larger than those found in Al0.15-LLZO and Ga0.15-LLZO made under the same conditions. Multiple Li_2O-GeO_2 eutectics are reported to exist below the sintering temperature [261], similar to that with Al_2O_3 (in which there is a single eutectic below 1150 °C), which may explain this observation and suggest liquid phase

Table 5.6: Calculated values of conductivity σ, capacitance C and relative permittivity ϵ_r from the high- and low-frequency component fits of Li/Ge0.10-LLZO/Li cell impedance spectra (Figure 5.13), taken at 25 °C. l is the pellet thickness, A is the area of the electrode and n is the non-ideality factor for capacitance.

Li/Ge0.10-LLZO/Li			
R_1 **[Ω]**	6707	R_2 **[Ω]**	5.0x10^5
σ_1 **[S cm^{-1}]**	4.4x10^{-5}	σ_2 **[S cm^{-1}]**	5.8x10^{-7}
CPE$_1$ [F s^{n-1}]	1.1x10^{-9}	**CPE$_2$ [F s^{n-1}]**	3.9x10^{-9}
n_1	0.78	n_2	0.83
C_1 **[F]**	3.8x10^{-11}	C_2 **[F]**	1.1x10^{-9}
C_1 **x** l/A **[F cm^{-1}]**	1.1x10^{-11}	C_2 **/** A **[F cm^{-2}]**	3.1x10^{-9}
ϵ_{r1}	126	R_2 **x** $A/2$ **[Ω cm^2]**	8.0x10^5

sintering is involved, aiding grain growth. No visible pores can be seen in the grains and the geometrically-calculated relative density is 98 %, using the lattice parameters from Rietveld refinement [206] of the neutron diffraction data (Section 5.2.4).

Chemical analysis using time of flight (TOF)-SIMS mapping showed a distribution of Ge homogeneously across the grains (Figure 5.15), with a slight enrichment at the grain boundaries (which are also enriched in O and Li, supporting the proposal of a liquid phase Li_2O-GeO_2 eutectic forming during the sintering process.

5.2.4 Site Preference of Germanium

Following first principles predictions of Miara *et al.* [155] that Ge^{4+} has a preferential defect energy for substitution at the Zr site in LLZO, an attempt was made to target this site for doping by controlling the stoichiometry of the starting materials. The resulting material was not stabilised in the cubic phase (as indicated by the double peaks in the XRD pattern indicative of the tetragonal $I4_1/acd$ structure), and contained impurity phases that included $La_2Zr_2O_7$ and GeO_2 (see XRD pattern, Appendix A.1, Figure A.3).

Neutron Diffraction of Ge0.10-LLZO

Rietveld refinement of the neutron powder diffraction pattern (ND) of Ge0.10-LLZO containing a small amount of $La_2Zr_2O_7$ impurity shown in Figure 5.16 and Table 5.7 suggested that the Ge^{4+} substitutes for Li^+ at the 24d tetrahedral site, giving a best fit for this site when the concentration was fixed at 0.10 Ge a.p.f.u. The germanium was allowed to be refined at both Li1 and Li2 sites, but led to a preferential occupancy of the Li1 (24d) site only. Refining at the Zr site yielded unfavourable occupancies of Zr and Ge (too high), and preferential occupancy of the Li1 site when it was allowed to be refined together with the Zr site for Ge occupancy. The corresponding XRD pattern is shown in Appendix A.1, Figure A.4.

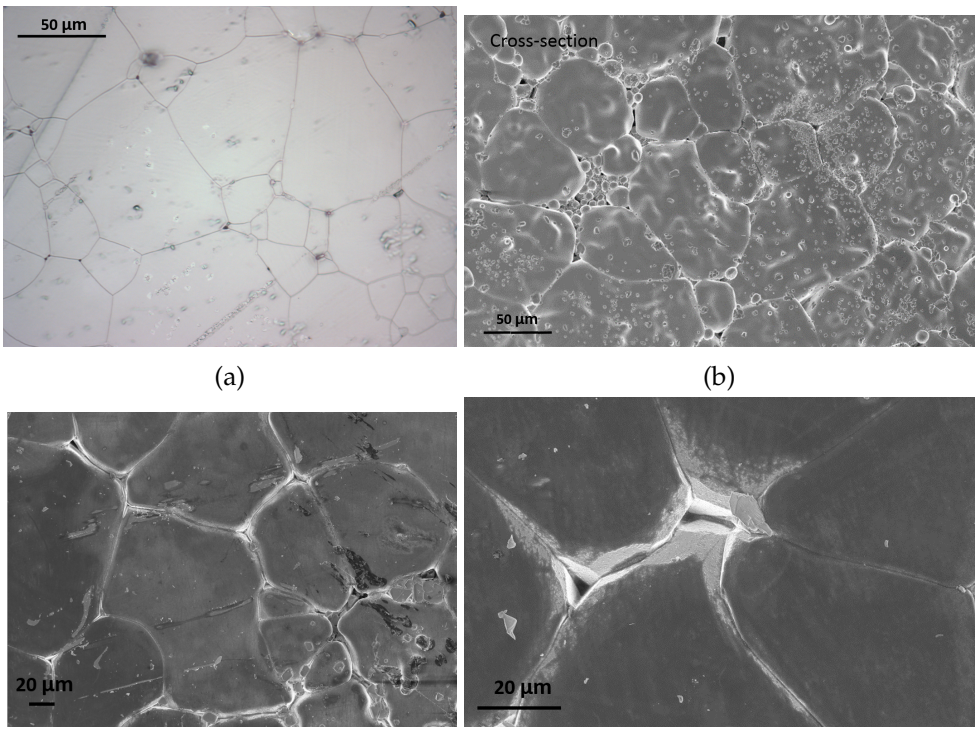


Figure 5.14: Images of Ge0.10-LLZO pellets, thermally etched at 900 °C. (a) Optical microscope image polished to a 1 µm roughness finish and etched; (b) cross-sectional and (c and d) surface secondary electron images taken at 5 kV accelerating voltage.

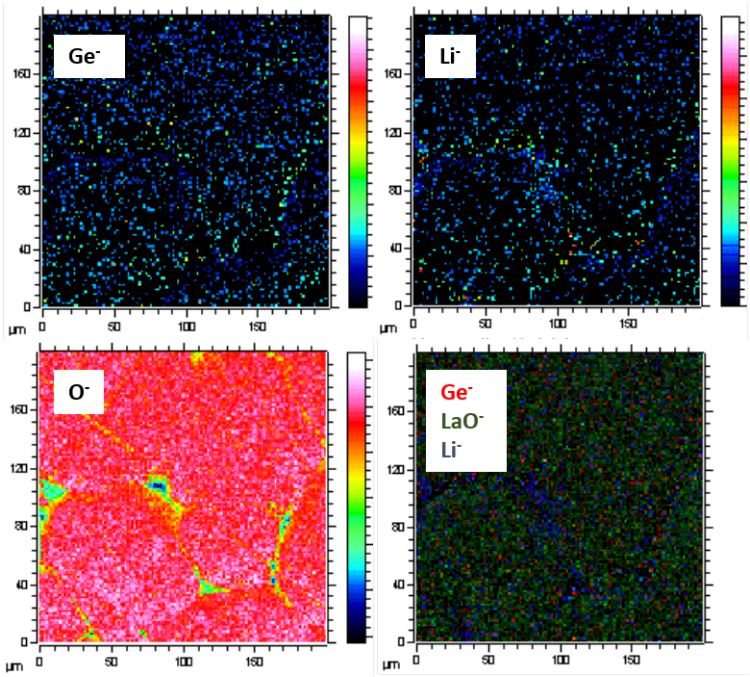


Figure 5.15: TOF-SIMS maps of the surface of a Ge0.10-LLZO pellet, showing $^{74}Ge^-$, $^{7}Li^-$, $^{16}O^-$ secondary ion maps and an overlay of $^{74}Ge^-$, $^{155}(LaO)^-$ and $^{7}Li^-$ species. Maps were taken with a Bi^+primary ion beam (25 kV, 0.2 pA) and a Cs^+ sputter gun (1 kV, 64 nA) operated in non-interlaced burst alignment mode (using a 1s:1s:1s sputter:wait:analyse cycle).

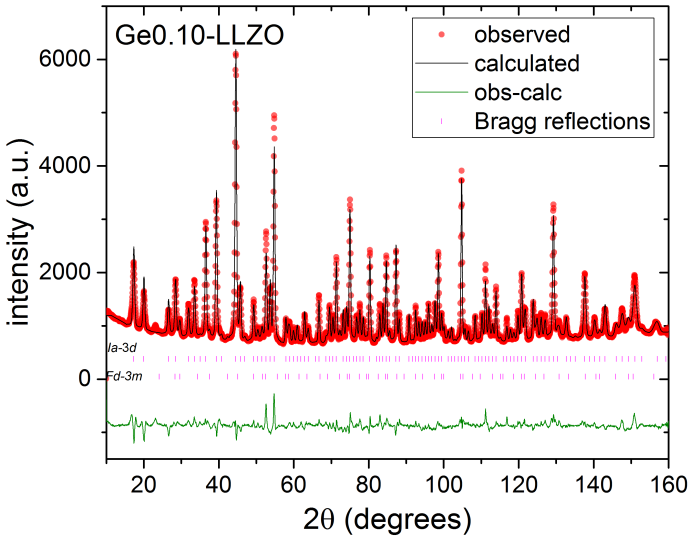


Figure 5.16: Neutron powder diffraction pattern with Rietveld refinement, showing observed, calculated and difference (obs-calc) patterns fitting to $Ia\bar{3}d$ space group and pyrochlore $La_2Zr_2O_7$ impurity (space group $Fd\bar{3}m$), occupying 5.79 wt% of the total (with the Bragg reflections shown as short vertical lines).

Table 5.7: Neutron powder diffraction data of Ge0.10-LLZO determined by Rietveld refinement. Space group: $Ia\bar{3}d$ (no. 230); lattice parameter: $a = b = c = 12.963\,57 \pm 0.000\,13$ Å. R-factors: $R = 7.91$, $\chi^2 = 12.9$. B_{iso} is the isotropic atomic displacement parameter; the constraint on this parameter is such that B_{iso}(Li1)= B_{iso}(Ge). The density of the Ge0.10-LLZO powder phase is refined as 5.143 g cm^{-3}.

Species	**Site**	**x/a, y/b, z/c**	**B_{iso}**	**Occupancy**
Li1	24*d*	0.375, 0, 0.25	2.58(5)	2.83(2)
Li2	96*h*	0.0997(2), 0.6865(2), 0.5770(2)	0.500	3.78(2)
La	24*c*	0.125, 0, 0.25	0.748(6)	3.000
Zr	16*a*	0, 0, 0	0.724(6)	2.000
Ge	24*d*	0.375, 0, 0.25	2.58(5)	0.100
O	96*h*	-0.03226(2), 0.05363(2), 0.14945(2)	1.142(6)	12.000

The EIS and ND findings support the view that occupancy of 24*d* Li sites by aliovalent dopants (as seen with Al^{3+} and in some literature reports, Ga^{3+}) can enhance the lithium conductivity of LLZO. Using the higher valent dopant Ge^{4+} enables the stabilisation of the cubic phase with a lower dopant content than when cations with lower oxidation states are used. However, Ge0.10-LLZO is not able to provide the highest values of conductivity

reported for some Ga-LLZO compositions, suggesting site blocking arguments on the lithium sub-lattice do not tell the whole story. Further verification of Ge site occupancy through other techniques, such as ^{73}Ge nuclear magnetic resonance (NMR), would be useful here to confirm; however this NMR active nucleus has a low natural abundance (7.8 %) a small gyromagnetic ratio and spin 9/2, making lineshape analysis potentially tricky.

5.2.5 Oxidation State of Germanium

X-ray photoelectron spectroscopy was used to verify the oxidation state of Ge in Ge0.10-LLZO. Figure 5.17 shows Al 2p and Ge 2p core spectra comparisons for Ge0.10-LLZO sintered in oxygen and argon atmospheres, to provide a comparison of oxidising and slightly reducing sintering conditions, and Al0.15-LLZO sintered in argon. The samples were transferred using a glove box module to prevent air exposure and all measurements and data treatment were made by Dr Anna Regoutz at Imperial College London.

Small Ge 2p peaks at about 1219 eV confirm the presence of Ge in Ge0.10-LLZO; these are superimposed on a broad C Auger feature so are difficult to fit for accurate quantification, but their position in both samples can be ascribed to a Ge(IV) oxidation state (not Ge(II) or metallic Ge, which would occur at lower and higher binding energies, respectively). Additionally, no appreciable Al 2p peak can be seen.

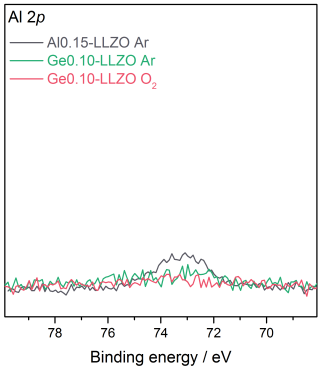
5.2.6 Redox Stability Measured by Cyclic Voltammetry

To check the electrochemical stability of Ge0.10-LLZO, and to ensure the Ge^{4+} is redox stable against Li metal electrodes across an operational voltage range, cyclic voltammetry was performed on a cell using Li metal electrodes (Figure 5.18). The voltage range was −0.5 V to 4 V vs. Li^+/Li, with a scan rate of 10 mV s^{-1}. A set of lithium stripping (positive current) and deposition (negative current) peaks are seen either side of the 0 V point, but no other redox peaks can be seen at higher voltages, indicating the stability of Ge0.10-LLZO against redox processes in the presence of Li metal and a lack of degradation reactions involving Li^+ ions.

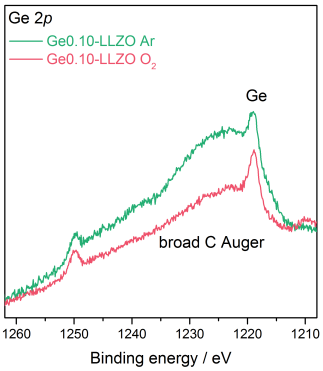
5.3 Summary

This chapter explored the synthesis and processing parameters of doped LLZO garnets, and studied the feasibility of using germanium as a supervalent dopant at the lithium sublattice.

A number of steps were taken to optimise the synthesis conditions, by varying the atmosphere, temperature and duration of high temperature treatments of the LLZO powders and pellets. It was found that the optimal conditions for phase pure, dense garnets were thermal treatment at 800 °C in dry flowing oxygen for 6 hours to obtain the cubic powder, followed by sintering the pellets at 1150 °C for 6 hours in an argon atmosphere, with all processing steps carried out in a glove box to prevent reaction with



(a)



(b)

Figure 5.17: XPS Al 2p and Ge 2p core spectra of Al0.15-LLZO and Ge0.10-LLZO pellet samples, sintered in both oxygen and argon. All peak binding energies are referenced to the C-C adventitious carbon peak at 285 eV and peak intensities are normalised to the La peak for each sample.

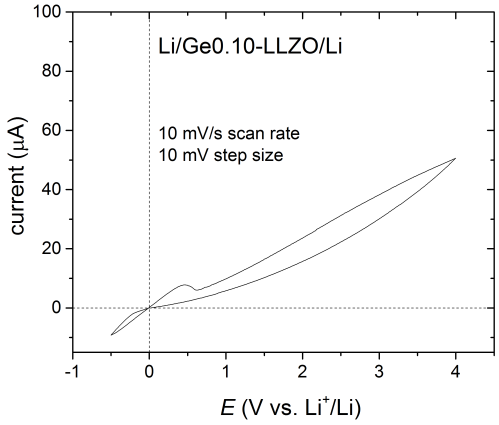


Figure 5.18: Cyclic voltammogram of a Li/Ge0.10-LLZO/Li cell at a scan rate of $10\,\mathrm{mV\,s^{-1}}$ in the potential range from $-0.5\,\mathrm{V}$ to $4\,\mathrm{V}$ vs. $\mathrm{Li^+/Li}$.

moisture. The presence of Li_2ZrO_3 and $La_2Zr_2O_7$ impurities were commonly encountered, illustrating the need to control well the starting material stoichiometry to obtain the metastable LLZO cubic phase desired. Bimodal particle sizes in the powders were obtained using these conditions, which led to tightly packed grains with bimodal size distribution in the dense LLZO pellets. Sometimes coloured pellets were obtained, and it is suggested that the creation of colour centres under the reducing argon atmosphere sintering conditions may be the cause, resulting in the formation of lithium and oxygen vacancies. This was not explored further here. Finally, the effect of the crucible used during sintering was investigated - providing evidence of the mobile nature of Al^{3+}, Ga^{3+} (as well as Li^+, indirectly) in the LLZO pellets during high temperature treatment. Evidence of the formation of an Al_2O_3-Li_2O eutectic was seen, and the influence of alumina crucibles in providing a source of Al^{3+} was confirmed.

Germanium was shown to be effective as a dopant in stabilising the cubic phase and providing an enhancement in conductivity (up to $3.4 \times 10^{-4}\,S\,cm^{-1}$ at room temperature for the Ge0.10-LLZO composition). ICP showed a cooperative effect between Al and Ge cations in entering the Ge-LLZO pellets. Ge was shown to be present as Ge^{4+} and produced a Ge-LLZO electrolyte cell which is redox stable against lithium metal under an operational voltage range. Neutron diffraction refinement suggests that Ge substitutes at the Li 24*d* site, in similarity to Al^{3+} reported in Al-LLZO.

5.4 Suggested Future Work

A method for imaging the atomic arrangement in LLZO using STEM was developed, allowing challenging sample damaging effects to be overcome, but Li and lighter elements could not be resolved, even with high resolution aberration-corrected setup. Further work would include imaging lamella samples of LLZO, and to study interfaces and grain boundaries on an atomically-resolved scale, in addition to studying the oxygen vacancies.

Germanium doped LLZO is not the most promising composition in terms of ionic conductivity, but may be interesting to study further with regards to its electrochemical cyclability (see Chapter 8) trends, in particular regarding the composition of its grain boundaries.

Chapter 6

Moisture-Induced Degradation in $Li_7La_3Zr_2O_{12}$

This chapter contains results and discussion of several investigations into the sensitivity towards moisture of doped $Li_7La_3Zr_2O_{12}$ (LLZO). A method to induce proton-lithium (H^+/Li^+) exchange using liquid H_2O in powder and pellet samples is introduced, and various characterisation techniques are described - nuclear magnetic resonance (NMR), inductively coupled plasma – optical emission spectroscopy (ICP-OES) and X-ray diffraction (XRD) to assess the effect of H^+/Li^+ exchange on structure and Li content. Additionally, diffusion coefficients for chemical and tracer diffusion of protons are found using a depth-profiling method with secondary ion mass spectrometry (SIMS) and an isotopic exchange route using isotopically-labelled D_2O. The effect of the proton exchange on the transport properties including conductivity and polarisation resistance of the pellets using electrochemical impedance spectroscopy (EIS) analysis is discussed.

Finally, the phenomenon of corrosion layer formation of LiOH and Li_2CO_3 on the surface of the LLZO pellets is explored, which is analysed using different surface analysis techniques for different probing depths: X-ray photoelectron spectroscopy (XPS), low energy ion scattering (LEIS), and SIMS.

The water-garnet interaction is important to understand from a fundamental perspective, in particular with regards to the effect on bulk and interfacial transport properties in all-solid-state systems- but it is also of interest to assess the suitability of the garnet electrolyte to be used in aqueous battery systems as a separator (and also in Li-O_2 or Li-CO_2 systems with an air cathode), and to understand the stability in air during handling and operation. Aqueous batteries offer several advantages over organic electrolyte-based cells including low cost, reliability, and the ability to be used at with air-cathode in Li-O_2 cells (owing to their stability in air) [77]. Aqueous liquid electrolytes typically have a higher lithium ion conductivity than their non-aqueous alternatives and do not suffer from the flammability issues associated with using an organic liquid electrolyte. The use of a 'mediator-ion' solid electrolyte in such aqueous systems could enable the separation of catholyte and anolyte components whilst allowing selective alkali-metal-ion transport. If successful, this would circumvent problems associated with aqueous batteries in which soluble intermediates are formed and lead to chemical crossover between anode and

cathode, resulting in self-discharge, poor efficiency and the evolution of H_2 and O_2 gas (resulting from degradation of H_2O and the electrodes). An understanding of the transport properties of the proton-exchanged material could also enable us to test the ability of the garnet to act as a mixed proton and lithium conductor.

6.1 H_2O Reactivity of LLZO Powder

In the first set of experiments, powder samples were exposed to moisture-rich environments in the form of liquid H_2O at room temperature (RT) and at 100 °C, to promote a bulk exchange of H^+ and Li^+ in the material. It was noted by a simple pH paper test that after 30 minutes RT immersion in H_2O, the pH increased from 7 to 8. XRD was used to determine the crystallographic phase of the resulting exchanged powders. Proton and lithium NMR were used to probe the local environment of the Li^+ and H^+ ions and to determine their mobility in the bulk material.

6.1.1 Powder Characterisation

Powder samples of nominal composition $Ga_{0.15}Li_{6.55}La_3Zr_2O_{12}$ (Ga0.15-LLZO), with particle size 2 to 20 µm, were mixed with high purity deionised water (resistance 18.2 MΩ cm at 20 °C) with a 1:40 wt% LLZO:H_2O ratio and left stirring for 20 hours at both RT and 100 °C. The samples were filtered through filter paper, rinsed with fresh H_2O to remove soluble LiOH, then dried in an oven at 100 °C before final drying in a Buchi oven under argon. XRD patterns were taken of the milled powder before and after the treatments, using Kapton tape to protect them from the atmosphere during measurement (Figure 6.1).

The XRD patterns were refined by the Rietveld pattern refinement method [206] (Figure 6.2), but the occupancies of the atoms are fixed in their theoretical positions with no vacancies (with Ga in the tetrahedral 24*d* Li site, and Li occupying 2.8 24*d* sites and 3.6 96*h* sites per formula unit in all cases), as we cannot refine the atomic positions of Li or H using XRD and the quality of the data is insufficient to resolve O atomic positions and vacancies. The goodness of fit parameter, χ^2 (see Chapter 4, Section 4.2.3 for details) is large, owing mainly to the difficulty of fitting the raised background profile from the Kapton tape, with the small peaks lost in the noisy background at low intensities. The possibility of a symmetry change to a noncentrosymmetric $I\bar{4}3d$ space group, as suggested by other groups [159], is not verifiable under the limitations of the quality of the diffraction data here.

The lattice parameter for cubic LLZO ($Ia\bar{3}d$ space group) in the pristine powder is refined as 12.9879(5) Å and for the RT H_2O-immersed powder is 12.985(4) Å, indicating a negligible change in lattice parameter during proton-lithium exchange under these conditions. However, in the 100 °C H_2O sample, the lattice parameter increases slightly to 13.031(4) Å. Likewise, in the pellet exchange experiment, in Section 6.2, the lattice parameter increases from 12.9739(6) Å in the pristine pellet to 12.995(1) Å in a pellet immersed in 100 °C H_2O for 30 minutes (H_2O/30). This increase in lattice parameter in

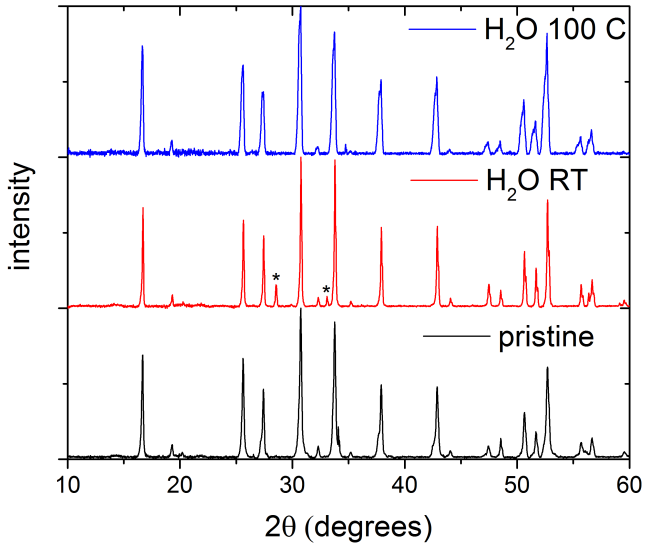


Figure 6.1: Powder XRD patterns before (pristine), and after H_2O reaction of Ga0.15-LLZO at room temperature (RT) and 100 °C. The samples were measured under Kapton tape, with the background subtracted here. * indicates $La_2Zr_2O_7$ peaks.

the 100 °C H_2O-immersed powder indicates a high degree of protonation of the sample and is reported by other groups as being due to the replacement of strong Li-O bonds with weaker O-H—O bonds [124, 164].

The pristine and RT H_2O-immersed powders have a slight Li_2ZrO_3 impurity (space group $C12/c1$), which is found to occupy 3.7 wt% in the pristine and 3.6 wt% in the RT H_2O powders. It would be expected that the 100 °C H_2O-immersed powder would also contain this impurity, but owing to a noisy background in the XRD pattern, fitting the data with this impurity was not possible and yielded a poor fit. Additionally, the presence of pyrochlore $La_2Zr_2O_7$ (space group $Fd\bar{3}m$) is clearly found only in the RT H_2O-immersed powder sample (5.5 wt%).

The formation of $La_2Zr_2O_7$ is usually associated with Li loss in LLZO, so it might be expected that in the RT sample a net loss of lithium occurs, which is not compensated for by the insertion of protons into the lattice. Perhaps at this lower temperature much lower mobilities of the Li^+ and H^+ ions exist, which limits the ability for protons to enter the garnet lattice, or that LiOH forms immediately upon Li ions leaving the garnet lattice - and is not dissolved quickly enough for the LLZO particles to be free for H^+ exchange and incorporation, resulting in a net decrease in total (Li + H) content. Accordingly, no pyrochlore impurity is found in the 100 °C H_2O-immersed powder sample, which might indicate a greater ease of overcoming this potential barrier for proton insertion at this higher temperature. Several reports in the literature describe a number of proton insertion regimes in garnets which vary with temperature [118, 159], ascribing the differences in phase formation as being due to temperature-dependent Li and H dynamics.

ICP analysis was performed on Al-LLZO powders which were allowed to undergo proton-lithium exchange in H_2O at 100 °C. The Al content was found to be 0.09 atoms per

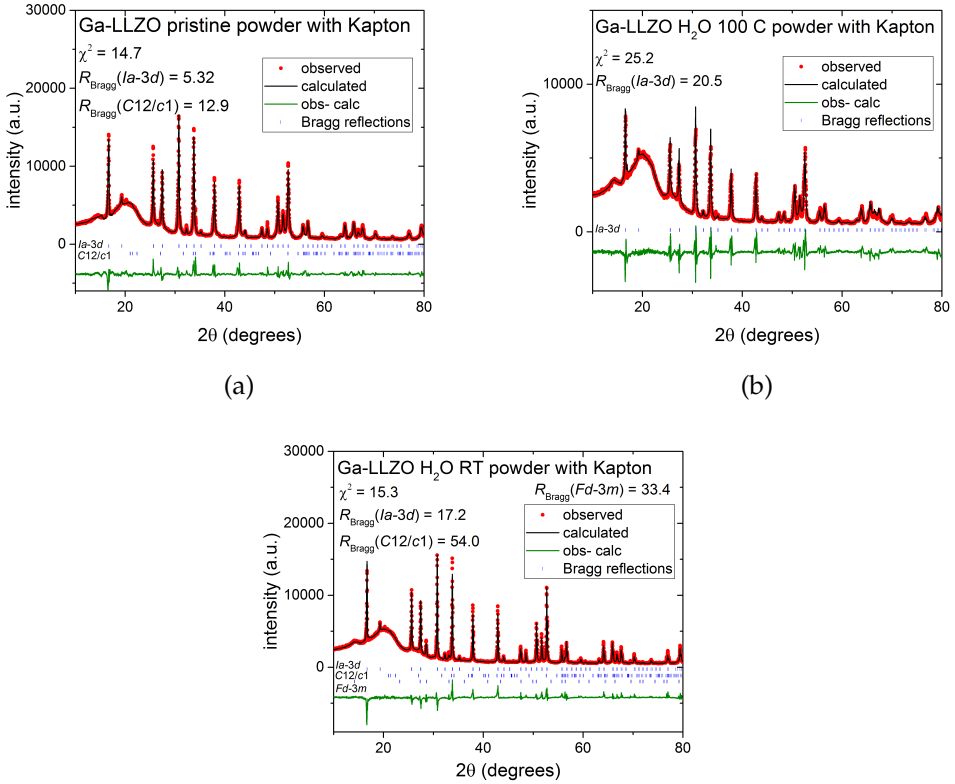


Figure 6.2: Rietveld refinements of powder XRD patterns before and after H_2O reaction of Ga0.15-LLZO, at room temperature (RT) and 100 °C. Figure shows powder XRD patterns measured under Kapton tape on a Panalytical instrument, showing the raised background from the polymer tape. (a) Pristine Ga0.15-LLZO powder, fitted with the cubic $Ia\bar{3}d$ space group and Li_2ZrO_3 ($C12/c1$ space group); (b) Ga0.15-LLZO powder immersed in 100 °C H_2O; (c) Ga-LLZO powder immersed in RT H_2O, fitted with an additional impurity phase, $La_2Zr_2O_7$ ($Fd\bar{3}m$ space group). The goodness of fit for the whole profile, χ^2 and the intensity-based R-factors (R_{Bragg}) for each phase are given.

formula unit (a.p.f.u.), and the corresponding Li content was measured as 5.38 a.p.f.u. The theoretical Li content for the measured Al dopant concentration (assuming substitution at the Li position) is 6.73 a.p.f.u. Hence, the difference in Li content (1.35 a.p.f.u.) might be assumed to be due to H^+ insertion during the exchange process, giving the composition $Li_{5.38}H_{1.35}Al_{0.09}La_3Zr_2O_{12}$, if constant oxygen stoichiometry is assumed. This corresponds to 20 % of Li removed during exchange. Nyman *et al.* [160] found a 20 % Li loss after 30 minutes room temperature exchange in $Li_5La_3Ta_2O_{12}$ powder, whereas Ma *et al.* [164] found a 64 % exchange in Al-LLZO powder in H_2O. It is expected that the extent of H^+/Li^+ exchange in powdered LLZO under these conditions will be greater than in the pellet samples (Section 6.2), owing to the larger surface area available for exchange to occur.

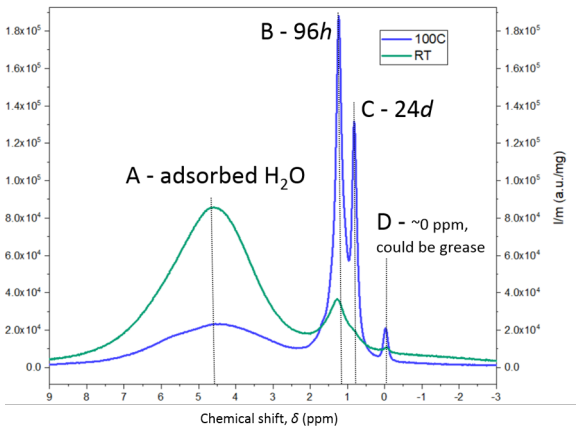


Figure 6.3: ^{1}H NMR spectra of protonated powder Ga0.15-LLZO samples (100 °C and RT H_2O exchange). A, B, C and D indicate different chemical shift δ environments: B is a 96*h* Li site, C a 24*d* Li site, D is possibly grease or dirt. The intensity I is divided by the mass of sample m, on the y-axis.

6.1.2 Nuclear Magnetic Resonance

^{1}H NMR was measured on the water-exchanged powder Ga0.15-LLZO samples (following both RT and 100 °C H_2O exchanges) to probe the proton chemical environments in each case. Temperature-dependent relaxation time measurements (pulsed field gradient NMR) of the protonated samples were also attempted; all NMR measurements here were made by Steffen Emge in Professor Clare Grey's group at Cambridge University. Difficulty with short relaxation times and thus low signal intensity made ^{1}H NMR difficult to interpret; however, as seen in the ^{1}H spectra in Figure 6.3, there is a clear difference between the RT and 100 °C protonated samples, in terms of the intensities of the peaks at different chemical shifts, δ.

The relative intensities and sharpness of each peak differs for the two samples (see Table 6.1 for the normalised intensities). The two sharp peaks seen in the 100 °C exchanged sample correspond to intercalated protons, tentatively assigned to 96*h* and 24*d* Li sites for the labelled peaks B and C, respectively. The most intense peak is associated with the 96*h* site, which is in agreement with literature suggesting a preference for protons to exchange with these Li sites [157, 159]. The chemical shift marked A in Figure 6.3 at 4.65 ppm is close to that of water, so could correspond to adsorbed water in the sample, which is the most populated ^{1}H region in the room temperature protonated powder, suggesting that most of the protons present in the sample are not intercalated in the lattice. This agrees with earlier observations of pyrochlore phases in the room-temperature treated samples and an unchanged lattice parameter after treatment, indicating minimal proton-lithium exchange (see Section 6.1.1).

The pulsed field gradient (PFG) NMR (Figure 6.4) shows no visible decay of the ^{7}Li signal, which indicates that the Li mobility has decreased significantly to the extent where it cannot be measured. The lower limit for the measurable diffusion coefficient under the setup here is approximately 10^{-14} to 10^{-15} m^2 s^{-1}. The Li diffusivity was measured using PFG NMR on the pristine sample (see Chapter 7, Section 7.3.1) and found to be of the

Table 6.1: Normalised peak intensities of chemical shifts A to D in Figure 6.3 of ^{1}H NMR on protonated powder Ga0.15-LLZO samples (100 °C and RT H_2O exchange). The intensity of the signal is divided by the mass of the sample, where the peak integral is normalised against the peak with the lowest intensity in the spectrum.

	A	B	C	D
Chemical shift (ppm)	4.65	1.31	0.87	-0.04
Normalised intensities: RT	198.91	11.65	2.54	1
Normalised intensities: 100 °C	62.63	38.00	16.57	1.76

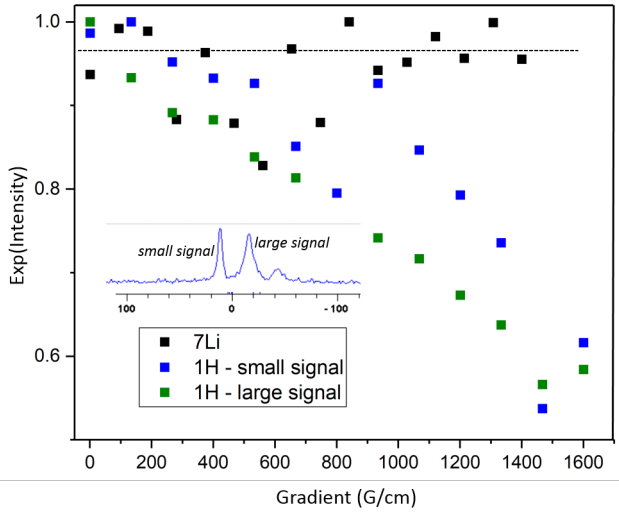


Figure 6.4: ^{1}H and ^{7}Li PFG NMR on 100 °C protonated Ga0.15-LLZO powder. The 'small signal' data points correspond to a higher chemical shift peak of the inset PFG static NMR spectrum (possibly adsorbed water), the 'large signal' data points correspond to a lower shift (possibly the sum of the intercalated protons).

order 10^{-13} m^2 s^{-1}, indicating a clear drop in mobility following proton exchange. The ^{1}H PFG NMR signals show decay processes, which we have attempted to fit to calculate diffusion coefficients, with values the order of 10^{-12} m^2 s^{-1} (see Table A.1). This is several orders of magnitude higher than the diffusivities calculated in the protonated pellets from SIMS experiments (see later, Section 6.2). However, the NMR diffusion measurements on the protons are complicated to analyse due to diffracted diffusion processes [66, 262] (see Appendix A.2, Figure A.5), and thus should be interpreted with caution.

6.2 Proton Exchange and Diffusion in LLZO Pellets

These experiments were designed to reveal the chemical degradation processes involved during proton-lithium exchange in LLZO pellets, focussing specifically on the formation of a protonated garnet region, as separated from LiOH and Li_2CO_3 corrosion layer

formation, through the removal of these water-soluble corrosion products during the experimental process. This was verified by LEIS analysis of the surface of the washed pellets (Section 6.4.1), which showed negligible surface LiOH. Pellets of LLZO were immersed in a heated water bath and the chemical reactivity was investigated using focussed ion beam (FIB)-SIMS depth-profiling. The transport properties of the degraded pellets were tested using isotopic labelling followed by SIMS analysis (Section 6.2.5), as well as impedance spectroscopy (Section 6.3).

6.2.1 Experimental Method

Ga0.15-LLZO pellets (nominal composition $Li_{6.55}Ga_{0.15}La_3Zr_2O_{12}$), polished to 4000 grit SiC paper were immersed in a liquid deionised water bath at 100 °C for 5, 15 and 30 minutes to study the proton-lithium exchange process and chemical diffusion of protons. For the tracer diffusion experiments, these pre-treated H_2O samples were dropped in liquid D_2O (99.9+% isotope fraction, Alfa Aesar) under the same temperature but with a duration one fifth that of the pre-treatment in H_2O, to favour a tracer-, not chemical diffusion of D^+ [263]. After immersion in liquid H_2O and/or D_2O, samples were quenched to room temperature and dried under dynamic vacuum for 10 minutes in the glove box antechamber before transferring to the glove box prior to FIB-SIMS and EIS analysis.

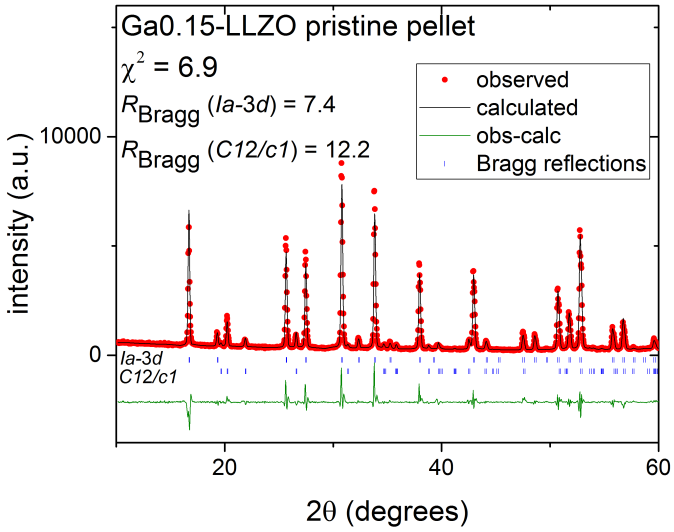
High temperature exchanges were considered more useful for studying the chemical and tracer diffusion, as the samples could be hypothetically 'quenched' at RT (i.e. during measurement) - reducing the motion of the ions (an effect which would be more pronounced for larger values of activation energy, E_a). This was only an approximation, as the true mobility of the protons at RT is not proven. Additionally, higher temperatures enable accelerated moisture ageing, to increase the kinetics of the reaction and to promote the formation of a large and 'quantifiable' degradation layer enabling us to probe macroscopic effects with EIS. The exposure time was varied to determine the progress of the exchange process product formation to different depths.

6.2.2 Sample Characterisation

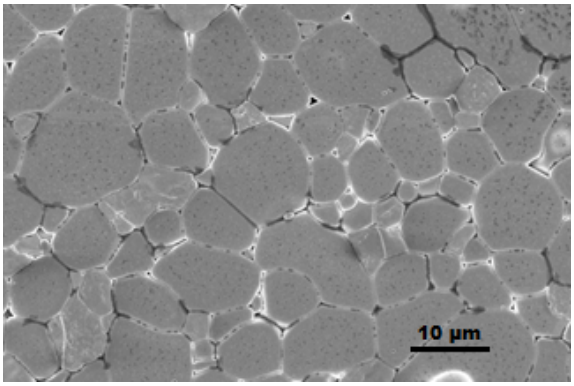
Pellets of Ga0.15-LLZO of relative densities greater than 90 % as calculated geometrically and by Archimedes' method were produced. The XRD pattern, taken of the pellet whilst spinning (Figure 6.5a), shows a cubic phase, with space group $Ia\bar{3}d$, and a Li_2ZrO_3 impurity (15.2 wt% at the near-surface measured region as refined by the Rietveld method).

Grain boundaries and grain morphology can be revealed on thermal treatment of the pellet (thermal etching at 900 °C, see SEM image Figure 6.5b), showing a bimodal distribution of grain sizes, some up to 20 µm in diameter, others of the order of a few micrometres. The grain boundaries appear to be composed of a secondary phase which is expected to be amorphous as it is not detected by XRD, and are likely to be formed as a result of liquid-phase sintering of the pellet, a process which has been discussed previously (Chapter 4, Section 4.1.2 and Chapter 5, and the phase diagram in Figure 4.1) [121, 168].

By using small crater sizes (7 µm by 7 µm) in the FIB-SIMS instrument through selected area analysis using secondary electron and ion imaging, areas within grains of Ga0.15-LLZO were selected for depth-profiling (verified after milling to check for grain boundaries or inhomogeneities within the crater area), thus selectively following in-grain diffusion, eliminating grain boundary and impurity contributions.



(a)



(b)

Figure 6.5: Pristine Ga0.15-LLZO pellet characterisation by XRD and SEM. (a) Pellet XRD pattern of Ga0.15-LLZO showing Li_2ZrO_3 ($C12/c1$ space group) and cubic garnet $Ia\bar{3}d$ phases refined using Rietveld fitting. The goodness of fit for the whole profile, χ^2 and the intensity-based R-factors (R_{Bragg}) for each phase are given. (b) SEM secondary electron image of thermally etched Ga0.15-LLZO showing bimodal grain distribution and Li_2ZrO_3 impurity grains.

6.2.3 Focussed Ion Beam - Secondary Ion Mass Spectrometry

FIB-SIMS was used to image the samples and record mass spectra from the surface of the materials, and used in depth-profiling mode to obtain chemical information as a function of depth, detecting negative and positive secondary ion signals simultaneously. Transfer of the pre-mounted samples was done by sealing the samples in a container in

the glove box, and transferring to the SIMS chamber before immediately pumping down to high vacuum (with a pressure less than 1×10^{-6} mbar). This meant that the samples for analysis were exposed to ambient air for a matter of no more than a few minutes.

In the chemical diffusion and proton exchange experiments (H_2O - only samples), $^{17}(OH)^-$ and $^1H^-$ secondary ions were used to characterise diffusion profiles as an indicator of H^+ diffusion into the garnets. The higher mass species $^{17}(OH)^-$ is preferentially used in the data analysis on the basis of its higher intensity due to the nature of the quadrupole FIB-SIMS detector, which can have interferences from scattered ions and stray electrons at the lower-mass end of the spectrum. The intensity ratio ($^{17}(OH)^-/^{16}O^-$) enables the diffusant concentration of protons to be profiled since the yield of $^{16}O^-$ in the Ga0.15-LLZO matrix is expected to be constant. LaO^+ secondary ions were profiled as a high intensity positive ion marker of the corresponding LLZO matrix species. To correct for changes in sputter rate resulting from sputtering through modified layers in the garnet, the positive ion intensities can be given as a ratio to the $^{69}Ga^+$ secondary ion intensity. The $^{69}Ga^+$ signal comprises of contributions from both the primary ion beam of the instrument (the main contributor) and the gallium dopant in Ga0.15-LLZO. This was verified in a separate experiment in which an isotopically-pure (99 %) source of ^{69}Ga was used as the primary ion beam source, and Ga in Ga0.15-LLZO was monitored by profiling the ^{71}Ga isotope (40 % natural abundance), giving a $^{71}Ga^+/^{69}Ga^+$ ratio of 0.02 in LLZO.

Reference signals for all secondary ions recorded were established by collecting depth profiles and mass spectra on a pristine Ga0.15-LLZO reference sample with each analysis session using the same conditions. The 'bulk' non-protonated Ga0.15-LLZO region of the water-treated samples (at the end of the depth profiles) were thus verified to have H^- and OH^- secondary ion intensities below their reference levels in the pristine sample and could be thus used as internal standards for unprotonated Ga0.15-LLZO within the depth profiles.

6.2.4 H_2O Reaction and Chemical Diffusion

The reaction of Ga0.15-LLZO with (atmospheric) H_2O to form LiOH at the surface of the material due to the brief exposure to ambient air during the transfer of the sample from the glove box to the SIMS chamber, can be seen in the elevated counts for Li^+, OH^- and H^- secondary ions compared to the bulk (>0.1 µm, where the secondary ion signals are stable) in the SIMS depth profiles of the pristine pellet (Figures 6.6a and 6.6b). This is also seen in the profiles of $Li^+/(Li^+, bulk)$ and $H^-/(H^-, bulk)$ for the pristine sample (Figure 6.6c), showing a flat profile after an initial elevated ratio at the surface. This is expected to be absent in the samples measured with EIS, owing to the absence of air exposure during cell setup and measurement.

Figure 6.7 shows the secondary electron and positive ion images of the pellets following immersion in liquid H_2O. It can be seen that pellets maintain their mechanical integrity; however, areas which appear to be located along the grain boundaries appear darker in the electron images, suggesting a lower secondary electron yield in these regions

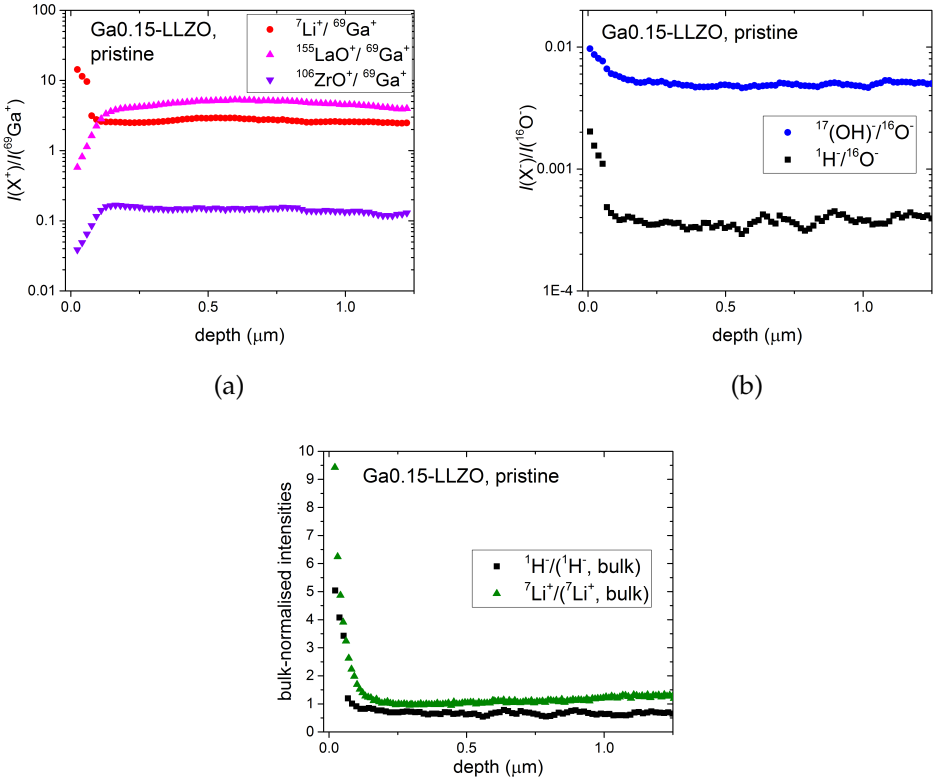


Figure 6.6: FIB-SIMS depth profiles in pristine Ga0.15-LLZO; (a) positive secondary ions $^{7}Li^{+}$ and $^{155}(LaO)^{+}$ and $^{106}(ZrO)^{+}$ with intensities I, divided by the intensity of $^{69}Ga^{+}$ secondary ions; (b) negative ions $^{17}(OH)^{-}$ and $^{1}H^{-}$ intensities divided by the intensity of $^{16}O^{-}$ secondary ions; (c) $^{7}Li^{+}$ and $^{1}H^{-}$ intensities, divided by the intensity in the bulk (taken at end of depth profile). The crater size is 7 µm by 7 µm and the primary ion beam current is 590 pA, giving a dose rate of 7.5x10^{15} ions cm^{-2} s^{-1}.

after exposure to water. This may be due to a change in the composition of the Al_2O_3-Li_2O eutectic in the grain boundary regions on reaction with H_2O [167]. This will be correlated later (Section 6.3) to a three orders of magnitude increment of the resistance in the grain boundaries upon reaction with H_2O.

Figure 6.8 shows two surface secondary negative ion mass spectra of an area 100 µm by 100 µm on the pristine and 30 minutes H_2O-immersion at 100 °C pellets (H_2O/30).[1] Both pellets have a strong $^{16}O^{-}$ peak associated with oxygen in the garnet structure, but the pristine pellet has noticeable extra peaks associated with impurities indicated by $^{17}(OH)^{-}$, $^{12}C^{-}$ and $^{13}(CH)^{-}$ species in the mass spectrum which are likely to have been introduced during the handling and sample transfer in air. As discussed previously, LiOH has been reported to form on the surface of LLZO during air exposure, slowly transforming to Li_2CO_3 [168]. LiOH is soluble in water, and given the large excess of H_2O used during pellet immersion for the exchange experiments, the LiOH product can be expected to be

[1]For brevity, future terminology such as H_2O/30 is used to indicate 'after 30 minutes of immersion in H_2O at 100 °C'; likewise H_2O/30/D_2O/6 means 'after 30 minutes of immersion in H_2O followed by 6 minutes of immersion in D_2O at 100 °C', in Section 6.2.5.

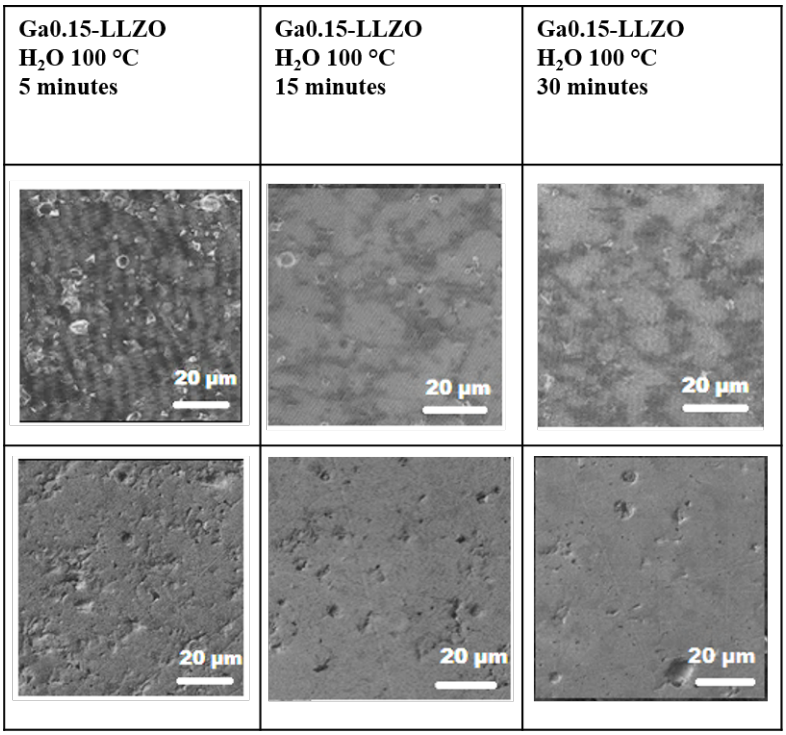
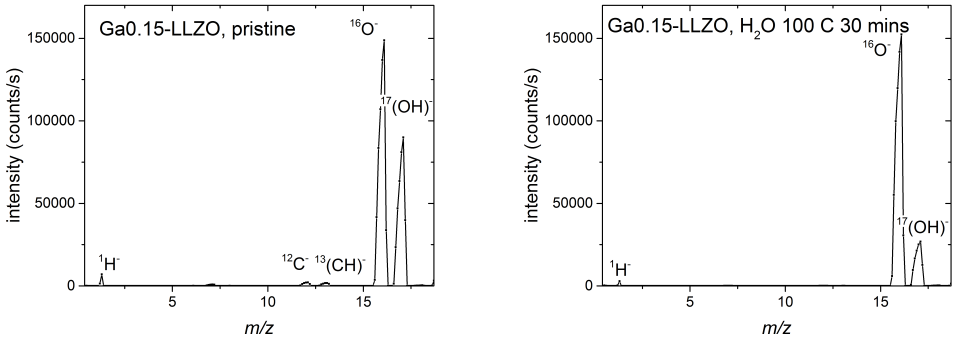


Figure 6.7: Secondary electron (top row) and secondary positive ion (bottom row) images of H_2O-immersed Ga0.15-LLZO pellets at 100 °C for three different immersion times.

washed off in the H_2O-exposed sample. Hence the appearance in particular of the OH^- peak is more pronounced in the surface of the pristine sample than the water-bath sample (the $^{17}(OH)^-/^{16}O^-$ ratios for these samples are 0.60 and 0.18, respectively).



(a) (b)

Figure 6.8: Negative secondary ion mass spectra of (a) pristine and (b) H_2O/30 Ga0.15-LLZO, taken with 500 pA primary ion beam current over an area 100 µm by 100 µm, giving a dose rate of $3.1x10^{13}$ ions cm^{-2} s^{-1}.

On exposing the samples to liquid H_2O at 100 °C, the in-grain FIB-SIMS depth profiles show four regions of differing secondary ion intensity and behaviour (Figure 6.9 shows the profiles for the 30 minutes H_2O-immersed sample, 'H_2O/30'). The first region, up to about 0.15 µm depth in the H_2O/30 sample, can be described by high ion counts of Li^+, OH^- and H^- secondary ions. This first region is likely to be caused by the front of

the H^+/Li^+ exchange process and the formation of a thin corrosion layer of LiOH at the surface, segregated during the transfer of the sample in air to the FIB-SIMS instrument. The depth of this region is in reality unlikely to be 0.15 µm, as it likely has a much lower density and thus higher sputter rate than LLZO. The steady state regime for dynamic SIMS (dose > 10^{15} ions cm^{-2}) should have been reached in this region (and from the beginning of the sputter process), as a dose rate of 7.5x10^{15} ions cm^{-2} s^{-1} is used.

The second region between 0.15 µm and 1.35 µm (total thickness 1.2 µm) shows a plateau in the intensity ratios of Li^+, OH^- and H^- secondary ions indicating a region of equilibrated H^+ concentration, in the form of a stable H-Ga0.15-LLZO phase. At the edge of this region, at about 1 µm depth, the $Li^+/(Li^+$, bulk) ratio starts to gently rise with depth, Figure 6.9b, showing a diffusion profile of Li from the Ga0.15-LLZO into the H-Ga0.15-LLZO region. This continues until about 2 µm depth and is accompanied by decreasing OH^- and H^- counts (Figures 6.9a and 6.9b). This observed behaviour is ascribed to a chemical diffusion of protons into Ga0.15-LLZO. After 2 µm, flat profiles are seen for all species, indicating a region of unmodified, non-protonated Ga0.15-LLZO (with approaching-background values for OH^- and H^- counts). A schematic diagram of these regions is shown later in Figure 6.17, and depths for each region in each sample are summarised in Table 6.2.

The H-Ga0.15-LLZO region between 0.15 µm and 1.35 µm, given the stoichiometry, should not change. However, in this region, the LaO^+ secondary ion counts are lower relative to the counts in the bulk Ga0.15-LLZO (Figure 6.9c). This does not necessarily mean a lower concentration of La in the material, as the secondary ion yield during SIMS depends on a number of factors outlined in the SIMS equation (see Chapter 4, Equation 4.22), including the ionisation factor of each species under the primary ion beam (which is an unknown here and depends on the matrix behaviour), and the sputter rate. It might be that these regions of lower LaO^+ counts are altered regions with different ionisation (yield) behaviour under the Ga^+ primary ion beam with respect to bulk Ga0.15-LLZO, which would support the proposal that this region corresponds to an area of H-Ga0.15-LLZO. The ZrO^+/LaO^+ ratio shown in Figure 6.9c is stable with depth, indicating there is not a change in stoichiometry of the garnet following H_2O immersion associated with the formation of the H-Ga0.15-LLZO phase, but rather the yield of ZrO^+ and LaO^+ is suppressed by the presence of H.

The possibility of a secondary phase in the top 1 to 2 µm of the $H_2O/30$ sample can also be ruled out by XRD patterns of the pellets. The sampling depth of X-ray diffraction is about 5 µm, and the XRD pattern in Figure 6.10 shows no additional crystalline secondary phases (although a slight background at low angles is present, likely caused by scattering of X-rays by the pellet edge), confirming that the cubic garnet structure is maintained following the H^+/Li^+ exchange. This is in agreement with previous reports of the stability of the cubic $Ia\bar{3}d$ phase following proton exchange [164, 165]. A symmetry change to the noncentrosymmetric space group, $I\bar{4}3d$, as suggested by some authors for deep proton-lithium exchange and high temperature treatment [116, 264], is again not able to be verified here owing to the limitations of the quality of the diffraction data.

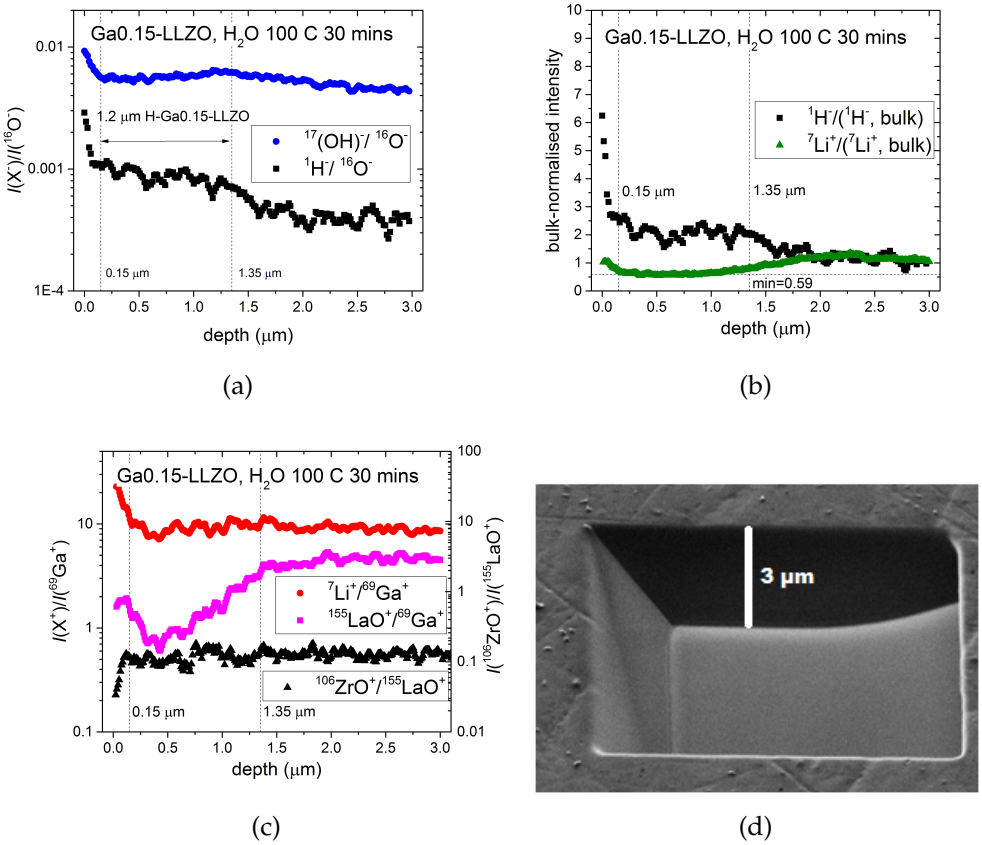


Figure 6.9: FIB-SIMS depth profiles of H_2O/30 Ga0.15-LLZO. (a) Negative secondary ions $^{17}(OH)^-$ and $^1H^-$ with intensities I, divided by the intensity of $^{16}O^-$ secondary ions; (b) $^7Li^+$ and $^1H^-$ intensities, divided by the intensity in the bulk (taken at end of depth profile); (c) $^7Li^+$ and $^{155}(LaO)^+$ intensities divided by the intensity of $^{69}Ga^+$ and $^{106}(ZrO)^+$ intensity divided by the intensity of $^{155}(LaO)^+$ secondary ions; and (e) secondary electron image of the depth profile crater, showing the depth measurement with sample at a 45° tilt. The crater size is 7 µm by 7 µm and the primary ion beam current is 590 pA, giving a dose rate of 7.5x10^{15} ions cm^{-2} s^{-1}.

Increasing the immersion time in liquid H_2O at 100 °C leads to an increase in the thickness of the H-Ga0.15-LLZO region formed, within the timescales of this experiment (see Table 6.2 and dashed profile Figure 6.12a). Immersion for 5 minutes in H_2O (H_2O/5, Figure 6.11a) gives a H-Ga0.15-LLZO layer 0.07 µm thick. After 15 minutes exposure, this H-Ga0.15-LLZO region increases in length to 0.72 µm thickness (H_2O/15, Figure 6.11b). After 30 minutes, this increases further to 1.2 µm thickness (seen already in Figure 6.9a).

As previously mentioned, the diffusion tails in the negative ion profiles can be interpreted as the diffusion of protons into Ga0.15-LLZO, which are accompanied by a diffusion of lithium from the bulk through the H-Ga0.15-LLZO in the opposite direction to the protons. Chemical diffusion is defined as occurring in a presence of concentration (or chemical potential) gradient and it results in net transport of mass. The motion of H^+ into the sample during H^+/Li^+ exchange can be said to be a chemical diffusion process. By normalising the OH^- and H^- secondary ion counts after the H^+/Li^+ exchange to their bulk values (taken as their value at the end of the depth profile), we can

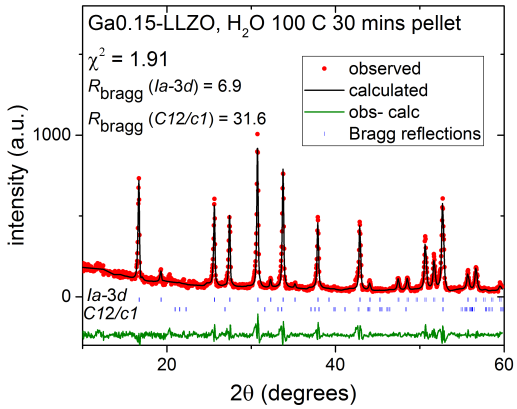
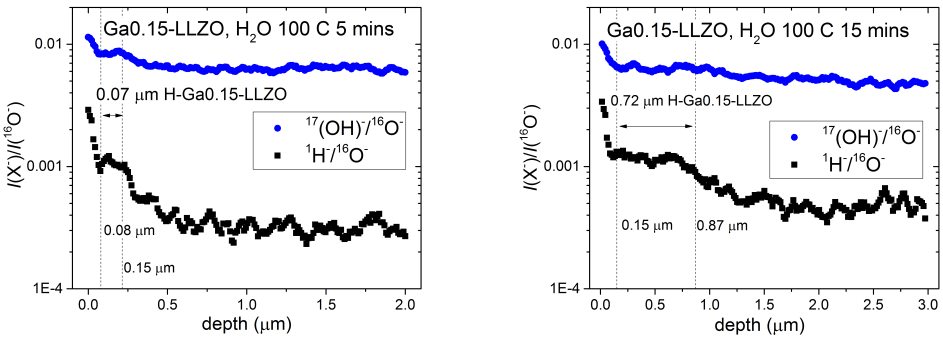


Figure 6.10: XRD pattern on H_2O/30 Ga0.15-LLZO pellet showing Li_2ZrO_3 ($C12/c1$ space group) and cubic garnet $Ia\bar{3}d$ phases refined using Rietveld fitting. The goodness of fit for the whole profile, χ^2 and the intensity-based R-factors (R_{Bragg}) for each phase are given.

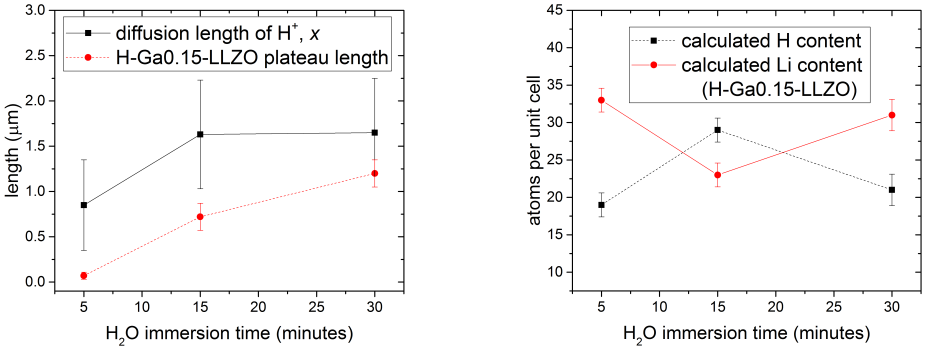


(a) (b)

Figure 6.11: Negative secondary ions $^{17}(OH)^-$ and $^1H^-$ with intensities I, divided by the intensity of $^{16}O^-$ secondary ions in FIB-SIMS depth profiles of (a) H_2O/5 and (b) H_2O/15 Ga0.15-LLZO pellets. The crater size is 7 µm by 7 µm and the primary ion beam current is 590 pA, giving a dose rate of 7.5x10^{15} ions cm^{-2} s^{-1}.

estimate the diffusion length of the protons (distance at which background concentration is reached) within Ga0.15-LLZO by subtracting the beginnings of the diffusion tail (after the H-Ga0.15-LLZO region) from the depth at which the bulk (or 'background') OH^- or H^- counts are reached. The resulting lengths (x) are 0.85 µm, 1.63 µm and 1.65 µm, for 5, 15 and 30 minutes immersion (t), respectively (Figure 6.12a), corresponding to a chemical diffusivity, $D_C(H^+)$, of the order of 10^{-16} m^2 s^{-1} at 100 °C in all three samples, using the relationship $x = 4\sqrt{Dt}$, assuming Crank's solution for diffusion (as outlined in Chapter 2) and setting D=D_C).

The number of H and Li atoms per unit cell in H-Ga0.15-LLZO can also be estimated by using bulk Ga0.15-LLZO as an internal standard, calculating the ratio of Li counts in H-Ga0.15-LLZO (i.e. the minimum Li value here) to the Li counts in the bulk (assumed to be equivalent to a composition $Li_{6.55}Ga_{0.15}H_0La_3Zr_2O_{12}$, or $Li_{52.4}Ga_{1.2}H_0La_{24}Zr_{16}O_{96}$



(a) (b)

Figure 6.12: Plots showing (a) the measured length of the H-Ga0.15-LLZO region (red dashed line) and the chemical diffusion length of H^+ (black solid line) and (b) the calculated H and Li content in H-Ga0.15-LLZO (red and black, respectively), for the H_2O-immersed Ga0.15-LLZO pellets over different times.

in the unit cell). The difference in the number of Li in the bulk versus H-Ga0.15-LLZO is expected to be compensated for by H. See Table 6.2 for a summary of these values.

By invoking the Nernst-Einstein relationship for conductivity-diffusivity (Equation 6.1), where k is Boltzmann's constant, T is the temperature and q is the effective charge of the carrier, and the diffusivity is the EIS-derived value D^σ:

$$D^\sigma = \frac{\sigma kT}{nq^2} \tag{6.1}$$

using the value for the number of charge carriers, N, as the number of protons as predicted above (and $n = N/\text{unit cell volume}$), we can obtain estimates of the proton conductivity σ in the LLZO samples, which gives a mean value of approximately $8 \times 10^{-8}\,\text{S}\,\text{cm}^{-1}$.

Table 6.2: Overview of calculated values for the 100 °C H_2O-immersed Ga0.15-LLZO pellets. 'min' and 'max' denote the lowest and highest values, respectively.

	Ga0.15-LLZO H_2O/5	**Ga0.15-LLZO H_2O/15**	**Ga0.15-LLZO H_2O/30**
H_2O immersion time (minutes)	5	15	30
Corrosion layer LiOH thickness (µm)	0.08 ± 0.02	0.15 ± 0.05	0.15 ± 0.05
H-Ga0.15-LLZO end depth (µm)	0.15 ± 0.02	0.87 ± 0.10	1.35 ± 0.10
H-Ga0.15-LLZO length (µm)	0.07 ± 0.04	0.72 ± 0.15	1.20 ± 0.15
OH^-, H^- background counts depth reached (µm)	1.0 ± 0.5	2.5 ± 0.5	3.0 ± 0.5
'Diffusion length' x of protons (µm)	0.85 ± 0.5	1.63 ± 0.6	1.65 ± 0.6
Minimum value of $Li^+/(Li^+$, bulk) in H-Ga0.15-LLZO	0.64 ± 0.03	0.44 ± 0.03	0.59 ± 0.04
Calculated H and Li content per unit cell (N) in H-Ga0.15-LLZO	Li33H19	Li23H29	Li31H21
Proton diffusivity, $D_C(H^+)$ at 100 °C, calculated from $x = 4\sqrt{D_C t}$ ($m^2\,s^{-1}$)	$2x10^{-16}$ (min= $2x10^{-17}$; max=$4x10^{-16}$)	$2x10^{-16}$ (min= $7x10^{-17}$; max=$4x10^{-16}$)	$1x10^{-16}$ (min= $4x10^{-17}$; max=$2x10^{-16}$)
Proton conductivity σ_H at 100 °C, calculated from Nernst-Einstein relation ($S\,cm^{-1}$)	$7x10^{-8}$ (min= $1x10^{-8}$; max=$2x10^{-7}$)	$1x10^{-7}$ (min= $5x10^{-8}$; max=$3x10^{-7}$)	$5x10^{-8}$ (min= $2x10^{-8}$; max=$9x10^{-8}$)

Points of note include the result that, in addition to the growth of the H-Ga0.15-LLZO region with immersion time, the Li content changes, and with it the calculated H content. After 5 minutes immersion in H_2O ($H_2O/5$), the Li content in the H-Ga0.15-LLZO region is equal to N(Li) of 33 atoms per unit cell. After 15 minutes ($H_2O/15$), this drops to 23 (with N(H) increasing to 29), but after 30 minutes, falls to 31 (Figure 6.12b). It is difficult to say if these fluctuations are meaningful or whether they are part of a larger trend which we are unable to see due to the small sampling size. The experiment would need to be continued with much longer immersion times to reveal this.

However, if these changes are meaningful, the observed Li contents for these three samples might be explained by a fast initial exchange step, in which Li^+ exchanges with H^+ in the water and forms an initial, unequilibrated H-Ga0.15-LLZO garnet region (seen after 5 minutes). With time, this region becomes enriched with protons, diffusing under a chemical gradient (15 minutes). Eventually, H-Ga0.15-LLZO becomes enriched in Li and depleted in H as a result of extension of the diffusion front of protons into bulk Ga0.15-LLZO and the counter flux of lithium. It might be expected that at some given time, under these particular exchange conditions, an equilibrium is reached, whereby the advancement of the protonated front is stopped (H-Ga0.15-LLZO stops growing) and the H and Li content in H-Ga0.15-LLZO reaches an equilibrium (or fixed value).

The calculated chemical diffusion coefficient of protons, $D_C(H^+)$, in Ga0.15-LLZO obtained from the diffusion length x, is of the same order of magnitude ($10^{-16}\,m^2\,s^{-1}$) at 100 °C for each sample. The calculated conductivity σ_H of the protons in H-Ga0.15-LLZO under the experimental conditions here, from $D_C(H^+)$ and N, comes to around $8 \times 10^{-8}\,S\,cm^{-1}$, which 4-5 orders of magnitude lower than the Li conductivity at room temperature in pristine Ga0.15-LLZO ($10^{-3}\,S\,cm^{-1}$). By using an activation energy value of 0.2 eV from EIS measurements, this gives a Li conductivity of the order of $10^{-2}\,S\,cm^{-1}$ at 100 °C in pristine Ga0.15-LLZO, which is 6 orders of magnitude higher than the proton conductivity at this temperature from the diffusion length measurement found in this experiment (see Table 6.3).

Table 6.3: Measured and calculated transport properties of Li^+ and H^+ in pristine Ga0.15-LLZO and $H_2O/30$ H-Ga0.15-LLZO.

	Ga0.15-LLZO pristine	**H-Ga0.15-LLZO $H_2O/30$**
$D_C(H^+)$ 100 °C ($m^2\,s^{-1}$)	-	$\sim 10^{-17}$
σ_H 100 °C ($S\,cm^{-1}$)	-	$\sim 10^{-8}$
σ_{Li} RT ($S\,cm^{-1}$)	$\sim 10^{-3}$	-
σ_{Li} 100 °C ($S\,cm^{-1}$)	$\sim 10^{-2}$	-

Table 6.3 shows that the proton mobility in the exchanged sample is much slower than the Li mobility in pristine Ga0.15-LLZO at 100 °C, which might explain the formation of a reasonably sharp H-Ga0.15-LLZO junction during the proton exchange. There is

currently very little literature on diffusivity of protons in the lithium-conducting garnet ceramics; however, molecular dynamics simulations by Yow *et al.* [124] estimated that for a protonated sample $Li_{6.5}H_{0.5}La_3Zr_2O_{12}$, a proton conductivity σ_H of 8.5×10^{-7} S cm^{-1} at 100 °C with an activation energy of 0.31 eV. This is in reasonable agreement with our extracted values from the diffusion length. These values here are several orders lower than the diffusivity calculated from ^{1}H PFG NMR on the protonated powders; however, the interpretation of the NMR data is difficult as discussed previously (Section 8.3.3), and there are likely to be large differences between the powder and pellet samples in terms of proton content and ionic mobility.

6.2.5 D_2O Reaction and Tracer Diffusion

Tracer diffusion was used to probe the inherent diffusivity of protons in the sample once H^+/Li^+ exchange has occurred, using D_2O as a source of D^+. Tracer diffusion, with the diffusion coefficient D^* as described in Chapter 2, Section 2.2, is a spontaneous mixing of molecules taking place in the absence of a concentration (or chemical potential) gradient. This type of diffusion can be followed using isotopic tracers, hence the name. The tracer diffusion is usually assumed to be identical to self-diffusion (assuming no significant isotopic effect), and takes place under equilibrium.

In these experiments the H_2O - immersed samples were subsequently immersed in liquid D_2O at 100 °C for a time one-fifth that of their immersion time in H_2O. Figure 6.13 shows a surface negative ion mass spectrum of $H_2O/30/D_2O/6$. In addition to the peaks seen in the $H_2O/30$ sample (Figure 6.8b), there appears two extra peaks for the secondary ion species $^2D^-$ and $^{18}(OD)^-$. The minimum increment used here is too large (0.1 atomic mass units) to separate the intensities resulting from $^{18}O^-$ minor isotope and $^{18}(OD)^-$ secondary ions; however, we can verify the presence of the mass/charge (m/z) 18 peak as being due to $^{18}(OD)^-$ secondary ions, by noting the m/z 18/16 ratio is 1.5 %, well above the natural abundance level for ^{18}O (0.2 %) [265], so we can attribute this to the presence of D^+ in the sample.

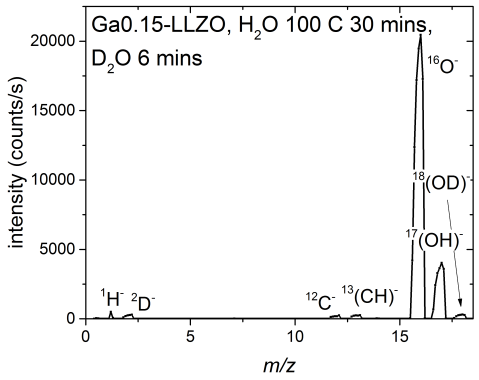
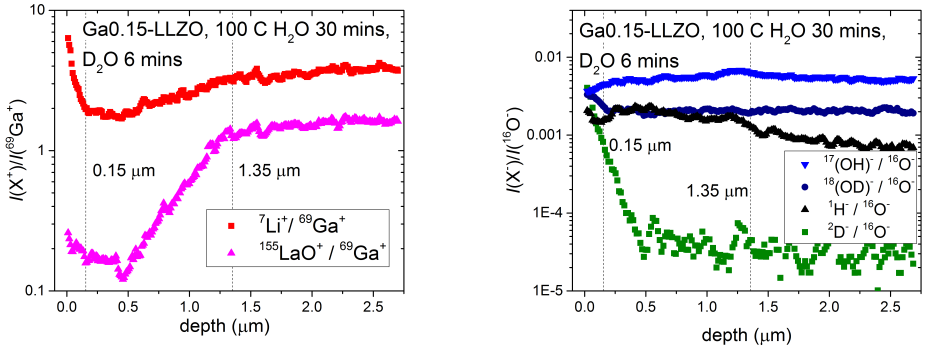


Figure 6.13: Negative secondary ion mass spectrum of $H_2O/30/D_2O/6$ Ga0.15-LLZO, taken with 113 pA primary ion beam current over an area 100 µm by 100 µm, giving a dose rate of 7.1x10^{12} ions cm^{-2} s^{-1}. The mass to charge m/z 18/16 ratio is 1.5 %.



(a) (b)

Figure 6.14: FIB-SIMS depth profiles of $H_2O/30/D_2O/6$ Ga0.15-LLZO. (a) Positive secondary ions $^{7}Li^{+}$ and $^{155}(LaO)^{+}$ with intensities I, divided by the intensity of $^{69}Ga^{+}$; (b) negative secondary ions $^{17}(OH)^{-}$, $^{18}(OD)^{-}$, $^{1}H^{-}$ and $^{2}D^{-}$ intensities divided by the intensity of $^{16}O^{-}$ secondary ions. The crater size is 7 µm by 7 µm and the primary ion beam current is 590 pA, giving a dose rate of $7.5x10^{15}$ ions cm^{-2} s^{-1}.

As in the H_2O-immersed samples, the shape of the secondary ion profiles (Figure 6.14) show an initial surface region of high Li^{+}, OH^{-} and H^{-} intensity (and additionally OD^{-} and D^{-}) caused by a corrosion layer, followed by a plateau region corresponding to H-Ga0.15-LLZO, which eventually changes to bulk Ga0.15-LLZO. The length of the plateau region H-Ga0.15-LLZO is unchanged from the initial H_2O treatment (extending to about 1.35 µm depth), but in the negative ion depth profiles we follow the OD^{-} and D^{-} secondary ions introduced by the tracer diffusion experiment. These profiles (most pronounced for D^{-}) show a decreasing profile starting at the near-surface and extending into the bulk. The extent of these profiles are small, likely due to the short exposure time in D_2O , but the main change in the profile occurs within the region of H-Ga0.15-LLZO. We can thus try to find the diffusivity of D^{+} in this region by fitting the OD^{-} profiles.

The isotopic fraction of OD^{-}, $C(OD)$, is given by Equation 6.2, from the intensities I of the secondary ions OD^{-} and OH^{-}:

$$C(\mathrm{OD}) = \frac{I(\mathrm{OD}^{-})}{I(\mathrm{OD}^{-}) + I(\mathrm{OH}^{-})} \tag{6.2}$$

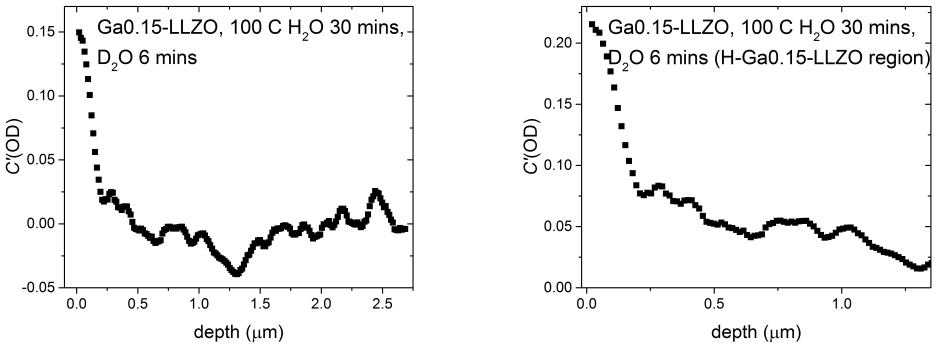
The normalised concentration $C'(OD)$ is given by Equation 6.3:

$$C'(\mathrm{OD}) = \frac{C(\mathrm{OD}) - C_{\mathrm{bg}}(\mathrm{OD})}{C_{\mathrm{source}}(\mathrm{OD}) + C_{\mathrm{bg}}(\mathrm{OD})} \tag{6.3}$$

$C_{bg}(OD)$ is the background isotopic fraction of OD^{-}, taken from the value in bulk Ga0.15-LLZO (or alternatively the equivalent H_2O-immersed sample average value). $C_{source}(OD)$ is the source concentration of the labelled species (i.e. 99.8 %, taken from the nominal concentration in the D_2O solution). Note the background and tracer OD^{-} fraction will include a contribution from $^{18}O^{-}$ counts, which we have noted previously is negligible compared to the counts from OD^{-} species.

Using the example of the $H_2O/30/D_2O/6$ sample, where $C_{bg}(OD)$ is 0.277 (taken

from the $H_2O/30$ sample SIMS profile under the same measurement conditions), Figure 6.15a gives the resultant profile for C'(OD) across the whole depth profile. Limiting the profile to the H-Ga0.15-LLZO region only (up to 1.35 µm), then C_{bg}(OD) is 0.208, and the resulting normalised fraction C′(OD) is shown in Figure 6.15b.



(a) (b)

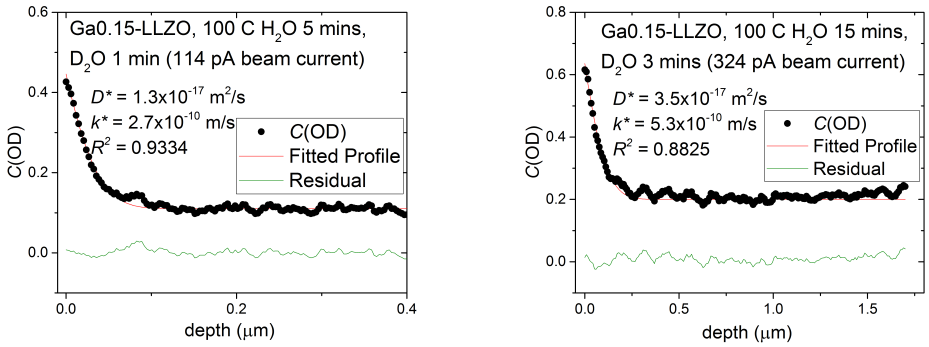
Figure 6.15: Normalised isotopic fraction of OD^-, C'(OD), as a function of depth in $H_2O/30/D_2O/6$ Ga0.15-LLZO. (a) The whole depth profile and (b) up to 1.35 µm corresponding to the H-Ga0.15-LLZO region.

Profiles measured under a lower primary ion beam current, which have a greater number of data points per unit depth (i.e. higher depth resolution), were fitted - examples are shown in Figure 6.16. The curve fitting and generation of the plots was generated using a custom software package, TraceX [266], using the Crank solution to the one-dimensional diffusion equation in a semi-infinite domain, with a surface exchange boundary and uniform initial conditions, to extract the tracer diffusivity of D^+ (D^*) and surface exchange coefficient k^*, fitting using a non-linear least squares method.

The mean value for D^* using low current depth profiles measured (four in total, using the primary ion beam currents 114 pA and 324 pA) is $3.2 \times 10^{-17}\,m^2\,s^{-1}$, with a standard deviation of $0.78 \times 10^{-17}\,m^2\,s^{-1}$. Adjusting for profiles within the H-Ga0.15-LLZO region only, the mean value for D^* is $2.5 \times 10^{-17}\,m^2\,s^{-1}$, with a standard deviation of $0.82 \times 10^{-17}\,m^2\,s^{-1}$.

The D^* tracer diffusivity is thus measured to be $\sim 10^{-17}\,m^2\,s^{-1}$ at 100 °C in Ga0.15-LLZO, which is about one order of magnitude lower than the chemical diffusivity estimated from the H_2O experiments ($D_C(H^+)$). The tracer diffusivity is expected to be lower than the chemical diffusivity, as the tracer diffusion lacks the chemical gradient found in the chemical diffusion process. However, it is difficult to isolate the diffusion of D^+ in LLZO from interferences caused by the corrosion layer, particularly in such short profiles, which provides a significant source of error.

A more accurate value would involve fully protonating the Ga0.15-LLZO to form a very deep (or infinite) region of equilibrated H-Ga0.15-LLZO and then performing the tracer diffusion experiments over a larger length scale. Translating the tracer diffusion to a proton conductivity through the Nernst-Einstein relation gives $10^{-8}\,S\,cm^{-1}$ at 100 °C, assuming the diffusivity corresponds to long-range correlated motion. Again, this is close



(a) (b)

Figure 6.16: Isotopic fraction of OD^-, $C(OD)$, as a function of depth with Crank solution fit to tracer diffusivity D^* and surface exchange coefficient k^* in (a) $H_2O/5/D_2O/1$ measured with 114 pA primary ion beam current and (b) $H_2O/15/D_2O/3$ with 324 pA primary ion beam current. The primary ion dose rates are 1.45x10^{15} ions cm^{-2} s^{-1} and 4.13x10^{15} ions cm^{-2} s^{-1}, respectively. The residual is the difference between the data points and the fitted profile.

to molecular dynamics simulation results reported [124] (with a value of 8.5×10^{-7} S cm^{-1} for $Li_{6.5}H_{0.5}La_3Zr_2O_{12}$ at 100 °C). It should be remembered that DC ionic conductivity, σ_i, as given in Equation 6.4, depends on charge q, number density n and mobility μ of the mobile species i.

$$\sigma_i = n_i q_i \mu_i \tag{6.4}$$

Consequently, we are making a number of assumptions, in applying the Nernst-Einstein relation, about the proton conductors in the H-Ga0.15-LLZO - including that the tracer diffusion, D^* can be approximated to the self-diffusion, that the number of protons available for conduction n_H is equal to the number of protons in H-Ga0.15-LLZO, and we are also making assumptions about their mobility. For the protons to contribute to conductivity, they need to be part of an open interconnected structure of diffusion channels; however, in this work we do not know about this, neither do we know the type and size of bottlenecks and the match between conduction path dimensions and mobile cation size, which are all critical factors for enabling conduction.

An additional effect which is not investigated here is the isotopic mass effect: normally in translating tracer diffusivity to self-diffusion, the mass effect is ignored. For example in solid oxide fuel cells where the oxygen isotopes ^{16}O and ^{18}O are used, the increase in mass in replacing ^{16}O by ^{18}O is 12 %, which is a relative mass change considered small enough to ignore. However, here the difference is a much larger one (D is twice the mass of H, giving a 100 % mass increase), so it is likely that this will have an effect on the different interactions of each isotope with the surrounding lattice, thus impacting on the transport properties. Heavier isotopes have, in classical terms, lower vibrational bond frequencies, or viewed quantum mechanically, they have a lower zero-point energy and require a higher activation energy for bond cleavage. Another possibility is the effect

of quantum tunnelling, which exists particularly for light elements, whereby a reacting species tunnels through the potential energy barrier rather than going over it, producing a large isotope mass effect. A more detailed discussion of mass effects observed in Li metal, both classical and quantum, is discussed by Lodding *et al.* [267] It may be necessary to include a mass correction factor in future work when highly quantitative data is being collected.

Another consideration which is not explored here is the mechanism for proton transport. Quite often in the diffusion of protons in metal oxides, protons are reported to associate with the oxide ions and form hydroxide ions. As the proton has no electron shell, it interacts strongly with the electron cloud of the oxide ion, forming a strong O-H bond. Two mechanisms for proton transport exist in principle in normal oxide structures, the free transport mechanism [32] and the Grotthuss mechanism [268]. The free transport mechanism involves protons jumping from one oxide ion to another, between which the proton rotates so as to reorientate its electron cloud ready for the next jump. In the Grotthuss mechanism, the proton is transported as a passenger on an oxide ion. Hence it is a transport of hydroxide ions, moving via an oxygen vacancy or interstitial hydroxide ion. H_2O or H_3O^+ ions may also serve as vehicles for proton diffusion in more open structures.

To summarise, Figure 6.17 shows a schematic of the processes occurring during the experiments described in this section. The left-hand image shows the proton-lithium exchange reaction (immersion of pellet in liquid H_2O) in the first step. H^+/Li^+ exchange occurs at the surface, resulting in the formation of LiOH corrosion layer products which are readily washed away in the water bath. This is followed by the formation of a H-Ga0.15-LLZO region, followed by a region of Ga0.15-LLZO which contains a chemical diffusion profile of H^+ until the bulk, non-protonated Ga0.15-LLZO, is reached. The protons create a region of H-Ga0.15-LLZO but the extent of H^+/Li^+ exchange might be limited by Li^+ and H^+ ionic mobilities within the H-Ga0.15-LLZO.

The right-hand image in Figure 6.17 shows the second step of the experiment in which the H_2O-immersed sample is exchanged in D_2O. In this step, there is some exchange between Li^+ and D^+ at the surface, but once inside the material, the D^+ shows a concentration gradient, or diffusion profile across the H-Ga0.15-LLZO, formed in the first step.

6.3 Effect of Protonation on Lithium Ionic Transport

6.3.1 Impedance Method

The pellets were measured using electrochemical impedance spectroscopy (EIS) in the frequency range of 1 Hz to 13 MHz, using either cold-pressed Li metal foil or gold-sputtered electrodes; see Chapter 4, Section 4.7.1 for more details. Impedance data was collected over a range of temperatures (−100 to 25 °C). Three pellet types were tested according to the variety of atmosphere and moisture treatments they experienced: pristine, air-exposed and water-exposed ($H_2O/15$ and $H_2O/30$). The pristine samples

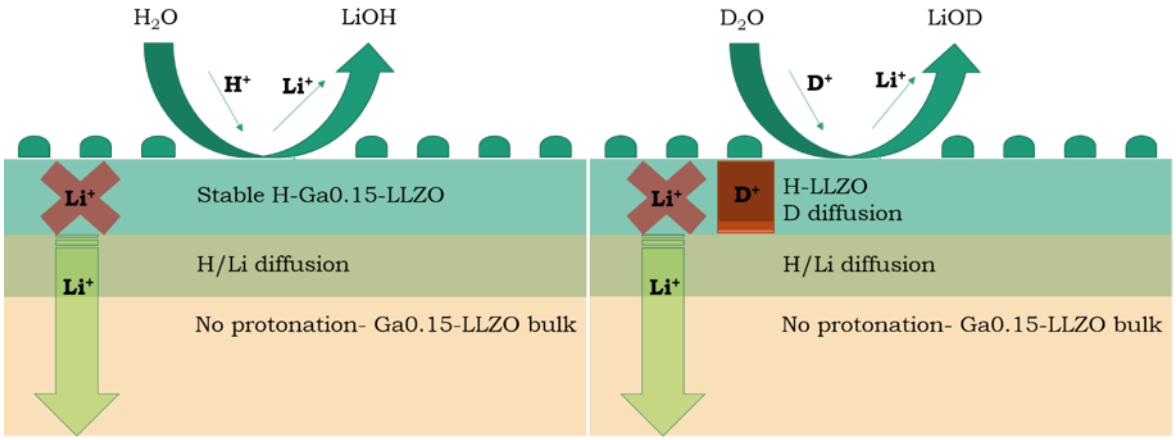


Figure 6.17: Schematic of possible ionic transport arrangements within a Ga0.15-LLZO grain; (left) during H_2O immersion (H^+/Li^+ exchange step); showing relatively fast chemical diffusion of H in the Ga0.15-LLZO grain, with a diffusion profile of H into bulk Ga0.15-LLZO after the formation of a H-Ga0.15-LLZO region; (right) during the D_2O immersion, with tracer diffusion of D^+ across the H-Ga0.15-LLZO region.

were not removed from the glove box at any time prior to being placed in a coin cell and measured in the impedance analyser, being measured only with Li electrodes. The air-exposed samples were removed from the glove box and allowed to be in contact with the air during transfer to and from the Au-sputtering equipment. The water-exposed samples were treated in the same way as described previously for the water-exchange pellet experiments. The measurements in this experiment were made by Dr. Ola Hekselman at Imperial College London.

The impedance spectra were fitted with equivalent circuits consisting of parallel combinations of a resistor (R) and a constant-phase element (CPE), denoted hereafter by R//CPE, arranged in series. An additional resistance element (R_{int}) in series was also included to account for inductive effects, resulting in a deformation of the high frequency semicircle. It was found that a resistance corresponding to the sample wiring was $5\,\Omega$ at room temperature. For all Nyquist plots, a constant-phase element (CPE) was used to model the non-ideal capacitive behaviour represented by depressed semicircles. Details of the fitted components for all samples are summarised in Table 6.4.

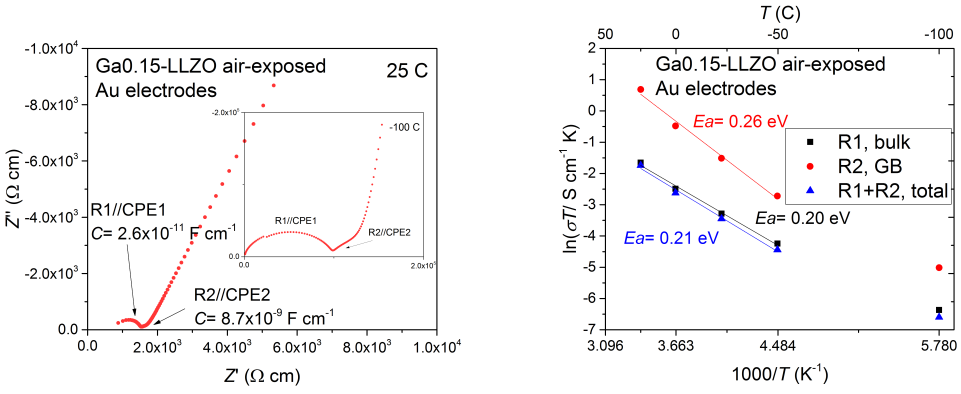
Table 6.4: Equivalent circuit model fits at 25 °C of impedance spectra parameters for pristine, air-exposed, $H_2O/15$ and $H_2O/30$ Ga0.15-LLZO cells with Li and Au symmetric electrodes.

		Pristine Li	**In air Li**	**In air Au**	**H_2O/15 Li**	**H_2O/30 Li**
R//CPE-1 (bulk)	R_{bulk} x A/l [Ω cm]	8.6x10^{2}	-	1.6x10^{3}	1.8x10^{3}	2.4x10^{3}
	σ_{bulk} [S cm^{-1}]	1.2x10^{-3}	-	6.4x10^{-4}	5.5x10^{-4}	4.1x10^{-4}
	E_a [eV]	-	0.18	0.20	0.14	0.18
	C x l/A [F cm^{-1}]	3.7x10^{-11}	-	2.6x10^{-11}	2.8x10^{-11}	9.8x10^{-11}
R//CPE-2 (grain boundary, GB)	R_{GB} x A/l [Ω cm]	3.5x10^{2}	-	1.0x10^{2}	2.1x10^{5}	5.0x10^{5}
	E_a [eV]	-	0.28	0.26	0.12	0.17
	C x l/A [F cm^{-1}]	4.6x10^{-8}	-	8.7x10^{-9}	1.8x10^{-9}	1.2x10^{-9}
R//CPE-(1+2) (total)	R_{total} x A/l [Ω cm]	1.2x10^{3}	2.3x10^{3}	1.7x10^{3}	2.1x10^{5}	5.0x10^{5}
	σ_{total} [S cm^{-1}]	8.2x10^{-4}	4.3x10^{-4}	5.9x10^{-4}	4.8x10^{-6}	2.0x10^{-6}
	E_a [eV]	-	0.22	0.21	0.16	0.17
	C x l/A [F cm^{-1}]	-	1.3x10^{-10}	-	-	-
R//CPE-3 (charge transfer, CT)	ASR (i.e. R_{CT} x $A/2$) [Ω cm^2]	9.4	392.5	-	2.4x10^{3}	-
	C/A [F cm^{-2}]	8.8x10^{-5}	5.6x10^{-5}	-	8.7x10^{-5}	-

6.3.2 Impedance Results

Air-Exposed Ga0.15-LLZO

The impedance spectra for the air-exposed Ga0.15-LLZO pellet measured with symmetrical Au electrodes (Figure 6.18a) comprises two high frequency depressed semicircles denoted by the contributions R1//CPE1 and R2//CPE2, with associated geometry-corrected capacitance values of 2.6×10^{-11} F cm^{-1} and 8.7×10^{-9} F cm^{-1} at 25 °C, respectively. The relatively low capacitance value for the high frequency contribution R1//CPE1 is typical for bulk ion transport [239]. The R2//CPE2 component is obscured by the Warburg lithium-blocking Au electrodes at low frequencies, but can be resolved at low temperatures (less than 0 °C, see inset of Figure 6.18a). The capacitance value derived from this contribution could either be associated with inter-grain ionic transport, or an interface process, which is investigated later. The activation energies were extracted from variable temperature data taken from −100 to 25 °C and fitted to an Arrhenius-type fit, shown in Figure 6.18b. The total conductivity, σ_{total} is 5.9×10^{-4} S cm^{-1} at 25 °C.



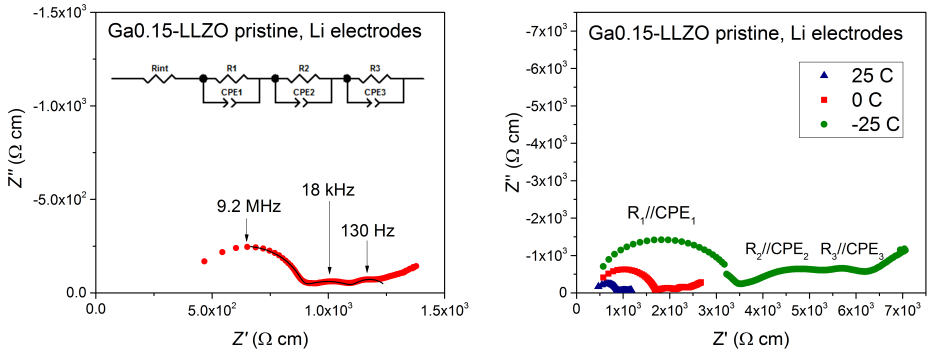
(a) (b)

Figure 6.18: (a) Nyquist plot at room temperature and (inset) −100 °C and (b) Arrhenius plots of bulk, grain boundary (GB) and total conductivities for the Ga0.15-LLZO air-exposed sample with symmetrical Au electrodes.

Pristine Ga0.15-LLZO

In the pristine samples tested with symmetrical Li electrodes, the impedance spectra (Figure 6.19) comprise an incomplete semicircle at the high-frequency region (which closes at lower temperature), followed by two depressed semicircles at the medium and the low frequencies, which are fitted to the three parallel R//CPE circuits. Again, the high frequency semicircle is attributed to the bulk (within-grain) ionic transport, and the geometrically-corrected capacitance and ionic conductivity values extracted from the fitted high frequency semicircle are 3.7×10^{-11} F cm^{-1} and 1.2×10^{-3} S cm^{-1} at 25 °C, respectively. This bulk conductivity is comparable to the highest reported literature values [113, 137, 151].

The intermediate-frequency component, R2//CPE2, has a geometry-corrected capacitance of 4.6×10^{-8} F cm^{-1} at −25 °C, which was found to be associated with



(a) (b)

Figure 6.19: Nyquist plots of Ga0.15-LLZO pristine pellets with symmetrical Li electrodes at room temperature (a), with equivalent circuit model (inset) and (b) overlay of spectra measured at 25 °C, 0 °C and −25 °C. The solid line denotes fitting using the equivalent circuit model.

inter-grain ionic transport in the Ga0.15-LLZO pellet. This was confirmed by evaluating the impedance of the second semicircle with a pellet of the same material of different thicknesses. The impedance values for this process varied proportionally with the thickness of the pellet which, when corrected for by cell dimensions to give resistivity, gave a value with a variance of less than 5 % (see Appendix A.3, Tables A.2 and A.3, supporting the assigned process as being associated with inter-grain transport and not a surface-related process (which would be thickness-independent).

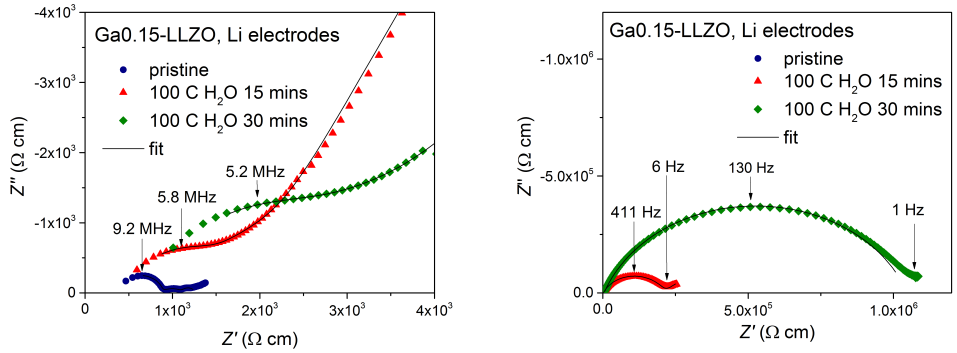
The nature of the inter-grain impedance can be two-fold: (i) transport across grain-grain interfaces or (ii) a precipitation of an interconnected secondary phase within the grain boundaries. Compositional information and more detailed investigations of electrochemical properties of the grain boundaries in Ga0.15-LLZO are needed to fully understand this. The presence of Li_2ZrO_3 as a minor secondary phase is not expected to contribute to ionic transport of Ga0.15-LLZO as no interconnected grains, which could provide continuous pathways for ionic transport, were observed in secondary electron and ion images. It might be that in the air-exposed sample, whose capacitance value for this second semicircle is lower than in the pristine sample, could contain a contribution from the surface layer formed as a result of corrosion layer growth, in addition to air reactivity of the grain boundaries.

The third, low-frequency semicircle component, R3//CPE3, seen in the cells tested with Li electrodes is associated with an electrolyte/electrode interface and can be described by the charge transfer resistance of two symmetric interfaces. In the pristine sample, this semicircle has an associated area-corrected capacitance of $8.8 \times 10^{-5}\,\mathrm{F\,cm^{-2}}$, and a value of area-specific charge transfer resistance (ASR) of $9.4\,\Omega\,\mathrm{cm}^2$. This is amongst the lowest values reported in the literature to-date for the interface between Li metal and garnet electrolytes, where the lowest values have been achieved by surface modification techniques by adding an interlayer between the Li metal and LLZO. This low value seen here is likely due to careful moisture-controlled processing and handling of Ga0.15-LLZO

in this work. In the air-exposed sample, the charge transfer component has an ASR equal to 392.5 Ω cm^2, indicating a higher barrier to charge transfer when compared to the pristine sample, likely caused by the formation of a small corrosion layer on the garnet surface, which supports this hypothesis.

Water-Treated Ga0.15-LLZO

The impedance spectra for the water-treated samples were measured with both Au and Li foil symmetric electrodes and compared to the pristine samples. Both the water-treated 15 minutes (H_2O/30) and 30 minutes (H_2O/30) samples display similar spectral form to the pristine spectra (Figure 6.20), with three distinguishable semicircles which are fitted to parallel R//CPE elements, using the equivalent circuit in Figure 6.19a.



(a) (b)

Figure 6.20: Nyquist plots of Ga0.15-LLZO pristine, air-exposed and 100 °C H_2O-immersed pellets with symmetrical Li and sputtered Au electrodes at room temperature. (a) High frequency region; (b) lower frequencies.

The fitted values from the impedance plots are given in Table 6.4. Three clear trends can be seen:

1. σ_{bulk}(pristine) > σ_{bulk}(H_2O/15) > σ_{bulk}(H_2O/30). The apparent bulk ionic conductivity found from the R1//CPE1 (bulk transport) contribution decreases by one order of magnitude in the protonated samples. This is attributed to an additional resistance in series due to the formation of a proton-rich H-Ga0.15-LLZO layer with high resistivity (Figure 6.21) which, although small in comparison to the total pellet thickness (~ 1 %), contributes to an increase in the bulk resistance. It has been suggested that extensive proton-lithium exchange in LLZO would lead to a reduced Li^+ mobility as the mobile octahedral Li sites are depopulated [157, 159, 164]. The total bulk conductivity in the water-exchanged LLZO is of the order of magnitude of the most frequently reported values for garnet electrolytes in the literature, which could suggest a degree of facile proton-lithium exchange during processing and handling in these materials. This highlights the importance and controlled moisture-free handling of garnets in order to prevent unwanted performance losses of the cells due to degradation processes.

2. R_{GB}(pristine) << $R_{GB}(H_2O/15)$ < $R_{GB}(H_2O/30)$. The apparent grain boundary resistance subtracted from the R2//CPE2 contribution seems to be more heavily affected by the moisture reactivity. In this case, the resistance increases by three orders of magnitude following water treatment. Importantly, the impedance measurements in the pristine sample show a lower grain boundary resistance than the bulk, indicating a higher Li mobility that could also be correlated to higher H^+/Li^+ exchange rates in the grain boundaries. The change in appearance of the grain boundaries in the electron and ion images after water treatment (Figure 6.7) also indicate reactivity leading to a less conductive grain boundary, which is mirrored in the change in transport properties seen in EIS measurements. Shimonishi *et al.* [165] reported a similar decrease in grain boundary conductivity in LLZO pellets in H_2O at 50 °C, attributing the change to segregation of resistive decomposition products at the grain boundaries which were not detectable by XRD. The existence of a liquid phase sintering process leading to enriched Al and Li grain boundaries has been previously reported [140, 146] and may be one of the factors contributing to higher reactivity towards proton-lithium exchange here.

3. The ASR for the charge transfer (R3//CPE3) follows ASR(pristine) < ASR(air-exposed) << $ASR(H_2O/15)$. The ASR in the pristine sample with Li electrodes is $9.4\,\Omega\,cm^2$, a very low value for this material. In the air exposed sample, this increases to $392.5\,\Omega\,cm^2$. The $H_2O/15$ protonated sample has an area specific resistance almost three orders of magnitude greater than the pristine sample, with a value of $2.4 \times 10^3\,\Omega\,cm^2$, indicating a large increase in the resistance at the H-Ga0.15-LLZO/Li metal interface. The $H_2O/30$ sample charge transfer component cannot be resolved as it occurs at too low frequencies at room temperature. Most reports to-date have focussed on the presence of LiOH and Li_2CO_3 following air exposure formed during the exchange process as the cause of increased interfacial resistance [168, 169, 269], which is generally recovered on mechanically abrading the corrosion layer [173]. For the first time, the effect of an extensively proton-rich, lithium-depleted LLZO surface on the interfacial properties with lithium metal electrodes is observed here (with a clean surface, free of LiOH and Li_2CO_3 species). The increased ASR following the proton-lithium exchange is most likely a result of decreased charge carrier mobility in this modified interfacial region. This behaviour is much more difficult to reverse with post-treatments, and represents a significant factor to consider when engineering interfaces of the LLZO electrolyte with lithium metal electrodes, with implications on cell performance such as fast charge/discharge cycles and preventing dendrite formation.

A closer look at the bulk resistance for the three samples, combined with the estimated H-Ga0.15-LLZO thickness as measured by FIB-SIMS depth-profiling, can allow the approximate resistivity of the H-Ga0.15-LLZO material ($\rho_{H\text{-}LLZO}$) to be calculated. Figure 6.21 shows a schematic of the protonated region of the pellet under EIS measurements, with l' being the thickness of the H-Ga0.15-LLZO region in the protonated samples, and l'' being the thickness of the unmodified, non-protonated, pure Ga0.15-LLZO in these

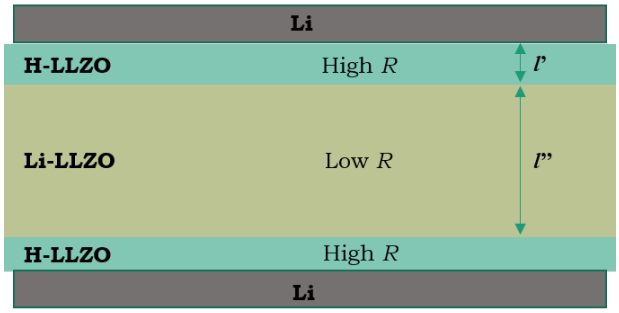


Figure 6.21: Schematic illustrating the true thickness, l'', of the pure LLZO region and the thickness of the H-LLZO region, l', following H^+/Li^+ exchange in H_2O. R denotes the resistance.

samples (and l the total pellet thickness). In the pristine sample, R_{bulk}(pristine) is equal to $8.6 \times 10^2\ \Omega\,cm$, which allows the resistivity of the pristine Ga0.15-LLZO, $\rho_{pristine}$, to be found.

Using Equations 6.5 and 6.6:

$$R_{bulk}(H_2O) = R'_{H\text{-}LLZO} + R''_{LLZO} = \frac{2l'}{A}\rho_{H\text{-}LLZO} + \frac{l''}{A}\rho_{pristine} \tag{6.5}$$

$$l'' = l - 2l' \tag{6.6}$$

the corresponding resistivities of the H-Ga0.15-LLZO region in both protonated samples are found to be (see Appendix A.4, Table A.4):

$\rho_{H\text{-}LLZO}(H_2O/15) = 1.2 \times 10^5\ \Omega\,cm$

$\rho_{H\text{-}LLZO}(H_2O/30) = 1.4 \times 10^5\ \Omega\,cm$

This corresponds to bulk conductivities in the protonated garnets of:

$\sigma_{H\text{-}LLZO}(H_2O/15) = 8.6 \times 10^{-6}\ S\,cm^{-1}$ at 25 °C

$\sigma_{H\text{-}LLZO}(H_2O/30) = 7.1 \times 10^{-6}\ S\,cm^{-1}$ at 25 °C

which is almost three orders of magnitude lower than the pristine Ga0.15-LLZO (where $\sigma_{H\text{-}LLZO,\,bulk}$ is $1.2 \times 10^{-3}\ S\,cm^{-1}$). This low conductivity can be related to a very low ionic mobility in the protonated phase. It might be expected that the highly resistive H-LLZO would lead to a splitting of the bulk impedance contribution into two arcs, leading to a broadening of the arc if the two bulk processes are not separable in the Nyquist plot. Further experiments and analyses would be needed to explore this.

The low mobility could be associated with a decrease in the Li charge carrier concentration and a concomitant change in the conduction mechanism, as suggested by previously reported *ab initio* studies [109], and in agreement with the ^{7}Li PFG NMR results which showed a dramatic decrease in Li mobility (Section 6.1.2), as well as our chemical and tracer diffusion experiments on the protons, which showed them to have lower mobility than the Li ions (at 100 °C). However, further analysis should be performed to prove a change in the activation energy and evaluate possible cooperative effects of H and Li charge carriers in these phases.

Such large resistive contributions to the bulk and grain boundary resistance from

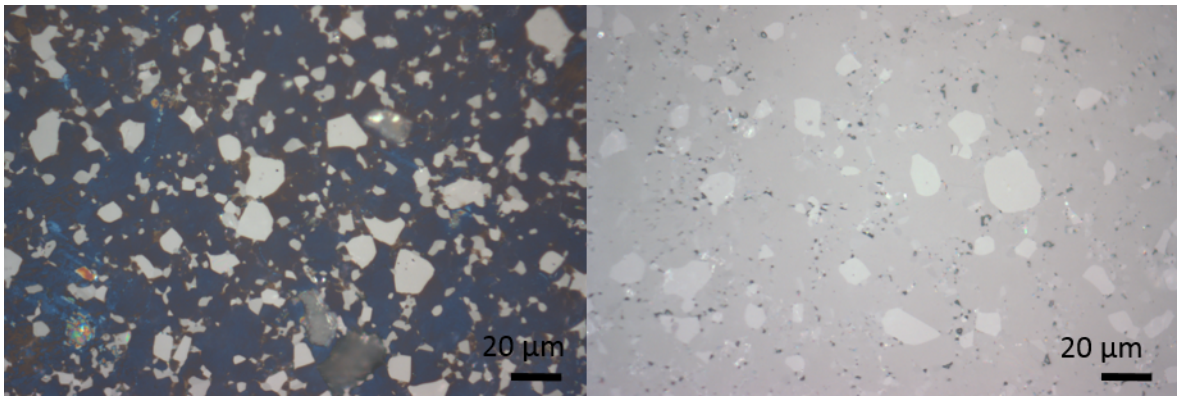


Figure 6.22: Optical microscope images of a LLZO-$La_2Zr_2O_7$ mixed phase pellet at 50x magnification polished to 0.1 µm after air exposure (left image), and after polishing the surface a second time (right image).

the protonated H-Ga0.15-LLZO and the grain boundaries highlight the importance of controlled handling and synthesis of these highly moisture-sensitive garnet materials, in order to avoid regions of protonated LLZO forming and causing an overall reduction in conductivity.

6.4 Surface Corrosion Layer Formation

The formation of corrosion layers of LiOH and Li_2CO_3, which are created at the LLZO pellet surface during the proton exchange process, is investigated here. Highly surface sensitive (confined to the top atomic layer) LEIS is used to determine the composition of the corrosion layer as it first forms and its transformation over time, and XPS is used to verify this. The formation of a corrosion layer is visible under optical observation, and under an optical microscope the formation of a surface layer after air exposure can be seen. The optical images in Figure 6.22 of a mixed phase LLZO-$La_2Zr_2O_7$ pellet polished to 0.1 µm show an optically dark region formed on the LLZO grains, leaving the lighter unreactive $La_2Zr_2O_7$ grains unchanged. After polishing again with diamond powder, the corrosion layer is removed.

6.4.1 Low Energy Ion Scattering

LLZO pellets were subject to different ageing treatments in air and water; Figure 6.23 shows ^{4}He LEIS depth profiles with over an analysis area of 750 µm by 750 µm. The dose per cycle was 7x10^{14} ions cm^{-2} for the ^{4}He analysis gun, and 3.4x10^{15} ions cm^{-2} for the Ar sputter gun, to ensure that most of the sputtering was carried out by the lower energy sputter gun to allow reasonable depth calibration and to minimise intermixing from the higher energy ^{4}He projectiles. LEIS measurements were taken by Dr Andrea Cavallaro at Imperial College London.

The oxygen intensity (which is normalised to the sum of all the surface species) can be used as a marker for the corrosion layer formation. In Figure 6.23, the x-axis represents the depth of the analysis in terms of the total argon sputtering dose; 0 ions cm^{-2} corresponds

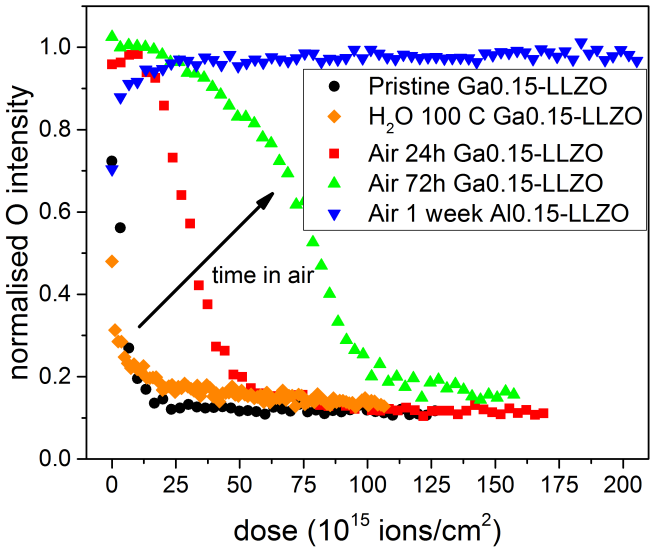


Figure 6.23: 3 keV ^{4}He LEIS depth profile with a 0.5 keV Ar sputter gun showing normalised oxygen intensities (with respect to the sum of all surface species) for Ga- and Al- doped LLZO pellets following different atmospheric treatments. The sputter area is 1500 µm by 1500 µm and the analysis area is 750 µm by 750 µm.

to the sample surface. It can be seen that with increasing air exposure time, the thickness of this corrosion layer increases such that after 1 week in air, the signal from the bulk pellet is not reached even after 2x10^{17} ions cm^{-2} dose (equivalent to 58 cycles of the sputter gun, or 58 atomic layers, approximately).

The corrosion layer detected here can be attributed to being composed of LiOH, not Li_2CO_3 as there is no C signal detected by LEIS at the surface of the samples after a week of air exposure. This is shown by the sub-surface scan spectra, acquired after 3 sputter cycles, in the 800 to 2800 eV energy range of both Al0.15-LLZO and Ga0.15-LLZO pellets after 1 week of air exposure (Figures 6.24a and 6.24b). It appears that LiOH forms quickly at the surface during air exposure, then slowly transforms to Li_2CO_3. This has been observed in previous studies on Al-, Ta- and Nb-doped LLZO [124, 137, 159], where it is suggested that the energetically favoured process is the direct reaction with gas phase H_2O to form LiOH, followed by reaction with CO_2 to form the carbonate, rather than the direct reaction with CO_2 in air [147].

The LEIS sub-surface spectrum (Figure 6.24c) and depth profile (Figure 6.24d) for Ge0.10-LLZO, which was exposed to air for one week and then stored in a glove box for several months, has surface regions of high C and O counts due to the surface corrosion layers of LiOH and Li_2CO_3 formed under the two different atmospheres. There is a sharp step change in the O, Zr and La counts at a dose of about 7.5x10^{16} ions cm^{-2} as we go into the bulk, equivalent to 22 sputter cycles, so we can estimate the total corrosion layer to be approximately 22 atomic layers thick. The thickness of the carbon is much less than this, which could support the theory that the LiOH slowly transforms to Li_2CO_3 (through the presence of small quantities of CO_2 in the glove box). It should be noted that the large

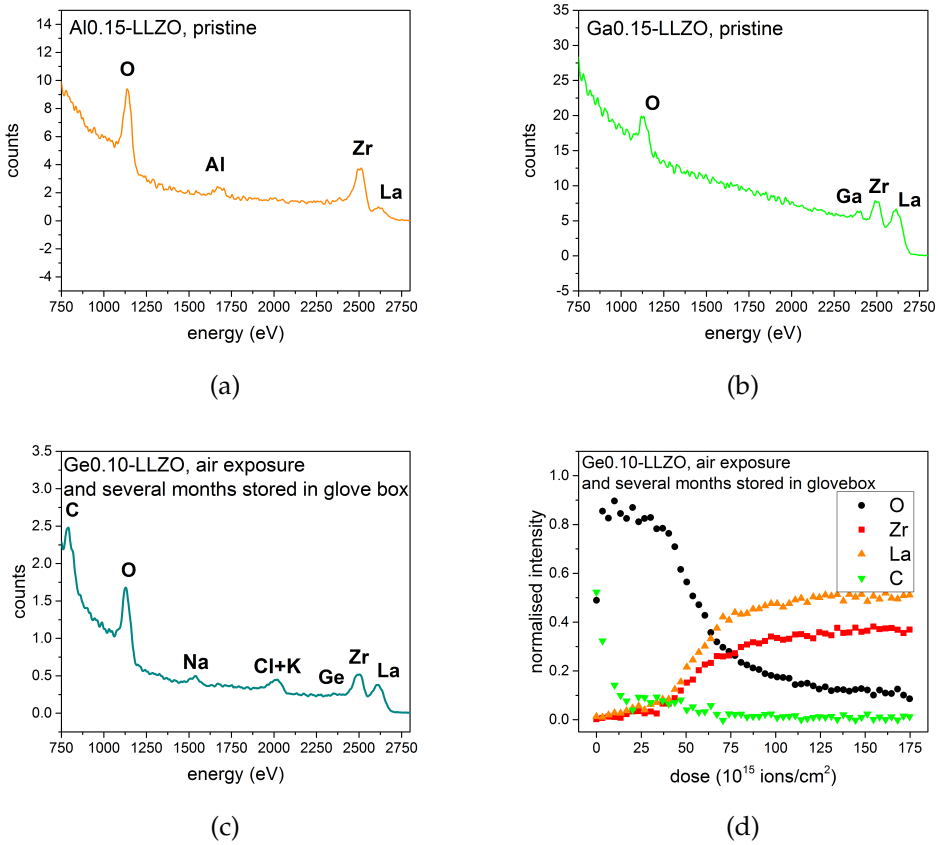


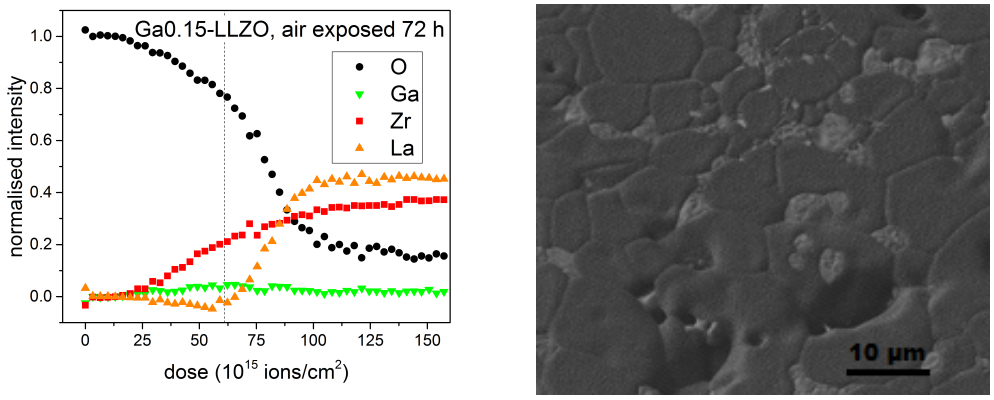
Figure 6.24: Sub-surface 3 keV ^{4}He LEIS spectra of (a) Al0.15-LLZO and (b) Ga0.15-LLZO pellets after 1 week air exposure, after a sputter dose of 1x10^{16} ions cm^{-2}; (c) Ge0.10-LLZO surface scan after a sputter dose of 8.8x10^{16} ions cm^{-2} and (d) Ge0.10-LLZO depth profile after storage in the glove box for several months following air exposure.

analysis area for LEIS means that grain boundary and/or impurity grain effects cannot be decoupled here.

The LEIS spectra previously discussed are on pure-phase LLZO garnets; however, if we do the same depth-profiling (Figure 6.25a) on a Ga0.15-LLZO pellet containing Li_2ZrO_3 impurity grains, which has been exposed to air for 72 hours, the Zr signal loses its sharp interface in the depth profile. This is due to the unreactive Li_2ZrO_3 grains at the surface which produce a Zr signal in the first 50-60x10^{15} ions cm^{-2} (15-17 atomic layers), with Ga0.15-LLZO hidden under the corrosion layer. The exposed Li_2ZrO_3 grains can be seen in the secondary ion image as bright regions, lacking the rough corrosion layer found on the rest of the sample surface (Figure 6.25b).

6.4.2 X-ray Photoelectron Spectroscopy

The pellet samples were measured using XPS to determine surface species before and after air exposure. For this analysis, samples were finely polished down to 4000 grit SiC paper and cleaned with acetone and isopropyl alcohol and a lint-free cloth, except for the air-exposed sample. Samples were transferred under argon with a glove box module



(a) (b)

Figure 6.25: 3 keV ^{4}He LEIS depth profile and secondary ion image of Ga0.15-LLZO air-exposed pellet containing Li_2ZrO_3 grains.

and the data was collected with a 200 µm by 200 µm beam (see Chapter 4, Section 4.3.1 for measurement details). All measurements and data treatment were made by Dr Anna Regoutz at Imperial College London.

The air-exposed Ge0.10-LLZO pellet with LEIS measurements in Figures 6.24c and 6.24d was measured in XPS and the spectra are shown below in Figure 6.26. A pristine reference sample of the same material which was never removed from the glove box prior to measurement is also shown. The probing depth (3 times the mean free path) for the analyses is approximately 5 nm [173].

Table 6.5: Quantification of XPS Li, La and Zr ratios in Ge0.10-LLZO samples.

Sample	**Li:La:Zr**
in air Ge0.10-LLZO	6.6 : 1.5 : 1.3
pristine Ge0.10-LLZO	6.6 : 2.4 : 2.3
nominal Ge0.10-LLZO	6.6 : 3 : 2

The Zr and La 3d peaks are very comparable for the two samples (not shown). The Li 1s peak is relatively much higher than the Zr 4s peak for the air exposed sample versus the pristine sample, as might be expected if a Li-rich corrosion layer is present. It shifts to lower binding energies towards the Zr 4s peak in the pristine sample, indicative of weaker Li bonding in the surface compared to the air-exposed sample. In the O 1s spectra, the higher binding energy peak corresponding to an OH bonded species is also much greater than the low energy peak associated with a metal-oxide (i.e. within the garnet lattice) for the air compared to the pristine sample. Finally, in the C 1s spectra, both samples show small peaks at high binding energies (> 287 eV) associated with double bonded oxygen-carbon species, in particular hydrogencarbonate and carbonate species (highest in binding energy) [270], but the intensity is greater for the air-exposed sample.

The Li:La:Zr ratio for the pristine and the air-exposed sample is 6.6:1.5:1.3 and

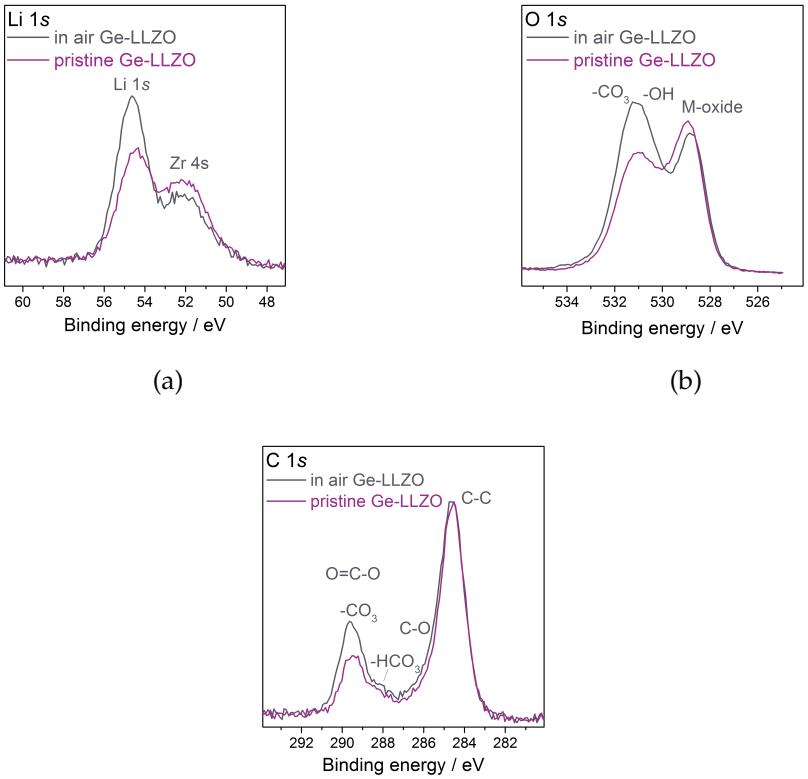


Figure 6.26: XPS Li 1s, O 1s and C 1s core spectra for air-exposed and pristine Ge0.10-LLZO samples.

6.6:2.4:2.3, respectively (Table 6.5). The pristine sample is close to being as expected for the nominal pristine LLZO stoichiometry; the air-exposed sample is enriched in Li relative to La and Zr at the surface, again indicative of a Li-rich corrosion layer.

6.5 Summary

The proton-lithium exchange mechanism was studied on powder and pellet samples to better understand the role of the reaction on the chemical transformations within doped-LLZO, on its surface chemical properties and on its ionic transport properties. A summary of the findings are given below:

1. Proton-lithium exchange in powdered Ga0.15-LLZO:
   In this series of experiments, powder samples of Ga0.15-LLZO underwent H^+/Li^+ exchange by immersing the powders in liquid H_2O at room temperature and 100 °C for a fixed time (20 hours). Care was taken to remove any corrosion product formed during the process through careful washing and drying of the samples.

   The cubic $Ia\bar{3}d$ lattice structure was maintained following the exchange process, as verified by powder XRD, and the lattice parameter was found to change as refined by Rietveld analysis of the XRD patterns; in the RT-immersed sample, the

parameter decreased (from 12.988 Å to 12.985 Å); in the 100 °C sample, it increased (to 13.031 Å). Additionally, a pyrochlore $La_2Zr_2O_7$ impurity, normally associated with Li loss, was present after the RT H_2O treatment only. These observations may indicate a difference in exchange kinetics of the proton exchange process at these two temperatures and perhaps a difference in the nature of the H-O bonding on insertion of H^+ species into the lattice - the barrier to H^+ insertion may not be overcome at room temperature, resulting in a net Li loss and formation of pyrochlore, whereas at 100 °C, it could be that the protons are present as H_3O^+, resulting in a lattice expansion versus the unexchanged LLZO.

The NMR ^1H spectra support these findings, showing a difference in the relative intensities of the chemical shift peaks associated with intercalated protons and adsorbed water for the room temperature compared to the 100 °C-treated samples, with a larger fraction of intercalated protons in the 100 °C H_2O sample. PFG NMR on the 100 °C H_2O powder yielded an incalculable lithium ion diffusivity owing to markedly slower kinetics of lithium in the sample compared to those of pristine sample. Decay processes for the protons were seen but could not be assigned a diffusivity with confidence owing to the complicated signal. These findings imply slow lithium ion diffusion in the protonated LLZO sample.

2. Proton-lithium exchange in Ga0.15-LLZO pellets:
Pellets of Ga0.15-LLZO were immersed in 100 °C liquid H_2O for a range of times, and FIB-SIMS was used to depth profile within grains to follow the chemical changes as a function of depth.

   The water-treated sample has a surface free from corrosion species (LiOH and Li_2CO_3) and surface impurities (such as carbon-based species) relative to the pristine samples. A proton-rich H-Ga0.15-LLZO region forms on proton-lithium exchange in the pellet samples, and as the exposure time increases, its thickness increases, and there is a change in Li and H content.

   Li and H diffusion profiles are seen in the samples; the diffusion length of the protons increases with the immersion time. The chemical diffusion coefficient, $D_C(H^+)$, of the protons at 100 °C is calculated to be 1×10^{-16} to 2×10^{-16} $m^2\,s^{-1}$ for the three samples. This corresponds to a conductivity at 100 °C of the order of 10^{-8} $S\,cm^{-1}$ at (compared to the Li conductivity from EIS measurements as 10^{-2} $S\,cm^{-1}$ at 100 °C).

3. Tracer diffusion using D_2O on Ga0.15-LLZO pellets:
The H_2O-immersed pellets were then immersed in D_2O to enable tracer diffusion to occur, which was also followed using FIB-SIMS depth-profiling in the Ga0.15-LLZO grains. The times chosen were too short to collect an accurate diffusion profile of D^+; however, there was a clear movement of D^+ into the samples. The tracer diffusivity (D^*) was difficult to find from fitting the profiles, but within the H-Ga0.15-LLZO regions tested, it was estimated to be approximately 10^{-17} $m^2\,s^{-1}$, one order of magnitude smaller than the chemical diffusivity.

4. Effect on transport properties, EIS measurements:
   Pristine, air-exposed and water-immersed pellets of Ga0.15-LLZO were measured with impedance analysis using Au and Li electrodes to determine the effect of moisture reactivity on the transport properties.

   Electrochemical impedance data showed a reduction in total conductivity from the pristine to the water-treated samples due to a decrease in charge carrier mobility in the protonated H-Ga0.15-LLZO region, which has a calculated bulk resistivity of approximately $10^5\,\Omega\,\mathrm{cm}$ in both $H_2O/15$ and $H_2O/30$ samples. This bulk resistivity is almost three orders of magnitude higher than in pristine, pure LLZO with R_{bulk}(pristine) equal to $8.6 \times 10^2\,\Omega\,\mathrm{cm}$. A second semicircle component in the impedance spectra, R2//CPE2, was seen in all samples and attributed to a grain boundary contribution, which is shown to be very susceptible to moisture; after water treatment, the resistance, R_{GB}, for this component increases by three orders of magnitude to $5 \times 10^5\,\Omega\,\mathrm{cm}$ after 30 minutes. The ASR with Li electrodes dramatically increased after the proton exchange (from $9.4\,\Omega\,\mathrm{cm}^2$ in the pristine to $392.5\,\Omega\,\mathrm{cm}^2$ in the air-exposed sample to $2.4 \times 10^3\,\Omega\,\mathrm{cm}^2$ in the $H_2O/15$ sample).

5. Air-reactivity, surface corrosion layer formation:
   LLZO pellets were allowed to be in contact with ambient air for a range of times, and the chemical nature of the corrosion layer formed at the surface was investigated with LEIS and XPS. LiOH quickly forms on the surface of a variety of doped LLZO pellets (Al, Ga, Ge) – the corrosion layer is visible in an optical microscope and can be polished away with fine diamond paste. This is followed by a slow transformation to Li_2CO_3 in both air and under glove box conditions (where the CO_2 content is unknown, but should be minimal).

To summarise, it has been shown that proton-lithium exchange processes proceed very readily in the garnet LLZO materials, resulting in changes to Li stoichiometry and transport properties. The crystal structure remains unchanged, but the highly reactive nature of the grain boundaries with moisture in the pellets is not chemically characterised, and may lead to loss of mechanical integrity over long time periods. The formation of H-LLZO with low Li mobility (compared to the pristine LLZO) has detrimental implications on performance, but the extent to which H-LLZO forms and its ability to passivate further degradation reactions needs to be explored. This coupled with further knowledge on H and Li individual ionic mobilities would be important for assessing the suitability as a separator in aqueous cells. It might be that higher pH systems would work in this setup, acting to slow the exchange process.

6.6 Suggested Future Work

To localise the H and Li in the protonated sampled, in-situ neutron diffraction could be carried out, in particular under different protonation conditions (temperature, partial pressure of water). As the proton-lithium exchange experiments on the pellets were

carried out under a small range of times, the experiment should be extended to include longer immersion times. This could be monitored with the aid of a pH meter and with ICP analysis of the resulting solution and pellet following the exchange. This will enable an understanding of the nature of the equilibrated region of H-LLZO and to study its transport properties using, for example, EIS and tracer diffusion experiments.

More information on the chemistry of grain boundaries and their reactivity with moisture will be important to explain the dramatic resistivity changes following water-immersion and proton exchange. This information will require the use of high resolution mapping in SIMS, and also scanning transmission electron microscopy (STEM) analysis of lamellas in order to look at the atomic arrangements at the grain boundaries. TOF-SIMS linescan-type mapping could be utilised for long diffusion length studies following long exchange times.

More NMR and computational work to probe O-H bonding interactions in H-LLZO is important to understand the stability and kinetics in H-LLZO. For example, using D_2O or ^{17}O-H_2O, NMR might also be able to give improved structural information. Any intercalation of water would be detectable by using ^{17}O-H_2O.

Lithium tracer diffusion work (Chapter 7) to find the lithium mobility in the protonated samples. Combining the effect of the proton-lithium exchange on the lithium kinetics with tracer experiments would be interesting in order to probe the true Li transport in the exchanged material following moisture reactivity, and highly important to learn more about the true nature of Li transport in the degraded material.

It has been proposed that a direct reaction with CO_2 might involve removal of Li, which is then compensated for by the creation oxygen vacancies [119]; to investigate this, an experiment could be performed in which the oxygen in LLZO could be isotopically labelled with exchange in ^{18}O gas, then allowing it to react with air or CO_2 to form a corrosion layer, using LEIS to determine the nature of the oxygen species in the corrosion layer. As LEIS can distinguish between different isotopes of O, we can find out if the O in the corrosion layer is formed with oxygen from within the garnet lattice (as it will be enriched in ^{18}O versus ^{16}O isotopes).

Finally, the interaction of dopants on the extent of proton-lithium exchange and ionic mobility will be another useful piece of information to correlate the ionic mobilities in H-LLZO with the Li content, conduction pathways and structural distortion in the material.

Chapter 7

Lithium Isotopic Exchange, Diffusion and Transport in $Li_7La_3Zr_2O_{12}$

This chapter provides details of various experiments used to investigate the lithium diffusion properties of $Li_7La_3Zr_2O_{12}$ (LLZO). The primary focus is the development of isotopic tracer methods coupled with secondary ion mass spectrometry (SIMS) for the determination of lithium diffusion coefficients, D(Li), in the garnet electrolytes. A second method for probing the lithium dynamics, solid state nuclear magnetic resonance (NMR), using pulsed field gradient and $T1$ spin-lattice relaxation measurements on LLZO, is discussed. Diffusion coefficients for the lithium ions in LLZO as estimated from tracer experiments, NMR and electrochemical impedance analysis are compared and used to comment on the lithium transport mechanism in LLZO.

7.1 Lithium Isotopic Exchange Techniques

Measuring the diffusion of lithium in fast ionic conductors, such as LLZO, is currently limited to a handful of techniques, dominated largely by the microscopic techniques of NMR spectroscopy [48, 67, 134], muon spin-relaxation (μ^+SR) [51] and quasi-elastic neutron scattering (QENS) [50], which are typically measured using powder samples and probe long-range diffusion indirectly, measuring atomic scale lithium jumps. Pulsed gradient NMR has recently been used for micrometre-scale (i.e. macroscopic) analysis, using powder and membrane samples of LLZO [66], but requires high temperature measurements and complex interpretation. To convert jump frequencies (probed on a short length scale) into diffusivities, model assumptions have to be applied. Additionally, the observed lithium mobility may be dependent on the particle size of the sample, as the ions 'turn around' at the end of the particle, resulting in a decrease in the apparent diffusivity for smaller particles [66]. A common macroscopic technique for measuring lithium transport, electrochemical impedance spectroscopy (EIS), is an indirect method which converts conductivity measurements to charge diffusivity D^σ using the Nernst-Einstein relation by assuming a mass concentration gradient and a Haven ratio of unity (single charge carrier contribution). As EIS is not *a priori* lithium selective, it includes contributions from other charge carriers such as protons, so a number of assumptions have

to be made with regard to the transport number of lithium in the system under study. However, under favourable conditions, it allows the separation of processes with different relaxation times under an alternating current, such as grain, grain boundary and interface impedance. Neutron radiography (NR) has been used to measure macroscopic lithium tracer diffusion coefficients in some materials [62, 63, 271], and works by virtue of the large difference in neutron absorption coefficients between the two stable lithium isotopes. These techniques and their relationship with long-range lithium diffusion are described in more detail in Chapter 2.

In this section, a new methodology for determining lithium diffusion coefficients involving stable tracer experiments is described, whereby a ^{6}Li:^{7}Li isotope couple is allowed to inter-diffuse and the resulting isotopic profiles are studied using SIMS analysis. By using tracer experiments, a direct measurement for the diffusion coefficient is possible without depending on model-based correction factors which are needed for, i.e. NMR measurements of long-scale ionic motion. This is achieved by measuring the diffusion profiles of the atoms of interest (lithium in this case) during the diffusion event, allowing the measurement of true long-range diffusion on a macroscopic and easily visualisable scale.

A limited number of tracer-based experiments can be found in the literature on lithium-based systems using SIMS analysis on isotope couples. Some previous work has been done using SIMS depth-profiling on the lithium thin film oxide $^{6}LiMn_2O_4$ [272] by applying a potential step across a liquid-oxide junction with ^{7}Li-enriched $LiClO_4$, thereby obtaining a chemical and electrical diffusivity of lithium ions. Amorphous α-Li_3PO_4 [55] has also been studied, using a thin film of the material coupled to either a liquid electrolyte or a deposited thin film oxide, and measured using linescan analysis with SIMS following annealing at different temperatures. Single crystal measurements on $LiNbO_3$ [57, 58] and γ-$LiAlO_2$ [60], in which isotopically-enriched thin films are deposited on the single crystals (solved as Case 2 for a solid-solid interface described in Chapter 2, Section 2.2.3), have also been reported using TOF-SIMS analysis. These experiments were achievable at elevated temperature ranges, with diffusion lengths in the several-hundred nanometres range for the measurements owing to the relatively slow diffusion of lithium (with a diffusion coefficient, $D \sim 10^{-20}\,m^2\,s^{-1}$ at room temperature in $LiNbO_3$).

Below a method for isotopic lithium exchange on LLZO, using an all-solid-state method with lithium metal as the tracer isotope source, is introduced.

7.1.1 Solid State Diffusion Method

In this method, a metallic source of lithium tracer ions is used (^{6}Li metal), which is contacted on the natural lithium isotopic abundance LLZO pellet. This method was selected to simulate the real setup of an all-solid-state lithium metal battery, enabling the interface behaviour of the lithium metal with LLZO to be studied. Following the contact of the ^{6}Li metal with the LLZO pellet, the diffusion of ^{6}Li from the enriched metal source through LLZO is followed as a function of time (and distance), using focussed ion beam (FIB)-SIMS depth-profiling, both through the interface of the metal-LLZO

("direct depth-profiling" method) and at varying distances from the lithium metal edge ("sampling" method). Figures 7.1a and 7.1b show examples of the depth profile craters for the two measurement types. FIB-SIMS depth-profiling was chosen as the desired analysis method, owing to the ease of sample preparation (avoiding the need for cutting and polishing post-exchange required for time of flight (TOF)-SIMS linescan analysis, commonly used for ^{18}O exchange and diffusion [45]), whilst enabling relatively deep depth profiles (several micrometres) to be made, which is not possible in the TOF-SIMS depth-profiling mode.

This method does not include an equilibrium pre-anneal step, and the couple contains two chemically non-identical parts, so the experiment is measuring a chemical diffusion (D_C) of ^6Li in LLZO, rather than a true self-diffusion; it is thus expected that the measured diffusivity here will be somewhat higher than the true self-diffusion D^* in the absence of a chemical gradient. The data obtained, given enough data points, could then be fitted to a solution for diffusion from a source of changing concentration using a finite difference simulation method, to find the diffusion coefficient D. The ^6Li metal used (Sigma Aldrich) is nominally 95.4 % enriched, and LLZO has a nominal natural abundance isotopic fraction (C_{bg}) of ^6Li equal to 7.59 % [265]. The isotopic fraction of ^6Li, $C(^6Li)$, is given by Equation 7.1:

$$C(^6Li) = \frac{I(^6Li^+)}{I(^6Li^+) + I(^7Li^+)} \tag{7.1}$$

This can be expressed as the normalised concentration of ^6Li , $C'(^6Li)$, by Equation 7.2:

$$C'(^6Li) = \frac{C(^6Li) - C_{bg}(^6Li)}{C_{source}(^6Li) + C_{bg}(^6Li)} \tag{7.2}$$

$C_{bg}(^6Li)$ is the background isotopic fraction of ^6Li, taken from the value in the bulk LLZO and $C_{source}(^6Li)$ is the source concentration of the labelled species (i.e. the concentration of ^6Li in the metal source).

7.2 Method Development

This section gives details of method development, including the optimisation of the experimental conditions, and preliminary results for the tracer-based SIMS diffusivity measurement experiment outlined above.

7.2.1 Secondary Ion Energy Spectrum

Firstly, an investigation into the energy offset for lithium ion detection in the SIMS setup was made, using the enriched ^6Li metal source. In the secondary ion energy spectrum (Figure 7.2) atomic molecular species (such as $^6LiH^+$) have a sharp peak at low energies, whereas atomic species (i.e. $^7Li^+$) have a much broader distribution peaking at higher energies. This can be used to discriminate against a molecular species occurring at the same mass by using an energy offset. Ideally we want to be at the maximum in the

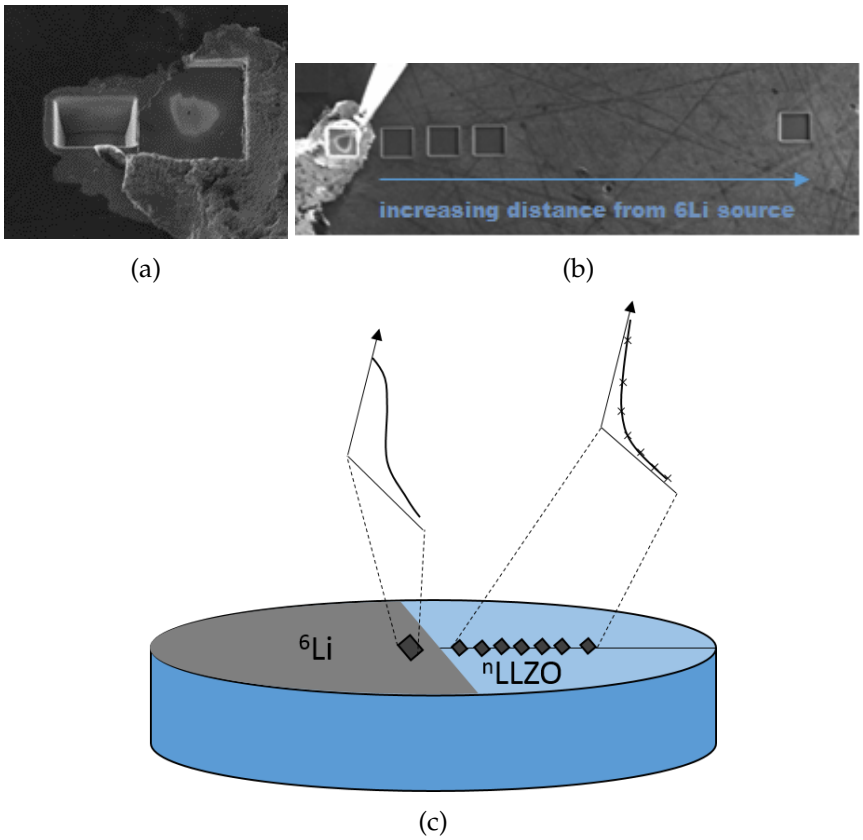


Figure 7.1: The solid state diffusion method: Pellet of LLZO with flat top surface, partially contacted by ^{6}Li metal. (a) Li metal-LLZO interface depth profile craters (x2) in the ^{6}Li-LLZO diffusion couple, referred to as the "direct depth-profiling" method and (b) consecutive depth-profiling at increasing distances from ^{6}Li metal on the surface of a natural abundance Li (^{n}Li) LLZO pellet (^{n}LLZO), termed the "sampling" method; (c) schematic of the two methods.

atomic secondary ion signal for the best counting statistics and selectivity (or at about 20 V in Figure 7.2). We can test the effect of the energy offset on the measured lithium isotopic fraction by measuring short depth profiles in the nominally 95.4 % enriched ^{6}Li metal on a Si(001) wafer at different energy offsets for the ^{6}Li isotope in the FIB-SIMS. This was carried out with offset voltages of 40 V, 20 V and 0 V, and the resultant mean ^{6}Li isotopic fractions are given in Table 7.1. It can be seen that the closest value to the expected isotopic fraction is found when using a voltage offset of 20 V; however, there is very little appreciable change arising from the offset voltage used in the 0 to 40 V range. As such, the value of 0.95 (2 significant figures) taken with a 0 V offset is used as the value for $C_{\text{source}}(^{6}\text{Li})$ in the following exchange experiments. It is possible that this variation in isotopic fraction would be more pronounced in LLZO, as the concentration of ^{6}Li is much lower, reducing the counting statistics and leading to greater error in the determination of the lithium isotopic fraction.

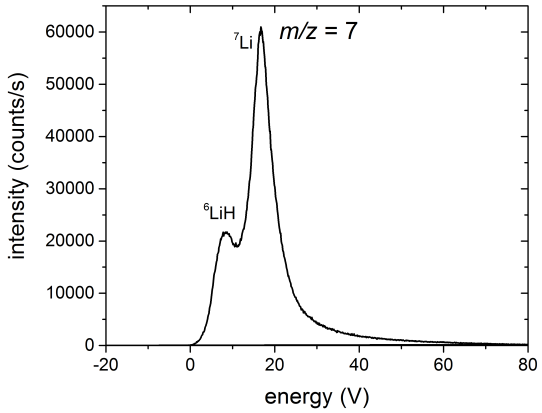


Figure 7.2: FIB-SIMS secondary ion energy spectrum for $m/z = 7$ species; measured on ^{6}Li metal.

Table 7.1: Measured ^{6}Li isotopic fractions $C(^6\text{Li})$ on ^{6}Li metal, with different voltage offsets.

	$C(^6\text{Li})$ from specification	$C(^6\text{Li})$ 0 V offset	$C(^6\text{Li})$ 20 V offset	$C(^6\text{Li})$ 40 V offset
Mean	0.954	0.9487	0.9548	0.9569
Deviation from specification	-	-0.0053	+0.0008	+0.0029
Standard deviation	-	0.0005	0.0015	0.0022

7.2.2 Verification of Isotopic Exchange

The first stage in the development of a solid state method for measuring lithium diffusivity involved the creation of a diffusion couple of ^{6}Li metal and LLZO pellet. Due to limitations when handling the materials (the ^{6}Li metal needs handling in an inert atmosphere and is provided in large chunks in mineral oil which need to be cut and flattened to the desired shape), a crude couple was made in which the ^{6}Li metal was placed onto half of the surface of a semi-circular LLZO pellet and pressed down, with a sharp edge made with a scalpel, illustrated in Figure 7.1c. After leaving for some time at room temperature in the glove box, the metal had fallen away from the pellet (nominal composition Ge0.05-LLZO), leaving some small regions where the metal remained adhered to the surface. It is likely that the poor cleanliness of the sample resulted in part of the metal reacting and coming away from the pellet, as later analyses in which the handling was better controlled ensured the metal was well contacted and did not come away. The sample was transferred in an argon-filled container to the FIB-SIMS instrument for analysis after the ^{6}Li metal had been in contact with the LLZO pellet for an exchange time of 17 hours.

From EIS measurements on the same sample, the length at which background

concentration is reached was estimated to be approximately 140 µm, using $x' = \frac{x}{2\sqrt{Dt}}$ equal to 2 (i.e. $x = 4sqrt(Dt)$ (see Chapter 2, Section 2.2.3 for discussion) and the Nernst-Einstein conductivity-diffusivity relationship. Table 7.2 summarises these values.

Table 7.2: Estimated diffusion length x for $x' = 2$ from exchange time t and diffusivity D^{σ} calculated from EIS conductivity measurements for the first ^{6}Li isotopic exchange experiment.

Room temperature conductivity σ, from EIS	**Calculated room temperature diffusivity D^{σ}, from Nernst-Einstein**	**Exchange time t**	**Length x, from $x = 4\sqrt{D^{\sigma}t}$**
3×10^{-5} S cm^{-1}	2×10^{-14} m^2 s^{-1}	17 hours	140 µm

Subsequently, a mass spectrum in positive secondary ion mode with 2.7 nA primary ion beam current was taken at 500 µm from the edge of the position where the lithium metal was attached (chosen to be much larger than $x = 4\sqrt{(Dt)}$), and the ^{6}Li isotopic fraction $C(^{6}\text{Li})$ here was found to be 0.0764, which is in agreement with the literature background value of 0.0759 [265]. Hence, this is taken as the C_{bg} value in this experiment.

Next, a series of depth profiles were taken at increasing length intervals from the edge of the original location of the ^{6}Li metal (Figure 7.3a), as marked by a piece of residual ^{6}Li (white region in Figure 7.3a). Depth profiles of around 3 µm depth and with crater size 15 µm by 15 µm were taken with a primary ion beam current of 5 nA. It was hoped the change in isotopic fraction of ^{6}Li in Ge0.05-LLZO could be followed as a function of distance from the ^{6}Li source.

Each depth profile was collected under dual polarity detection mode, as a function of depth. The primary SIMS beam used is $^{69}Ga^{+}$. To correct for surface roughness and sputter rate and to allow better comparison between analyses, the reference secondary ions $^{16}O^{-}$ and $^{69}Ga^{+}$ are used, with other secondary ion species given as ratios of intensities with respect to these species in some figures.

The first depth profile (Labelled 1 in Figure 7.3a and shown in Figures 7.3b to 7.3d) involved sputtering through a small amount of ^{6}Li metal still adhered to the surface, which has a mean measured isotopic fraction $C(^{6}\text{Li})$ here of 0.62 (from Equation 7.1). At about 2.5 µm depth, the interface with the LLZO pellet is reached, indicated by the sudden increase in LaO^{+} counts (Figure 7.3b). There is also a crossover in the dominant lithium isotope counts here, and $C(^{6}\text{Li})$ drops to 0.42 (Figure 7.3d). The fluctuations in ion counts in the ^{6}Li metal region are likely due to the roughness of the metal (which has probably reacted with air during the short transfer step to the FIB-SIMS instrument). This small piece of ^{6}Li metal remaining on the surface is too small to act as a semi-infinite source of ^{6}Li isotope, and itself undergoes lithium exchange, dropping from a $C(^{6}\text{Li})$ of 0.95 to a $C(^{6}\text{Li})$ of 0.62 after 24 hours total exchange time.

An estimate of the number of Li ions exchanged can be calculated from this drop of 65.2 % : assuming complete contact of ^{6}Li metal in a piece measuring about 3 µm thick

with 30 µm radius and thus containing approximately 4x10^{14} Li atoms, this represents a net flux of Li of 2.6x10^{14} Li atoms in 24 hours across the Li/LLZO boundary. Half of these correspond to ^{6}Li ions moving into LLZO, and *vice versa* (1.3x10^{13} Li), corresponding to a rate (or flux) of 5.4x10^{13} Li cm^{-2} s^{-1}.

This evidences the mass transport between LLZO and the ^{6}Li metal in the absence of an applied electric field. Understanding the surface exchange (or flux of lithium) across this solid/solid interface in terms of mass transport (in addition to charge transport, as probed by EIS) is an important step towards comprehending the dynamic processes at these electrode-electrolyte interfaces.

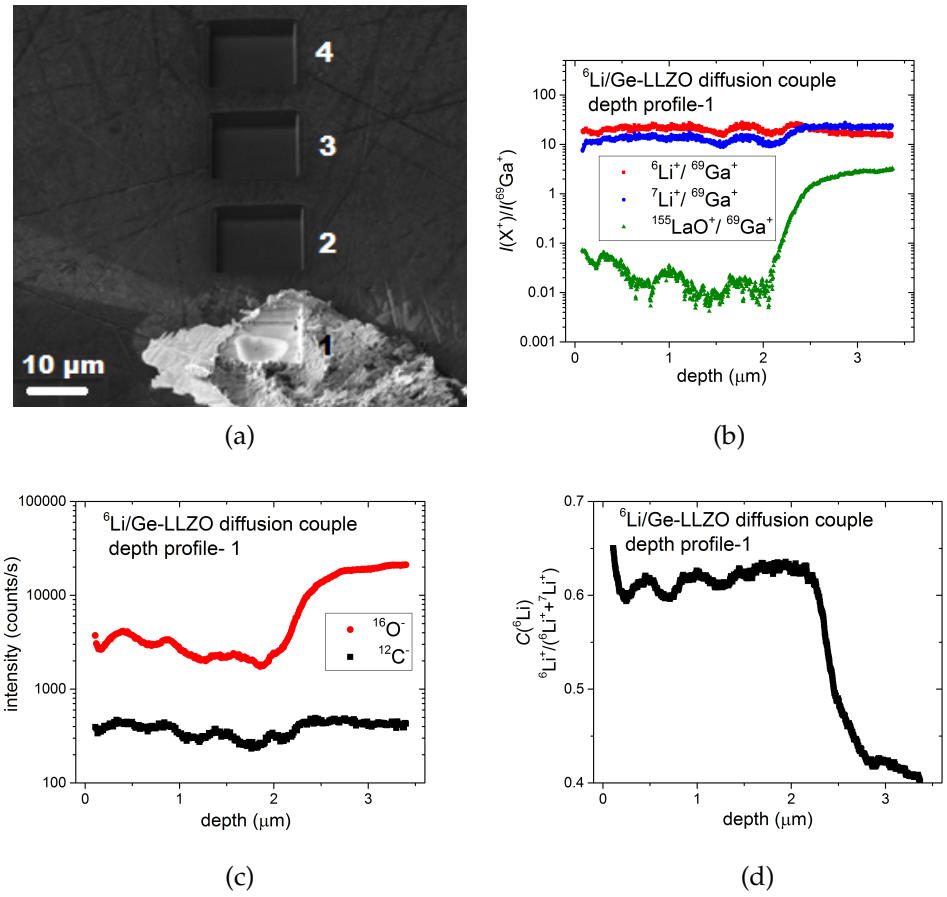


Figure 7.3: (a) Location of the first four FIB-SIMS depth profiles for isotopic ratio measurements on the ^{6}Li/Ge0.05-LLZO couple, with increasing distance from the ^{6}Li source (bottom of image), taken as a secondary electron image. FIB-SIMS depth profile number 1, through the ^{6}Li metal/LLZO interface: (b) positive secondary ions $^6Li^+$, $^7Li^+$ and $^{155}(LaO)^+$ with intensities I, divided by intensity of $^{69}Ga^+$ secondary ions; (c) negative secondary ion $^{16}O^-$ and $^{12}C^-$ intensities; (d) ^{6}Li isotopic fraction, $C(^6Li)$. The interface boundary between the ^{6}Li metal and the LLZO pellet is located at approximately 2.5 µm depth in the figures. The crater size is 15 µm by 15 µm and the primary ion beam current is 5 nA, giving a dose rate of 1.4x10^{16} ions cm^{-2} s^{-1}.

A summary of the $C(^6Li)$ in the depth profiles taken at increasing distance from the edge of the ^{6}Li source is given in Figures 7.4a to 7.4c. There is a general trend of decreasing $C(^6Li)$ at a given depth in each depth profile with increasing distance from the ^{6}Li metal, which tends towards the isotopic background C_{bg} value, of 0.0764, between 200 and

500 µm. A plot of effective distance from ^{6}Li source against isotopic fraction measured (Figure 7.4c) converts each data point in the depth profiles to a value in terms of distance from the ^{6}Li metal, treating it as a point source. Crudely taking the length, x, at which C_{bg} is reached, we can estimate the chemical diffusivity, $D_C(^6\text{Li})$, from $x = 4\sqrt{(D_C t)}$. For values of x between 200 and 500 µm, $D_C(^6\text{Li})$ is 5×10^{-14} to 2×10^{-13} m^2 s^{-1}. This is greater (faster diffusion) than the D^σ value predicted from EIS measurements, and is expected to be larger than the self-diffusion as it is a chemical diffusion that is being measured here.

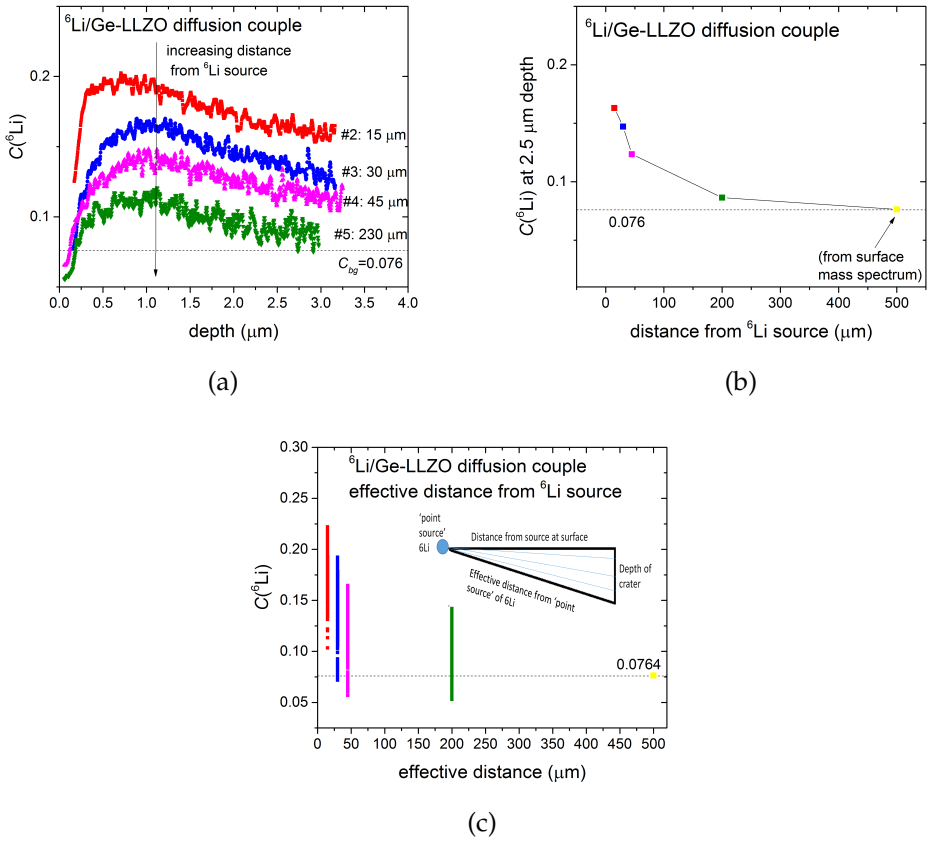


Figure 7.4: ^{6}Li isotopic fractions $C(^6\text{Li})$ for FIB-SIMS depth profiles at varying distances from the ^{6}Li metal source. (a) Overlay of depth profiles at 15 to 230 µm distance from the source; (b) $C(^6\text{Li})$ values of each depth profile at 2.5 µm depth (the isotopic fraction of the surface mass spectrum at 500 µm is given too); (c) data points at 15 to 500 µm from the source, showing $C(^6\text{Li})$ at an 'effective distance' from the source, calculated from the depth at which the data point is collected and distance of the centre of the depth profile along the pellet surface from the source of ^{6}Li. The primary ion beam dose rate is 1.4x10^{16} ions cm^{-2} s^{-1}.

From the depth profiles, it is clear that there is a variation in the measured ^{6}Li isotopic fraction with depth of measurement in the same depth profile. In particular, the beginnings of each profile (the first 0.5 µm in profiles #2 to #5, Figure 7.4a) show lower $C(^6\text{Li})$ than the rest of the profile. This change with depth suggests that there may be both surface and bulk diffusion occurring with different kinetics, or some change in the detected lithium isotope concentrations with depth due to measurement effects. In addition, as seen in Figure 7.3d and discussed previously, the changing source concentration of ^{6}Li

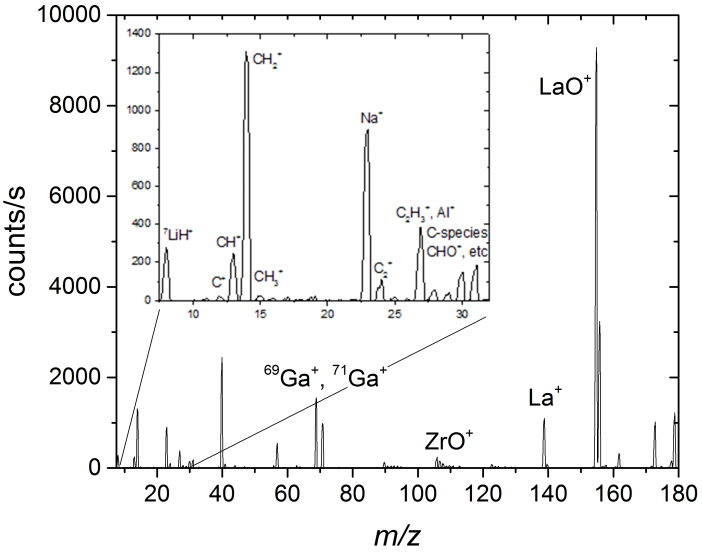


Figure 7.5: FIB-SIMS surface positive ion mass spectrum (where m/z is mass to charge ratio) over 100 µm by 100 µm area of LLZO pellet after ^{6}Li exchange, with 300 pA primary ion beam current, giving a dose rate of 1.9x10^{13} ions cm^{-2} s^{-1}.

(the metal is not acting as a large enough reservoir) will complicate the interpretation here.

7.2.3 Mass Interferences and Surface Chemistry

To investigate these surface phenomena, the presence of interferences with the same mass as the lithium species (with a mass to charge ratio, m/z, of 6 or 7) was explored by taking mass spectra at the surface of LLZO, shown in Figure 7.5.

The mass spectrum in Figure 7.5 shows species indicative of matrix species in LLZO detected as Li^+, LaO^+ and ZrO^+ secondary ions, $^{69}Ga^+$ species from the primary ion beam, as well as additional, largely carbon-based, peaks. C^+ and $^7LiH^+$ are examples of detected secondary ion species which could result in possible interferences and affect the measured $C(^6Li)$, if their partner species C^{++} (m/z = 6) and $^6LiH^+$ (m/z = 7) exist. We can try to correlate the presence of other carbon species with the existence of a C_2^{++} species in the depth profiles; however this is not straightforward owing to differences in ionisation behaviour of the species.

Previous results (Chapter 6) show that corrosion layers of LiOH and Li_2CO_3 form on the surface of the garnet pellets during air exposure, resulting from proton-lithium exchange processes, in addition to the creation of a lithium-depleted, proton-rich H-LLZO region immediately below the corrosion products. It was shown that the storage and transfer of LLZO from the glove box into the air is enough to observe LiOH formed at the surface, in the first 0.1 µm of depth profiles of the samples, and a sample with a history of handling in air will definitely have been subject to corrosion processes.

The Ge0.05-LLZO pellet used in the first set of diffusion experiments had previously

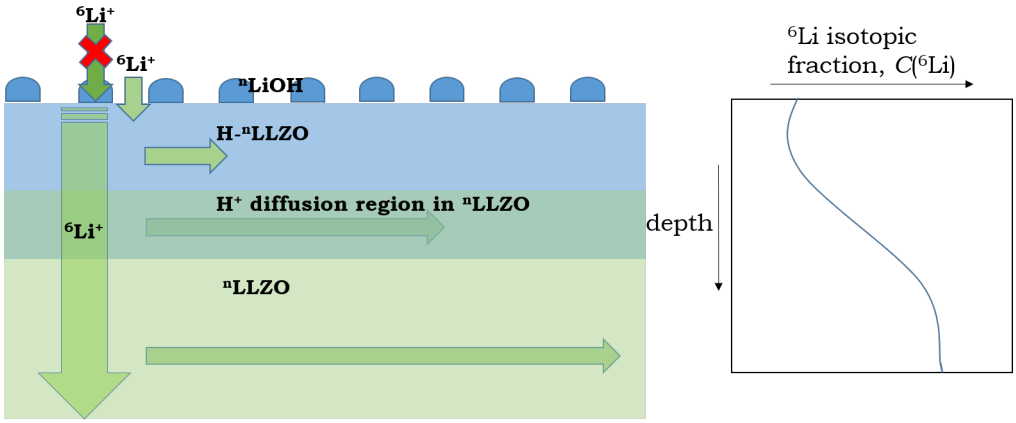


Figure 7.6: Schematic of possible Li diffusion pathways in a LLZO grain which has undergone proton-lithium exchange; (left hand image): showing the different regions of LLZO (proton-rich H-^{n}LLZO and lithium-rich ^{n}LLZO, and region of H^+ diffusion, where n indicates natural isotopic abundance lithium), corrosion product (LiOH), and the diffusivity of ^{6}Li through these regions (arrows), giving rise to the observed ^{6}Li isotopic fraction profile with depth (right hand image).

been exposed to air (for example, during EIS measurements) prior to the lithium exchange experiment being carried out, so the diffusion profiles seen in Figure 7.4a would be subject to the effect of these corrosion products (also illustrated in the poor adherence of the ^{6}Li metal on the pellet described previously). These layers may have an effect on the observed lithium isotopic fraction at the surface - and deeper into the material - by altering the diffusive behaviour of lithium at the surface (corrosion layers, likely low D(Li)) and near-surface (H-LLZO region, seen in Chapter 6 to have lower lithium mobility), compared to the bulk LLZO material. The ^{6}Li diffusion would have to proceed via a complicated multi-layered pathway (illustrated in Figure 7.6), through regions of corrosion phases (LiOH and H-LLZO), each with a different lithium diffusivity and exchange coefficient at each interface. A region of low diffusivity close to the surface followed by fast bulk diffusion would give rise to the observed shape of ^{6}Li isotopic fractions seen in Figure 7.4a (schematic in Figure 7.6).

By using the multiple-sampling method, taking consecutive depth profiles from the ^{6}Li source, we can at least assume that each depth profile has the same surface and interference species, so we are able to take a direct comparison of the profiles on the same sample and negate these surface effects. The effect of surface roughness was also investigated but not discussed here (see Appendix A.6).

7.2.4 Charging Effects

Another aspect of the experimental procedure was investigated - the role of sample charging during measurement. That the incoming positively charged ion beam induces positive charges on the sample surface, thus changing the secondary ion extraction potential (see the secondary ion energy curve, Figure 7.2), is often a problem during SIMS depth-profiling of electronically-insulating materials. This in turn results in an altered energy of extracted secondary ions, with the outcome that extracted secondary ions may

shift out of the energy acceptance window [274]. This effect can be minimised/avoided in the FIB-SIMS by tuning the detector to adjust the energy acceptance window, using metal clips on the sample to act as a ground between the sample and the metal sample holder and performing analyses close to the clip.

However, during heavy sputter processes, where a large primary beam current is applied over a small area, orders of magnitude more positive charges are induced on the sample surface, and high-mobility ions may migrate away from the region of positive charge (into the bulk). This results in an artefact in the ion distribution caused by migration of the ion in the electric field. This is especially problematic in insulating materials such as SiO_2 embedded with alkali metals [274].

To investigate the effect of charging, experiments were performed on an undoped LLZO pellet sample with and without the application of a tungsten needle at the surface adjacent to the area under analysis. An in-situ micromanipulator (Kleindiek) was used for touching the needle down onto the samples. The samples were (as always), attached to the metal sample holder with the use of a steel clip measuring about $\frac{1}{2}$ to $\frac{1}{4}$ the total surface area of the pellet sample. Both mass spectra and depth profiles were taken of the same area. A comparison is given in Figure 7.7.

It appears from the results of these experiments that using a tungsten needle has some effect on the measured secondary ion signals during depth-profiling, but that the metal clip and sample holder are enough to prevent charging of the (nominally electronically insulating) sample under these conditions, as the ions are not seen to migrate away from the primary ion beam in both cases - they remain stable with depth in the bulk material. The energy window of lithium detection for both isotopes is not shifting appreciably during measurement, as indicated by the similar isotopic fraction profiles with and without using a needle (Figures 7.7c and 7.7d), which means we are sitting at a good energy offset value for atomic lithium detection in both ^{6}Li and ^{7}Li isotope cases.

The relative intensities of the ions do differ (Figures 7.7a and 7.7b.), in that the $^7Li^+/LaO^+$ ratio increases on contacting the tungsten needle on the surface, and the $^{69}Ga^+$ counts rise slightly with depth greater than 1 µm. The other ion intensities also display a sharper/faster drop to stable counts when the needle is applied; they drop to their plateau values at ~ 0.5 µm depth compared to ~ 1 µm in the sample without needle contact.

The mass spectra data (Figures 7.7e and 7.7f) also show that on applying the needle, the Li counts are slightly higher, but all other species are reduced in counts (also in line with the depth profiles).

It should be noted that the Ga^+ primary ion beam is operating under dynamic sputtering conditions (dynamic SIMS, see Chapter 4) from the beginning of the depth profiles under these conditions (1 nA current over 15 µm by 15 µm crater area). The dose of the Ga^+ ions is the number of ions that are impacted and absorbed by the target through a given area. Beam current is a measure of the rate of flow of energy (or ion delivery per unit time), with units of Amperes, equivalent to charge per unit time, $C\,s^{-1}$, where $1\,C = 6.242x10^{18}$ electrons. The flux is the dose as a function of time. For example, the

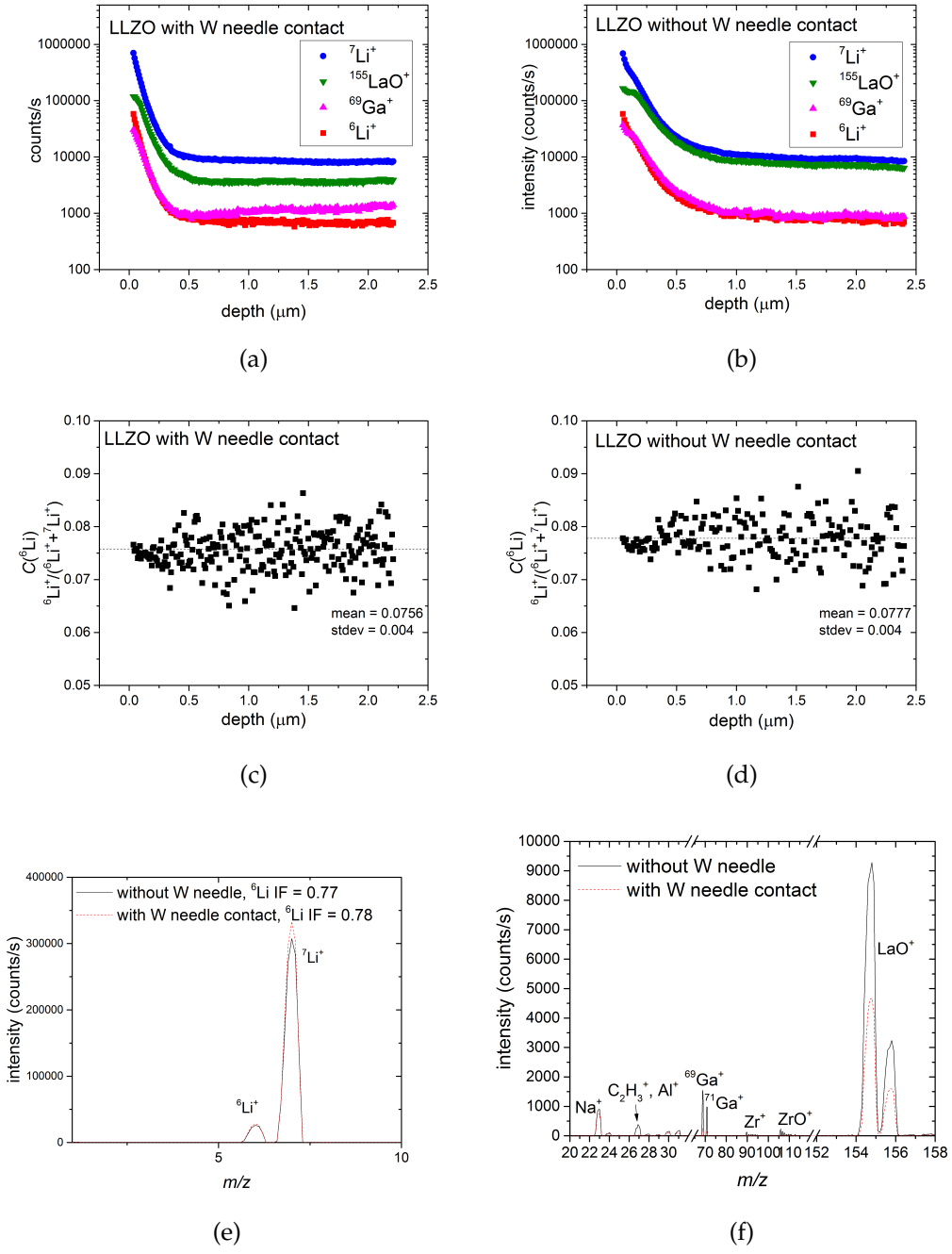


Figure 7.7: Effect of a tungsten needle contact on LLZO pellet. Depth profiles over 15 µm by 15 µm area with with 1 nA primary ion beam current (giving a dose rate of 2.8x10^{15} ions cm^{-2} s^{-1}), with and without a tungsten needle: (a,b) intensities of secondary positive ions $^{7}Li^{+}$, $^{6}Li^{+}$, $^{155}(LaO)^{+}$ and $^{69}Ga^{+}$; (c,d) $C(^{6}Li)$ isotopic fractions (IF); (e,f) positive ion mass spectra with 300 pA primary ion beam current rastered over 100 µm by 100 µm area (giving a dose rate of 1.9x10^{13} ions cm^{-2} s^{-1}).

amount of Ga^{+} ions impacting the crater area per unit time is given by 1x10^{-9} x 6.242x10^{18}. This is equivalent to 6.242x10^{9} ions/s. Dividing by the crater area, 225 µm^{2}, gives a flux of 2.77x10^{15} ions s^{-1} cm^{-2}. So after 1 second, the dose is 2.77x10^{15} ions cm^{-2}. This is above the 10^{15} ions cm^{-2} threshold for the steady state regime for dynamic SIMS from the outset, which means that the primary ion implantation and removal processes are

equally matched during the depth-profiling.

7.2.5 Thin Film Lithium-6 Sources

Another important issue in the development of a solid state diffusion experiment route is to enable maximum contact at the interface of the Li metal and LLZO, to ensure the diffusion is across a homogeneous boundary in a system of interest for solid state battery development.

Because of the difficulties in handling and controlling the thickness and cleanliness of the ^{6}Li metal (which was provided by the supplier in large chunks in mineral oil), some experiments were attempted in which Li metal was evaporated onto the surface of Al0.15-LLZO pellets by thermal evaporation. Thermal evaporation is a common method of physical vapour deposition (PVD) and uses a resistive heat source to evaporate a solid material in a vacuum environment to form a thin film. The material is heated in a high vacuum chamber to produce a vapour stream, which traverses the vacuum chamber with thermal energy and coats the substrate [275].

In these experiments, thermal evaporation was performed using a Lesker Spectros instrument, with the help of Mr Roland Leber of Dr Heutz's research group at Imperial College London. Because the instrument is purged with N_2 gas, the setup involved the use of a capping layer to prevent the reaction of the lithium metal to form Li_3N.

Aluminium/Lithium Thin Films

Owing to time constraints, and difficulties with the system, the first set of samples were coated with Li metal (50 nm, monitored by a quartz microbalance) and capped with Al metal (20 nm). A Si(001) wafer was also used as a reference and coated along with the Al0.15-LLZO pellets. When analysed in the FIB-SIMS, depth profiles of the samples (Figures 7.8a to 7.8d) showed an OH^- secondary ion peak in the samples which was most pronounced in Al0.15-LLZO between the bulk substrate and the Al top coating. Because the OH^- peak is present in the Si(001) sample, it is likely that it arises from LiOH produced when the Li metal film reacts with air after removing the sample from the evaporating chamber. This implies the Li is not sufficiently protected by the Al layer. There could be a more pronounced peak on the Al0.15-LLZO substrate owing to the known reactivity of LLZO with air to form hydroxide species. We were unable to transfer the substrates to the evaporation chamber without exposing them to the air - which could have led to some LiOH formed during reactivity of Al0.15-LLZO in air prior to deposition of the films. There also appeared to be some intermixing between the thin film layers, probably as a result of them being too thin, as the edges of each layer is not very sharp in the depth profiles. Depth profiles are given in terms of sputter time rather than depth, as the sputter rate changes through the layers and sputter time is not linearly correlated to depth.

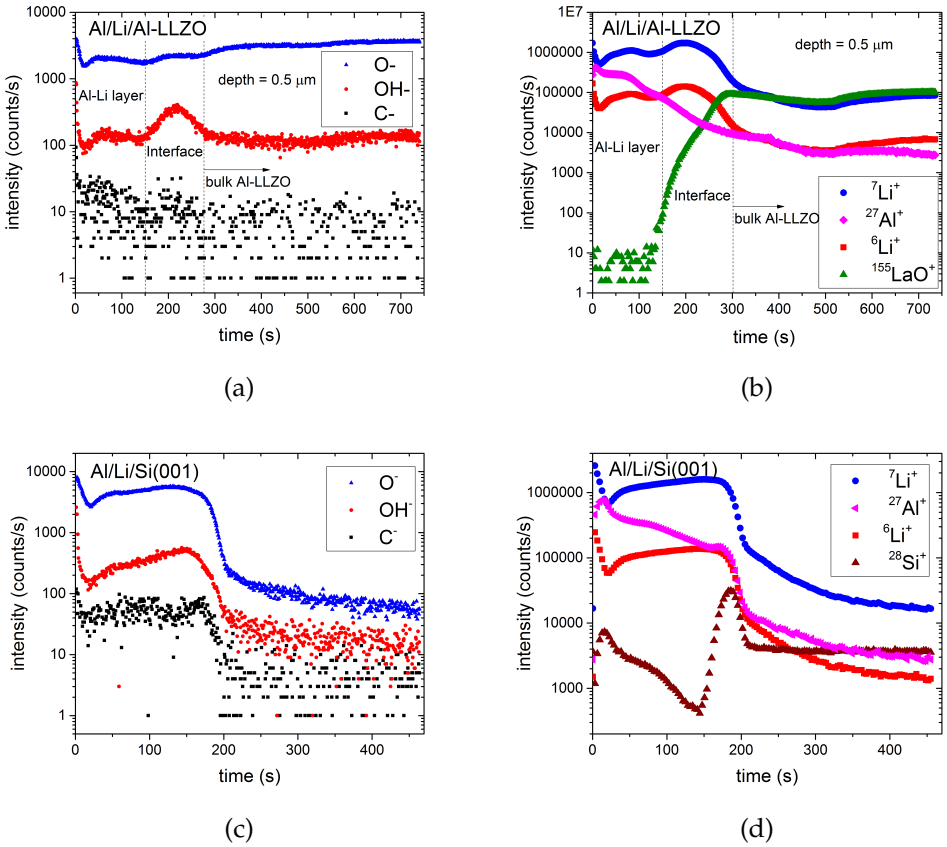


Figure 7.8: FIB-SIMS depth profiles showing secondary ion intensities taken at 386 pA over a crater area 15 µm by 15 µm of Al and Li films deposited on: (a,b) Al0.15-LLZO, crater depth 0.5 µm; and (c,d) Si(001) wafer, crater depth 0.8 µm. The primary ion beam dose rate is 1.1x10^{15} ions cm^{-2} s^{-1}.

LiF/Lithium Thin Films

To enable faster deposition, and obtain a thicker set of thin film layers, LiF was next used instead of Al as a capping layer, as it can be heated more quickly than metallic sources. 100 nm of Li metal was capped by 50 nm of LiF.

However, because of the time still taken to deposit the two layers (several hours in total), and the temperature changes during deposition it was decided, that for the lithium isotopic diffusion experiments, to use a natural isotopic abundance Li metal for the deposited layer, and to apply the tracer ^{6}Li metal afterwards. This way the diffusion process occurs within a user-defined short time at room temperature. Figure 7.9 shows unexchanged profiles for the LiF/Li/Al-LLZO sample. We again observed an OH^- peak in both Si(001) and Al-LLZO samples, which appears at the interface of the Li and LiF layers (around 50 to 100 s sputter time in Figure 7.9c), likely occurring due to reactivity of the Li during unclean handling. The mean lithium isotopic fraction is 0.077, and there are clear differences in sputter rate throughout the layers, indicated by the large changes in ion counts (particularly $^{69}Ga^+$, seen in Figure 7.9b). Normalising positive ion counts to the $^{69}Ga^+$ counts (Figure 7.9d) allows the difference in sputter rate to be removed, and shows the bulk Al0.15-LLZO is reached between 100 to 200 s sputter time.

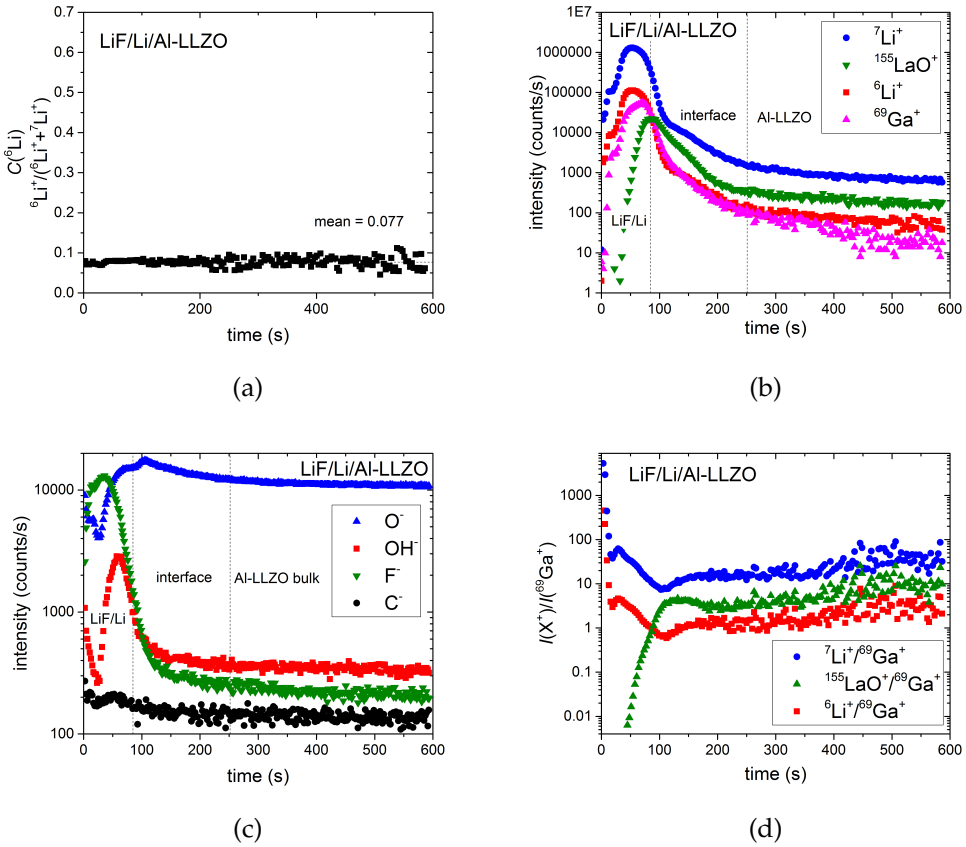


Figure 7.9: FIB-SIMS depth profiles on LiF/Li/Al0.15-LLZO sample (100 nm Li, 50 nm LiF); crater has dimensions 15 µm by 15 µm, depth approximately 1 µm. the primary ion beam current is 1 nA, giving a dose rate of 2.8x10^{15} ions cm^{-2} s^{-1}. (a) $C(^6Li)$ isotopic fraction; (b) positive secondary ion intensity; (c) negative secondary ion intensity; (d) positive ion intensity I given as a ratio to $^{69}Ga^+$ intensity.

^{6}Li Exchange with LiF/Lithium Thin Films

Next, ^{6}Li metal was applied to the layered LiF/Li/Al-LLZO sample to create a diffusion couple, and depth profiles were taken at increasing distances from the edge of the ^{6}Li metal. Figure 7.10a shows the first set of depth profiles measured 5 hours after applying the ^{6}Li metal. They are located 180 µm and 420 µm from the source, with depths of 0.7 µm and 1 µm, respectively. $C(^6Li)$ for both depth profiles begins at the background level (until about 0.2 µm depth), corresponding to a degraded region of LiF/Li on top of the Al0.15-LLZO pellet where Li diffusion is slow (seen from the negative depth profiles of the unexchanged sample under the same conditions, Figure 7.9c). The isotopic fraction then increases with depth for some time until a plateau is reached. The maximum $C(^6Li)$ increases with proximity to the ^{6}Li source. This implies that Li exchange is occurring in Al0.15-LLZO as it is becoming enriched in ^{6}Li, but that diffusion occurs slowly through the LiF/Li mixed layer which has reacted with the air, again showing differences in surface and bulk Li diffusion, akin to the first experiments performed on bare LLZO with ^{6}Li metal.

The analysis was performed a day later on the same sample, with isotopic fraction

depth profiles in Figure 7.10b. The same behaviour is seen for the samples analysed on the same day as the exchange started, with increasing maximum concentrations of ^{6}Li as the distance from the metal source decreases, except that on day 2 the background concentration (0.077) is reached more slowly (at longer distance) than on day 1, as the Li has been diffusing through Al0.15-LLZO for longer. A summary of all 5 depth profile measurements is given in Figure 7.10d, showing the isotopic fraction $C(^6\text{Li})$ at 1 µm depth for each of the depth profiles measured.

We can very crudely estimate the Li diffusivity in the sample from the data points in Figure 7.10d, by estimating the length x at which background is reached on day 1 and day 2, and using $x = 4\sqrt{Dt}$ to find D, where t is 5 hours on day 1 and 24 hours on day 2. The values are summarised in Table 7.3, and show that D found from these experiments is of the same order of magnitude as D^σ(Li) expected from Nernst-Einstein conductivity conversions from EIS on Al0.15-LLZO (assuming that the number of charge carriers is equal to the total number of Li ions in the garnet).

Table 7.3: Estimated Li diffusivity from length x for $x' = 2$ and exchange time t in ^{6}Li/LiF/Li/Al0.15-LLZO isotopic exchange experiments, from Figure 7.10d.

Day of ^{6}Li exchange	**Exchange time t (hours)**	**Length x from Figure 7.10d (µm)**	**Diffusivity D, from $x = 4\sqrt{Dt}$ ($m^2\ s^{-1}$)**	**EIS-estimated diffusivity D^σ**
Day 1	5	400-600	$5 - 8\text{x}10^{-13}$	$\sim 5\text{x}10^{-13}$
Day 2	24	600-800	$3 - 5\text{x}10^{-13}$	$\sim 5\text{x}10^{-13}$

This method shows promise in creating a LLZO/Li couple which has intimate contact between layers, ideally using a thick lithium metallic film only, which can later be contacted to a source of ^{6}Li using ^{6}Li metal. Using a labelled ^{6}Li metallic film deposited directly would be ideal for ensuring that the diffusion occurs directly from the metal into the garnet, without an additional diffusion layer and could be used with the direct depth-profiling or linescan method using TOF-SIMS; however, as seen before in Section 7.2.2 with the decrease in $C(^6\text{Li})$ of the residual metallic isotope source, the film would also be no longer acting as a semi-infinite ^{6}Li source and would quickly deplete in ^{6}Li, which could complicate the interpretation of diffusion profiles unless very short exchange times were used. Any thin-film method would need to be performed with an instrument with a modified setup from the current system used here, to prevent any reaction of garnet or metal in the diffusion couple - ideally coupled to a glove box, using argon purge gas in the PVD chamber and using a transfer module to carry to the FIB-SIMS to ensure the Li metal is protected. The cleanliness of the setup is critical for ensuring intimate contact of the diffusion couple and accurate determination of diffusion coefficients.

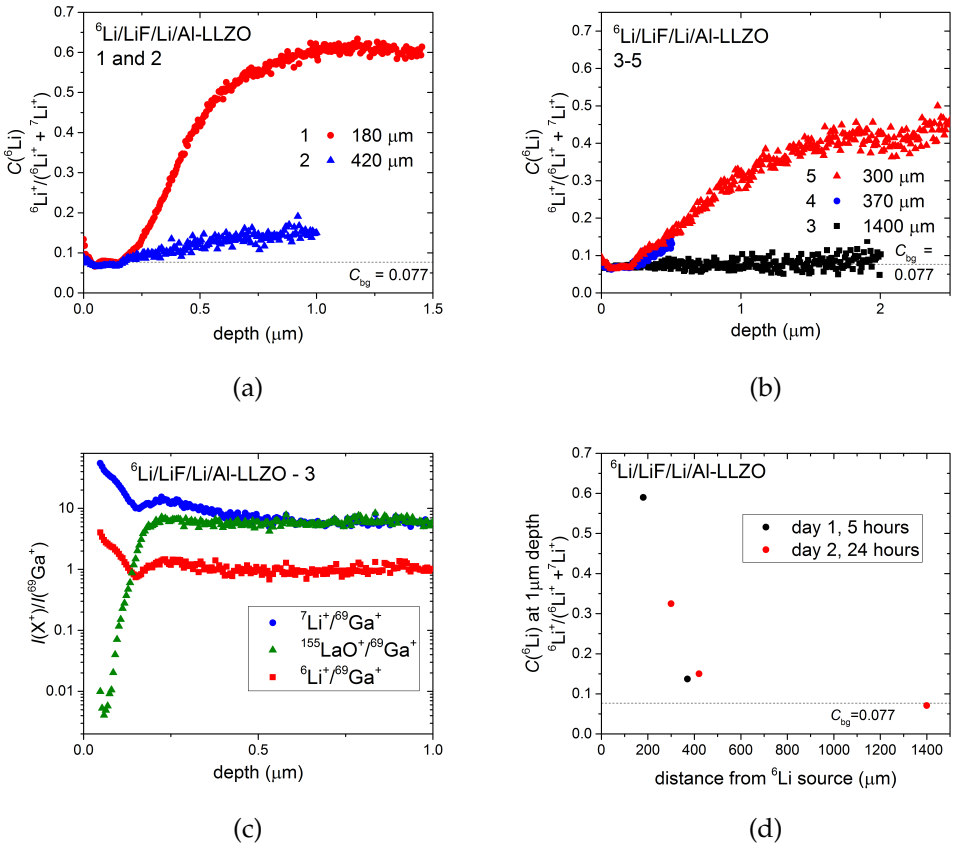


Figure 7.10: ^{6}Li isotopic exchange depth profiles using ^{6}Li metal source on LiF/Li/Al0.15-LLZO sample (100 nm Li, 50 nm LiF), at increasing distance from ^{6}Li source. The primary ion beam dose rate is 2.8x10^{15} ions cm^{-2} s^{-1}. (a) Isotopic fraction depth profiles 1 to 2 measured on day 1 (5 hours exchange time); (b) depth profile isotopic fractions 3 to 5 measured 1 day after the exchange started (day 2, 24 hours exchange time); (c) positive secondary ion counts normalised to Ga^+ in depth profile 3; (d) summary of ^{6}Li isotopic fractions at 1 µm depth as a function of distance from ^{6}Li metal.

7.2.6 Summary of Solid State Diffusion Method

The solid state lithium tracer diffusion method using SIMS and a ^{6}Li metal/LLZO diffusion couple is a macroscopic method for following the mass transport of lithium in LLZO pellets. It has a number of experimentally-related difficulties which, if overcome, would make it a highly valuable tool in evaluating lithium diffusivity in garnets and other lithium conducting materials. Results can be correlated with other experimental techniques to contribute to a fuller understanding of lithium transport mechanisms in these systems.

The work introduced here shows that sample handling and cleanliness prior to the exchange experiment being performed are key for ease of interpreting diffusion profile data - this can be clearly linked to the reactivity of LLZO in the presence of moisture and CO_2 as discussed in Chapter 6. Surface and bulk differences in Li diffusivity arise from the formation of corrosion and altered layers following lithium-proton exchange processes, and contamination of LLZO surfaces with carbon-based impurities; these

protonated phases have much lower lithium diffusivities than the fast Li-conducting LLZO. Obtaining ^{6}Li metal is difficult, and requires careful cleaning and handling of the material, so using ^{6}Li-enriched LLZO made from $^6Li_2CO_3$ or other suitable precursors and making a diffusion couple with natural abundance lithium metal, which is available as thin sheets, may be sensible.

The relative masses of the metal and the LLZO pellet are important to know if we are in a semi-infinite diffusion regime, where the amount of Li atoms available for exchange in the metal is far in excess of the number of Li atoms in LLZO, as the fitting of the resulting diffusion profiles depends on these boundary conditions.

Interface considerations are also important, as the quality of the Li metal/LLZO contact will affect the diffusion profiles obtained (and whether we model the source as a point source or plane sheet).

Finally, owing to the inherently fast diffusion of Li in the garnet material, which reaches 10^{-13} m^2 s^{-1} at room temperature, timings have to be carefully considered to ensure the beginning of the diffusion profile can be measured in order to accurately fit k and D using finite difference simulations, rather than leaving it too long for the Li to diffuse and consequently measuring a flat profile. To enable this, linescan analyses with TOF-SIMS (measuring diffusion lengths of several hundred micrometres) could be used; however, this requires cutting and polishing the exchanged sample with care to prevent reactions of Li metal and LLZO.

The advantage of the direct depth-profiling over the linescan method is the ability to select regions within grains, therefore ensuring in-grain diffusion only is measured. In the case of a large-area measurement (i.e. linescan analysis, large area depth profiles, or multiple sampling methods), grain boundary effects may also be distorting the diffusion profile - leading to a long tail in the profile, as in the case of fast Li diffusion along the grain boundaries. This would be a useful parameter to quantify, especially in light of the findings in Chapter 6 which found the grain boundaries to be very susceptible to proton-lithium exchange.

7.3 Nuclear Magnetic Resonance Results

Solid state NMR measurements were carried out in Professor Grey's group at Cambridge University in collaboration with Dr Lauren Marbella and Steffen Emge. Pulsed field gradient (PFG) NMR measurements were conducted to extract the Li diffusion coefficients for the garnet samples, and measured over a range of temperatures to give the activation energy. Variable temperature $T1$ (spin-lattice) relaxation experiments were also used to measure the activation energies for Li ion hopping.

7.3.1 ^{7}Li Pulsed Field Gradient (PFG) NMR

Preliminary room temperature PFG NMR measurements were made in which the time that the Li ions were allowed to diffuse during the experiment was varied to determine the length scales that could be probed within the experiment (see Appendix A.5.1 Figure

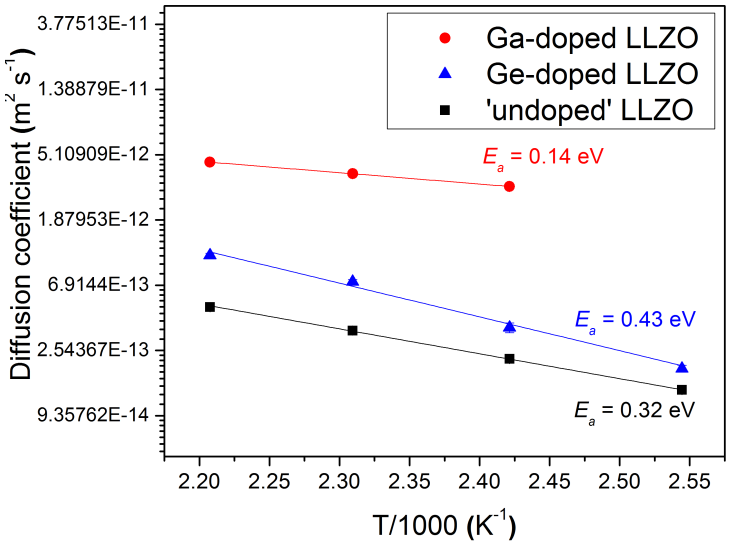


Figure 7.11: Variable temperature PFG NMR data for Ga-, Ge-doped and undoped LLZO powders used to derive activation energies, E_a.

A.6). This was followed by variable temperature PFG NMR over the temperature range 120 to 180 °C (140 to 180 °C for Ga-LLZO), Figure 7.11, using typical diffusion times Δ of 50 to 150 ms (which was expected to be probing the equilibrated Li diffusivity, close to that expected for tracer diffusion). It was found that the apparent ^{7}Li diffusion coefficient for a Ga0.15-LLZO powder sample is 6.2×10^{-13} m^2 s^{-1} at room temperature, which is very close to that expected from impedance measurements (see predicted values in Table 7.4), and corresponds to room temperature lithium conductivities of 10^{-3} S cm^{-1}. Undoped LLZO (partly cubic-stabilised with Al from the crucible, measured by inductively coupled plasma (ICP) spectroscopy to contain 0.16 Al atoms per formula unit) had a room temperature ^{7}Li diffusivity of 6.5×10^{-15} m^2 s^{-1}, which is lower than the EIS-derived diffusivity by about one order of magnitude. The Ge0.10-LLZO powder sample had a room temperature diffusion coefficient of 2.6×10^{-15} m^2 s^{-1}, which is two orders of magnitude lower than predicted from EIS. The EIS-derived diffusivities assume the number of available charge carriers to be equal to the amount of Li in the garnet lattice which, according to some papers, may be an overestimate [50, 51, 150]. In this case, we are overestimating the diffusivity by applying this assumption. In addition, the discrepancy may be caused by the effect of grain boundaries or particle size (a large low Li mobility grain boundary contribution or small particle sizes resulting in ion 'turn around' and a reduced apparent diffusivity in the NMR measurements). It might also be that the sample degraded over time before NMR measurement. The activation energies were also extracted using the PFG NMR method, and are summarised in column 3 of Table 7.5. The activation energies are in good agreement with the EIS-derived values.

Table 7.4: Room temperature diffusion coefficients D(Li) for three LLZO samples as predicted from EIS measurements, and experimentally measured values from PFG NMR experiments. Where sample composition was measured using inductively coupled plasma (ICP) spectroscopy, the measured dopant stoichiometry is given.

Sample	**Nominal composition or stoichiometry from ICP**	**Conductivity, from EIS (S cm^{-1})**	**Predicted diffusivity D, from EIS (m^2 s^{-1})**	**Diffusivity D, from PFG NMR (m^2 s^{-1})**
Ga0.15-LLZO	$Li_{6.55}Ga_{0.15}La_3Zr_2O_{12}$	1.2x10^{-3}	8.2x10^{-13}	6.2x10^{-13}
Ge0.10-LLZO	$Li_{6.6}Ge_{0.1}La_3Zr_2O_{12}$	10^{-5} to 10^{-4}	10^{-15} to 10^{-14}	2.6x10^{-15}
	ICP: Ge=0.05, Al=0.12	6x10^{-4}	3.8x10^{-13}	
'undoped' cubic LLZO	$Li_{7-3x}Al_xLa_3Zr_2O_{12}$ ICP: Al=0.16	3.8x10^{-5}	2.4x10^{-14}	6.5x10^{-15}

Table 7.5: Activation energies from EIS, PFG and $T1$ NMR measurements of LLZO samples.

Sample	**Activation energy (eV), EIS**	**Activation energy (eV), PFG NMR**	**Activation energy (eV), $T1$ NMR**
Ga0.15-LLZO	0.17	0.14	0.094
Ge0.10-LLZO	$\sim$ 0.4	0.43	0.134
'undoped' cubic LLZO	$\sim$ 0.4	0.32	-

7.3.2 ^{7}Li Spin Lattice Relaxation ($T1$) NMR

^{7}Li spin-lattice relaxation ($T1$) values were measured as a function of temperature in the temperature range 20 to 180 °C in order to extract activation energies for Ga- and Ge-doped LLZO samples (see column 4 of Table 7.5 and Appendix A.5.2 Figure A.7). These were fitted using an Arrhenius fit to extract the activation energies. In general, the activation energies measured with this method are lower than those obtained by EIS measurements. The absolute values of the activation energies are sensitive to different length scales and degrees of long-range order probed by each technique. NMR $T1$ data is highly sensitive to local ion hopping, such as the rapid oscillation over the low energy barrier between the split Li sites (octahedral and tetrahedral). In tracer techniques this local oscillatory behaviour is averaged out and only long-range ionic transport in the bulk contributes, whereas EIS data contains contributions from the entire sample, including grain boundary resistance, unless the responses from the different contributions are clearly separable. This is likely to be the reason for the lower E_a values from $T1$ NMR experiments.

7.4 Summary

Owing to the importance of lithium oxides for lithium ion batteries as electrode materials and solid state electrolytes, the scientific effort on the realisation of relevant diffusion experiments needs to be significantly improved. More tracer-based experiments are especially necessary to obtain reliable comparative data to established non-tracer methods like impedance spectroscopy or nuclear magnetic resonance spectroscopy, which probe diffusion and conductivity on different time and length scales.

This chapter included the preliminary development of a macroscopic tracer diffusion technique, using lithium stable isotopes and SIMS analysis, to determine the long-range lithium transport in LLZO electrolytes, highlighting the challenges in designing a workable experiment. By comparing the results of this method with microscopic (EIS and $T1$ relaxation NMR) and other macroscopic techniques (PFG NMR), as well as computational studies in the literature, we can begin to build a picture of the true nature of lithium diffusion in LLZO.

As discussed in Chapter 2, Section 2.2.4, when comparing macroscopic (long-range diffusive processes) and microscopic (local, atomic scale influences) measures of diffusion, a correlation factor is used to account for the non-ideality of the macroscopic diffusion process and is defined by the ratio of the two diffusion coefficients [40, 41]. This chapter uses diffusion coefficients derived from EIS measurements, PFG NMR and chemical and tracer diffusion (SIMS tracer experiments). The errors associated with the derivation of these diffusion coefficients from EIS and also the tracer diffusion measurement are very large here, and these results are very qualitative, and must be considered as work in progress.

Amongst the NMR samples, only the Ga-LLZO PFG NMR and EIS derived values for diffusivity are in agreement (with the activation energies in good agreement for all samples, see Section 7.3). This also suggests that both long-range charge transport (EIS) and local mass transport (NMR) are linked in Ga-LLZO and suggests that the motion of Li on both macroscopic and microscopic scales are equivalent, implying the motion is to some extent uncorrelated, and only related to short-range local hops. This is contrary to the literature consensus of correlated lithium motion in garnets. It is unclear why this is seen here, and only for Ga-LLZO. The NMR extracted diffusivities can be thought to approach tracer-diffusion values for long relaxation times (see Appendix A.5.1 for plots of D_{apparent} and mean square displacement ($\sqrt{x^2}$) as a function of diffusion time Δ).

When comparing chemical diffusivities D_C measured by isotopic exchange and extracted over large areas using the multiple profiling method with the EIS derived diffusivities, D^σ, the chemical diffusion coefficients were found to of the same order of magnitude or slightly higher than the EIS-derived values. The Haven ratio links the tracer diffusion to the EIS-derived charge transport diffusivity, and exceeds unity when the diffusion proceeds by correlated motion. In this case, we have not found true self (tracer) diffusion; rather, we have measured chemical diffusion. Here the relative values of D_C and D^σ might indicate some extent of correlated motion of Li (a Haven ratio of ≥ 1), where the chemical diffusion measured here is expected to be larger than the tracer

diffusion D^*. This would need to be confirmed by finding the true tracer diffusivity (i.e. using a ^{6}Li-LLZO/^{n}LLZO couple) in a more rigorous set of experiments with modelling of the diffusion. Additionally, the assumptions made when deriving diffusion coefficients from EIS measurements were based on all the lithium being available for charge transfer, which is unlikely. Using a value of approximately 10 % of the total Li atoms (as predicted by Ahmad [150]) in the Nernst-Einstein equation (i.e. N drops from a nominal 52.4 Li to 0.52 Li in Ga- and Al-LLZO), the derived diffusivity D^σ increases by about one order of magnitude, which may explain this discrepancy.

Sample and measurement effects need to be considered; for example, the NMR measures powder samples and is affected by particle size and measurement conditions (i.e. diffusion time Δ and gradient strength g, which determine the measured apparent diffusivity). Additionally, NMR does not account for morphological effects such as grain boundaries. EIS measurements in LLZO are subject to errors in fitting, and as seen previously (Chapter 5, Section 5.2.2), the bulk and grain boundary resistance contributions are difficult to separate in measurements taken at room temperature. Finally, the large area sampling method used to extract D in the tracer experiments here follow transport across both grains and grain boundaries. Perfecting the within-grain method (which will require short diffusion lengths of less than 5 µm) of tracer diffusion would enable purely intra-grain Li transport to be found.

Ab initio molecular dynamics simulations by Jalem *et al.* [110] have suggested that lithium mobility in the cubic LLZO takes place through a correlated, concerted migration mechanism, which is governed by two main factors: (i) the electrostatic repulsions of certain neighbouring Li sites, preventing Li occupation of consecutive $24d-48g/96h-24d$ (Td-Oh-Td) sites, and (ii) the unstable residence of Li at the tetrahedral $24d$ site which can trigger ion mobility and reconfiguration of surrounding Li neighbours to accommodate the initiated movement. The notion of the lithium motion being correlated is in tentative agreement with the tracer diffusivity trends explored here.

There is still a way to go in perfecting the tracer method for LLZO materials; however, the findings outlined in this chapter show the feasibility of using a range of methods to find the self-diffusion of lithium, which could be used in a complementary way to understand the bulk and grain boundary diffusion when compared to other measurement methods.

7.5 Suggested Future Work

The solid state method of tracer diffusion using a thin film of ^{6}Li-enriched material (either the metal, or an oxide) looks to be the most promising way forward with this technique. Both within grain and inter-grain diffusion could be followed by adjusting the diffusion times and sample preparation for analysis (using FIB-SIMS depth-profiling for selective area diffusion and linescan, or large area depth-profiling, in the TOF-SIMS for grain and grain boundary diffusion). SIMS mapping could also be carried out by cutting a trench perpendicular to the surface, applying ^{6}Li metal to allow exchange to occur, then mapping the revealed cross-section. Accurate fitting of the diffusion profiles using finite difference

simulations to correctly model the boundary conditions is suggested to evaluate D^* and k^* in this system.

Variable high temperature measurements could be made to extract activation energies from the diffusion coefficients, and this could serve as a method to suppress the Li motion at room temperature during post-analysis. In addition, adding an anneal step at elevated temperature and then measuring the broadening of profile as a function of time could also work [57, 58].

Chapter 8

Symmetric Cell Cycling and Failure in $Li_7La_3Zr_2O_{12}$ / Lithium Metal Cells

As described in Chapter 3, the cell performance of $Li_7La_3Zr_2O_{12}$ (LLZO) electrolyte-based lithium batteries has a strong dependence on the interfacial properties between the lithium metal and the solid electrolyte; the interfacial resistance (also known as the area specific resistance, ASR, normalised by the area of the electrode), provides a measure of the ease of transport at this interface, and has shown to depend on the interfacial contact between electrode and electrolyte components, as well as the charge carrier mobility. This interfacial resistance was seen to be compromised in samples of LLZO following proton-lithium exchange in water and after being exposed to air (Chapter 3, Section 3.4 and Chapter 6, Section 6.3). The cell performance can be measured by galvanostatic (constant current) charge/discharge cycling, measuring the voltage response for different applied current densities with time. The measured voltage response gives information on the resistance of the cell, and whether short-circuiting has occurred following 'cell failure'. Most reports in the literature of short-circuit in LLZO/Li metal cells cite the cause of cell failure as the propagation of lithium dendrites, which cause an irreversible deterioration in cell performance after a given threshold 'critical' current density.

This chapter includes preliminary work investigating the differences in the critical currents for both gallium- and aluminium-doped LLZO (Ga-LLZO and Al-LLZO, respectively), illustrating the effect of dopants on the chemical and electrochemical properties of the electrolyte with a lithium metal electrode.

8.1 Characterisation of Pristine Pellets

Both Al-LLZO and Ga-LLZO compositions, with 0.15 atoms per formula unit nominal dopant concentration, were used in this chapter as characterised in previous chapters in this thesis. Their X-ray diffraction (XRD) patterns (Appendix A.7, Figure A.12) show cubic $Ia\bar{3}d$ symmetry with a small Li_2ZrO_3 impurity, as seen previously (Chapter 6, Figure 6.5a). Scanning electron microscope (SEM) images (Figure 8.1) of the thermally etched (at 900 °C for 30 minutes in an argon atmosphere) plane and cross-sections (fracture surfaces) of the pellets show similar grain size distributions for both compositions, ranging from

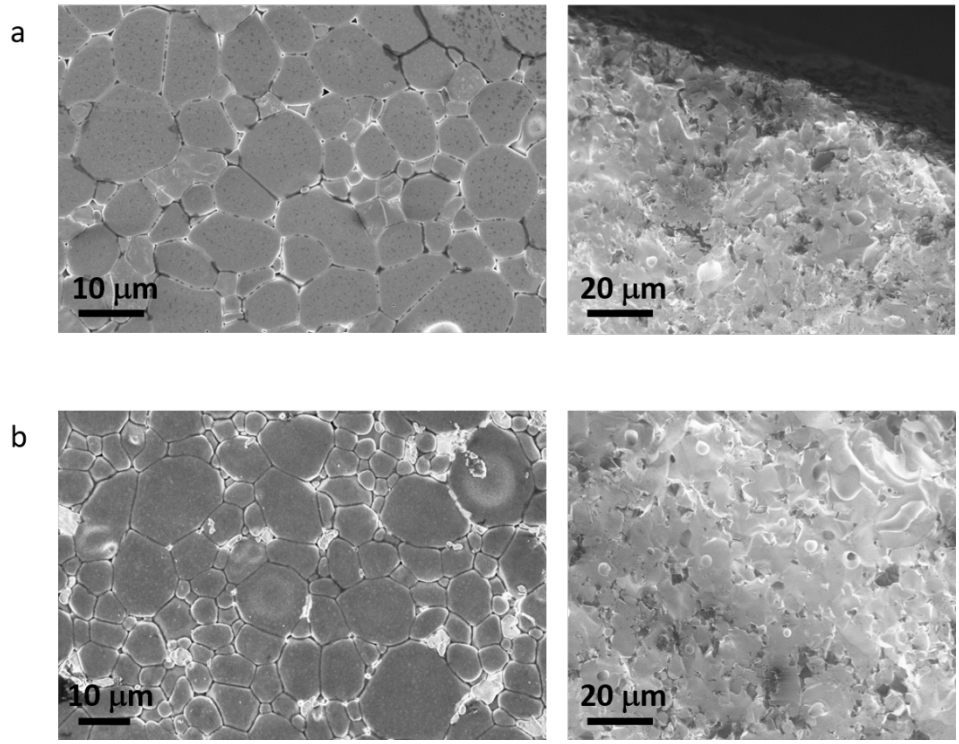


Figure 8.1: SEM secondary electron images of thermally etched plane (left) and fracture surface (right) pellets recorded at 5 kV for (a) Ga-LLZO and (b) Al-LLZO.

several micrometres to about 20 µm. This is about the same average distribution reported by Cheng *et al.* [147] which gave a low ASR with Li metal electrodes (as compared to larger grain sizes of 100 to 200 µm). The density of both pellets is high (greater than 95 % as measured geometrically), with good inter-grain contact. Regions of the pellet which appear brighter in the images (and look slightly coarse), are grains of Li_2ZrO_3. From these images it is difficult to comment on the appearance of the grain boundaries, except that from experience and other literature, a glassy phase is usually formed as a result of liquid-phase sintering processes [123]. Overall, the microstructures of the two compositions are very similar.

Electrochemical impedance spectroscopy (EIS) was carried out on Li/LLZO/Li symmetric cells, hot-pressing the Li metal as described in Chapter 4, Section 4.7.1 onto thermally etched LLZO pellet surfaces. The impedance was measured at room temperature between 0.1 Hz and 13 MHz and fitted to an equivalent circuit given in the inset of Figure 8.2, modelling the depressed semicircles with parallel resistor-constant phase element (R//CPE) contributions. Fitted parameters are summarised in Table 8.1.

The total conductivity (σ_{total}) for the Ga-LLZO and Al-LLZO pellets comes to $7.5 \times 10^{-4}\,\text{S}\,\text{cm}^{-1}$ and $3.5 \times 10^{-4}\,\text{S}\,\text{cm}^{-1}$, respectively. The grain boundary resistance is greater for the Al-LLZO pellet, but difficulties in fitting the room temperature impedance spectra at high frequencies into grain boundary and bulk contributions make the determination of meaningful normalised grain boundary conductivity σ_{GB} values according to the brick-layer model difficult (normalising to electrolyte thickness l and electrode area A). From previous experiments at low temperatures (Chapter 6, Section

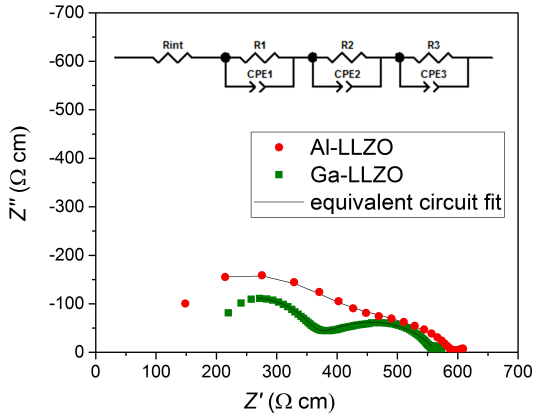


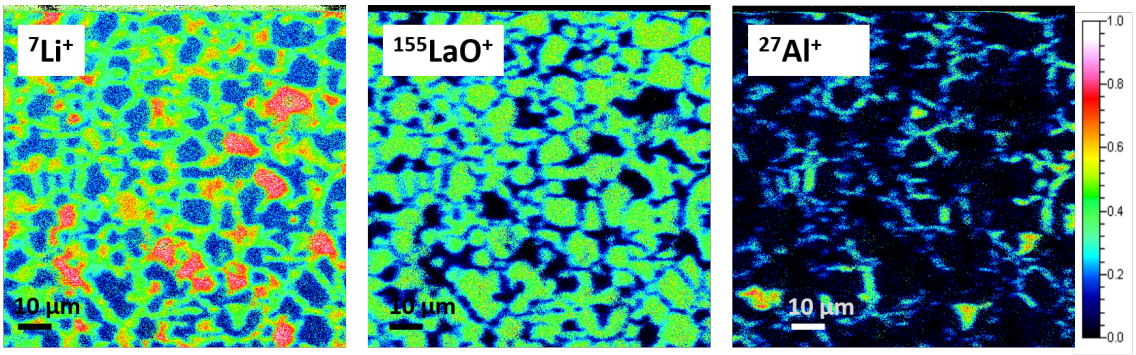
Figure 8.2: Room temperature EIS Nyquist plot of Al-LLZO and Ga-LLZO symmetric cells with Li electrodes; frequency range 0.1 Hz to 13 MHz, and fitted the equivalent circuit shown. Z' and Z'' are the real and imaginary parts of the impedance, respectively.

Table 8.1: Equivalent circuit model fits at 25 °C of impedance spectra for pristine Ga-LLZO and Al-LLZO pellet cells with Li symmetric electrodes.

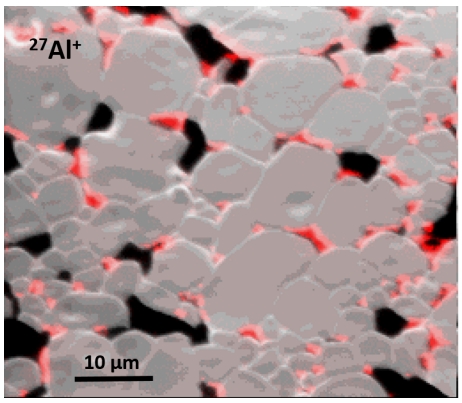
	Ga-LLZO	**Al-LLZO**
C_{bulk} **x** l/A **[F cm^{-1}]**	3.95x10^{-11}	1.4x10^{-11}
σ_{bulk} **[S cm^{-1}]**	1.1x10^{-3}	7.7x10^{-4}
C_{GB} **x** l/A **[F cm^{-1}]**	5.1x10^{-9}	1.7x10^{-10}
σ_{GB} **[S cm^{-1}]**	2.4x10^{-3}	6.4x10^{-4}
σ_{total} **[S cm^{-1}]**	7.5x10^{-4}	3.5x10^{-4}
ASR (R_{CT} x A/2) [Ω cm^2]	16.7	12.1

6.3.2), we know the intermediate frequency region does correspond to a grain boundary response, and the capacitance C_{GB} measured here (10^{-9} to 10^{-10} F) is in agreement.

The interfacial resistance, given as an area specific resistance (ASR), is low compared to literature-reported values without the use of interlayers (16.7 and 12.1 Ω cm^2 for Ga- and Al-LLZO, respectively), indicating intimate contact between the lithium metal and LLZO. The low ASR value is most likely due to a combination of careful moisture control (preventing LiOH and Li_2CO_3 forming on the pellet surface), and to hot-pressing of the Li metal, aiding the wetting of lithium. These conditions are known to be important in ensuring a homogenous current distribution and improving cyclability [173, 174]. The origin of the slightly lower value for Al-LLZO is unclear; it shows the opposite trend to that observed by Rettenwander *et al.* [113] in Ga- and Al- co-doped LLZO; Cheng *et al.* [147] described a reduction in ASR for smaller grained samples of Al-LLZO, with a larger areal density of higher-conductive grain boundaries at the surface being the reason for the improved interfacial resistance, but this is unproven and disputed by other authors [123]. In fact, in our Al0.15-LLZO samples, the grain boundary conductivity is actually



(a)



(b)

Figure 8.3: Pristine Al-LLZO pellet surface: (a) TOF-SIMS maps of $^{7}Li^{+}$, $^{155}(LaO)^{+}$ and $^{27}Al^{+}$ secondary ions with a Bi^{+} primary ion beam (25 kV, 0.2 pA) and O_2^{+} sputter gun (1 kV, 300 nA) operated in non-interlaced burst alignment mode (using a 1s:1s:1s sputter:wait:analyse cycle) and 195 nm resolution; (b) FIB-SIMS map of $^{27}Al^{+}$ secondary ions with 200 nm resolution, using 1.95 nA primary ion beam current over 60.8 µm by 60.8 µm area, i.e. using a $3.3x10^{14}$ ions cm^{-2} s^{-1} dose rate, overlaid with the secondary ion image (the dark regions are Li_2ZrO_3 grains).

lower than the bulk (Table 8.1), and we know that the in these materials, assigning grain boundary and bulk transport properties from EIS measurements is not trivial. As the microstructures of the two compositions in these experiments are similar, the difference may instead arise from chemical differences in grains and grain boundaries afforded by the different dopants used and their corresponding electrochemical properties.

8.1.1 Secondary Ion Mass Spectrometry Mapping

Time of flight (TOF)- and focussed ion beam (FIB)- secondary ion mass spectrometry (SIMS) elemental mapping was carried out on pristine Al- and Ga-LLZO samples in order to highlight any initial chemical inhomogeneity present.

Figures 8.3a and 8.4 show the TOF-SIMS maps for Al-LLZO and Ga-LLZO pellet surfaces, under the same analysis conditions. Unfortunately due to problems in the synthesis, secondary phases of Li_2ZrO_3 exist, visible as lithium-rich regions in the SIMS maps. From the elemental mapping of Al-LLZO, it is clear that Al tends to segregate at the grain boundaries (see Figure 8.3a, third image from left, and Figure 8.4a). The Ga-LLZO

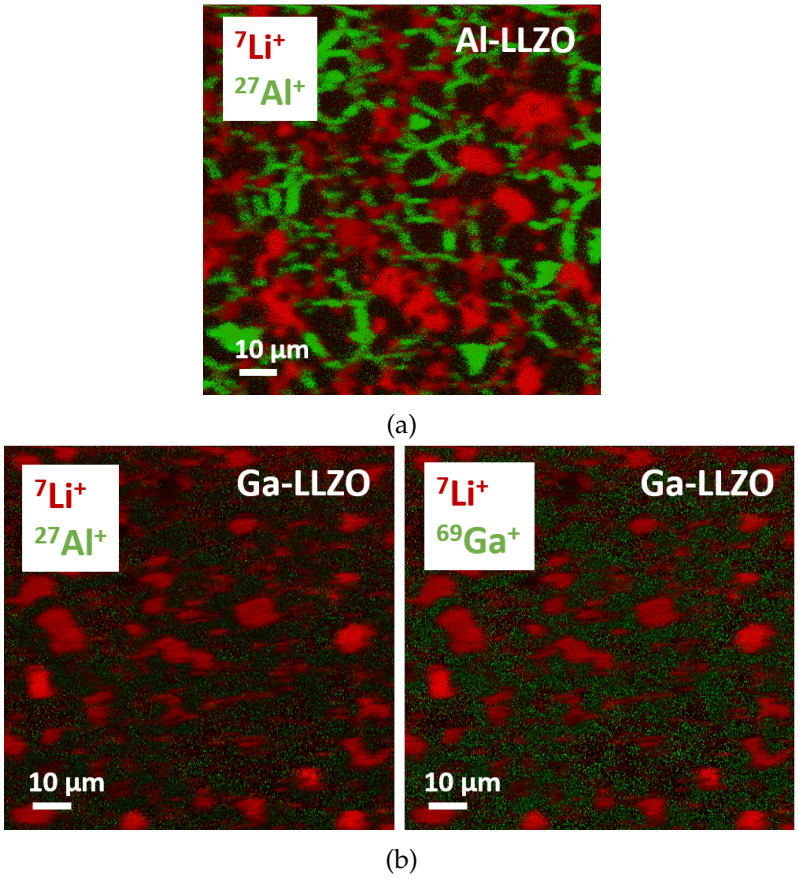


Figure 8.4: TOF-SIMS secondary ion maps showing $^{7}Li^{+}$ (red), $^{27}Al^{+}$ (green) and $^{69}Ga^{+}$ (green) overlaid secondary ions; Al-LLZO (a) and Ga-LLZO (b). The resolution is 195 nm, and images are taken with a Bi^{+} primary ion beam (25 kV, 0.2 pA) and a O_2^{+} sputter gun (1 kV, 300 nA) operated in non-interlaced burst alignment mode (using a 1s:1s:1s sputter:wait:analyse cycle).

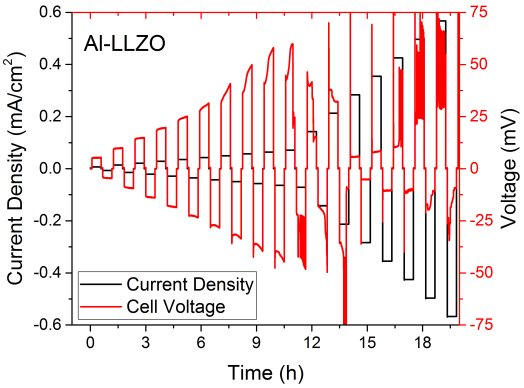
TOF-SIMS maps shows a less distinct demarcation of aluminium at the grain boundaries as compared to the grains (see left-hand image of Figure 8.4b), and an even distribution of Ga within the grains but not along the grain boundaries (right-hand image, Figure 8.4b). Areas of Li_2ZrO_3 grains show up as rich in $^7Li^+$. The FIB-SIMS map of Al-LLZO (Figure 8.3b) show a similar segregation of aluminium at the grain boundaries in Al-LLZO which is less apparent in the Ga-LLZO sample (not shown here, see Appendix A.7 Figure A.11). $^{69}Ga^+$ mapping was not used for the FIB-SIMS maps here as the main contributor will be from the $^{69}Ga^+$ primary beam.

8.2 Galvanostatic Cycling with Lithium Electrodes

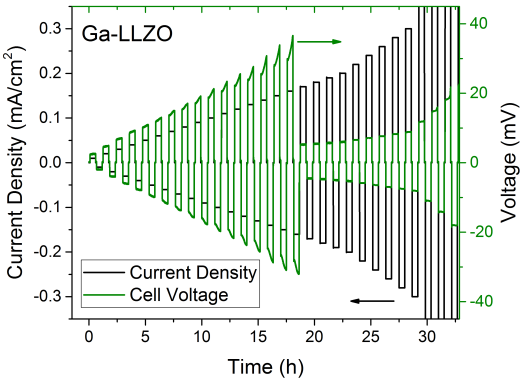
The symmetric Li/LLZO/Li cells were cycled at room temperature with increasing current densities, starting from 0.01 mA cm^{-2} with progressive steps of 0.01 to 2 mA cm^{-2}. Each step was held for 30 minutes, with a 5-minute rest period between current density steps (see Figure 8.5). This was continued until the cell showed cell failure. The reproducibility of the galvanostatic profiles seen in Figure 8.5 was very good, showing profiles of similar current-voltage dependence and the same critical current for cell failure for both Ga- and Al-LLZO cells (more than ten repeats on new cells for each electrolyte composition).

In the current experimental design, the cell impedance is dominated by the solid electrolyte layer. This means, from the viewpoint of experimental diagnostics, that the resistance R of the cell can be used to monitor the growth and penetration of a lithium metal network through the solid electrolyte. Before a short-circuit occurs due to complete lithium metal penetration, there is typically a decrease in cell resistance as the lithium metal network advances through the solid electrolyte [186]. As we increase the applied current, we expect an increase in the voltage with a fixed proportionality constant if nothing changes in the system, according to Ohm's Law. In the Ga-LLZO cell (green square data points in Figure 8.6) up to the point of dendrite formation (at 0.16 mA cm^{-2}), the cell resistance drops progressively as the current density is increased; however, the resistance does not follow Ohmic behaviour (R is changing). This behaviour was consistently observed in all Ga-LLZO cells tested, with the critical current for dendrite formation repeatedly found to be 0.16 mA cm^{-2}, after which the resistance drops significantly. Above current densities of 0.16 mA cm^{-2}, the cell continues to function, with an incremental increase in measured voltage above about 0.2 mA cm^{-2} (Figure 8.5b) as the current is increased. However, this value of current density is still ascribed to be the critical current density for dendrite formation in the Ga-LLZO cell.

Different behaviour was seen in the Al-LLZO cell, with the cell resistance (red circular data points, Figure 8.6) decreasing initially (up to about 0.04 mA cm^{-2} current density), but then followed by an increase in cell resistance until 0.09 mA cm^{-2}. From 0.1 mA cm^{-2}, cell failure occurs, but the resistance shows a more gradual tailing off than in Ga-LLZO, which is always seen in the Al-LLZO cells. The voltage output is much less stable at current densities above 0.1 mA cm^{-2} (the critical current density) in Al-LLZO and fluctuates



(a)



(b)

Figure 8.5: Galvanostatic cycling of symmetrical cells, stepping the current density from 0.01 to 2 mA cm^{-2} (high limit not shown), with a step size of 0.01 to 2 mA cm^{-2}. (a) Al-LLZO; (b) Ga-LLZO. Each current density step was held for 30 minutes, with a 5-minute rest period between steps.

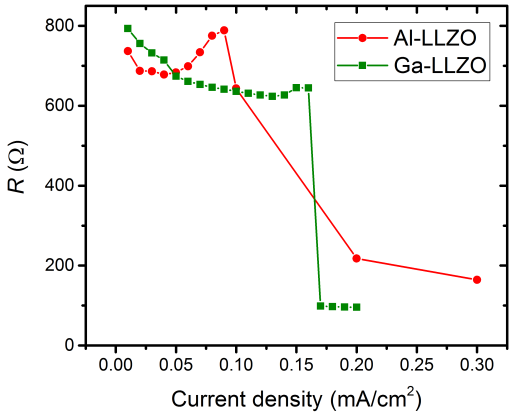


Figure 8.6: Measured resistance R as a function of applied current density during galvanostatic cycling of Li/LLZO/Li cells (with Al-LLZO and Ga-LLZO, red circles and green squares, respectively).

during periods of constant applied current (Figure 8.5a). These systematically-observed differences in behaviour during cycling suggests a difference in the nature and properties of the dendrites which form and lead to cell failure for Ga-LLZO compared to Al-LLZO.

8.3 Post-Mortem Analysis

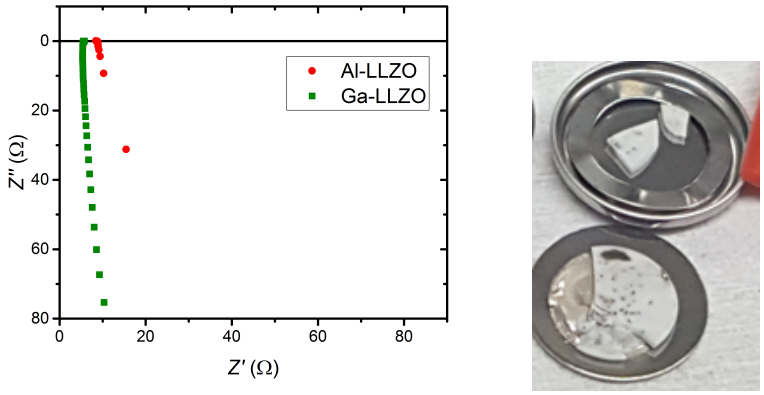
Following cycling and cell failure, the cells were measured again using EIS (Figure 8.7a). In both cases, the Nyquist plots show a near-linear response typical of a purely resistive component, indicative of an electronically-conducting dendrite network across the thickness of the LLZO pellets.

The cells were disassembled in the argon atmosphere glove box, and under visual inspection, dendrites could be seen as black marks on the surfaces and fracture surfaces of the pellets (Figure 8.7b). X-ray diffraction was taken on powders of cycled LLZO, using Kapton tape to protect the samples and assembled in an air-tight holder in the glove box. No clear differences in the XRD patterns in both Ga- and Al-LLZO before and after cycling were visible (see Appendix A.7 Figure A.13).

8.3.1 Secondary Ion Mass Spectrometry

Closer inspection of the cycled pellets using FIB-SIMS and SEM imaging revealed three modes of degradation as a result of electrochemical cycling which are not visible in the pristine samples. The first is an interconnected network of web-like features along grain boundaries of the cell (Figure 8.8a), which has been reported by other authors previously [123, 187, 276]. These networks span the full length of the pellet in some areas, revealed by cross-sectioning by fracturing (seen in Al-LLZO, Figure 8.8a central image), which would be expected to result in short-circuiting of the cell.

The second set of features are intra-grain regions, smaller than the size of the grains themselves, which at first sight appear to be pore-like regions that have formed during



(a) (b)

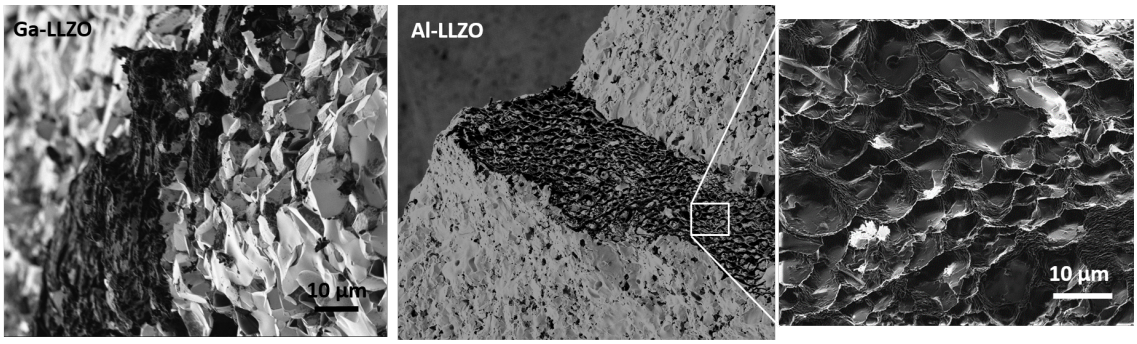
Figure 8.7: (a) Room temperature EIS Nyquist plot of Al-LLZO and Ga-LLZO symmetric cells with Li electrodes after short-circuiting has occurred; (b) disassembled coin cell (Li/Ga-LLZO/Li) post-cycling, showing dark patches on the Ga-LLZO pellet indicative of lithium dendrite formation.

cycling and subsequently fill with a secondary phase. This is similar to observations made by Aguesse *et al.* [187]; however, it is difficult to be sure if these regions are confined to the surface of the pellets in contact with lithium metal electrodes, and whether or not they were pre-existing prior to cycling as pores or surface impurities in the material. Thirdly, small dendritic-like features appear to branch into the grains in some cases (Figure 8.8b). The web-like grain boundary network of dendrites are more pronounced and extended in Al-LLZO than in Ga-LLZO, and the intra-grain secondary phases are more prevalent, which is likely to be related to the lower critical current needed for cell failure in Al-LLZO.

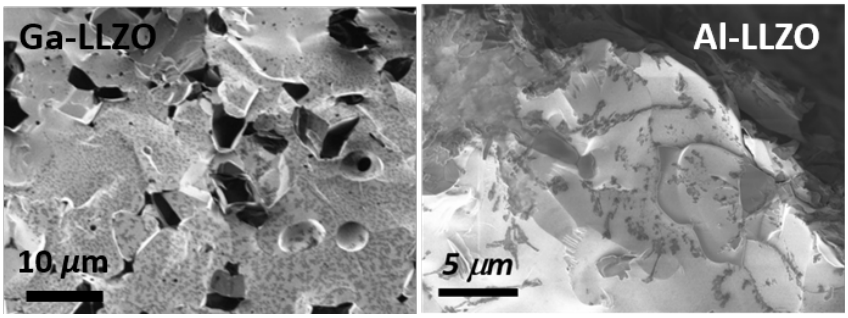
To investigate the chemical changes in the pellets following cycling, selected area FIB-SIMS depth-profiling was carried out on different regions of the pellets, in both grains and in regions associated with dendritic features following cycling.

In-Grain Chemical Analysis

Figure 8.9a shows SIMS depth profiles in the grains of Al-LLZO, before (pristine) and after cycling, using the same dose rate for the primary beam. The relative intensity ratios of the detected secondary ion species in the grains differ slightly before and after cycling - $^{7}Li^{+}$ appears more enhanced after cycling (the mean Li/LaO ratio greater than 0.1 µm depth increases from 1.01 to 1.61), whereas $^{27}Al^{+}$ drops relative to $^{106}(ZrO)^{+}$ (the mean Al/ZrO ratio drops from 1.85 in the pristine to 1.00 in the cycled sample). This was consistently seen across multiple samples. The SIMS maps of the surface of the Al-LLZO pellet are shown Figure 8.9b, which includes a region of residual Li electrode in the centre of the images. The residual Li electrode material has probably reacted with carbon-based species during transfer and handling, forming a crust which is depleted in $^{7}Li^{+}$ secondary ion intensity compared to the LLZO grains (see Figure 8.9b $^{7}Li^{+}$ map, in green). However, grain boundary regions and small features within grains formed after cycling appear enriched in Li^{+} and Al^{+} (Figure 8.9b red $^{27}Al^{+}$ map) compared to LLZO grains (which



(a)



(b)

Figure 8.8: Dendritic features in LLZO following cycling. (a) Dendritic web-like network revealed by fracturing the LLZO pellets after cycling (Ga-LLZO, left and Al-LLZO, centre and right), images taken in FIB-SIMS secondary electron mode. (b) Fine intra-grain dendrite features in cycled Ga-LLZO (left) and Al-LLZO (right), taken with FIB-SIMS and SEM secondary electron imaging, respectively.

are the only regions in which $^{155}(LaO)^+$ is detected, blue map).

The same analysis was carried out on Ga-LLZO (Figure 8.10a shows in-grain depth profiles before and after cycling, with secondary ion maps in Figure 8.10b). In the post-cycling analysis, we used $^{71}Ga^+$ secondary ions as a marker for the gallium dopant in Ga-LLZO, as a new FIB gallium source was used, which was measured to be comprised of 99 % ^{69}Ga and 1 % ^{71}Ga isotopes, thus allowing the separation of contributions from the primary beam source of Ga (^{69}Ga), and Ga in the sample (^{71}Ga). In the case of Ga-LLZO, there was less of a marked difference in the relative intensity ratios of the secondary ion species detected in the grains before and after cycling (Figure 8.10a depth profiles), but as seen in Al-LLZO, the $^7Li^+$ ratio increases slightly (Li/LaO mean ratio increase from 2.01 in the pristine sample to 2.15 after cycling) and the $^{27}Al^+$ ratio drops slightly after cycling (the Al/ZrO ratio drops from 1.01 to 0.52 in the cycled sample compared to the pristine). Surface SIMS maps in Figure 8.10b show $^{71}Ga^+$ distributed across the grains, with small patches of Al^+-enriched material, possibly corresponding to dendritic features seen as dark patches close to grain boundaries in the secondary electron image, but no significant enhancements at grain boundary regions, as seen in Al-LLZO after cycling.

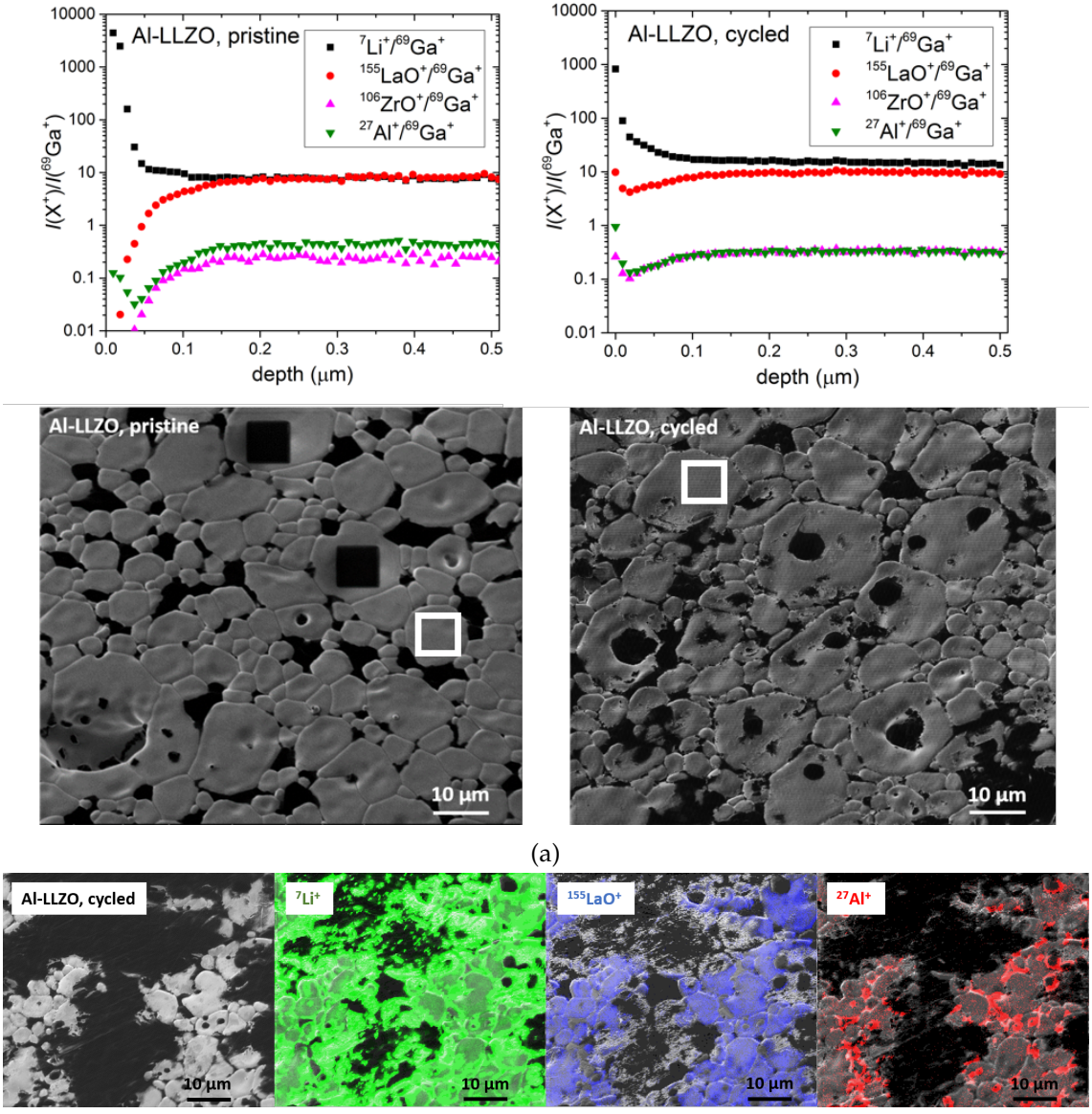
This difference in segregating behaviour of aluminium, which is more pronounced in the Al-LLZO pellets, may help to explain the easier formation of dendrites in Al-LLZO compared to Ga-LLZO during cell cycling, despite the comparable ASR for both samples (Section 8.1, Table 8.1). The difference in relative secondary ion intensities in the grains is less clear, except that Al segregating into the grains as a result of cycling and dendrite formation may explain the drop in the Al^+ ion ratios.

Post-Cycling Features Chemical Analysis

Chemical analysis of some of the features present in the samples post-cycling were carried out using SIMS depth-profiling (Figure 8.11). An analysis of the extended dendritic feature in Ga-LLZO after cycling is shown in Figure 8.11a. Owing to the morphology of the dendrite, some contributions from the grains beneath the feature are present, and the depth of the crater was not measured; however, the dendrite shows dominant secondary ion intensity ratios of $^7Li^+$ and $^{27}Al^+$, implying it is Li- and Al- rich, but not Ga-enriched (indicated by a low $^{71}Ga^+$ intensity ratio). A curious feature seen in Al-LLZO post-cycling are surface growths, rich in aluminium and lithium, which appear to form and crystallise in the centre of Al-LLZO grains (Figure 8.11b). A depth profile of residual Li metal from the electrode still adhered to the surface of Al-LLZO post-cycling (Figure 8.11c) was also measured; again, showing enrichment of Al and Li species compared to LLZO grains.

Figure 8.12 shows FIB-SIMS secondary ion maps of the dendritic feature in the fracture surface of Al-LLZO following cycling. The rough morphology of the feature makes chemical assignment difficult, and the Al distribution is ambiguous, however a clear depletion of LaO^+ in the dendritic web is seen, with the intensity confined to the Al-LLZO grains in between the dendrites. However, the dendritic feature does contain Li (dark patches likely correspond to areas which have reacted with air).

These dendrites and degradation features following cycling are thus shown to all



(a)

(b)

Figure 8.9: (a) Al-LLZO in-grain depth profiles (example regions indicated by white squares), before (top left) and after (top right) electrochemical cycling with lithium electrodes, and (bottom) corresponding secondary electron images of the pellet surfaces (depth profile craters shown in image as dark squares in left-hand image). Depth profiles show the intensity I of secondary ions as a ratio to $^{69}Ga^{+}$ secondary ion intensity, and measure 7 µm by 7 µm, using a primary ion beam current of 340 pA (a dose rate of 4.3x10^{15} ions cm^{-2} s^{-1}). (b) FIB-SIMS maps of Al-LLZO surface after cycling: secondary electron image (left) and $^{7}Li^{+}$, $^{155}(LaO)^{+}$ and $^{27}Al^{+}$ secondary ion maps, overlaid with the secondary electron image (the dark patch in the centre is residual Li metal from the electrode which has subsequently reacted), with 200 nm resolution, and a primary ion dose rate of 1.7x10^{14} ions cm^{-2} s^{-1}.

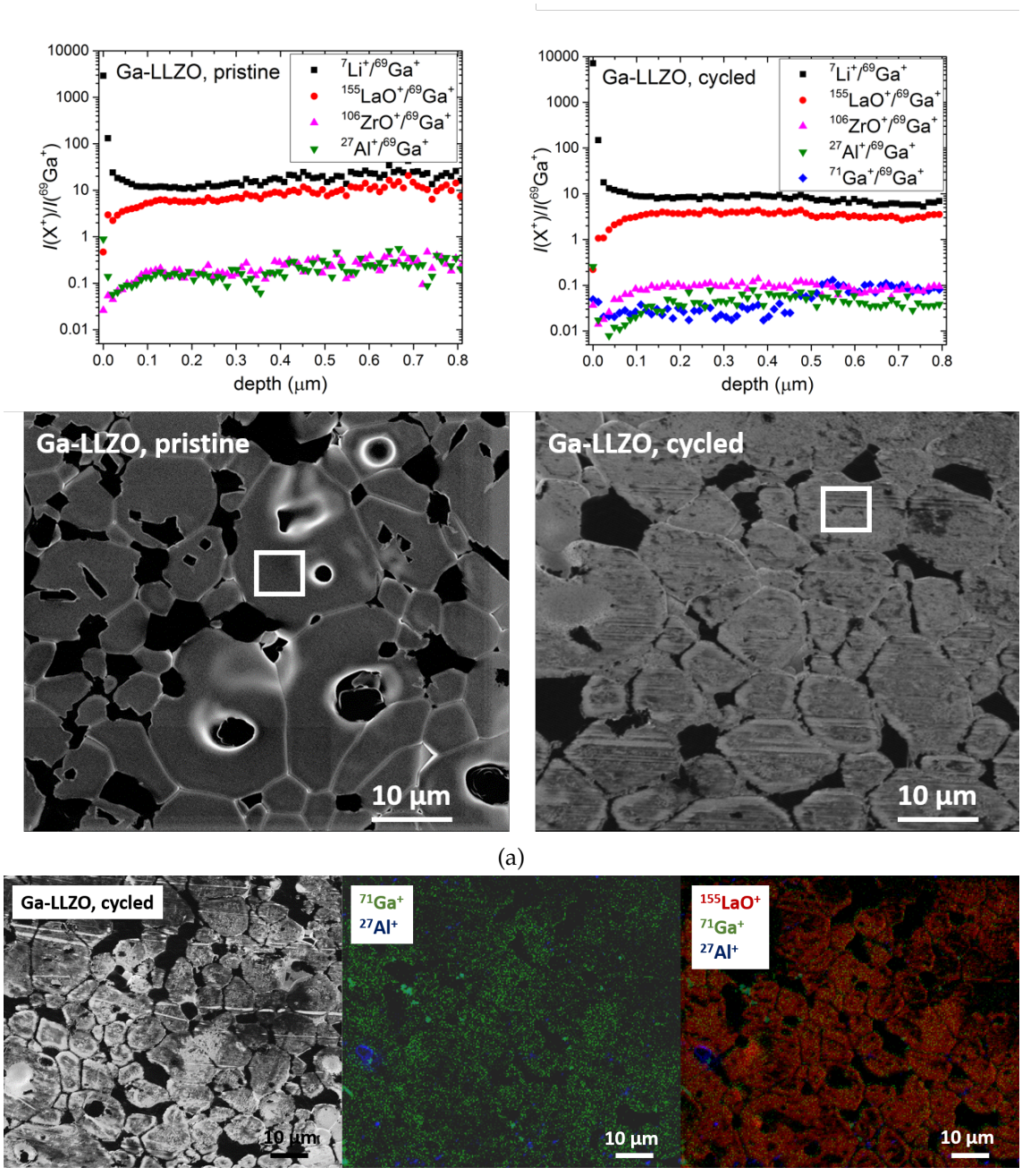
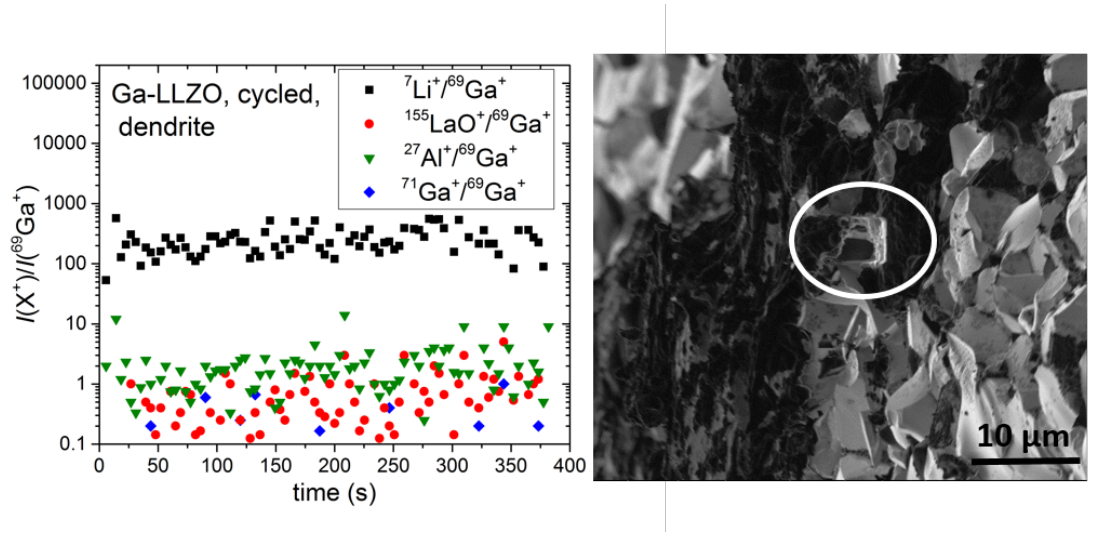
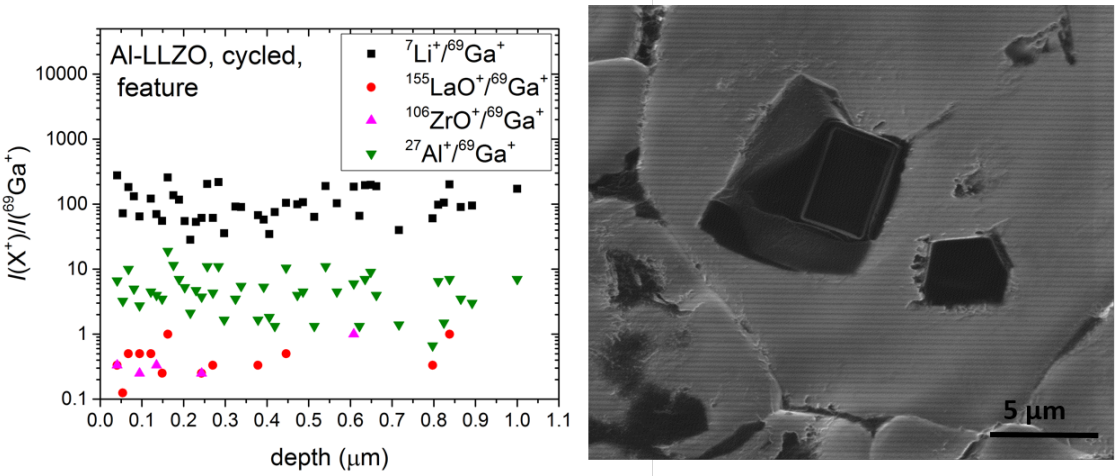


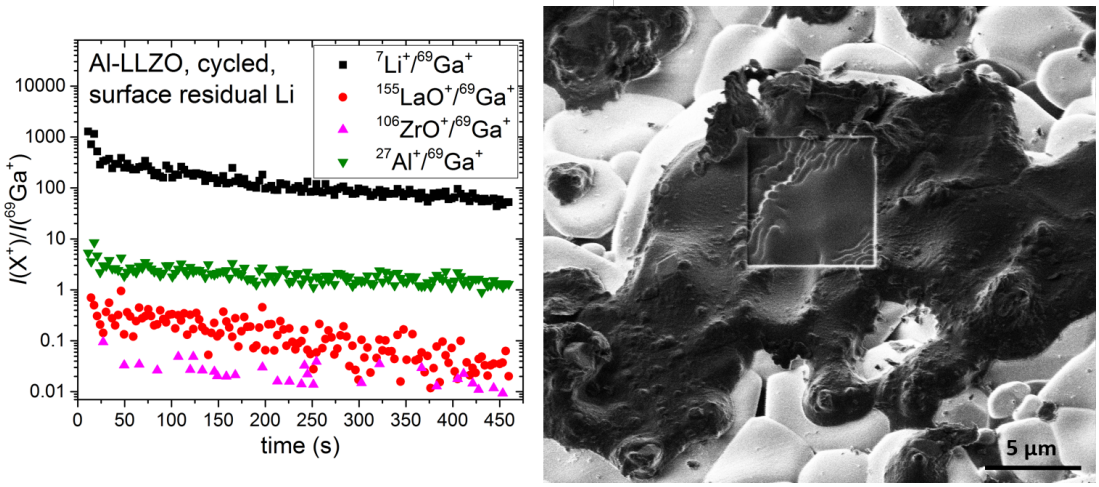
Figure 8.10: (a) Ga-LLZO in-grain depth profiles (example regions indicated by white squares), before (top left) and after (top right) electrochemical cycling with lithium electrodes, and (bottom) corresponding secondary electron images of the pellet surfaces. Depth profiles show intensity (I) of secondary ions as a ratio to $^{69}Ga^{+}$ secondary ion intensity, and measure 7 μm by 7 μm, using a primary beam current of 340 pA (a dose rate of 4.3x10^{15} ions cm^{-2} s^{-1}). (b) FIB-SIMS maps of Ga-LLZO surface after cycling: secondary electron image (left) and $^{71}Ga^{+}$, $^{27}Al^{+}$ and $^{155}(LaO)^{+}$ secondary ion maps, overlaid with the secondary electron image, with 200 nm resolution, and a primary ion dose rate of 1.7x10^{14} ions cm^{-2} s^{-1}.



(a)



(b)



(c)

Figure 8.11: SIMS depth profile chemical analysis of features post-cycling, showing the depth profile on the left and the secondary electron image of the feature on the right. (a) Dendritic feature on fracture surface of cycled Ga-LLZO, using a primary ion dose rate of 4.4×10^{15} ions cm^{-2} s^{-1}. (b) Intra-grain growth on the surface of cycled Al-LLZO, using a primary ion dose rate of 1.3×10^{16} ions cm^{-2} s^{-1}. (c) Residual Li metal from electrode on the surface of cycled Al-LLZO, using a primary ion dose rate of 4.4×10^{15} ions cm^{-2} s^{-1}.

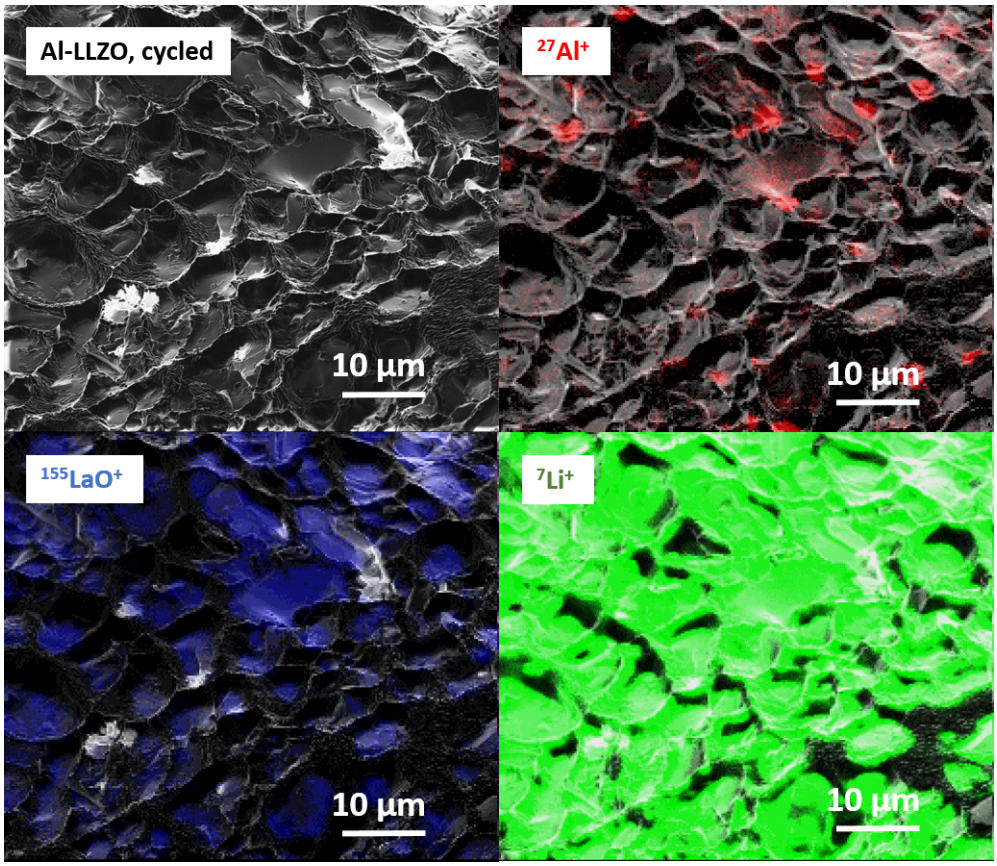


Figure 8.12: FIB-SIMS maps of Al-LLZO dendritic feature after cycling: secondary electron image (top left) and $^{7}Li^+$, $^{155}(LaO)^+$ and $^{27}Al^+$ secondary ion maps, overlaid with the secondary electron image, with 200 nm resolution, and a primary ion dose rate of 1.7x10^{14} ions cm^{-2} s^{-1}.

contain both Al and Li as their principle constituents through these SIMS analyses.

8.3.2 X-ray Photoelectron Spectroscopy

Al-LLZO pellet samples were measured using X-ray photoelectron spectroscopy (XPS) before and after cycling. For this analysis, the pellet from a disassembled cell was polished down on one side to remove residual Li metal from the electrode, using 4000 grit SiC emery paper, to expose regions of dendrites to the surface for analysis. On one of the pieces of cycled pellet, a small area of Li metal was purposefully left to act as a reference for metallic lithium. Dark areas were visible by eye and in the XPS optical microscope on the cycled pellet sample, corresponding to dendritic regions. We thus selected two areas for analysis on the same cycled sample; one on one of these dark regions, labelled 'cycled-Li' in Figure 8.13, and the other on a region where the dendrites were absent (by eye, labelled 'cycled-white' in Figure 8.13). Samples were transferred under argon with a glove box transfer module and the data was collected with a 400 µm by 400 µm beam area on the pristine un-cycled sample, and 200 µm by 200 µm beam area for cycled samples (see Chapter 4, Section 4.3.1 for measurement details). Peak intensities are normalised to La. All measurements and data treatment were made by Dr Anna Regoutz at Imperial College London. The Li 1s, O 1s, Al 2p and C 1s core spectra are given in Figure 8.13; note the probe depth is less than 10 nm.

As can be seen in the Li 1s core spectra, the peak for metallic Li and Li in LLZO (from the pristine spectrum) have very similar binding energies and cannot be separated. However, the cycled pellet dendritic region, 'cycled-Li', peak has a shift to higher binding energy (not seen in the dendrite-free region of the same sample, 'cycled-white'). This binding energy could correspond to either LiOH or Li_2CO_3 (but not Li_2O). This is also seen in the C 1s and O 1s spectra for this sample, which have significantly higher intensities for both adventitious C (lowest binding energy) and HCO_3 and CO_3 species in the C 1s spectra, as well as higher intensities for the O species. It might be that these species exist as a result of the reaction of Li dendrites either with protons and/or carbon species in the cell components or with the tools used to handle the cells. A shift in binding energy of the Li 1s peak due to Al-Li alloying is not confirmed here.

Interestingly, the cycled sample contains significantly larger amounts of Al at the analysis surface than does the pristine sample (see Table 8.2), with a shift of the peaks to higher binding energies. This could indicate segregation of Al from the LLZO as a result of the cycling process towards the electrodes, and possibly the association of Al with the Li dendrites, in agreement with the SIMS results of the post-cycling dendritic features and grain boundary regions (though not the grains, where the Al:La ratio drops after cycling). It must be noted that due to the high area of analysis in XPS compared to FIB-SIMS (several hundreds of micrometres), the separation of chemical information on the grains, grain boundaries and dendritic features are not possible with XPS; rather a net chemical view is taken, which implies that the Al-rich dendritic features dominate the analysis here. In addition, the probing depth of the two techniques varies greatly, with XPS probing only the top few nanometres of the material surface. The 'cycled-white'

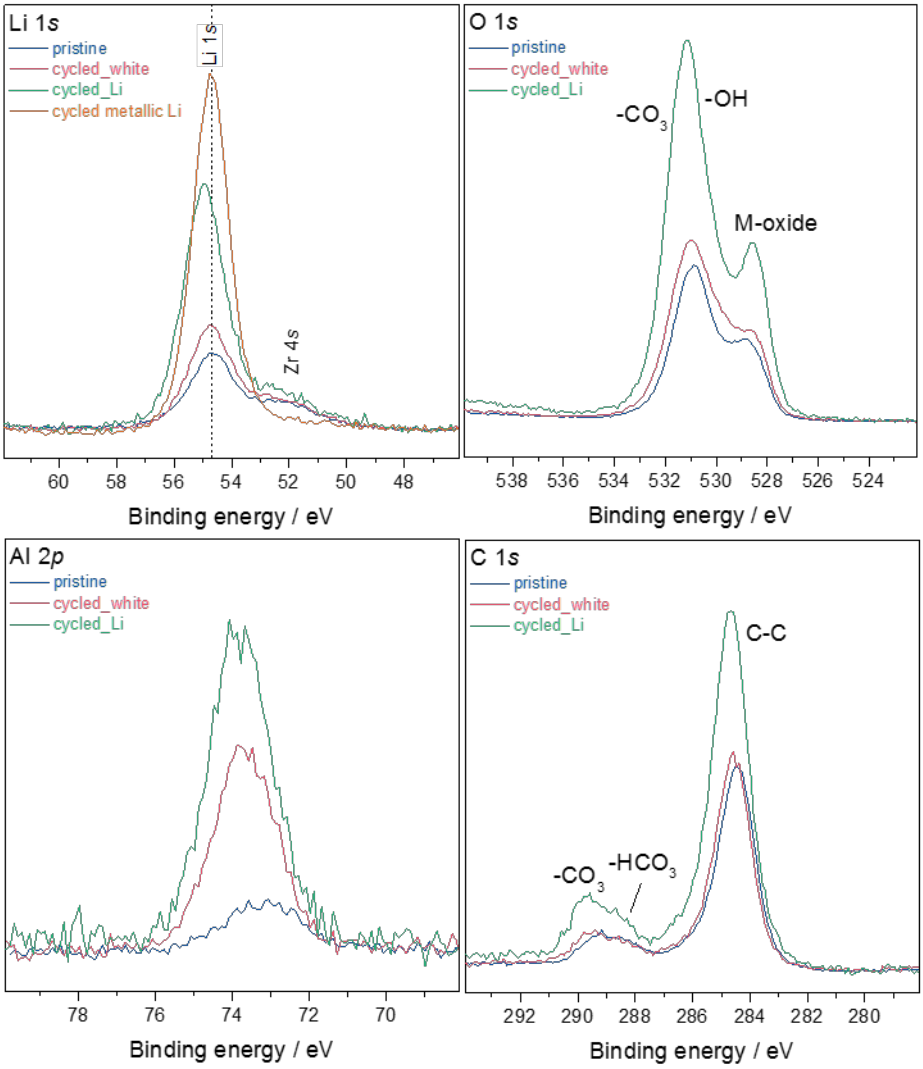


Figure 8.13: XPS Li 1s, O 1s and C 1s core spectra of Al-LLZO pristine and cycled pellets. 'cycled-white' corresponds to a region on the cycled pellet which appeared to lack the presence of dark dendritic features by optical inspection. Those areas which appeared dark from the presence of dendrites are labelled 'cycled-Li'.

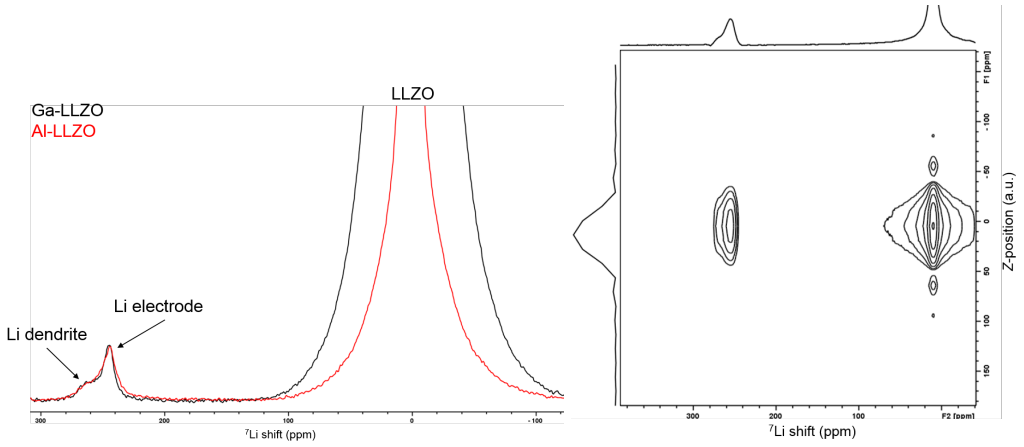
areas, which appeared dendrite-free by eye, also showed an enhancement in Al, and it is unclear what the origin of this enhancement is (the existence of secondary phases formed on cycling in the analysis area here cannot be ruled out). No measurements were taken on the Ga-LLZO pellets at the time, but should be carried out to determine if the same Al enhancement close to the dendrites and peak shifts are seen in Ga-LLZO post-cycling. Another factor to consider is the gradient in Al and other light cation concentrations in LLZO pellets, due to crucible and heating effects, seen in Chapter 5, Section 5.1.2. These effects cannot be separated from cycling effects described here.

Table 8.2: Quantification of XPS La and Al ratios, in cycled and pristine Al-LLZO samples.

Sample	**La:Al ratio**
Pristine Al-LLZO	3:0.75
Cycled-white Al-LLZO	3:2.08
Cycled-Li Al-LLZO	3:2.66

8.3.3 Nuclear Magnetic Resonance

To investigate further the possibility of a Li-Al alloy forming as a dendrite in the samples, ^{7}Li nuclear magnetic resonance (NMR) and magnetic resonance imaging (MRI) measurements were made on both Ga- and Al-LLZO pellets containing dendrites, using a difference in Knight shift for the metallic lithium component, which would indicate a change in environment of the metallic species [277]. Measurements were carried out by Dr Lauren Marbella in Professor Grey's group at Cambridge University. Measurements were made on the cycled pellets with lithium electrodes still attached and the samples were orientated with electrodes perpendicular to the magnetic field B_0 during measurement. Unfortunately, there was not a dramatic difference in the chemical shifts between the different pellets (Figure 8.14a). While this does not rule out the incorporation of other metals (Al, etc) into the dendrites, they may be present in such a low percentage that they do not dramatically influence the Knight shift of the ^{7}Li signal. However, a peak for the Li dendrite, shown as a shoulder of the peak for the Li metal electrode, is seen. ^{27}Al NMR was also attempted, but the background signal of ^{27}Al coming from the probe was large and we were unable to see a ^{27}Al metal signal from the sample, if there was one. The ^{7}Li MRI (Figure 8.14b) shows the orientation of the dendrites as a two-dimensional image, spanning the area between the two electrodes (along the Z-position, represented by the y axis in Figure 8.14b). The x-axis gives the chemical shift of ^{7}Li, with the region at about 260 ppm indicative of the Li dendrite (where 0 ppm indicates the Li in LLZO). The spatial resolution is about 100 µm, so fine features are not visible.



(a) (b)

Figure 8.14: (a) 1D ^{7}Li NMR of Ga- and Al-LLZO dendritic pellets with lithium electrodes oriented perpendicular to magnetic field B_0, with signals normalised to the LLZO ^{7}Li peak. (b) 2D ^{7}Li MRI of cycled Al-LLZO showing dendrites spanning the electrolyte (Z-position indicates fracture surface of pellet, along the direction between the two lithium electrodes).

8.4 Discussion and Summary

Electrochemical cycling experiments on Li/Ga-LLZO/Li and Li/Al-LLZO/Li cells show marked differences in cycling behaviour for the two doped compositions of LLZO tested. Ga-LLZO showed a higher critical current density (0.16 mA cm^{-2}) for cell failure caused by dendrite formation, and a less detrimental performance at higher current densities. On the other hand, Al-LLZO showed cell failure at the lower critical current density of 0.1 mA cm^{-2}, with erratic voltage profiles at higher applied currents.

Post-mortem analysis revealed a greater extended network of Li dendrites in the Al-LLZO cycled pellet, with more visible degradation features after cell failure occurred. In both compositions, SIMS chemical analysis showed that dendritic features were enriched in Al and Li species, whereas the LLZO grains were depleted in Al^+ and enriched in Li^+ after cycling compared to in their pristine state. XPS chemical analysis over large areas showed that cycled pellets showed a net enrichment in Al in the near-surface region close to the original location of the electrodes.

Although we were unable to see evidence of Al-Li alloying in NMR experiments, there is clearly an affinity for Li dendrites with aluminium from the LLZO pellet samples. Whether this takes the form of an Al-Li metallic alloy is unclear. It might be instead that the grain boundaries, known to be enriched in Al (and more so in Al-LLZO than in Ga-LLZO), are acting as fast pathways for Li dendrites through some wetting mechanism favoured by the Al-rich composition of the grain boundaries. As discussed in Chapter 3, Section 3.4, it has been suggested that lithium aluminates found in grain boundaries of garnets will react with lithium metal [135]. It might also be feasible that Joule heating of the dendrites caused by local high current density may result in the formation of molten Li, which could act to leach Al out of the grains.

Detecting the presence of gallium in the dendritic features was a challenge owing to the

low level of dopant concentrations and the interference from the primary beam ($^{69}Ga^{+}$) in FIB-SIMS analyses. XPS measurements and other means of detection should be explored. It cannot therefore be ruled out that dendritic features form with Ga-Li compositions in Ga-LLZO. Li-Ga alloying was reported to form at 300 °C during cycling of Ga-LLZO in previous work [185] (and see Appendix A.7 Figure A.14 for a phase diagram of Ga-Li), but it is unclear if this is the case during room temperature cycling (where local heating may occur, reaching an unknown temperature). The formation of Li-Ga compounds will need to be investigated further, especially the formation of lithium gallium oxides at the grain boundaries of Ga-LLZO which have been reported previously [131]. The presence and/or different distribution of gallium at the interface with Li metal in Ga-LLZO may, perhaps, also favour a homogeneous current distribution and reduce the ability for dendrites to form, improving the cycling performance of these systems compared to Al-LLZO.

In summary, the chemical nature of the grains and grain boundaries in LLZO is an important factor for determining cell operating behaviour, when all other parameters are fixed (including the microstructure). This work illustrates the role of aluminium in the formation of lithium dendrites during cell cycling of LLZO, and its ability to promote cell failure through the propagation of dendrites, and is seen in the greater propensity for dendrite formation and concurrent cell failure in Al-LLZO compared to Ga-LLZO electrolyte cells.

8.5 Suggested Future Work

This work is an initial investigation into the role of the chemical composition of LLZO on the electrochemical performance when used in a cell with lithium metal electrodes. A variety of further work could be explored to understand better the phenomena observed here.

The experiment could be repeated with Al-free LLZO samples (pellets sintered in Pt or ZrO_2 crucibles, which will need hot-pressing or spark plasma sintering to obtain the required density), to observe differences in cyclability and to understand the role of Al in the formation and propagation of lithium dendrites. In addition, a cell setup composed of Li^0/Al^0/Al-free LLZO/Al^0/Li^0 (where ^{0} denotes the metallic species) could be adopted for cycling to see if the same behaviour is observed as in the Al-LLZO cell. ^{27}Al NMR could be used to probe the nature of the Al species in the sample following cycling.

Using an isotopically-labelled ^{6}Li metal electrode for cycling experiments combined with SIMS and NMR post-cycling, could help to determine where the Li in the dendrites comes from, and distinguish between the intra- and inter-granular degradation seen in the cycled material; is the source of lithium the electrode or the lithium in the pellet, or both? Time constraints would apply in this setup to minimise the self-diffusion of lithium between cycling and analysis.

The cycling behaviour and critical current on LLZO stabilised with other dopants, for example Ge, would be an interesting extension of this work, especially if we are able to correlate the critical current to the Al content in the pellet or to the chemical interaction

of dopant cations with lithium.

In addition to cycling experiments described in this chapter, uni-directional plating/discharge experiments could be used to quantify the amount of Li deposited, which could also be combined with a labelled ^{6}Li electrode to detect the motion of lithium, correlating voltage output with content of plated Li. Finally, performing the cycling experiments in-situ would allow the formation and growth of dendrites to be observed (using, e.g., in-situ SIMS and NMR).

Chapter 9

Conclusions and Further Work

9.1 Conclusions

Substantial interest in developing the next generation of energy storage devices based on battery technologies has led to the concept of an all-solid-state lithium ion battery, hailed as the possible solution to many of the drawbacks of conventional liquid-based systems. The properties of the solid electrolyte are pivotal in dictating the overall cell performance and multiple chemistries and structures have been explored in the search for suitable candidates, as discussed in Chapter 3. The garnet-structured oxide, based on the formula $Li_7La_3Zr_2O_{12}$ (LLZO), has the potential to be used in an all-solid-state configuration owing to its large electrochemical window, high ionic conductivity and chemical stability. This material was selected for study in this thesis, with the aim of answering questions on aspects of the fundamental understanding of its properties through experimental investigation, which were identified as lacking in the literature.

The synthesis of highly conductive ceramic pellets of LLZO was explored in Chapter 5, in which an optimised method was developed for fabricating pure-phase, dense microstructures of Ga- and Al-doped LLZO, to enable high ionic conductivities and favourable transport properties to be achieved. It was found that the optimal thermal treatment conditions were 800 °C in dry flowing oxygen for 6 hours to obtain the cubic powder, followed by sintering the pellets at 1150 °C for 6 hours in an argon atmosphere, with all processing steps carried out in a glove box to prevent reaction with moisture. The careful handling carried out provided low interfacial resistances with lithium electrodes, an important factor in enabling high power densities and cyclability of the cells.

The transient nature of the meta-stable cubic ($Ia\bar{3}d$) LLZO was frequently observed in the form of impurity phases, highlighting the need for a highly controlled synthesis procedure, with implications for the large-scale production of these materials. The structure was confirmed by X-ray diffraction and aberration-corrected high resolution scanning transmission electron microscopy (STEM). STEM measurements of the powders proved a challenge, owing to the radiolysis (bond-breaking) of the specimen under the influence of the electron beam, preventing the imaging of light atoms (Li, H).

The effect of the crucible type used during sintering was also explored using low energy ion scattering (LEIS) - providing evidence of the mobile nature of Al^{3+}, Ga^{3+}

(as well as Li^+, indirectly) in the LLZO pellets during high temperature treatment. As these cations are important in controlling structural, microstructural and ionic transport properties in the electrolyte, understanding their distribution in LLZO pellets is crucial if the materials are to be used commercially. Evidence of the formation of an Al_2O_3-Li_2O eutectic was seen, as described by others [128, 140, 146], and the influence of alumina crucibles in providing a source of Al^{3+} was confirmed.

Using Ge(IV) as a dopant to stabilise cubic LLZO was investigated, and found to stabilise the cubic phase with the highest conductivity ($3.4 \times 10^{-4}\,S\,cm^{-1}$ at room temperature) using 0.10 Ge atoms per formula unit, confirming the work of Huang [133]. Neutron diffraction suggested an occupancy of the tetrahedral 24*d* Li sites, and X-ray photoelectron spectroscopy (XPS) confirmed an oxidation state of +4. This followed the expected trend for concentration and site occupancy of supervalent dopants (such as Ga^{3+} and Al^{3+}) on the lithium sublattice in LLZO, following charge balance and crystal radius arguments. The site occupancy (24*d*) and sintering behaviour is the same as that previously reported for Al^{3+}. However, the ionic conductivities achieved with Ge(IV) doping are not able to reach the high reported values for Ga0.15-LLZO compositions [113, 137, 138], and a greater understanding of ionic transport in these complex systems is required, as touched on in Chapter 3.

The stability of LLZO in air and water was investigated in Chapter 6, and the associated degradation processes were characterised, chemically and electrochemically, correlating the moisture reactivity of LLZO with its electrochemical performance. Powder samples of Ga0.15-LLZO underwent H^+/Li^+ exchange by immersing the powders in liquid H_2O at room temperature (RT) and 100 °C. The cubic $Ia\bar{3}d$ lattice structure was maintained following the exchange process, as verified by powder X-ray diffraction; the lattice parameter was found to increase following high temperature exchange only, and in the RT exchange, a $La_2Zr_2O_7$ secondary phase was formed. These observations indicated a difference in exchange kinetics and in the nature of the H-O bonding of the proton exchange process at these two temperatures. ^1H nuclear magnetic resonance (NMR) measurements supported these findings, showing a difference in the relative intensities of the chemical shift peaks associated with intercalated protons and adsorbed water for the RT compared to the 100 °C-treated samples, with a larger fraction of intercalated protons in the latter. Pulsed field gradient (PFG) NMR on the 100 °C H_2O powder yielded an incalculable lithium ion diffusivity owing to markedly slower kinetics of lithium in the sample compared to those of pristine sample. Decay processes for the protons were seen but could not be assigned a diffusivity with confidence owing to the complicated signal. These findings implied slow lithium ion diffusion in the protonated LLZO sample.

Pellets of Ga0.15-LLZO were immersed in 100 °C liquid H_2O for a range of times, and focussed ion beam – secondary ion mass spectrometry (FIB-SIMS) was used to follow the chemical changes within the grains as a function of depth. The water-treated sample had a 'clean' surface relative to the pristine samples, in terms of corrosion layer thickness and surface chemistry. A proton-rich H-Ga0.15-LLZO region formed on proton-lithium exchange in the pellet samples, and as the exposure time increased, so did its thickness.

Li and H diffusion profiles were seen in the samples; the diffusion length of the protons increased with the immersion time. The chemical diffusion coefficient, $D_C(H^+)$, of the protons at 100 °C was calculated to be 1×10^{-16} to 2×10^{-16} $m^2\,s^{-1}$ for the three samples, corresponding to a conductivity at 100 °C of the order of 10^{-8} $S\,cm^{-1}$ (compared to the Li conductivity from electrochemical impedance (EIS) measurements of 10^{-2} $S\,cm^{-1}$ at 100 °C).

Tracer diffusion using D_2O was attempted in H-Ga0.15-LLZO. The times chosen were too short to collect an accurate diffusion profile of D^+; however, there was a clear movement of D^+ into the samples. The tracer diffusivity (D^*) was difficult to find by fitting the profiles using Crank's solution but, within the H-Ga0.15-LLZO regions tested, it was estimated to be approximately 10^{-17} $m^2\,s^{-1}$ at 100 °C, one order of magnitude smaller than the chemical diffusivity.

LLZO pellets were allowed to be in contact with ambient air for a range of times, and the chemical nature of the corrosion layer formed at the surface was investigated with LEIS and XPS. LiOH quickly formed on the surface of doped LLZO pellets, followed by a slow transformation to Li_2CO_3.

EIS measurements showed a reduction in total conductivity from the pristine to the water-treated samples, due to a decrease in charge carrier mobility in the protonated H-Ga0.15-LLZO region, which had a calculated bulk resistivity of approximately 10^5 Ω cm. This bulk resistivity R_{bulk} is almost three orders of magnitude higher than in pristine, pure LLZO with R_{bulk}(pristine) equal to 8.6×10^2 Ω cm. The grain boundaries were very susceptible to moisture; after water treatment, the grain boundary resistance R_{GB} increased by three orders of magnitude to 5×10^5 Ω cm after 30 minutes in H_2O. The area specific resistance with Li electrodes dramatically increased after proton exchange (from 9.4 Ω cm^2 in the pristine, to 392.5 Ω cm^2 in the air-exposed sample, and to 2.4×10^3 Ω cm^2 after 15 minutes in H_2O). The work demonstrated the significant deterioration in the Li-ion mobilities of the Li metal/Ga0.15-LLZO interfaces and in the bulk and grain boundaries upon reaction with H_2O due to the H^+/Li^+ exchange reaction. This highlighted the link between proton-lithium exchange processes in lithium-conducting garnets and the impact on charge carrier transport, which has important implications on cell performance in lithium metal batteries using LLZO electrolytes.

In Chapter 7, an experimental methodology for determining macroscopic diffusion of lithium in LLZO was presented, using a stable lithium isotope exchange technique. The results from this technique were then compared to other macroscopic (PFG NMR) and microscopic (EIS and $T1$ spin-lattice relaxation NMR) techniques. Amongst the NMR measurements, only the Ga-LLZO PFG NMR and EIS derived values for diffusivity were in agreement (with the activation energies in good agreement for all samples). This suggested that both long-range charge transport (EIS) and local mass transport (NMR) are linked in Ga-LLZO and suggested that the motion of Li ions on both macroscopic and microscopic scales are equivalent, implying the motion is to some extent uncorrelated. This is contrary to the literature consensus of correlated lithium motion in garnets, but requires further investigation owing to the limitations of the techniques used. The

NMR extracted diffusivities can be thought to approach tracer-diffusion values for long relaxation times.

When comparing chemical diffusivities D_C measured by isotopic exchange and extracted over large areas using the multiple profiling method with the EIS derived diffusivities D^σ, the chemical diffusion coefficients were found to be of the same order of magnitude or slightly higher than the EIS-derived values (D_C of $10^{-13}\,m^2\,s^{-1}$ in Al0.15-LLZO). The chemical diffusion measured here is expected to be larger than the tracer diffusivity D^*. A number of assumptions and experimental limitations have to be taken into consideration when comparing across the multiple techniques, which have been discussed. That said, the tracer lithium diffusion method was shown to be a promising complementary technique for observing true, long-range diffusion of lithium ions in lithium conductors, given further development.

Finally, Chapter 8 explored the differences in the critical currents for both Ga- and Al-doped LLZO, illustrating the effect of dopants on the chemical and electrochemical properties of the electrolyte with a lithium metal electrode. Electrochemical cycling experiments on Li/Ga-LLZO/Li and Li/Al-LLZO/Li cells showed marked differences in cycling behaviour for the two doped compositions of LLZO tested. Ga-LLZO showed a higher critical current density ($0.16\,mA\,cm^{-2}$) for cell failure caused by dendrite formation, and a less detrimental performance at higher current densities. On the other hand, Al-LLZO showed cell failure at the lower critical current density of $0.1\,mA\,cm^{-2}$, with erratic voltage profiles at higher applied currents.

Post-mortem analysis revealed a greater extended network of Li dendrites in the Al-LLZO cycled pellet, with more visible degradation features after cell failure occurred. In both compositions, SIMS chemical analysis revealed that dendritic features were enriched in Al and Li species, whereas the LLZO grains were depleted in Al^+ and enriched in Li^+ after cycling compared to in their pristine state. XPS chemical analysis over large areas showed that cycled pellets showed a net enrichment in Al in the near-surface region close to the original location of the electrodes; however, this could not be separated from the effect of the crucible during sintering. Although evidence of Al-Li alloying in NMR experiments was not seen, there was clearly an affinity for Li dendrites with aluminium from the LLZO pellet samples. The chemical nature of the grains and grain boundaries in LLZO was found to be an important factor for determining cell operating behaviour, when all other parameters are fixed (including the microstructure). This work illustrated the role of aluminium in the formation of lithium dendrites during cell cycling of LLZO, and its ability to promote cell failure through the propagation of dendrites, and is seen in the greater propensity for dendrite formation and concurrent cell failure in Al-LLZO compared to Ga-LLZO electrolyte cells.

9.2 Suggested Further Work

Based on the findings of this thesis, a number of research questions remain which could shape the course of further study.

A method for imaging the atomic arrangement in LLZO using STEM was developed, allowing challenging sample damaging effects to be overcome, but Li and other light elements could not be resolved, even with high resolution aberration-corrected setup. Further work should be considered to image lamella samples of LLZO, and to study interfaces and grain boundaries on an atomically-resolved scale. Sometimes coloured pellets of LLZO were obtained during the synthesis procedure, and it is suggested that the creation of colour centres under the reducing argon atmosphere sintering conditions may be the cause, resulting in the formation of lithium and oxygen vacancies. These oxygen vacancies might be able to be imaged using a high resolution STEM method, and following the work of Kilner [46] and Kubicek [28], studied through isotopic exchange techniques, correlating synthesis conditions (i.e. temperature, oxygen partial pressure) to the formation of oxygen vacancies. The use of oxygen vacancies in garnets as a donor dopant to stabilise the cubic phase and control the lithium content and conductivity as an alternative strategy to cation doping would be an interesting avenue to explore.

Proton-lithium exchange experiments on LLZO pellets were carried out under a small range of exchange times; the experiments should thus be extended to include longer immersion times, enabling the study of the equilibrated region of H-LLZO and to better follow proton diffusivity using tracer experiments. Time of flight (TOF)-SIMS linescan-type mapping could be utilised for long diffusion length studies following long exchange times. More NMR and computational work to probe O-H bonding interactions in protonated H-LLZO is important in order to understand the stability and kinetics in H-LLZO, including the interaction of dopants. For example, using D_2O or ^{17}O-H_2O, NMR might also be able to give improved structural information.

Additionally, combining the effect of proton-lithium exchange on the lithium kinetics using lithium tracer experiments would be interesting in order to probe the true Li transport in the exchanged material following moisture reactivity, and highly important in order to learn more about the nature of Li transport in the degraded material. More information on the chemistry of grain boundaries in LLZO and their reactivity with moisture will be important in order to explain the dramatic resistivity changes following water-immersion and proton exchange. This information will require the use of high resolution mapping in SIMS, and also STEM analysis of lamellas in order to look at the atomic arrangements at the grain boundaries. A knowledge of the differences in the grain boundary chemistry of Ge-, Ga- and Al-LLZO is also important to understand electrochemical and transport properties, extending the work in Chapter 8 on the role of dopants on dendrite formation.

A knowledge of the proton-lithium exchange reaction and moisture degradation processes of garnets could enable the exploration of the material to be used as a separator in aqueous battery systems, and to be used with in lithium-air cells, in addition to being of importance for handling of the material for use in real devices.

The solid state method of tracer diffusion using a thin film of ^{6}Li-enriched material (either the metal, or an oxide) looks to be a promising technique for probing lithium diffusivity. Both within-grain and inter-grain diffusion could be followed by adjusting

the diffusion times and sample preparation for analysis (using FIB-SIMS depth-profiling for selective area diffusion and linescan, or large area depth-profiling, in the TOF-SIMS for grain and grain boundary diffusion). SIMS mapping could also be carried out by cutting a trench perpendicular to the surface, applying ^{6}Li metal to allow exchange to occur, then mapping the revealed cross-section. Accurate fitting of the diffusion profiles using finite difference simulations to correctly model the boundary conditions is suggested to evaluate D^* and k^* using this experimental setup. Variable, high temperature measurements could be made to extract activation energies from the diffusion coefficients, and this could serve as a method to in effect suppress the Li motion at room temperature during post-analysis. In addition, adding an anneal step at elevated temperature and then measuring the broadening of diffusion profiles as a function of time could also be done [57, 58].

Lithium tracer diffusion experiments, if developed further following from the work reported here, would be a highly useful and complementary method for understanding lithium transport in a variety of lithium-based systems, extending beyond garnets to other solid electrolytes and electrode materials. It could be used as a tool to understand expected bulk and interfacial lithium transport in battery materials as a function of temperature, state of charge and lithiation state.

Galvanostatic cycling experiments could be repeated with Al-free LLZO samples to observe differences in cyclability and to understand the role of Al in the formation and propagation of lithium dendrites. Using an isotopically-labelled ^{6}Li metal electrode for cycling experiments combined with SIMS and NMR post-cycling, would also help to determine where the Li in the dendrites comes from, and to distinguish between the intra- and inter-granular degradation seen in the cycled material.

Solving the dendrite and interface problem with lithium metal electrodes is critical for the realisation of all-solid-state batteries, and it is clear from this work that the answer relies on a complex mix of chemical, mechanical and electrochemical factors. In order to overcome the problem, it might be necessary to move to simple systems which can be more easily modelled, requiring collaboration between theorists and experimentalists, to uncover the underlying causes of lithium plating in solid electrolytes. Only then would the development of more complex architectures (such as surface-modified, or composite materials) be fruitful in providing a solution.

Bibliography

[1] K. Kaygusuz, "Energy for sustainable development: A case of developing countries," *Renewable and Sustainable Energy Reviews*, vol. 16, iss. 2, pp. 1116–1126, 2012. DOI: 10.1016/j.rser.2011.11.013. [Online]. Available: http://dx.doi.org/10.1016/j.rser.2011.11.013.

[2] IEA International Energy Agency, "Key World Energy Statistics," Paris, Tech. Rep., 2017, pp. 1–97. DOI: 10.1787/9789264039537-en. [Online]. Available: http://www.oecd-ilibrary.org/energy/key-world-energy-statistics-2009%7B%5C_%7D9789264039537-en.

[3] D. J. Mackay, *Sustainable Energy - Without the Hot Air*. Cambridge: UIT Cambridge Ltd, 2008.

[4] NASA/GISS, "Global land-ocean temperature index," NASA, Tech. Rep., 2017. [Online]. Available: https://climate.nasa.gov/vital-signs/global-temperature/.

[5] A. Giddens, "The Politics of Climate Change," *Policy and Politics*, vol. 43, iss. 2, pp. 155–162, 2015. DOI: 10.1332/030557315X14290856538163. arXiv: arXiv:1011.1669v3. [Online]. Available: http://dx.doi.org/10.1332/030557315X14290856538163.

[6] IPCC, *Climate Change 2013: The Physical Science Basis*, T. Stocker, D. Qin, G.-K. Plattner, M. Tignor, S. Allen, J. Boschung, A. Nauels, Y. Xia, V. Bex, and P. Midgley, Eds. Cambridge: Cambridge University Press, 2013. DOI: 9781107661820. [Online]. Available: https://www.ipcc.ch/pdf/assessment-report/ar5/wg1/WG1AR5%7B%5C_%7DFrontmatter%7B%5C_%7DFINAL.pdf.

[7] J. Busch, *Climate Change and Development in Three Charts*, 2015. [Online]. Available: https://www.cgdev.org/blog/climate-change-and-development-three-charts (visited on 01/03/2018).

[8] H. Ibrahim, A. Ilinca, and J. Perron, "Energy storage systems - Characteristics and comparisons," *Renewable and Sustainable Energy Reviews*, vol. 12, iss. 5, pp. 1221–1250, 2008. DOI: 10.1016/j.rser.2007.01.023.

[9] D. Rastler, "Electricity Energy Storage Technology Options: A White Paper Primer on Applications, Costs and Benefits," *Electric Power Research Institute*, pp. 1–170, 2010. [Online]. Available: http://large.stanford.edu/courses/2012/ph240/doshay1/docs/EPRI.pdf.

[10] G. E. Blomgren, "The Development and Future of Lithium Ion Batteries," *Journal of The Electrochemical Society*, vol. 164, iss. 1, A5019–A5025, 2017. DOI: 10.1149/2.0251701jes. [Online]. Available: http://jes.ecsdl.org/lookup/doi/10.1149/2.0251701jes.

[11] D. Howell, "U.S. Department of Energy Electric Vehicle Battery R&D Progress and Plans," in *IMLB 2016*, Chicago, 2016.

[12] J. Matthey, *Our Guide to Batteries*, Dundee, 2012. [Online]. Available: http://www.jmbatterysystems.com/JMBS/media/JMBS/Documents/JMBS-Guide-to-Batteries.pdf (visited on 02/03/2018).

[13] K. Amine, R. Kanno, and Y. Tzeng, "Rechargeable lithium batteries and beyond: Progress, challenges, and future directions," *MRS Bulletin*, vol. 39, iss. 05, pp. 395–401, 2014. DOI: 10.1557/mrs.2014.62. [Online]. Available: http://www.journals.cambridge.org/abstract%7B%5C_%7DS0883769414000621.

[14] V. R. Kumar, E. Weal, and J. C. Tan, *DoITPoMS: Lithium Batteries*, 2018. [Online]. Available: https://www.doitpoms.ac.uk/tlplib/batteries/batteries%7B%5C_%7Dlithium.php (visited on 02/14/2018).

[15] M. S. Whittingham, "Lithium batteries and cathode materials," *Chemical Reviews*, vol. 104, iss. 10, pp. 4271–4301, 2004. DOI: 10.1021/cr020731c.

[16] P. Vanysek, "Electrochemical Series," in *CRC Handbook of Chemistry and Physics*, J. R. Rumble Jr., Ed., 98th ed., 2005, pp. 77–83. DOI: 10.1136/oem.53.7.504. arXiv: 0202038 [quant-ph]. [Online]. Available: papers3://publication/uuid/F8394DAA-9AE4-4AA2-87A7-39F227EBD02A.

[17] P. G. Bruce, S. A. Freunberger, L. J. Hardwick, and J.-M. Tarascon, "Li-O_2 and Li-S batteries with high energy storage," *Nature Materials*, vol. 11, iss. 1, pp. 19–29, 2012. DOI: 10.1038/nmat3191. [Online]. Available: http://www.ncbi.nlm.nih.gov/pubmed/22169914.

[18] J.-M. Tarascon and M. Armand, "Issues and challenges facing rechargeable lithium batteries.," *Nature*, vol. 414, iss. 6861, pp. 359–367, 2001. DOI: 10.1038/35104644.

[19] M. Balaish, A. Kraytsberg, and Y. Ein-Eli, "A critical review on lithium-air battery electrolytes," *Physical Chemistry Chemical Physics*, vol. 16, iss. 7, pp. 2801–22, 2014. DOI: 10.1039/c3cp54165g. arXiv: c3cp54165g [10.1039]. [Online]. Available: http://www.ncbi.nlm.nih.gov/pubmed/24424632.

[20] A. L. Robinson and J. Janek, "Solid-state batteries enter EV fray," *MRS Bulletin*, vol. 39, iss. December, pp. 1046–1047, 2014. DOI: 10.1557/mrs.2014.285.

[21] P. Knauth, "Inorganic solid Li ion conductors: An overview," *Solid State Ionics*, vol. 180, iss. 14-16, pp. 911–916, 2009. DOI: 10.1016/j.ssi.2009.03.022. [Online]. Available: http://linkinghub.elsevier.com/retrieve/pii/S0167273809001179.

[22] M. Park, X. Zhang, M. Chung, G. B. Less, and A. M. Sastry, "A review of conduction phenomena in Li-ion batteries," *Journal of Power Sources*, vol. 195, iss. 24, pp. 7904–7929, 2010. DOI: 10.1016/j.jpowsour.2010.06.060. [Online]. Available: http://linkinghub.elsevier.com/retrieve/pii/S0378775310010463.

[23] J. B. Bates, N. J. Dudney, B. Neudecker, A. Ueda, and C. D. Evans, "Thin-film lithium and lithium-ion batteries," *Solid State Ionics*, vol. 135, iss. 1-4, pp. 33–45, 2000. DOI: 10.1016/S0167-2738(00)00327-1.

[24] P. Hartmann, T. Leichtweiss, M. R. Busche, M. Schneider, M. Reich, J. Sann, P. Adelhelm, and J. Janek, "Degradation of NASICON-type materials in contact with lithium metal: Formation of mixed conducting interphases (MCI) on solid electrolytes," *Journal of Physical Chemistry C*, vol. 117, iss. 41, pp. 21 064–21 074, 2013. DOI: 10.1021/jp4051275.

[25] J. Li, C. Ma, M. Chi, C. Liang, and N. J. Dudney, "Solid electrolyte: The key for high-voltage lithium batteries," *Advanced Energy Materials*, vol. 5, iss. 4, pp. 1–6, 2015. DOI: 10.1002/aenm.201401408.

[26] D. Santhanagopalan, D. Qian, T. McGilvray, Z. Wang, F. Wang, F. Camino, J. Graetz, N. Dudney, and Y. S. Meng, "Interface limited lithium transport in solid-state batteries," *Journal of Physical Chemistry Letters*, vol. 5, iss. 2, pp. 298–303, 2014. DOI: 10.1021/jz402467x. arXiv: arXiv:1011.1669v3.

[27] J. Maier, "Thermodynamics of electrochemical lithium storage," *Angewandte Chemie - International Edition*, vol. 52, iss. 19, pp. 4998–5026, 2013. DOI: 10.1002/anie.201205569.

[28] M. Kubicek, A. Wachter-Welzl, D. Rettenwander, R. Wagner, S. Berendts, R. Uecker, G. Amthauer, H. Hutter, and J. Fleig, "Oxygen Vacancies in Fast Lithium-Ion Conducting Garnets," *Chemistry of Materials*, vol. 29, iss. 17, acs.chemmater.7b01281, 2017. DOI: 10.1021/acs.chemmater.7b01281. [Online]. Available: http://pubs.acs.org/doi/abs/10.1021/acs.chemmater.7b01281.

[29] G. Li, G. R. Blake, and T. T. M. Palstra, "Vacancies in functional materials for clean energy storage and harvesting: the perfect imperfection," *Chem. Soc. Rev.*, vol. 46, pp. 1693–1706, 2017. DOI: 10.1039/C6CS00571C. [Online]. Available: http://xlink.rsc.org/?DOI=C6CS00571C.

[30] A. Moulson and J. Herbert, *Electroceramics: Materials, Properties, Applications*. 2nd ed. Chichester, England: John Wiley and Sons, 2003.

[31] F. A. Kröger and H. J. Vink, "Relations between the Concentrations of Imperfections in Solids," *Journal of Physics and Chemistry of Solids*, vol. 5, pp. 208–223, 1958.

[32] T. Norby and P. Kofstad, *Defects and Transport in Crystalline Solids*, 2009. [Online]. Available: https://www.uio.no/studier/emner/matnat/kjemi/KJM5120/v09/undervisningsmateriale/ (visited on 02/09/2018).

[33] J. Foord, *Statistical Thermodynamics of Defects in Solids*, Oxford, 2012. [Online]. Available: http : / / foord . chem . ox . ac . uk / teaching / 3rd - yr - solidssurfaces - solids4.pdf.

[34] L. Vegard, "Die Konstitution der Mischkristalle und die Raumfüllung der Atome," *Zeitschrift für Physik*, vol. 5, iss. 1, pp. 17–26, 1921. DOI: 10.1007/BF00549722.

[35] S. Mukhopadhyay, T. Thompson, J. Sakamoto, A. Huq, J. Wolfenstine, J. L. Allen, N. Bernstein, D. A. Stewart, and M. D. Johannes, "Structure and stoichiometry in supervalent doped $Li_7La_3Zr_2O_{12}$," *Chemistry of Materials*, vol. 27, iss. 10, pp. 3658–3665, 2015. DOI: 10.1021/acs.chemmater.5b00362.

[36] W. D. Kingery, H. K. Bowen, and D. R. Uhlmann, *Introduction to Ceramics*, 2nd ed. John Wiley and Sons, 1976.

[37] A. Fick, "Ueber Diffusion," *Annalen der Physik und Chemie*, vol. 170, iss. 1, pp. 59–86, 1855. DOI: 10.1002/andp.18551700105. [Online]. Available: http://doi.wiley.com/10.1002/andp.18551700105.

[38] J. Crank, *The Mathematics of Diffusion*, 2nd ed. Uxbridge: Oxford University Press, 1975.

[39] R. Zwanzig, "Incoherent Inelastic Neutron Scattering and Self-Diffusion," *Physical Review*, vol. 133, iss. 1A, A50–A51, 1964.

[40] S. de Groot and P. Mazur, *Non-Equilibrium Thermodynamics*, 2nd ed. Dover, 1984.

[41] G. Murch, "The Haven Ratio in Fast Ionic Conductors," *Solid State Ionics*, vol. 7, pp. 177–198, 1982.

[42] Y. Haven and K. Compaan, "Correlation Factors for Diffusion in Solids," *Transactions of the Faraday Society*, vol. 52, pp. 786–801, 1956. DOI: 10 . 1039 / TF9565200786.

[43] Y. Deng, C. Eames, J.-N. Chotard, F. Lalère, V. Seznec, S. Emge, O. Pecher, C. P. Grey, C. Masquelier, and M. S. Islam, "Structural and mechanistic insights into fast lithium-ion conduction in Li_4SiO_4-Li_3PO_4 solid electrolytes," *Journal of the American Chemical Society*, p. 150 629 004 023 002, 2015. DOI: 10.1021/jacs.5b04444. [Online]. Available: http://pubs.acs.org/doi/abs/10.1021/jacs.5b04444.

[44] R. Gomer, "Diffusion of adsorbates on metal surfaces," *Reports on Progress in Physics*, vol. 53, iss. 7, pp. 917–1002, 1990. DOI: 10.1088/0034-4885/53/7/002.

[45] R. J. Chater, S. Carter, J. A. Kilner, and B. C. H. Steele, "Development of a novel SIMS technique for oxygen self-diffusion and surface exchange coefficient measurements in oxides of high diffusivity," *Solid State Ionics*, vol. 53-56, iss. PART 2, pp. 859–867, 1992. DOI: 10.1016/0167-2738(92)90266-R.

[46] J. A. Kilner, B. C. Steele, and L. Ilkov, "Oxygen self-diffusion studies using negative-ion secondary ion mass spectrometry (SIMS)," *Solid State Ionics*, vol. 12, iss. C, pp. 89–97, 1984. DOI: 10.1016/0167-2738(84)90134-6.

[47] H. Mehrer, *Diffusion in Solids: Fundamentals, Methods, Materials, Diffusion-Controlled Processes*. Münster: Springer, 2007. DOI: 10.1007/978-3-540-71488-0. arXiv: arXiv:1011.1669v3. [Online]. Available: http://www.springer.com/us/book/9783540714866.

[48] P. Bottke, D. Rettenwander, W. Schmidt, G. Amthauer, and M. Wilkening, "Ion Dynamics in Solid Electrolytes: NMR Reveals the Elementary Steps of Li^+ Hopping in the Garnet $Li_{6.5}La_3Zr_{1.75}Mo_{0.25}O_{12}$," *Chemistry of Materials*, vol. 27, iss. 19, pp. 6571–6582, 2015. DOI: 10.1021/acs.chemmater.5b02231.

[49] A. Kuhn, M. Kunze, P. Sreeraj, H. D. Wiemhöfer, V. Thangadurai, M. Wilkening, and P. Heitjans, "NMR relaxometry as a versatile tool to study Li ion dynamics in potential battery materials," *Solid State Nuclear Magnetic Resonance*, vol. 42, pp. 2–8, 2012. DOI: 10.1016/j.ssnmr.2012.02.001.

[50] H. Nozaki, M. Harada, S. Ohta, I. Watanabe, Y. Miyake, Y. Ikedo, N. H. Jalarvo, E. Mamontov, and J. Sugiyama, "Li diffusive behavior of garnet-type oxides studied by muon-spin relaxation and QENS," *Solid State Ionics*, vol. 262, pp. 585–588, 2014. DOI: 10.1016/j.ssi.2013.10.014. [Online]. Available: http://dx.doi.org/10.1016/j.ssi.2013.10.014.

[51] M. Amores, T. E. Ashton, P. J. Baker, E. J. Cussen, and S. A. Corr, "Fast microwave-assisted synthesis of Li-stuffed garnets and insights into Li diffusion from muon spin spectroscopy," *Journal of Materials Chemistry A*, vol. 4, iss. 5, pp. 1729–1736, 2016. DOI: 10.1039/C5TA08107F. [Online]. Available: http://xlink.rsc.org/?DOI=C5TA08107F.

[52] J. Sugiyama, K. Mukai, Y. Ikedo, H. Nozaki, M. M. Nsson, and I. Watanabe, "Li diffusion in Li_xCoO_2 probed by muon-spin spectroscopy," pp. 1–5, 2009. DOI: 10.1103/PhysRevLett.103.147601. arXiv: 0909.2921. [Online]. Available: http://arxiv.org/abs/0909.2921%20http://dx.doi.org/10.1103/PhysRevLett.103.147601.

[53] H. Schmidt, "Li Diffusion in Lithium Containing Metal Oxides Investigated by Tracer Methods," *Diffusion Foundations*, vol. 8, pp. 109–128, 2016. DOI: 10.4028/www.scientific.net/DF.8.109. [Online]. Available: http://www.scientific.net/DF.8.109.

[54] J. N. Coles and J. V. P. Long, "An ion-microprobe study of the self-diffusion of Li^+ of lithium fluoride," *Philosophical Magazine*, vol. 29, iss. 3, pp. 457–471, 1974. DOI: 10.1080/14786437408213232. [Online]. Available: http://www.tandfonline.com/doi/abs/10.1080/14786437408213232.

[55] N. Kuwata, X. Lu, T. Miyazaki, Y. Iwai, T. Tanabe, and J. Kawamura, "Lithium diffusion coefficient in amorphous lithium phosphate thin films measured by secondary ion mass spectroscopy with isotope exchange methods," *Solid State Ionics*, vol. 294, pp. 59–66, 2016. DOI: 10.1016/j.ssi.2016.06.015. [Online]. Available: http://dx.doi.org/10.1016/j.ssi.2016.06.015.

[56] Y. Oishi, Y. Kamei, M. Akiyama, and T. Yanagi, "Self-diffusion coefficient of lithium in lithium oxide," *Journal of Nuclear Materials*, vol. 87, iss. 2-3, pp. 341–344, 1979. DOI: 10.1016/0022-3115(79)90570-1.

[57] J. Rahn, E. Hüger, L. Dörrer, B. Ruprecht, P. Heitjans, and H. Schmidt, "Li self-diffusion in lithium niobate single crystals at low temperatures.," *Physical Chemistry Chemical Physics*, vol. 14, iss. 7, pp. 2427–33, 2012. DOI: 10.1039/c2cp23548j. [Online]. Available: http://www.ncbi.nlm.nih.gov/pubmed/22246110.

[58] J. Rahn, P. Heitjans, and H. Schmidt, "Li Self-Diffusivities in Lithium Niobate Single Crystals as a Function of Li_2O Content," *Journal of Physical Chemistry C*, vol. 119, iss. 27, pp. 15 557–15 561, 2015. DOI: 10.1021/acs.jpcc.5b04391.

[59] A.-M. Welsch, H. Behrens, I. Horn, S. Roß, and P. Heitjans, "Self-Diffusion of Lithium in $LiAlSi_2O_6$ Glasses Studied Using Mass Spectrometry.," *The journal of physical chemistry. A*, vol. 116, iss. 1, pp. 309–318, 2012. DOI: 10.1021/jp209319b. [Online]. Available: http://dx.doi.org/10.1021/jp209319b.

[60] D. Wiedemann, S. Nakhal, J. Rahn, E. Witt, M. M. Islam, S. Zander, P. Heitjans, H. Schmidt, T. Bredow, M. Wilkening, and M. Lerch, "Unravelling Ultraslow Lithium-Ion Diffusion in γ-$LiAlO_2$: Experiments with Tracers, Neutrons, and Charge Carriers," *Chemistry of Materials*, vol. 28, iss. 3, pp. 915–924, 2016. DOI: 10.1021/acs.chemmater.5b04608.

[61] W. Möller, M. Hufschmidt, and T. H. Pfeiffer, "Diffusion studies by means of nuclear reaction depth profiling," *Nuclear Instruments and Methods*, vol. 149, iss. 1-3, pp. 73–76, 1978. DOI: 10.1016/0029-554X(78)90841-8.

[62] S. Takai, M. Kamata, S. Fujine, K. Yoneda, K. Kanda, and T. Esaka, "Diffusion coefficient measurement of lithium ion in sintered $Li_{1.33}Ti_{1.67}O_4$ by means of neutron radiography," *Solid State Ionics*, vol. 123, iss. 1, pp. 165–172, 1999. DOI: 10.1016/S0167-2738(99)00095-8.

[63] S. Takai, K. Kurihara, K. Yoneda, S. Fujine, Y. Kawabata, and T. Esaka, "Tracer diffusion experiments on LISICON and its solid solutions by means of neutron radiography," *Solid State Ionics*, vol. 171, iss. 1-2, pp. 107–112, 2004. DOI: 10.1016/S0167-2738(03)00305-9.

[64] S. Takai, T. Mandai, Y. Kawabata, and T. Esaka, "Diffusion coefficient measurements of $La_{2/3-x}Li_{3x}TiO_3$ using neutron radiography," *Solid State Ionics*, vol. 176, iss. 29-30, pp. 2227–2233, 2005. DOI: 10.1016/j.ssi.2005.06.012.

[65] K. D. Krsulich, "Pulsed Field Gradient Magnetic Resonance Measurements of Lithium-Ion Diffusion," PhD, Massachusetts Institute of Technology, 2014.

[66] K. Hayamizu, S. Seki, and T. Haishi, "Lithium ion micrometer diffusion in a garnet-type cubic $Li_7La_3Zr_2O_{12}$ (LLZO) studied using ^{7}Li NMR spectroscopy," *The Journal of Chemical Physics*, vol. 146, iss. 2, p. 024 701, 2017. DOI: 10.1063/1.4973827. [Online]. Available: http://aip.scitation.org/doi/10.1063/1.4973827.

[67] A. Kuhn, S. Narayanan, L. Spencer, G. Goward, V. Thangadurai, and M. Wilkening, "Li self-diffusion in garnet-type $Li_7La_3Zr_2O_{12}$ as probed directly by diffusion-induced ^7Li spin-lattice relaxation NMR spectroscopy," *Physical Review B*, vol. 83, iss. 9, p. 094 302, Mar. 2011. DOI: 10.1103/PhysRevB.83.094302. [Online]. Available: http://link.aps.org/doi/10.1103/PhysRevB.83.094302.

[68] G. H. Sørland, "Dynamic Pulsed-Field-Gradient NMR," in *Springer Series in Chemical Physics*, vol. 110, Berlin: Springer, 2014, ch. 1, pp. 1–35. DOI: 10.1007/978-3-662-44500-6.

[69] S. Adams and R. P. Rao, "Ion transport and phase transition in $Li_{7-x}La_3(Zr_{2-x}M_x)O_{12}$ ($M = Ta^{5+}, Nb^{5+}$, $x = 0, 0.25$)," *Journal of Materials Chemistry*, vol. 22, iss. 4, pp. 1426–1434, 2012. DOI: 10.1039/C1JM14588F. [Online]. Available: http://xlink.rsc.org/?DOI=C1JM14588F.

[70] M. Burbano, D. Carlier, F. Boucher, B. J. Morgan, and M. Salanne, "Sparse Cyclic Excitations Explain the Low Ionic Conductivity of Stoichiometric $Li_7La_3Zr_2O_{12}$," *Physical Review Letters*, vol. 116, iss. 13, p. 135 901, 2016. DOI: 10.1103/PhysRevLett.116.135901. [Online]. Available: http://link.aps.org/doi/10.1103/PhysRevLett.116.135901.

[71] C. Chen, Z. Lu, and F. Ciucci, "Data mining of molecular dynamics data reveals Li diffusion characteristics in garnet $Li_7La_3Zr_2O_{12}$," *Scientific Reports*, vol. 7, iss. January, p. 40 769, 2017. DOI: 10.1038/srep40769. [Online]. Available: http://www.nature.com/articles/srep40769.

[72] R. Jalem, M. Nakayama, W. Manalastas, J. A. Kilner, R. W. Grimes, T. Kasuga, and K. Kanamura, "Insights into the Lithium-Ion Conduction Mechanism of Garnet-Type Cubic $Li_5La_3Ta_2O_{12}$ by Ab-Initio Calculations," *Journal of Physical Chemistry C*, vol. 119, iss. 36, pp. 20 783–20 791, 2015. DOI: 10.1021/acs.jpcc.5b05068.

[73] J. B. Goodenough and Y. Kim, "Challenges for rechargeable Li batteries," *Chemistry of Materials*, vol. 22, iss. 3, pp. 587–603, 2010. DOI: 10.1021/cm901452z.

[74] J. B. Goodenough, "Changing Outlook for Rechargeable Batteries," *ACS Catalysis*, vol. 7, iss. 2, pp. 1132–1135, 2017. DOI: 10.1021/acscatal.6b03110.

[75] J. Janek and W. G. Zeier, "A solid future for battery development," *Nature Energy*, vol. 1, p. 141, 2016. DOI: 10.1038/NENERGY.2016.141.

[76] J. B. Bates, N. J. Dudney, G. R. Gruzalski, R. A. Zuhr, A. Choudhury, C. F. Luck, and J. D. Robertson, "Electrical properties of amorphous lithium electrolyte thin films," *Solid State Ionics*, vol. 53, iss. 56, pp. 647–654, 1992. DOI: 10.1016/0167-2738(92)90442-R.

[77] A. Manthiram, X. Yu, and S. Wang, "Lithium battery chemistries enabled," *Nature Reviews (Materials)*, vol. 2, p. 16 103, 2017. DOI: 10.1038/natrevmats.2016.103. [Online]. Available: http://dx.doi.org/10.1038/natrevmats.2016.103.

[78] C. Berthier, W. Gorecki, M. Minier, M. B. Armand, J. M. Chabagno, and P. Rigaud, "Microscopic investigation of ionic conductivity in alkali metal salts-poly(ethylene oxide) adducts," *Solid State Ionics*, vol. 11, iss. 1, pp. 91–95, 1983. DOI: 10.1016/0167-2738(83)90068-1.

[79] N. Kamaya, K. Homma, Y. Yamakawa, M. Hirayama, R. Kanno, M. Yonemura, T. Kamiyama, Y. Kato, S. Hama, K. Kawamoto, and A. Mitsui, "A lithium superionic conductor," *Nature materials*, vol. 10, iss. 9, pp. 682–686, 2011. DOI: 10.1038/nmat3066. [Online]. Available: http://dx.doi.org/10.1038/nmat3066.

[80] S. Wenzel, S. Randau, T. Leichtweiß, D. A. Weber, J. Sann, W. G. Zeier, and J. Janek, "Direct Observation of the Interfacial Instability of the Fast Ionic Conductor $Li_{10}GeP_2S_{12}$ at the Lithium Metal Anode," *Chemistry of Materials*, vol. 28, iss. 7, pp. 2400–2407, 2016. DOI: 10.1021/acs.chemmater.6b00610.

[81] Y. Mo, S. P. Ong, and G. Ceder, "First principles study of the $Li_{10}GeP_2S_{12}$ lithium super ionic conductor material," *Chemistry of Materials*, vol. 24, iss. 1, pp. 15–17, 2012. DOI: 10.1021/cm203303y.

[82] L. O. Hagman and P. Kierkegaard, "The Crystal Structure of $NaMe_2(PO_4)_3$; Me = Ge, Ti, Zr," *Acta Chemica Scandinavica*, vol. 22, pp. 1822–1832, 1968.

[83] J. B. Goodenough, H. Y.-P. Hong, and J. A. Kafalas, "Fast Na^+-ion transport in skeleton structures," *Materials Research Bulletin*, vol. 11, pp. 203–220, 1976. DOI: 10.1016/0025-5408(76)90077-5.

[84] P. Atkins and J. de Paula, *Atkins' Physical Chemistry*, 8th ed. Oxford University Press, 2006.

[85] L. Sebastian and J. Gopalakrishnan, "Lithium ion mobility in metal oxides: a materials chemistry perspective," *Journal of Materials Chemistry*, vol. 13, iss. 3, pp. 433–441, Feb. 2003. DOI: 10.1039/b211367h. [Online]. Available: http://xlink.rsc.org/?DOI=b211367h.

[86] H. Aono, E. Sugimoto, Y. Sadaoka, N. Imanaka, and G.-Y. Adachi, "Electrical property and sinterability of $LiTi_2(PO_4)_3$ mixed with lithium salt (Li_3PO_4 or Li_3BO_3)," *Solid State Ionics*, vol. 47, iss. 3-4, pp. 257–264, 1991. DOI: 10.1016/0167-2738(91)90247-9.

[87] H. Y. P. Hong, "Crystal structure and ionic conductivity of $Li_{14}Zn(GeO_4)_4$ and other new Li^+ superionic conductors," *Materials Research Bulletin*, vol. 13, iss. 2, pp. 117–124, 1978. DOI: 10.1016/0025-5408(78)90075-2.

[88] P. G. Bruce and A. R. West, "Ionic conductivity of LISICON solid solutions, $Li_{2+2x}Zn_{1-x}GeO_4$," *Journal of Solid State Chemistry*, vol. 44, iss. 3, pp. 354–365, 1982. DOI: 10.1016/0022-4596(82)90383-8.

[89] P. G. Bruce and A. R. West, "The A-C Conductivity of Polycrystalline LISICON, $Li_{2+2x}Zn_{1-x}GeO_4$, and a Model for Intergranular Constriction Resistances," *Journal of The Electrochemical Society*, vol. 130, iss. 3, pp. 662–669, 1983. DOI: 10.1149/1.2119778. [Online]. Available: http://jes.ecsdl.org/content/130/3/662.abstract.

[90] Y. Liu, C. Li, B. Li, H. Song, Z. Cheng, M. Chen, and P. He, "Germanium Thin Film Protected Lithium Aluminum Germanium Phosphate for Solid-State Li Batteries," *Advanced Energy Materials*, vol. 1702374, pp. 1–7, 2018. DOI: 10.1002/aenm.201702374. [Online]. Available: http://onlinelibrary.wiley.com/resolve/doi?DOI=10.1002/aenm.201702374.

[91] R. Kanno and M. Murayama, "Lithium Ionic Conductor Thio-LISICON: The Li_2S-GeS_2-P_2S_5 System," *Journal of The Electrochemical Society*, vol. 148, iss. 7, A742, 2001. DOI: 10.1149/1.1379028. [Online]. Available: http://jes.ecsdl.org/cgi/doi/10.1149/1.1379028.

[92] U. of Cambridge, *DoITPoMS: Barium Titanate and Phase Changes*, 2015. [Online]. Available: http://www.doitpoms.ac.uk/tlplib/ferroelectrics/phase%7B%5C_%7Dchanges.php (visited on 07/02/2015).

[93] J. Brous, I. Fankuchen, and E. Banks, "Rare earth titanates with a perovskite structure," *Acta Crystallographica*, vol. 6, iss. 1, pp. 67–70, 1953. DOI: 10.1107/S0365110X53000156.

[94] Y. Inaguma, C. Liquan, M. Itoh, T. Nakamura, T. Uchida, H. Ikuta, and M. Wakihara, "High ionic conductivity in lithium lanthanum titanate," *Solid State Communications*, vol. 86, iss. 10, pp. 689–693, 1993. DOI: 10.1016/0038-1098(93)90841-A.

[95] J. W. Fergus, "Ceramic and polymeric solid electrolytes for lithium-ion batteries," *Journal of Power Sources*, vol. 195, iss. 15, pp. 4554–4569, Aug. 2010. DOI: 10.1016/j.jpowsour.2010.01.076. [Online]. Available: http://linkinghub.elsevier.com/retrieve/pii/S037877531000234X.

[96] J. Emery, J. Buzare, O. Bohnke, and J. Fourquet, "Lithium-7 NMR and ionic conductivity studies of lanthanum lithium titanate electrolytes," *Solid State Ionics*, vol. 99, iss. 1-2, pp. 41–51, 1997. DOI: 10.1016/S0167-2738(97)00202-6.

[97] V. Cherepanov, I. Kolokolov, and V. L'vov, "The saga of YIG: spectra, thermodynamics, interaction and relaxation of magnons in a complex magnet," *Physics Reports*, vol. 229, iss. 3, pp. 81–144, 1993. DOI: 10.1016/0370-1573(93)90107. [Online]. Available: https://doi.org/10.1016/0370-1573(93)90107-O.

[98] E. J. Cussen, "Structure and ionic conductivity in lithium garnets," *Journal of Materials Chemistry*, vol. 20, iss. 25, pp. 5167–5173, 2010. DOI: 10.1039/b925553b. [Online]. Available: http://xlink.rsc.org/?DOI=b925553b.

[99] V. Thangadurai, H. Kaack, and W. J. F. Weppner, "Novel Fast Lithium Ion Conduction in Garnet-Type $Li_5La_3M_2O_{12}$," *Journal of the American Ceramic Society*, vol. 86, pp. 437–440, 2003.

[100] M. P. O'Callaghan, D. R. Lynham, E. J. Cussen, and G. Z. Chen, "Structure and Ionic-Transport Properties of Lithium-Containing Garnets $Li_3Ln_3Te_2O_{12}$ (Ln = Y, Pr, Nd, Sm-Lu)," *Chemistry of Materials*, vol. 18, pp. 4681–4689, 2006.

[101] M. P. O'Callaghan and E. J. Cussen, "Lithium dimer formation in the Li-conducting garnets $Li_{5+x}Ba_xLa_{3-x}Ta_2O_{12}$ ($0 < x < 1.6$)," *Chemical Communications*, vol. 12, iss. 20, pp. 2048–2050, 2007. DOI: 10.1039/b700369b.

[102] E. J. Cussen, "The structure of lithium garnets: cation disorder and clustering in a new family of fast Li^+ conductors," *Chemical communications*, pp. 412–413, 2006. DOI: 10.1039/b514640b.

[103] J. Awaka, N. Kijima, H. Hayakawa, and J. Akimoto, "Synthesis and structure analysis of tetragonal $Li_7La_3Zr_2O_{12}$ with the garnet-related type structure," *Journal of Solid State Chemistry*, vol. 182, iss. 8, pp. 2046–2052, Aug. 2009. DOI: 10.1016/j.jssc.2009.05.020. [Online]. Available: http://linkinghub.elsevier.com/retrieve/pii/S002245960900228X.

[104] J. Awaka, A. Takashima, K. Kataoka, N. Kijima, Y. Idemoto, and J. Akimoto, "Crystal Structure of Fast Lithium-ion-conducting Cubic $Li_7La_3Zr_2O_{12}$," *Chemistry Letters*, vol. 40, iss. 1, pp. 60–62, 2011. DOI: 10.1246/cl.2011.60.

[105] H. Xie, J. A. Alonso, Y. Li, M. T. Fern, and J. B. Goodenough, "Lithium Distribution in Aluminum-Free Cubic $Li_7La_3Zr_2O_{12}$," *Chemistry of Materials*, vol. 23, pp. 3587–3589, 2011.

[106] R. Murugan, V. Thangadurai, and W. Weppner, "Fast lithium ion conduction in garnet-type $Li_7La_3Zr_2O_{12}$," *Angewandte Chemie - International Edition*, vol. 46, iss. 41, pp. 7778–7781, 2007. DOI: 10.1002/anie.200701144. arXiv: arXiv:1408.1149.

[107] V. Thangadurai, S. Narayanan, and D. Pinzaru, "Garnet-type solid-state fast Li ion conductors for Li batteries: critical review," *Chemical Society Reviews*, vol. 43, iss. 13, pp. 4714–27, Jul. 2014. DOI: 10.1039/c4cs00020j. [Online]. Available: http://www.ncbi.nlm.nih.gov/pubmed/24681593.

[108] M. O'Callaghan, A. Powell, J. Titman, G. Chen, and E. J. Cussen, "Switching on fast lithium ion conductivity in garnets: The structure and transport properties of $Li_{3+x}Nd_3Te_{2-x}Sb_xO_{12}$," vol. 20, pp. 2360–2369, 2008. DOI: 10.1021/cm703677q. [Online]. Available: http://dx.doi.org/%2010.1021/cm703677q.

[109] M. Xu, M. S. Park, J. M. Lee, T. Y. Kim, Y. S. Park, and E. Ma, "Mechanisms of Li^+ transport in garnet-type cubic $Li_{3+x}La_3M_2O_{12}$ (M = Te, Nb, Zr)," *Physical Review B - Condensed Matter and Materials Physics*, vol. 85, iss. 5, pp. 1–5, 2012. DOI: 10.1103/PhysRevB.85.052301.

[110] R. Jalem, Y. Yamamoto, T. Kasuga, and K. Kanamura, "Concerted Migration Mechanism in the Li Ion Dynamics of Garnet-Type $Li_7La_3Zr_2O_{12}$," *Chemistry of Materials*, vol. 25, pp. 425–430, 2013. DOI: 10.1021/cm303542x.

[111] J. Han, J. Zhu, Y. Li, X. Yu, S. Wang, G. Wu, H. Xie, S. C. Vogel, F. Izumi, K. Momma, Y. Kawamura, Y. Huang, J. B. Goodenough, and Y. Zhao, "Experimental visualization of lithium conduction pathways in garnet-type $Li_7La_3Zr_2O_{12}$," *Chemical Communications*, vol. 48, iss. 79, pp. 9840–9842, Oct. 2012. DOI: 10.1039/

c2cc35089k. [Online]. Available: http://www.ncbi.nlm.nih.gov/pubmed/22936071.

[112] D. Wang, G. Zhong, W. K. Pang, Z. Guo, Y. Li, M. J. McDonald, R. Fu, J. X. Mi, and Y. Yang, "Toward Understanding the Lithium Transport Mechanism in Garnet-type Solid Electrolytes: Li^+ Ion Exchanges and Their Mobility at Octahedral/Tetrahedral Sites," *Chemistry of Materials*, vol. 27, iss. 19, pp. 6650–6659, 2015. DOI: 10.1021/acs.chemmater.5b02429.

[113] D. Rettenwander, G. Redhammer, F. Preishuber-Pflügl, L. Cheng, L. J. Miara, R. Wagner, A. Welzl, E. Suard, M. M. Doeff, M. Wilkening, J. Fleig, and G. Amthauer, "Structural and Electrochemical Consequences of Al and Ga Cosubstitution in $Li_7La_3Zr_2O_{12}$ Solid Electrolytes," *Chemistry of Materials*, vol. 28, iss. 7, pp. 2384–2392, 2016. DOI: 10.1021/acs.chemmater.6b00579.

[114] R. Wagner, G. J. Redhammer, D. Rettenwander, G. Tippelt, A. Welzl, S. Taibl, J. Fleig, A. Franz, W. Lottermoser, and G. Amthauer, "Fast Li-Ion-Conducting Garnet-Related $Li_{7-3x}Fe_xLa_3Zr_2O_{12}$ with Uncommon I4-3d Structure," *Chemistry of Materials*, vol. 28, iss. 16, pp. 5943–5951, 2016. DOI: 10.1021/acs.chemmater.6b02516.

[115] R. Wagner, G. J. Redhammer, D. Rettenwander, A. Senyshyn, W. Schmidt, M. Wilkening, and G. Amthauer, "Crystal Structure of Garnet-Related Li-Ion Conductor $Li_{7-3x}Ga_xLa_3Zr_2O_{12}$: Fast Li-Ion Conduction Caused by a Different Cubic Modification?" *Chemistry of Materials*, vol. 28, iss. 6, pp. 1861–1871, 2016. DOI: 10.1021/acs.chemmater.6b00038.

[116] C. Galven, E. Suard, D. Mounier, M.-P. Crosnier-Lopez, and F. Le Berre, "Structural characterization of a new acentric protonated garnet: $Li_{6-x}H_xCaLa_2Nb_2O_{12}$," *Journal of Materials Research*, vol. 28, iss. 16, pp. 2147–2153, 2013. DOI: 10.1557/jmr.2013.209. [Online]. Available: http://www.journals.cambridge.org/abstract%7B%5C_%7DS0884291413002094.

[117] N. Bernstein, M. D. Johannes, and K. Hoang, "Origin of the structural phase transition in $Li_7La_3Zr_2O_{12}$," *Physical Review Letters*, vol. 109, iss. 20, pp. 1–5, 2012. DOI: 10.1103/PhysRevLett.109.205702. arXiv: 1209.0690.

[118] G. Larraz, A. Orera, and M. L. Sanjuán, "Cubic phases of garnet-type $Li_7La_3Zr_2O_{12}$: the role of hydration," *Journal of Materials Chemistry A*, vol. 1, pp. 11 419–11 428, 2013. DOI: 10.1039/c3ta11996c. [Online]. Available: http://xlink.rsc.org/?DOI=c3ta11996c.

[119] Y. Wang and W. Lai, "Phase transition in lithium garnet oxide ionic conductors $Li_7La_3Zr_2O_{12}$: The role of Ta substitution and H_2O/CO_2 exposure," *Journal of Power Sources*, vol. 275, pp. 612–620, 2015. DOI: 10.1016/j.jpowsour.2014.11.062. [Online]. Available: http://dx.doi.org/10.1016/j.jpowsour.2014.11.062.

[120] W. Gu, M. Ezbiri, R. P. Rao, M. Avdeev, and S. Adams, "Effects of penta-and trivalent dopants on structure and conductivity of $Li_7La_3Zr_2O_{12}$," *Solid State Ionics*, vol. 274, pp. 100–105, 2015. DOI: 10.1016/j.ssi.2015.03.019.

[121] Y. Li, J.-T. Han, C.-A. Wang, H. Xie, and J. B. Goodenough, "Optimizing Li^+ conductivity in a garnet framework," *Journal of Materials Chemistry*, vol. 22, iss. 30, p. 15 357, 2012. DOI: 10.1039/c2jm31413d. [Online]. Available: http://xlink.rsc.org/?DOI=c2jm31413d.

[122] L. J. Miara, S. P. Ong, Y. Mo, W. D. Richards, Y. Park, J.-M. Lee, H. S. Lee, and G. Ceder, "Effect of Rb and Ta Doping on the Ionic Conductivity and Stability of the Garnet $Li_{7+2x-y}(La_{3-x}Rb_x)(Zr_{2-y}Ta_y)O_{12}$ ($0 \leq x \leq 0.375$, $0 \leq y \leq 1$) Superionic Conductor: A First Principles Investigation," *Chemistry of Materials*, vol. 25, iss. 15, pp. 3048–3055, Aug. 2013. DOI: 10.1021/cm401232r. [Online]. Available: http://pubs.acs.org/doi/abs/10.1021/cm401232r.

[123] C.-L. Tsai, V. Roddatis, C. Vinod Chandran, Q. Ma, S. Uhlenbruck, M. Bram, P. Heitjans, and O. Guillon, "$Li_7La_3Zr_2O_{12}$ Interface Modification for Li Dendrite Prevention," *ACS Applied Materials & Interfaces*, vol. 8, iss. 16, pp. 10 617–10 628, 2016. DOI: 10.1021/acsami.6b00831. [Online]. Available: http://pubs.acs.org/doi/abs/10.1021/acsami.6b00831.

[124] Z. F. Yow, Y. L. Oh, W. Gu, R. P. Rao, and S. Adams, "Effect of Li^+/H^+ exchange in water treated Ta-doped $Li_7La_3Zr_2O_{12}$," *Solid State Ionics*, vol. 292, pp. 122–129, 2016. DOI: 10.1016/j.ssi.2016.05.016. [Online]. Available: http://dx.doi.org/10.1016/j.ssi.2016.05.016.

[125] E. Rangasamy, J. Wolfenstine, J. L. Allen, and J. Sakamoto, "The effect of 24c-site (A) cation substitution on the tetragonal-cubic phase transition in $Li_{7-x}La_{3-x}A_xZr_2O_{12}$ garnet-based ceramic electrolyte," *Journal of Power Sources*, vol. 230, pp. 261–266, 2013. DOI: 10.1016/j.jpowsour.2012.12.076. [Online]. Available: http://dx.doi.org/10.1016/j.jpowsour.2012.12.076.

[126] J. L. Allen, J. Wolfenstine, E. Rangasamy, and J. Sakamoto, "Effect of substitution (Ta, Al, Ga) on the conductivity of $Li_7La_3Zr_2O_{12}$," *Journal of Power Sources*, vol. 206, pp. 315–319, 2012. DOI: 10.1016/j.jpowsour.2012.01.131. [Online]. Available: http://dx.doi.org/10.1016/j.jpowsour.2012.01.131.

[127] V. Thangadurai, "Fast Solid State Li ion Conducting Garnet-Type Structure Metal Oxides for Energy Storage," *The Journal of Physical Chemistry Letters*, vol. 1, pp. 3530–3537, Dec. 2014. DOI: 10.1021/jz501828v. [Online]. Available: http://pubs.acs.org/doi/abs/10.1021/jz501828v.

[128] Y. Jin and P. J. McGinn, "Al-doped $Li_7La_3Zr_2O_{12}$ synthesized by a polymerized complex method," *Journal of Power Sources*, vol. 196, iss. 20, pp. 8683–8687, Oct. 2011. DOI: 10.1016/j.jpowsour.2011.05.065. [Online]. Available: http://linkinghub.elsevier.com/retrieve/pii/S0378775311010913.

[129] R. Sudo, Y. Nakata, K. Ishiguro, M. Matsui, A. Hirano, Y. Takeda, O. Yamamoto, and N. Imanishi, "Interface behavior between garnet-type lithium-conducting solid electrolyte and lithium metal," *Solid State Ionics*, vol. 262, pp. 151–154, 2014. DOI: 10.1016/j.ssi.2013.09.024. [Online]. Available: http://linkinghub.elsevier.com/retrieve/pii/S0167273813004232.

[130] Y. Suzuki, K. Kami, K. Watanabe, and N. Imanishi, "Characteristics of discharge products in all-solid-state Li-air batteries," *Solid State Ionics*, vol. 278, pp. 222–227, 2015. DOI: 10.1016/j.ssi.2015.06.022. [Online]. Available: http://linkinghub.elsevier.com/retrieve/pii/S016727381500257X.

[131] H. El Shinawi and J. Janek, "Stabilization of cubic lithium-stuffed garnets of the type "$Li_7La_3Zr_2O_{12}$" by addition of gallium," *Journal of Power Sources*, vol. 225, pp. 13–19, Mar. 2013. DOI: 10.1016/j.jpowsour.2012.09.111. [Online]. Available: http://linkinghub.elsevier.com/retrieve/pii/S0378775312015480.

[132] M. Huang, A. Dumon, and C.-W. Nan, "Effect of Si, In and Ge doping on high ionic conductivity of $Li_7La_3Zr_2O_{12}$," *Electrochemistry Communications*, vol. 21, pp. 62–64, Jul. 2012. DOI: 10.1016/j.elecom.2012.04.032. [Online]. Available: http://linkinghub.elsevier.com/retrieve/pii/S1388248112002160.

[133] M. Huang, W. Xu, Y. Shen, Y.-H. Lin, and C.-W. Nan, "X-ray absorption near-edge spectroscopy study on Ge-doped $Li_7La_3Zr_2O_{12}$: enhanced ionic conductivity and defect chemistry," *Electrochimica Acta*, vol. 115, pp. 581–586, Jan. 2014. DOI: 10.1016/j.electacta.2013.11.020. [Online]. Available: http://www.scopus.com/inward/record.url?eid=2-s2.0-84888622307%7B%5C&%7DpartnerID=tZOtx3y1.

[134] H. Buschmann, J. Dölle, S. Berendts, A. Kuhn, P. Bottke, M. Wilkening, P. Heitjans, A. Senyshyn, H. Ehrenberg, A. Lotnyk, V. Duppel, L. Kienle, and J. Janek, "Structure and dynamics of the fast lithium ion conductor "$Li_7La_3Zr_2O_{12}$"," *Physical Chemistry Chemical Physics*, vol. 13, iss. 43, pp. 19 378–92, Nov. 2011. DOI: 10.1039/c1cp22108f. [Online]. Available: http://www.ncbi.nlm.nih.gov/pubmed/21986676.

[135] L. Cheng, J. S. Park, H. Hou, V. Zorba, G. Chen, T. Richardson, J. Cabana, R. Russo, and M. Doeff, "Effect of microstructure and surface impurity segregation on the electrical and electrochemical properties of dense Al-substituted $Li_7La_3Zr_2O_{12}$," *Journal of Materials Chemistry A*, vol. 2, iss. 1, p. 172, 2014. DOI: 10.1039/c3ta13999a. [Online]. Available: http://xlink.rsc.org/?DOI=c3ta13999a.

[136] B. Xu, H. Duan, W. Xia, Y. Guo, H. Kang, H. Li, and H. Liu, "Multistep sintering to synthesize fast lithium garnets," *Journal of Power Sources*, vol. 302, pp. 291–297, 2016. DOI: 10.1016/j.jpowsour.2015.10.084. [Online]. Available: http://dx.doi.org/10.1016/j.jpowsour.2015.10.084.

[137] C. Bernuy-Lopez, W. Manalastas, J. Miguel, A. Aguadero, F. Aguesse, and J. A. Kilner, "Atmosphere Controlled Processing of Ga-Substituted Garnets for High Li-Ion Conductivity Ceramics," *Chemistry of Materials*, vol. 26, pp. 3610–3617, 2014.

[138] J.-F. Wu, E.-Y. Chen, Y. Yu, L. Liu, Y. Wu, W. K. Pang, V. K. Peterson, and X. Guo, "Gallium-doped $Li_7La_3Zr_2O_{12}$ garnet-type electrolytes with high lithium-ion conductivity," *ACS Applied Materials and Interfaces*, vol. 9, iss. 2, pp. 1542–1552, 2017. DOI: 10.1021/acsami.6b13902.

[139] L. Buannic, B. Orayech, J.-M. López Del Amo, J. Carrasco, N. A. Katcho, F. Aguesse, W. Manalastas, W. Zhang, J. Kilner, and A. Llordés, "Dual Substitution Strategy to Enhance Li^+ Ionic Conductivity in $Li_7La_3Zr_2O_{12}$ Solid Electrolyte," *Chemistry of Materials*, vol. 29, iss. 4, pp. 1769–1778, 2017. DOI: 10.1021/acs.chemmater.6b05369. [Online]. Available: http://pubs.acs.org/doi/10.1021/acs.chemmater.6b05369.

[140] A. A. Hubaud, D. J. Schroeder, B. Key, B. J. Ingram, F. Dogan, and J. T. Vaughey, "Low temperature stabilization of cubic $(Li_{7-x}Al_{x/3})La_3Zr_2O_{12}$: role of aluminum during formation," *Journal of Materials Chemistry A*, vol. 1, iss. 31, pp. 8813–8818, 2013. DOI: 10.1039/c3ta11338h. [Online]. Available: http://xlink.rsc.org/?DOI=c3ta11338h.

[141] C. A. Geiger, E. Alekseev, B. Lazic, M. Fisch, T. Armbruster, R. Langner, M. Fechtelkord, N. Kim, T. Pettke, and W. Weppner, "Crystal Chemistry and Stability of "$Li_7La_3Zr_2O_{12}$" Garnet: A Fast Lithium-Ion Conductor," *Inorganic Chemistry*, vol. 50, iss. 3, pp. 1089–1097, 2011. DOI: 10.1021/ic101914e.

[142] Y. Li, J.-T. Han, C.-A. Wang, S. C. Vogel, H. Xie, M. Xu, and J. B. Goodenough, "Ionic distribution and conductivity in lithium garnet $Li_7La_3Zr_2O_{12}$," *Journal of Power Sources*, vol. 209, pp. 278–281, 2012.

[143] D. Rettenwander, P. Blaha, R. Laskowski, K. Schwarz, P. Bottke, M. Wilkening, C. A. Geiger, and G. Amthauer, "DFT Study of the Role of Al^{3+} in the Fast Ion-Conductor $Li_{7-3x}Al_{3+x}La_3Zr_2O_{12}$ Garnet," *Chemistry of Materials*, vol. 26, iss. 8, pp. 2617–2623, 2014. DOI: 10.1021/cm5000999. [Online]. Available: http://dx.doi.org/10.1021/cm5000999.

[144] A. Düvel, A. Kuhn, L. Robben, M. Wilkening, and P. Heitjans, "Mechanosynthesis of Solid Electrolytes: Preparation, Characterization, and Li Ion Transport Properties of Garnet-Type Al-Doped $Li_7La_3Zr_2O_{12}$ Crystallizing with Cubic Symmetry," *Journal of Physical Chemistry C*, vol. 1161, pp. 15 192–15 202, 2012.

[145] E. Rangasamy, J. Wolfenstine, and J. Sakamoto, "The role of Al and Li concentration on the formation of cubic garnet solid electrolyte of nominal composition $Li_7La_3Zr_2O_{12}$," *Solid State Ionics*, vol. 206, pp. 28–32, Jan. 2012. DOI: 10.1016/j.ssi.2011.10.022. [Online]. Available: http://www.scopus.com/inward/record.url?eid=2-s2.0-83655201181%7B%5C&%7DpartnerID=tZOtx3y1.

[146] S. Kumazaki, Y. Iriyama, K.-H. Kim, R. Murugan, K. Tanabe, K. Yamamoto, T. Hirayama, and Z. Ogumi, "High lithium ion conductive $Li_7La_3Zr_2O_{12}$ by inclusion of both Al and Si," *Electrochemistry Communications*, vol. 13, iss. 5, pp. 509–512, May 2011. DOI: 10.1016/j.elecom.2011.02.035. [Online]. Available: http://linkinghub.elsevier.com/retrieve/pii/S1388248111000981.

[147] L. Cheng, W. Chen, M. Kunz, K. Persson, N. Tamura, G. Chen, and M. Doeff, "Effect of Surface Microstructure on Electrochemical Performance of Garnet Solid Electrolytes," *ACS Applied Materials & Interfaces*, vol. 7, iss. 3, pp. 2073–2081, 2015. DOI: 10.1021/am508111r. [Online]. Available: http://pubs.acs.org/doi/abs/10.1021/am508111r.

[148] D. Rettenwander, C. A. Geiger, M. Tribus, P. Tropper, and G. Amthauer, "A synthesis and crystal chemical study of the fast ion conductor $Li_{7-3x}Ga_xLa_3Zr_2O_{12}$ with x = 0.08 to 0.84," *Inorganic Chemistry*, vol. 53, iss. 12, pp. 6264–6269, 2014. DOI: 10.1021/ic500803h.

[149] D. Rettenwander, J. Langer, W. Schmidt, C. Arrer, K. J. Harris, V. Terskikh, G. R. Goward, M. Wilkening, and G. Amthauer, "Site occupation of Ga and Al in stabilized cubic $Li_{7-3(x+y)}Ga_xAl_yLa_3Zr_2O_{12}$ garnets as deduced from ^{27}Al and ^{71}Ga MAS NMR at ultrahigh magnetic fields," *Chemistry of Materials*, vol. 27, iss. 8, pp. 3135–3142, 2015. DOI: 10.1021/acs.chemmater.5b00684.

[150] M. M. Ahmad, "Estimation of the concentration and mobility of mobile Li^+ in the cubic garnet-type $Li_7La_3Zr_2O_{12}$," *RSC Advances*, vol. 5, iss. 33, pp. 25 824–25 829, 2015. DOI: 10.1039/C4RA15972A. [Online]. Available: http://xlink.rsc.org/?DOI=C4RA15972A.

[151] R. Jalem, M. Rushton, W. Manalastas, M. Nakayama, T. Kasuga, J. A. Kilner, and R. W. Grimes, "Effects of Gallium Doping in Garnet-Type $Li_7La_3Zr_2O_{12}$ Solid Electrolytes," *Chemistry of Materials*, vol. 27, pp. 2821–2831, 2015. DOI: 10.1021/cm5045122. [Online]. Available: http://pubs.acs.org/doi/abs/10.1021/cm5045122.

[152] Y. Kihira, S. Ohta, H. Imagawa, and T. Asaoka, "Effect of Simultaneous Substitution of Alkali Earth Metals and Nb in $Li_7La_3Zr_2O_{12}$ on Lithium-Ion Conductivity," *ECS Electrochemistry Letters*, vol. 2, iss. 7, A56–A59, 2013. DOI: 10.1149/2.001307eel. [Online]. Available: http://eel.ecsdl.org/cgi/doi/10.1149/2.001307eel.

[153] T. Thompson, A. Sharafi, M. D. Johannes, A. Huq, J. L. Allen, J. Wolfenstine, and J. Sakamoto, "A Tale of Two Sites: On Defining the Carrier Concentration in Garnet-Based Ionic Conductors for Advanced Li Batteries," *Advanced Energy Materials*, n/a–n/a, 2015. DOI: 10.1002/aenm.201500096. [Online]. Available: http://doi.wiley.com/10.1002/aenm.201500096.

[154] R. D. Shannon, "Revised Effective Ionic Radii and Systematic Studies of Interatomic Distances in Halides and Chalcogenides," *Acta Crystallographica A*, vol. 32, pp. 751–767, 1976.

[155] L. J. Miara, W. D. Richards, Y. E. Wang, and G. Ceder, "First-Principles Studies on Cation Dopants and Electrolyte|Cathode Interphases for Lithium Garnets," *Chemistry of Materials*, vol. 27, iss. 11, pp. 4040–4047, 2015. DOI: 10.1021/acs.chemmater.5b01023.

[156] P. R. Slater and C. Greaves, "The ionic conductivity of proton containing garnets and their decomposition products," *Solid State Ionics*, vol. 53-56, pp. 989–992, 1992. DOI: 10.1016/0167-2738(92)90281-S.

[157] G. Larraz, A. Orera, J. Sanz, I. Sobrados, V. Diez-Gómez, and M. L. Sanjuán, "NMR study of Li distribution in $Li_{7-x}H_xLa_3Zr_2O_{12}$ garnets," *Journal of Materials Chemistry A*, vol. 3, iss. 10, pp. 5683–5691, 2015. DOI: 10.1039/C4TA04570J. [Online]. Available: http://xlink.rsc.org/?DOI=C4TA04570J.

[158] C. Liu, K. Rui, C. Shen, M. E. Badding, G. Zhang, and Z. Wen, "Reversible ion exchange and structural stability of garnet-type Nb-doped $Li_7La_3Zr_2O_{12}$ in water for applications in lithium batteries," *Journal of Power Sources*, vol. 282, pp. 286–293, 2015. DOI: 10.1016/j.jpowsour.2015.02.050. [Online]. Available: http://linkinghub.elsevier.com/retrieve/pii/S0378775315002736.

[159] A. Orera, G. Larraz, J. A. Rodríguez-Velamazán, J. Campo, and M. L. Sanjuán, "Influence of Li^+ and H^+ Distribution on the Crystal Structure of $Li_{7-x}H_xLa_3Zr_2O_{12}$ ($0 \leq x \leq 5$) Garnets," *Inorganic Chemistry*, vol. 55, pp. 1324–1332, 2016. DOI: 10.1021/acs.inorgchem.5b02708. [Online]. Available: http://pubs.acs.org/doi/10.1021/acs.inorgchem.5b02708.

[160] M. Nyman, T. M. Alam, S. K. McIntyre, G. C. Bleier, and D. Ingersoll, "Alternative Approach to Increasing Li Mobility in Li-La-Nb/Ta Garnet Electrolytes," *Chemistry of Materials*, vol. 22, iss. 19, pp. 5401–5410, Oct. 2010. DOI: 10.1021/cm101438x. [Online]. Available: http://pubs.acs.org/doi/abs/10.1021/cm101438x.

[161] C. Galven and J.-L. Fourquet, "Instability of the Lithium Garnet $Li_7La_3Sn_2O_{12}$: Li^+/H^+ Exchange and Structural Study," *Chemistry of Materials*, vol. 23, pp. 1892–1900, 2011.

[162] C. Galven, J. Dittmer, E. Suard, F. Le Berre, and M.-P. Crosnier-Lopez, "Instability of Lithium Garnets against Moisture. Structural Characterization and Dynamics of $Li_{7-x}H_xLa_3Sn_2O_{12}$ and $Li_{5-x}H_xLa_3Nb_2O_{12}$," *Chemistry of Materials*, vol. 24, iss. 17, pp. 3335–3345, 2012. DOI: 10.1021/cm300964k. [Online]. Available: http://pubs.acs.org/doi/abs/10.1021/cm300964k.

[163] L. Truong, J. Colter, and V. Thangadurai, "Chemical stability of Li-stuffed garnet-type $Li_{5+x}Ba_xLa_{3-x}Ta_2O_{12}$ (x = 0, 0.5, 1) in water: a comparative analysis with the Nb analogue," *Solid State Ionics*, vol. 247-248, pp. 1–7, 2013. DOI: 10.1016/j.ssi.2013.05.013. [Online]. Available: http://linkinghub.elsevier.com/retrieve/pii/S0167273813002531.

[164] C. Ma, E. Rangasamy, C. Liang, J. Sakamoto, K. L. More, and M. Chi, "Excellent Stability of a Lithium-Ion-Conducting Solid Electrolyte upon Reversible Li^+/H^+ Exchange in Aqueous Solutions.," *Angewandte Chemie (International ed. in English)*, vol. 54, iss. 1, pp. 129–133, Oct. 2015. DOI: 10.1002/anie.201408124. [Online]. Available: http://www.ncbi.nlm.nih.gov/pubmed/25331968.

[165] Y. Shimonishi, A. Toda, T. Zhang, A. Hirano, N. Imanishi, O. Yamamoto, and Y. Takeda, "Synthesis of garnet-type $Li_{7-x}La_3Zr_2O_{12-1/2x}$ and its stability in aqueous solutions," *Solid State Ionics*, vol. 183, iss. 1, pp. 48–53, 2011. DOI: 10.1016/j.ssi.2010.12.010. [Online]. Available: http://dx.doi.org/10.1016/j.ssi.2010.12.010.

[166] F. Aguesse, J. M. López del Amo, V. Roddatis, A. Aguadero, and J. A. Kilner, "Enhancement of the Grain Boundary Conductivity in Ceramic $Li_{0.34}La_{0.55}TiO_3$ Electrolytes in a Moisture-Free Processing Environment," *Advanced Materials Interfaces*, vol. 1, p. 1300143, Oct. 2014. DOI: 10.1002/admi.201300143. [Online]. Available: http://doi.wiley.com/10.1002/admi.201300143.

[167] Y. Li, J.-T. Han, S. C. Vogel, and C.-A. Wang, "The reaction of $Li_{6.5}La_3Zr_{1.5}Ta_{0.5}O_{12}$ with water," *Solid State Ionics*, vol. 269, pp. 57–61, Jan. 2015. DOI: 10.1016/j.ssi.2014.11.010. [Online]. Available: http://linkinghub.elsevier.com/retrieve/pii/S0167273814004585.

[168] L. Cheng, C. H. Wu, A. Jarry, W. Chen, Y. Ye, J. Zhu, R. Kostecki, K. Persson, J. Guo, M. Salmeron, G. Chen, and M. Doeff, "Interrelationships among Grain Size, Surface Composition, Air Stability, and Interfacial Resistance of Al-Substituted $Li_7La_3Zr_2O_{12}$ Solid Electrolytes," *ACS Applied Materials and Interfaces*, vol. 7, iss. 32, pp. 17 649–17 655, 2015. DOI: 10.1021/acsami.5b02528.

[169] A. Sharafi, S. Yu, M. Naguib, M. Lee, C. Ma, H. M. Meyer, J. Nanda, M. Chi, D. J. Siegel, and J. Sakamoto, "Impact of air exposure and surface chemistry on Li–$Li_7La_3Zr_2O_{12}$ interfacial resistance," *Journal of Materials Chemistry A*, vol. 5, iss. 26, pp. 13 475–13 487, 2017. DOI: 10.1039/C7TA03162A. [Online]. Available: http://xlink.rsc.org/?DOI=C7TA03162A.

[170] J. E. Ni, E. D. Case, J. S. Sakamoto, E. Rangasamy, and J. B. Wolfenstine, "Room temperature elastic moduli and Vickers hardness of hot-pressed LLZO cubic garnet," *Journal of Materials Science*, vol. 47, iss. 23, pp. 7978–7985, 2012. DOI: 10.1007/s10853-012-6687-5.

[171] S. Yu, R. D. Schmidt, R. Garcia-Mendez, E. Herbert, N. J. Dudney, J. B. Wolfenstine, J. Sakamoto, and D. J. Siegel, "Elastic Properties of the Solid Electrolyte $Li_7La_3Zr_2O_{12}$ (LLZO)," *Chemistry of Materials*, vol. 28, iss. 1, pp. 197–206, 2016. DOI: 10.1021/acs.chemmater.5b03854.

[172] M. Kotobuki, H. Munakata, K. Kanamura, Y. Sato, and T. Yoshida, "Compatibility of $Li_7La_3Zr_2O_{12}$ Solid Electrolyte to All-Solid-State Battery Using Li Metal Anode," *Journal of The Electrochemical Society*, vol. 157, iss. 10, A1076, 2010. DOI: 10.1149/1.3474232. [Online]. Available: http://jes.ecsdl.org/cgi/doi/10.1149/1.3474232.

[173] L. Cheng, E. J. Crumlin, W. Chen, R. Qiao, H. Hou, S. Franz Lux, V. Zorba, R. Russo, R. Kostecki, Z. Liu, K. Persson, W. Yang, J. Cabana, T. Richardson, G. Chen, and M. Doeff, "The origin of high electrolyte–electrode interfacial resistances in lithium cells containing garnet type solid electrolytes," *Physical Chemistry Chemical Physics*, vol. 16, iss. 34, p. 18 294, Jul. 2014. DOI: 10.1039/C4CP02921F. [Online]. Available: http://xlink.rsc.org/?DOI=C4CP02921F.

[174] A. Sharafi, E. Kazyak, A. L. Davis, S. Yu, T. Thompson, D. J. Siegel, N. P. Dasgupta, and J. Sakamoto, "Surface Chemistry Mechanism of Ultra-Low Interfacial Resistance in the Solid-State Electrolyte $Li_7La_3Zr_2O_{12}$," *Chemistry of Materials*, vol. 29, pp. 7961–7968, 2017. DOI: 10.1021/acs.chemmater.7b03002. [Online]. Available: http://pubs.acs.org/doi/abs/10.1021/acs.chemmater.7b03002.

[175] W. Luo, Y. Gong, Y. Zhu, Y. Li, Y. Yao, Y. Zhang, K. K. Fu, G. Pastel, C.-F. Lin, Y. Mo, E. D. Wachsman, and L. Hu, "Reducing Interfacial Resistance between Garnet-Structured Solid-State Electrolyte and Li-Metal Anode by a Germanium Layer," *Advanced Materials*, vol. 29, p. 1 606 042, 2017. DOI: 10.1002/adma.201606042.

[176] X. Han, Y. Gong, K. Fu, X. He, G. T. Hitz, J. Dai, A. Pearse, B. Liu, H. Wang, G. Rubloff, Y. Mo, V. Thangadurai, E. D. Wachsman, and L. Hu, "Negating interfacial impedance in garnet-based solid-state Li metal batteries," *Nature Materials*, vol. 16, pp. 572–579, 2017. DOI: 10.1038/nmat4821. [Online]. Available: http://www.nature.com/doifinder/10.1038/nmat4821.

[177] W. Zhou, S. Wang, Y. Li, S. Xin, A. Manthiram, and J. B. Goodenough, "Plating a Dendrite-Free Lithium Anode with a Polymer/Ceramic/Polymer Sandwich Electrolyte," *Journal of the American Chemical Society*, vol. 138, iss. 30, pp. 9385–9388, 2016. DOI: 10.1021/jacs.6b05341.

[178] Y. Zhu, X. He, and Y. Mo, "Origin of Outstanding Stability in the Lithium Solid Electrolyte Materials: Insights from Thermodynamic Analyses Based on First-Principles Calculations," *ACS Applied Materials and Interfaces*, vol. 7, iss. 42, pp. 23 685–23 693, 2015. DOI: 10.1021/acsami.5b07517.

[179] S. Ohta, T. Kobayashi, and T. Asaoka, "High lithium ionic conductivity in the garnet-type oxide $Li_{7-X}La_3(Zr_{2-X}, Nb_X)O_{12}$ (X = 0-2)," *Journal of Power Sources*, vol. 196, iss. 6, pp. 3342–3345, 2011. DOI: 10.1016/j.jpowsour.2010.11.089.

[180] C. Ma, Y. Cheng, K. Yin, J. Luo, A. Sharafi, J. Sakamoto, J. Li, K. L. More, N. J. Dudney, and M. Chi, "Interfacial Stability of Li Metal-Solid Electrolyte Elucidated via in Situ Electron Microscopy," *Nano Letters*, vol. 16, iss. 11, pp. 7030–7036, 2016. DOI: 10.1021/acs.nanolett.6b03223.

[181] C. Monroe and J. Newman, "Dendrite Growth in Lithium/Polymer Systems," *Journal of The Electrochemical Society*, vol. 150, iss. 10, A1377, 2003. DOI: 10.1149/1.1606686. [Online]. Available: http://jes.ecsdl.org/cgi/doi/10.1149/1.1606686.

[182] ——, "The Impact of Elastic Deformation on Deposition Kinetics at Lithium/Polymer Interfaces," *Journal of The Electrochemical Society*, vol. 152, iss. 2, A396, 2005. DOI: 10.1149/1.1850854. [Online]. Available: http://jes.ecsdl.org/cgi/doi/10.1149/1.1850854.

[183] A. V. Virkar, "A model for degradation of electrochemical devices based on linear non-equilibrium thermodynamics and its application to lithium ion batteries," *Journal of Power Sources*, vol. 196, iss. 14, pp. 5970–5984, 2011. DOI: 10.1016/j.jpowsour.2011.03.005. [Online]. Available: http://dx.doi.org/10.1016/j.jpowsour.2011.03.005.

[184] R. Raj and J. Wolfenstine, "Current limit diagrams for dendrite formation in solid-state electrolytes for Li-ion batteries," *Journal of Power Sources*, vol. 343, pp. 119–126, 2017. DOI: 10.1016/j.jpowsour.2017.01.037. [Online]. Available: http://linkinghub.elsevier.com/retrieve/pii/S037877531730037X.

[185] W. Manalastas, "Development of ceramic lithium ion electrolytes for high performance batteries," PhD thesis, University of the Basque Country, 2016.

[186] L. Porz, T. Swamy, B. W. Sheldon, D. Rettenwander, T. Frömling, H. L. Thaman, S. Berendts, R. Uecker, W. C. Carter, and Y.-M. Chiang, "Mechanism of Lithium Metal Penetration through Inorganic Solid Electrolytes," *Advanced Energy Materials*, vol. 7, iss. 20, pp. 1–12, 2017. DOI: 10.1002/aenm.201701003.

[187] F. Aguesse, W. Manalastas, L. Buannic, J. M. Lopez del Amo, G. Singh, A. Llordes, and J. A. Kilner, "Investigating the dendritic growth during full cell cycling of garnet electrolyte in direct contact with Li metal," *ACS Applied Materials & Interfaces*, vol. 9, iss. 7, pp. 3808–3816, 2017. DOI: 10.1021/acsami.6b13925. [Online]. Available: http://pubs.acs.org/doi/abs/10.1021/acsami.6b13925.

[188] M. P. Pechini, *Method of preparing lead and alkaline earth titanates and niobates and coating method using the same to form a capacitor (U.S. Patent 3330697)*, 1967.

[189] B. Dunn and J. I. Zink, "Sol-gel chemistry and materials," *Accounts of Chemical Research*, vol. 40, iss. 9, p. 729, 2007. DOI: 10.1021/ar700178b.

[190] F. Tietz, T. Wegener, M. T. Gerhards, M. Giarola, and G. Mariotto, "Synthesis and Raman micro-spectroscopy investigation of $Li_7La_3Zr_2O_{12}$," *Solid State Ionics*, vol. 230, iss. C, pp. 77–82, 2013. DOI: 10.1016/j.ssi.2012.10.021. [Online]. Available: http://dx.doi.org/10.1016/j.ssi.2012.10.021.

[191] R. P. Rao, W. Gu, N. Sharma, V. K. Peterson, M. Avdeev, and S. Adams, "In situ neutron diffraction monitoring of $Li_7La_3Zr_2O_{12}$ formation: Toward a rational synthesis of garnet solid electrolytes.," *Chemistry of Materials*, vol. 27, iss. 8, pp. 2903–2910, 2015. DOI: 10.1021/acs.chemmater.5b00149.

[192] L. P. Cook and E. R. Plante, "Phase Diagram of the System Li_2O-Al_2O_3," *Ceramic Transactions*, vol. 83, iss. 1983, 1992.

[193] N. S. Kulkarni, T. M. Besmann, and K. E. Spear, "Thermodynamic Optimization of Lithia-Alumina," *Journal of the American Ceramic Society*, vol. 91, iss. 12, pp. 4074–4083, Dec. 2008. DOI: 10.1111/j.1551-2916.2008.02753.x. [Online]. Available: http://doi.wiley.com/10.1111/j.1551-2916.2008.02753.x.

[194] R. M. German, P. Suri, and S. J. Park, "Review: Liquid phase sintering," *Journal of Materials Science*, vol. 44, iss. 1, pp. 1–39, 2009. DOI: 10.1007/s10853-008-3008-0.

[195] J. H. Ahn, S. Y. Park, J. M. Lee, Y. Park, and J. H. Lee, "Local impedance spectroscopic and microstructural analyses of Al-in-diffused $Li_7La_3Zr_2O_{12}$," *Journal of Power Sources*, vol. 254, pp. 287–292, 2014. DOI: 10.1016/j.jpowsour.2013.12.115. [Online]. Available: http://dx.doi.org/10.1016/j.jpowsour.2013.12.115.

[196] Y. Li, Z. Wang, C. Li, Y. Cao, and X. Guo, "Densification and ionic-conduction improvement of lithium garnet solid electrolytes by flowing oxygen sintering," *Journal of Power Sources*, vol. 248, pp. 642–646, Feb. 2014. DOI: 10.1016/j.jpowsour.2013.09.140. [Online]. Available: http://linkinghub.elsevier.com/retrieve/pii/S0378775313016479.

[197] I. Owate and R. Freer, "Thermochemical Etching Method for Ceramics," *Journal of the American Ceramic Society*, vol. 75, iss. 5, pp. 1266–1268, 1992.

[198] Archimedes and T. L. Heath, "On Floating Bodies," in *The Works of Archimedes*, Cambridge University Press, 1897, pp. 253–300. [Online]. Available: https://archive.org/details/worksofarchimede00arch.

[199] S. AG, *Sartorius YDK 01 User's Manual: Methods for Determining Specific Gravity/Density*.

[200] J. Rodriguez-Carvajal, *FullProf Suite Version 2.05*, 2011.

[201] J. Thomson, "Thomson Scattering," *Cambridge Literary and Philosophical Society*, vol. 15, 1910.

[202] W. Bragg, "The Diffraction of Short Electromagnetic Waves by a Crystal," in *Proceedings of the Cambridge Philosophical Society*, 1912, pp. 43–57.

[203] B. Cullity, *Elements of X-Ray Diffraction*, 2nd ed., M. Cohen, Ed. Addison-Wesley Publishing Company Inc., 1978.

[204] Oxford University Chemistry Department, *Inorganic Chemistry Laboratory Undergraduate Practical Course*, 2011.

[205] A. Le Bail, H. Duroy, and J. L. Fourquet, "Ab-Initio Structure Determination of $LiSbWO_6$ by X-ray Powder Diffraction," *Materials Research Bulletin*, vol. 23, pp. 447–452, 1988.

[206] H. M. Rietveld, "A Profile Refinement Method for Nuclear and Magnetic Structures," *Journal of Applied Crystallography*, vol. 2, pp. 65–71, 1969. [Online]. Available: http://journals.iucr.org/j/issues/1969/02/00/issconts.html.

[207] J. Rodríguez-Carvajal, *The Rietveld Method*, 2015. [Online]. Available: https://www.ill.eu/fileadmin/users%7B%5C_%7Dfiles/documents/news%7B%5C_%7Dand%7B%5C_%7Devents/workshops%7B%5C_%7Devents/2015/FPSchool-2015/The%7B%5C_%7DRietveld%7B%5C_%7DMethod%7B%5C_%7DJRC.pdf (visited on 01/31/2018).

[208] L. B. McCusker, R. B. Von Dreele, D. E. Cox, D. Louër, and P. Scardi, "Rietveld refinement guidelines," *Journal of Applied Crystallography*, vol. 32, iss. 1, pp. 36–50, Feb. 1999. DOI: 10.1107/S0021889898009856. [Online]. Available: http://scripts.iucr.org/cgi-bin/paper?S0021889898009856.

[209] NIST, *Neutron Scattering Lengths*. [Online]. Available: https://www.ncnr.nist.gov/resources/n-lengths/elements/ (visited on 10/12/2015).

[210] G. E. Bacon, *Neutron Diffraction*, 3rd ed. Oxford: Clarendon Press, 1975.

[211] ILL, *Institut Laue Langevin*, 2018. [Online]. Available: https://www.ill.eu/ (visited on 01/30/2018).

[212] W. Voigt, "Über das Gesetz der Intensitätsverteilung innerhalb der Linien eines Gasspektrums," *Sitzungsberichte Königliche Bayerische Akademie der Wissenschaften*, vol. 42, pp. 603–620, 1912.

[213] G. K. Wertheim, M. A. Butler, K. W. West, and D. N. E. Buchanan, "Determination of the Gaussian and Lorentzian content of experimental line shapes," *Review of Scientific Instruments*, vol. 45, iss. 11, pp. 1369–1371, 1974. DOI: 10.1063/1.1686503. arXiv: arXiv:1011.1669v3.

[214] S. M. Mukhopadhyay, *Sample Preparation for Microscopic and Spectroscopic Characterisation of Solid Surfaces and Films*, S. Mitra, Ed. John Wiley and Sons, 2003, pp. 337–411.

[215] T. Koopmans, "Über die Zuordnung von Wellenfunktionen und Eigenwerten zu den Einzelnen Elektronen Eines Atoms," *Physica*, vol. 1, iss. 1-6, pp. 104–113, 1934. DOI: 10.1016/S0031-8914(34)90011-2. [Online]. Available: http://linkinghub.elsevier.com/retrieve/pii/S0031891434900112.

[216] R. Smart, S. McIntyre, M. Bancroft, and I. Bello, *X-ray Photoelectron Spectroscopy Tutorial*. [Online]. Available: http://mmrc.caltech.edu/SS%7B%5C_%7DXPS/XPS%7B%5C_%7DPPT/XPS%7B%5C_%7DSlides.pdf (visited on 02/01/2018).

[217] D. A. Shirley, "High-resolution X-ray photoemission spectrum of the valence bands of gold," *Physical Review B*, vol. 5, iss. 12, pp. 4709–4714, 1972. DOI: 10.1103/PhysRevB.5.4709.

[218] H. Shinotsuka, S. Tanuma, C. J. Powell, and D. R. Penn, "Calculations of electron stopping powers for 41 elemental solids over the 50 eV to 30 keV range with the full Penn algorithm," *Nuclear Instruments and Methods in Physics Research, Section B: Beam Interactions with Materials and Atoms*, vol. 270, iss. 1, pp. 75–92, 2012. DOI: 10.1016/j.nimb.2011.09.016.

[219] J. A. Kilner, S. J. Skinner, and H. H. Brongersma, "The isotope exchange depth profiling (IEDP) technique using SIMS and LEIS," *Journal of Solid State Electrochemistry*, vol. 15, iss. 5, pp. 861–876, Feb. 2011. DOI: 10.1007/s10008-010-1289-0. [Online]. Available: http://link.springer.com/10.1007/s10008-010-1289-0.

[220] H. H. Brongersma, M. Draxler, M. de Ridder, and P. Bauer, "Surface composition analysis by low-energy ion scattering," *Surface Science Reports*, vol. 62, iss. 3, pp. 63–109, 2007. DOI: 10.1016/j.surfrep.2006.12.002.

[221] H. H. Brongersma, "Low-Energy Ion Scattering," in *Characterization of Materials*, E. N. Kaufmann, Ed., John Wiley and Sons, 2012, pp. 2024–2044.

[222] H. Téllez, A. Aguadero, J. Druce, M. Burriel, S. Fearn, T. Ishihara, D. S. McPhail, and J. A. Kilner, "New perspectives in the surface analysis of energy materials by combined time-of-flight secondary ion mass spectrometry (ToF-SIMS) and high sensitivity low-energy ion scattering (HS-LEIS)," *Journal of Analytical Atomic Spectrometry*, vol. 29, iss. 8, p. 1361, 2014. DOI: 10.1039/C3JA50292A. [Online]. Available: http://xlink.rsc.org/?DOI=C3JA50292A.

[223] J. Goldstein, D. Newbury, P. Echlin, D. Joy, C. E. Lyman, E. Lifshin, L. Sawyer, J. Michael, P. Echlin, E. Lifshin, L. Sawyer, and J. Michael, *Scanning Electron Microscopy and X-ray Microanalysis*, 3rd ed., J. Goldstein, Ed. Boston: Springer, 2003. DOI: https://doi.org/10.1007/978-1-4615-0215-9. [Online]. Available: https://link.springer.com/book/10.1007/978-1-4615-0215-9%7B%5C#%7Dabout.

[224] L. Rayleigh, "Investigations in optics, with special reference to the spectroscope," *Philosophical Magazine Series 5*, vol. 8, iss. 49, pp. 261–274, 1879. DOI: 10.1080/14786447908639684. arXiv: 9605103 [cs]. [Online]. Available: http://www.tandfonline.com/doi/abs/10.1080/14786447908639684.

[225] T. B. Britton, *SEM, EDX, EBSD and FIB lecture slides; Postgraduate SEM Course*, Department of Materials, Imperial College London, 2015.

[226] SURF Group, *SEM EDX*, 2018. [Online]. Available: https://www.surfgroup.be/semedx.

[227] B. Hafner, *Scanning Electron Microscopy Primer*, 2007. [Online]. Available: http://www.charfac.umn.edu/sem%7B%5C_%7Dprimer.pdf (visited on 02/05/2018).

[228] P. J. Goodhew, J. Humphreys, and R. Beanland, *Electron microscopy and analysis*, 3rd ed. London: Taylor & Francis, 2001. DOI: 10.1037/0022-006X.76.3.524.

[229] D. B. Williams and C. B. Carter, *Transmission Electron Microscopy*. Springer US, 2009. DOI: 10.1007/978-0-387-76501-3.

[230] N. Ni, *An Introduction to STEM; Postgraduate SEM Course*, Department of Materials, Imperial College London, 2015.

[231] L. Jones, H. Yang, T. J. Pennycook, M. S. J. Marshall, S. Van Aert, N. D. Browning, M. R. Castell, and P. D. Nellist, "Smart Align—a new tool for robust non-rigid registration of scanning microscope data," *Advanced Structural and Chemical Imaging*, vol. 1, iss. 1, p. 8, 2015. DOI: 10.1186/s40679-015-0008-4. [Online]. Available: http://www.ascimaging.com/content/1/1/8.

[232] L. Jones, A. Varambhia, R. Beanland, D. Kepaptsoglou, I. Griffiths, A. Ishizuka, F. Azough, R. Freer, K. Ishizuka, D. Cherns, Q. M. Ramasse, S. Lozano-Perez, and P. D. Nellist, "Managing dose-, damage- and data-rates in multi-frame spectrum-imaging," *Microscopy*, iss. March, pp. 1–16, 2018. DOI: 10.1093/JMICRO/DFX125. [Online]. Available: https://academic.oup.com/jmicro/advance-article-abstract/doi/10.1093/jmicro/dfx125/4797531?redirectedFrom=fulltext%7B%5C%%7D0Ahttp://dx.doi.org/10.1093/jmicro/dfx125.

[233] O. Pecher, J. Carretero-Gonzalez, K. J. Griffith, and C. P. Grey, "Materials' methods: NMR in battery research," *Chemistry of Materials*, vol. 29, iss. 1, pp. 213–242, 2017. DOI: 10.1021/acs.chemmater.6b03183.

[234] M. Levitt, *Spin Dynamics- Basics of Nuclear Magnetic Resonance*. Chichester, England: John Wiley and Sons, 2008. [Online]. Available: http://www.southampton.ac.uk/%7B~%7Dmhl/publications/books/SpinDynamics/SD1/figures/index.html.

[235] E. R. Andrew, A. Bradbury, and R. G. Eades, "Nuclear magnetic resonance spectra from a crystal rotated at high speed," *Nature*, vol. 182, iss. 4650, p. 1659, 1958. DOI: 10.1038/1821659a0. arXiv: arXiv:1203.1851v1.

[236] I. J. Lowe, "Free induction decays of rotating solids," *Physical Review Letters*, vol. 2, iss. 7, pp. 285–287, 1959. DOI: 10.1103/PhysRevLett.2.285.

[237] Y. X. Xiang, G. Zheng, G. Zhong, D. Wang, R. Fu, and Y. Yang, "Toward understanding of ion dynamics in highly conductive lithium ion conductors: Some perspectives by solid state NMR techniques," *Solid State Ionics*, vol. 318, iss. December 2017, pp. 19–26, 2018. DOI: 10.1016/j.ssi.2017.11.025. [Online]. Available: https://doi.org/10.1016/j.ssi.2017.11.025.

[238] L. S. Cahill, "Sold-State NMR Studies of Lithium Ion Dynamics in Cathode Materials for Lithium Ion Batteries," PhD, McMaster University, 2008.

[239] J. T. S. Irvine, D. C. Sinclair, and A. R. West, "Electroceramics Characterization by Impedance Spectroscopy," *Advanced Materials*, vol. 2, iss. 3, pp. 132–138, 1990.

[240] B. Hirschorn, M. E. Orazem, B. Tribollet, V. Vivier, I. Frateur, and M. Musiani, "Determination of effective capacitance and film thickness from constant-phase-element parameters," *Electrochimica Acta*, vol. 55, iss. 21, pp. 6218–6227, 2010. DOI: 10.1016/j.electacta.2009.10.065. [Online]. Available: http://dx.doi.org/10.1016/j.electacta.2009.10.065.

[241] B. E. McNealy and J. L. Hertz, "On the use of the constant phase element to understand variation in grain boundary properties," *Solid State Ionics*, vol. 256, pp. 52–60, 2014. DOI: 10.1016/j.ssi.2013.12.030. [Online]. Available: http://dx.doi.org/10.1016/j.ssi.2013.12.030.

[242] D. Johnson, *ZView*, Southern Pines, North Carolina, USA, 2017.

[243] P. Manning, J. Sirman, and J. A. Kilner, "Oxygen self-diffusion and surface exchange studies of oxide electrolytes having the fluorite structure," *Solid State Ionics*, vol. 93, iss. 1-2, pp. 125–132, 1997. DOI: 10.1016/S0167-2738(96)00514-0. [Online]. Available: http://linkinghub.elsevier.com/retrieve/pii/S0167273896005140.

[244] S. Fearn, *An Introduction to Time-of-Flight Secondary Ion Mass Spectrometry (ToF-SIMS) and its Application to Materials Science*. Imperial College London: Morgan and Claypool, 2015. [Online]. Available: http://iopscience.iop.org/book/978-1-6817-4088-1.

[245] B. Hagenhoff, "Fundamentals of SIMS," in *SIMS Europe*, Münster, 2016.

[246] H. F. Winters and J. W. Coburn, "Influence of the altered layer on depth profiling measurements," *Applied Physics Letters*, vol. 28, iss. 4, pp. 176–179, 1976.

[247] J. C. Vickerman and I. S. Gilmore, *Surface Analysis - The Principle Techniques*, 2nd ed. John Wiley and Sons, 2009.

[248] R. A. De Souza, J. Zehnpfenning, M. Martin, and J. Maier, "Determining oxygen isotope profiles in oxides with Time-of-Flight SIMS," *Solid State Ionics*, vol. 176, iss. 15-16, pp. 1465–1471, 2005. DOI: 10.1016/j.ssi.2005.03.012.

[249] B. Hagenhoff, "Time-of-flight secondary ion mass spectrometry of insulators with pulsed charge compensation by low-energy electrons," *Journal of Vacuum Science & Technology A: Vacuum, Surfaces, and Films*, vol. 7, iss. 5, p. 3056, 1989. DOI: 10.1116/1.576315. [Online]. Available: http://link.aip.org/link/?JVA/7/3056/1%7B%5C&%7DAgg=doi.

[250] R. J. Chater, A. J. Smith, and G. Cooke, "Simultaneous detection of positive and negative secondary ions," *Journal of Vacuum Science & Technology B*, vol. 34, iss. 17, pp. 3–122, 2016. DOI: 10.1116/1.4943531. [Online]. Available: http://dx.doi.org/10.1116/1.4943531%7B%5C%%7D5Cnhttp://scitation.aip.org/content/avs/journal/jvstb/34/3?ver=pdfcov.

[251] F. A. Stevie, L. A. Giannuzzi, and B. I. Prenitzer, *Introduction to Focused Ion Beams*, L. A. Giannuzzi and F. A. Stevie, Eds. Springer, 2005.

[252] P. van der Heide, *Secondary Ion Mass Spectrometry: An Introduction to Principles and Practices*, 1st ed. Wiley, 2014.

[253] J. Biersack and J. Ziegler, *Stopping and Range of Ions in Materials (SRIM)*. [Online]. Available: http://www.srim.org/SRIM/SRIMINTRO.htm.

[254] CrystalMaker, *CrystalMaker*, Oxford, 2017. [Online]. Available: http://www.crystalmaker.com/crystalmaker/index.html.

[255] J. Wolfenstine, J. L. Allen, J. Read, and J. Sakamoto, "Chemical stability of cubic $Li_7La_3Zr_2O_{12}$ with molten lithium at elevated temperature," *Journal of Materials Science*, vol. 48, iss. 17, pp. 5846–5851, 2013. DOI: 10.1007/s10853-013-7380-z.

[256] P. Canepa, J. A. Dawson, G. Sai Gautam, J. M. Statham, S. C. Parker, and M. S. Islam, "Particle Morphology and Lithium Segregation to Surfaces of the $Li_7La_3Zr_2O_{12}$ Solid Electrolyte," *Chemistry of Materials*, vol. 30, pp. 3019–3027, 2018. DOI: 10.1021/acs.chemmater.8b00649. [Online]. Available: http://pubs.acs.org/doi/10.1021/acs.chemmater.8b00649.

[257] J. Fleig, "The grain boundary impedance of random microstructures: Numerical simulations and implications for the analysis of experimental data," *Solid State Ionics*, vol. 150, iss. 1-2, pp. 181–193, 2002. DOI: 10.1016/S0167-2738(02)00274-6.

[258] P. Bron, B. Roling, and S. Dehnen, "Impedance characterization reveals mixed conducting interphases between sulfidic superionic conductors and lithium metal electrodes," *Journal of Power Sources*, vol. 352, pp. 127–134, 2017. DOI: 10.1016/j.jpowsour.2017.03.103. [Online]. Available: http://dx.doi.org/10.1016/j.jpowsour.2017.03.103.

[259] D. Rettenwander, A. Welzl, L. Cheng, J. Fleig, M. Musso, E. Suard, M. M. Doeff, G. J. Redhammer, and G. Amthauer, "Synthesis, Crystal Chemistry, and Electrochemical Properties of $Li_{7-2x}La_3Zr_{2-x}Mo_xO_{12}$(x = 0.1-0.4): Stabilization of the Cubic Garnet Polymorph via Substitution of Zr^{4+} by Mo^{6+}," *Inorganic Chemistry*, vol. 54, iss. 21, pp. 10 440–10 449, 2015. DOI: 10.1021/acs.inorgchem.5b01895.

[260] A. Wachter-Welzl, J. Kirowitz, R. Wagner, S. Smetaczek, G. C. Brunauer, M. Bonta, D. Rettenwander, S. Taibl, A. Limbeck, G. Amthauer, and J. Fleig, "The origin of conductivity variations in Al-stabilized $Li_7La_3Zr_2O_{12}$ ceramics," *Solid State Ionics*, vol. 319, iss. January, pp. 203–208, 2018. DOI: 10.1016/j.ssi.2018.01.036. [Online]. Available: https://doi.org/10.1016/j.ssi.2018.01.036.

[261] M. K. Murthy and J. Ip, "Studies in Germanium Oxide Systems : I, Phase Equilibria in the System Li_2O-GeO_2," *Journal of the American Chemical Society*, vol. 47, iss. 7, pp. 328–331, 1964.

[262] K. Hayamizu, Y. Matsuda, M. Matsui, and N. Imanishi, "Lithium ion diffusion measurements on a garnet-type solid conductor $Li_{6.6}La_3Zr_{1.6}Ta_{0.4}O_{12}$ by using a pulsed-gradient spin-echo NMR method," *Solid State Nuclear Magnetic Resonance*, vol. 70, pp. 21–27, 2015. DOI: 10.1016/j.ssnmr.2015.05.002. [Online]. Available: http://dx.doi.org/10.1016/j.ssnmr.2015.05.002.

[263] R. Hancke, S. Fearn, J. A. Kilner, and R. Haugsrud, "Determination of proton- and oxide ion tracer diffusion in lanthanum tungstate (La/W = 5.6) by means of ToF-SIMS," *Physical Chemistry Chemical Physics*, vol. 14, p. 13971, 2012. DOI: 10.1039/c2cp42278f.

[264] M. L. Sanjuán, A. Orera, I. Sobrados, A. F. Fuentes, and J. Sanz, "Structural transition in orthorhombic $Li_{5-x}H_xLa_3Nb_2O_{12}$ garnets induced by a concerted lithium and proton diffusion mechanism," *Journal of Materials Chemistry A*, vol. 6, iss. 6, pp. 2708–2720, 2018. DOI: 10.1039/C7TA10431F. [Online]. Available: http://xlink.rsc.org/?DOI=C7TA10431F.

[265] K. J. R. Rosman and P. D. P. Taylor, "Isotopic compositions of the elements 1997," *Pure and Applied Chemistry*, vol. 70, iss. 1, pp. 217–235, 1998. DOI: 10.1351/pac199870010217. [Online]. Available: https://www.degruyter.com/view/j/pac.1998.70.issue-1/pac199870010217/pac199870010217.xml.

[266] S. J. Cooper, "Quantifying the Transport Properties of Solid Oxide Fuel Cell Electrodes," PhD, Imperial College London, 2015.

[267] A. Lodding, J. Mundy, and A. Ott, "Isotope Inter-Diffusion and Self-Diffusion in Solid Lithium Metal," *Physica Status Solidi (B)*, vol. 559, pp. 559–569, 1970. DOI: 10.1002/pssb.19700380206. [Online]. Available: http://www3.interscience.wiley.com/journal/112580964/abstract.

[268] C. de Grotthuss, "Sur la décomposition de l'eau et des corps qu'elle tient en dissolution à l'aide de l'électricité galvanique," *Annali Di Chimica*, iss. 58, pp. 54–73, 1806.

[269] S. Yu and D. J. Siegel, "Grain Boundary Contributions to Li-Ion Transport in the Solid Electrolyte $Li_7La_3Zr_2O_{12}$ (LLZO)," *Chemistry of Materials*, vol. 29, iss. 22, pp. 9639–9647, 2017. DOI: 10.1021/acs.chemmater.7b02805.

[270] K. Park, B. C. Yu, J. W. Jung, Y. Li, W. Zhou, H. Gao, S. Son, and J. B. Goodenough, "Electrochemical Nature of the Cathode Interface for a Solid-State Lithium-Ion Battery: Interface between $LiCoO_2$ and Garnet-$Li_7La_3Zr_2O_{12}$," *Chemistry of Materials*, vol. 28, iss. 21, pp. 8051–8059, 2016. DOI: 10.1021/acs.chemmater.6b03870.

[271] S. Takai, K. Yoshioka, H. Iikura, M. Matsubayashi, T. Yao, and T. Esaka, "Tracer diffusion coefficients of lithium ion in $LiMn_2O_4$ measured by neutron radiography," *Solid State Ionics*, vol. 256, pp. 93–96, 2014. DOI: 10.1016/j.ssi.2014.01.013. [Online]. Available: http://dx.doi.org/10.1016/j.ssi.2014.01.013.

[272] T. Okumura, T. Fukutsuka, Y. Uchimoto, N. Sakai, K. Yamaji, and H. Yokokawa, "Determination of lithium ion diffusion in lithium-manganese-oxide-spinel thin films by secondary-ion mass spectrometry," *Journal of Power Sources*, vol. 189, iss. 1, pp. 643–645, 2009. DOI: 10.1016/j.jpowsour.2008.09.043.

[273] E. Dologlou, "Self-diffusion in solid lithium," *Glass Physics and Chemistry*, vol. 36, iss. 5, pp. 570–574, 2010. DOI: 10.1134/S1087659610050056. [Online]. Available: http://link.springer.com/10.1134/S1087659610050056.

[274] S. Krivec, T. Detzel, M. Buchmayr, and H. Hutter, "On the temperature dependence of Na migration in thin SiO_2 films during ToF-SIMS O_2^+ depth profiling," *Applied Surface Science*, vol. 257, iss. 1, pp. 25–32, 2010. DOI: 10.1016/j.apsusc.2010.06.019. [Online]. Available: http://dx.doi.org/10.1016/j.apsusc.2010.06.019.

[275] N. Hardy, *What is Thin Film Deposition by Thermal Evaporation?* 2018. [Online]. Available: http://www.semicore.com/news/71-thin-film-deposition-thermal-evaporation (visited on 01/26/2018).

[276] E. J. Cheng, A. Sharafi, and J. Sakamoto, "Intergranular Li metal propagation through polycrystalline LLZO ceramic electrolyte," *Electrochimica Acta*, vol. 223, pp. 85–91, 2017. DOI: 10.1016/j.electacta.2016.12.018.

[277] W. Knight, "Nuclear Magnetic Resonance Shift in Metals," *Physical Review*, vol. 76, p. 1259, 1949. DOI: 10.1103/PhysRev.76.1259.2.

[278] J. Saint, M. Morcrette, D. Larcher, and J. M. Tarascon, "Exploring the Li-Ga room temperature phase diagram and the electrochemical performances of the Li_xGa_y alloys vs. Li," *Solid State Ionics*, vol. 176, iss. 1-2, pp. 189–197, 2005. DOI: 10.1016/j.ssi.2004.05.021.

Appendices

A.1 Synthesis and Doping of LLZO

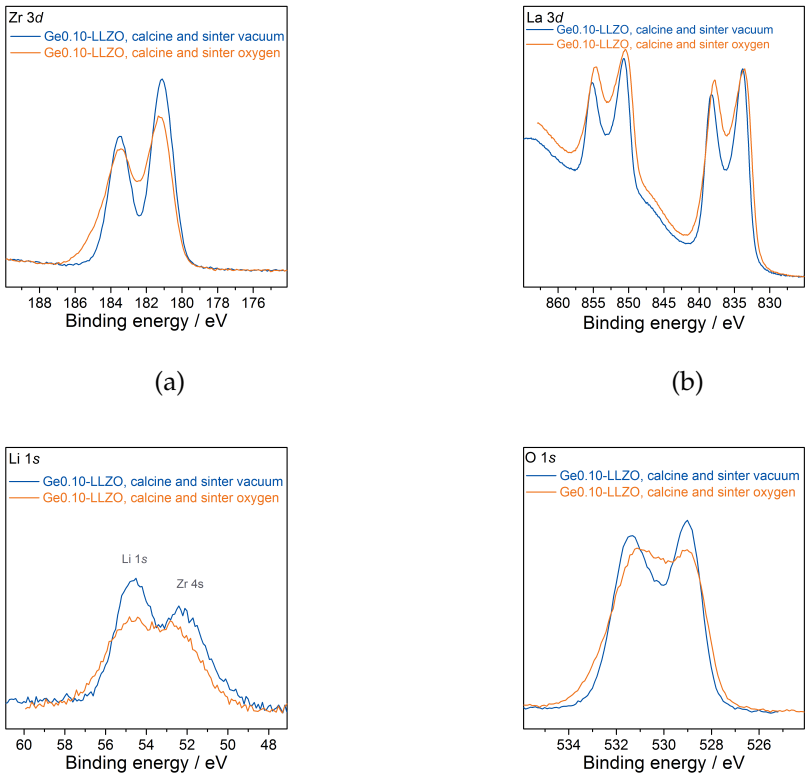


Figure A.1: XPS Zr 3d, La 3d, Li 1s and O 1s core spectra for Ge0.10-LLZO samples produced under oxygen and vacuum atmospheres. See Chapter 5 Section 5.1.1 for a discussion of charging effects depending on sintering atmosphere for the LLZO pellets.

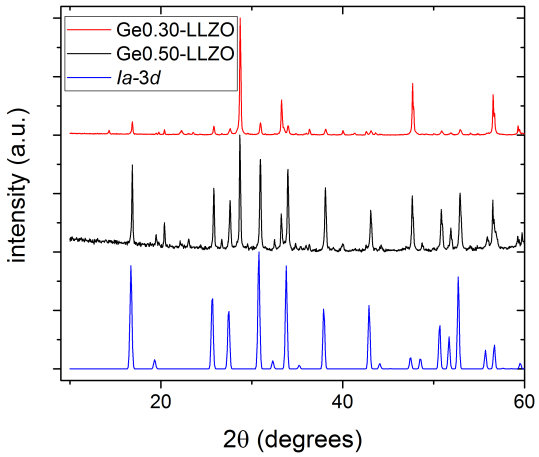


Figure A.2: XRD patterns of (top) Ge0.30- and (middle) Ge0.50-LLZO pellets and the theoretical reference pattern for cubic $Ia\bar{3}d$ (bottom). See Chapter 5 Section 5.2.1 for more details of Ge dopant concentration on the phase stability of Ge-LLZO.

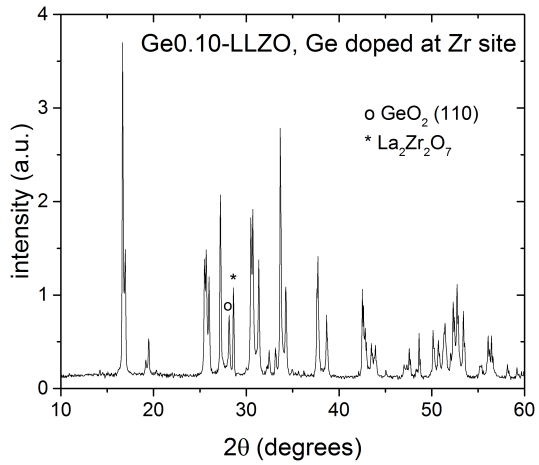


Figure A.3: XRD pattern of Ge0.10-LLZO pellet (doped at the Zr site). See Chapter 5 Section 5.2.4 for a discussion of the site preference of Ge as a dopant in LLZO.

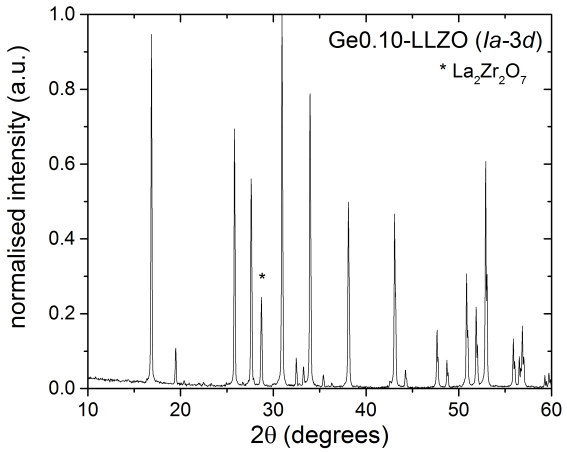
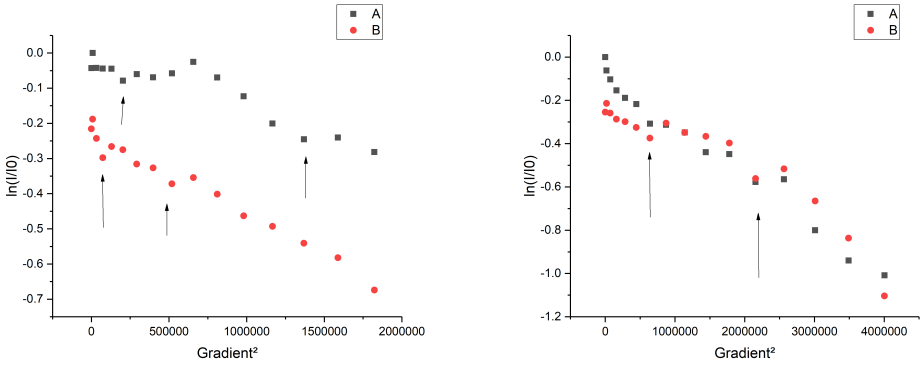


Figure A.4: XRD pattern of Ge0.10-LLZO powder, used for neutron diffraction. See Chapter 5 Section 4.2.2 for the neutron diffraction data of Ge0.10-LLZO.

A.2 ^{1}H Pulsed Field Gradient NMR

^{1}H NMR was carried out on proton exchanged powders of Ga0.15-LLZO. See Chapter 6 Section 6.1.2 for more details. Below shows the pulsed field gradient data used to find the proton diffusivity in the sample exchanged at 100 °C.



(a) (b)

Figure A.5: ^{1}H PFG NMR on 100 °C protonated Ga0.15-LLZO powder. A and B correspond to different chemical shifts for the static proton spectrum: 'A' is the peak at a higher chemical shift (possibly adsorbed water), and 'B' is the peak at a lower shift (possibly the sum of the intercalated protons).

Table A.1: Calculated ^{1}H diffusion coefficients D(H) from ^{1}H PFG NMR data (Figures 6.4 and A.5), in the protonated H-Ga0.15-LLZO powder, exchanged at 100 °C in H_2O. A and B correspond to different chemical shifts for the static proton spectrum: 'A' is the peak at a higher chemical shift (possibly adsorbed water), and 'B' is the peak at a lower shift (possibly the sum of the intercalated protons).

T (K)	***D*(H), chemical shift A ($m^2\ s^{-1}$)**	***D*(H), chemical shift B ($m^2\ s^{-1}$)**	**Δ (ms)**	**δ (μs)**
450	$3.844x10^{-12}$	$2.55x10^{-12}$	30	530
450	$3.854x10^{-12}$	$2.691x10^{-12}$	30	530
450	$4.936x10^{-12}$	$6.797x10^{-12}$	15	480
400	-	$4.456x10^{-12}$	15	480
350	-	$1.664x10^{-12}$	30	530
300	$9.679x10^{-12}$	$1.681x10^{-11}$	20	310

A.3 EIS Analysis of Pellets with Changing Thickness

The intermediate-frequency component, R2//CPE2, in the impedance spectra of Ga0.15-LLZO was found to be associated with inter-grain ionic transport in the Ga0.15-LLZO pellet. This was confirmed by evaluating the impedance of the second semicircle with a pellet of the same material of different thicknesses. The impedance values for this process varied proportionally with the thickness of the pellet which, when corrected for by cell dimensions to give resistivity, gave a value with a variance of less than 5 %, supporting the assigned process as being associated with inter-grain transport and not a surface-related process. See Chapter 6 Section 6.3 for more discussion.

Table A.2: EIS analysis of a Ga0.15-LLZO pellet with various thicknesses with symmetrical Li electrodes. R represents the impedance values obtained from fitting the data to R//CPE equivalent circuits, while l and A correspond to the sample thickness and area, respectively.

Sample		**R1//CPE1**		**R2//CPE2**	
	l (cm)	R (Ω)	RxA/l (Ω cm)	R (Ω)	RxA/l (Ω cm)
1	0.12	456.5	1117.5	1323.7	3240.4
2	0.086	322.4	1059.8	940.7	3092.8
3	0.05	191.0	1080.3	548.8	3103.4

Table A.3: Ratios of thickness, impedance and normalised impedance values to sample 1 for Ga0.15-LLZO with Li symmetrical electrodes (e.g. for sample 2 l_2/l_1 = 0.74, corresponding to 74 % of the thickness of sample 1). R represents impedance values obtained from fitting the data to R//CPE equivalent circuits, while l and A correspond to the sample thickness and area, respectively.

Sample		**R1//CPE1**		**R2//CPE2**	
	l (cm)	R (Ω)	RxA/l (Ω cm)	R (Ω)	RxA/l (Ω cm)
1	1.00	1.00	1.00	1.00	1.00
2	0.74	0.71	0.95	0.71	0.95
3	0.43	0.42	0.97	0.41	0.96

A.4 Calculating the Resistivity of Protonated H-Ga0.15-LLZO

The resistivity of the protonated region H-Ga0.15-LLZO in proton-exchanged pellets was calculated in Chapter 6 Section 6.3.2.

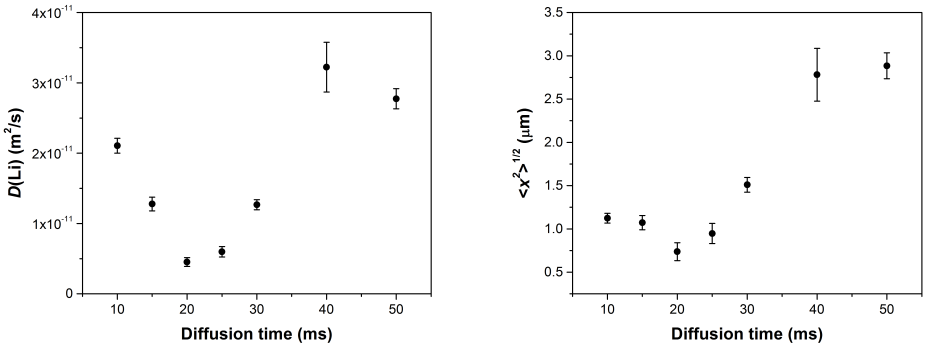
Table A.4: Resistance calculations for H-Ga0.15-LLZO region in for (H_2O/15) and (H_2O/30) Ga0.15-LLZO pellets, using EIS data and thickness estimates from FIB-SIMS depth profiles.

	H_2O/15	**H_2O/30**
ρ_{pristine} (Ω cm)	8.64x10^{2}	8.64x10^{2}
l' (cm)	5.70x10^{-4}	1.07x10^{-4}
$l'' = l - 2l'$ (cm)	6.74x10^{-2}	9.44x10^{-2}
l (cm)	6.86x10^{-2}	9.65x10^{-2}
A (cm^2)	0.28	0.28
$R'' = \rho l''/A$ (Ω)	206.06	291.17
$R = R' + R''$ (Ω)	441.70	830.70
$R' = R - R''$ (Ω)	235.64	539.53
$\rho' = R'A/l$ (Ω cm)	1.17x10^{5}	1.41x10^{5}
$\sigma' = l/\rho'$ (S cm^{-1})	8.56x10^{-6}	7.08x10^{-6}

A.5 ^{7}Li NMR

A.5.1 ^{7}Li Pulsed Field Gradient NMR

^{7}Li PFG measurements were performed at room temperature to extract Li ion diffusion coefficients for the Ga-doped LLZO solid electrolyte (see Chapter 7 Section 7.3.1). The time that the Li ions were allowed to diffuse during the experiment was varied to determine the length scales that we could probe within the experiment (Figures A.6a and A.6b).



(a) (b)

Figure A.6: (a) ^{7}Li diffusion coefficient D(Li) measured via PFG NMR as a function of diffusion time (Δ in the pulse sequence) for Ga0.15-LLZO. (b) Root mean squared displacement $\sqrt{x^2}$ of Li ions in Ga0.15-LLZO as a function of diffusion time Δ in the PFG experiment.

A.5.2 ^{7}Li Spin Lattice Relaxation ($T1$) NMR

^{7}Li variable temperature $T1$ (spin-lattice) relaxation NMR was also carried out on Ge- and Ga-doped LLZO powders to measure the activation energies for Li ion hopping (see Chapter 7 Section 7.3.2).

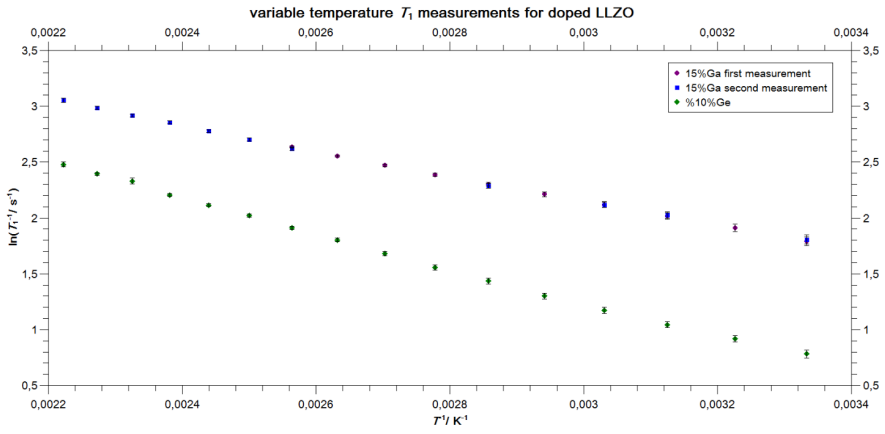


Figure A.7: $T1$ ^{7}Li NMR data for Ga- and Ge-doped LLZO powders used to derive activation energies, E_a.

A.5.3 XRD Patterns of Powders used for NMR Measurements

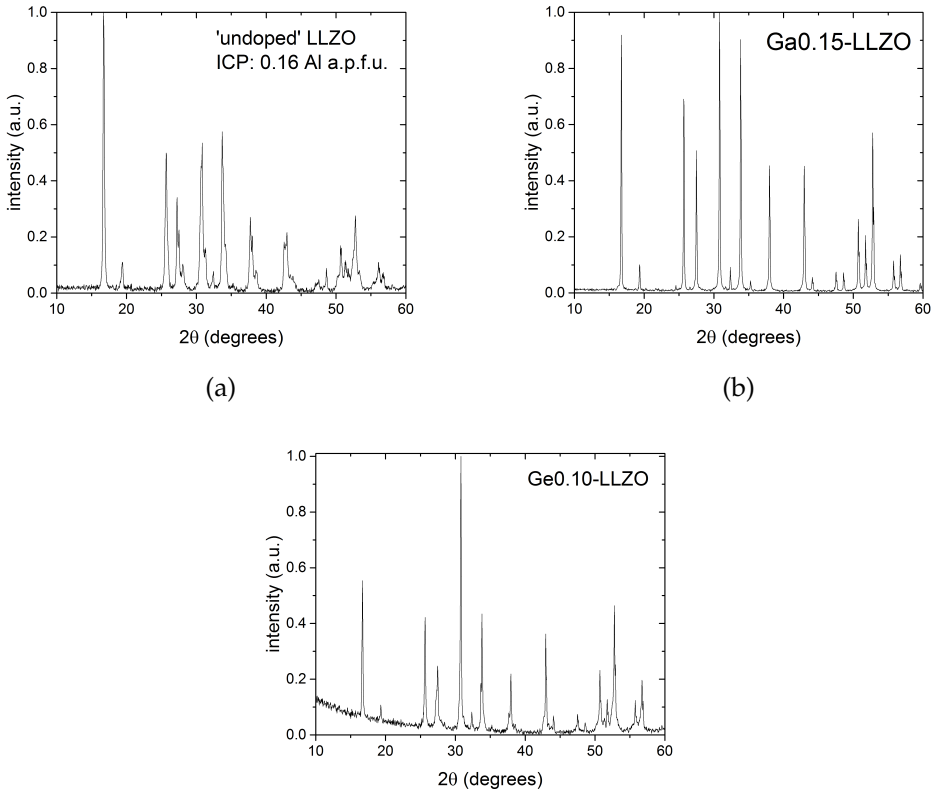


Figure A.8: XRD patterns of powders used for ^{7}Li NMR diffusivity measurements. (a) Undoped-LLZO; (b) Ga0.15-LLZO; (c) Ge0.10-LLZO.

A.6 Effects of Surface Roughness on FIB-SIMS Analysis of LLZO Pellets

The effect of surface roughness was investigated as it was considered an important factor in the facilitating of the proton-lithium exchange process (with a rougher surface providing a greater surface area for the reaction to occur), as well as the interpretation of FIB-SIMS depth profile data (morphological effects on the SIMS signal).

To test the effect of roughness, samples of LLZO (undoped) were either polished to 0.25 µm with diamond paste followed by thermal etching (900 °C for 30 minutes) to reveal the grains and reduce surface damage caused by the polishing process, or roughly polished (to #1200 grit in the glovebox), and measured in the FIB-SIMS under the same conditions. Figure A.10 shows the results for both rough-polished and etched pellets.

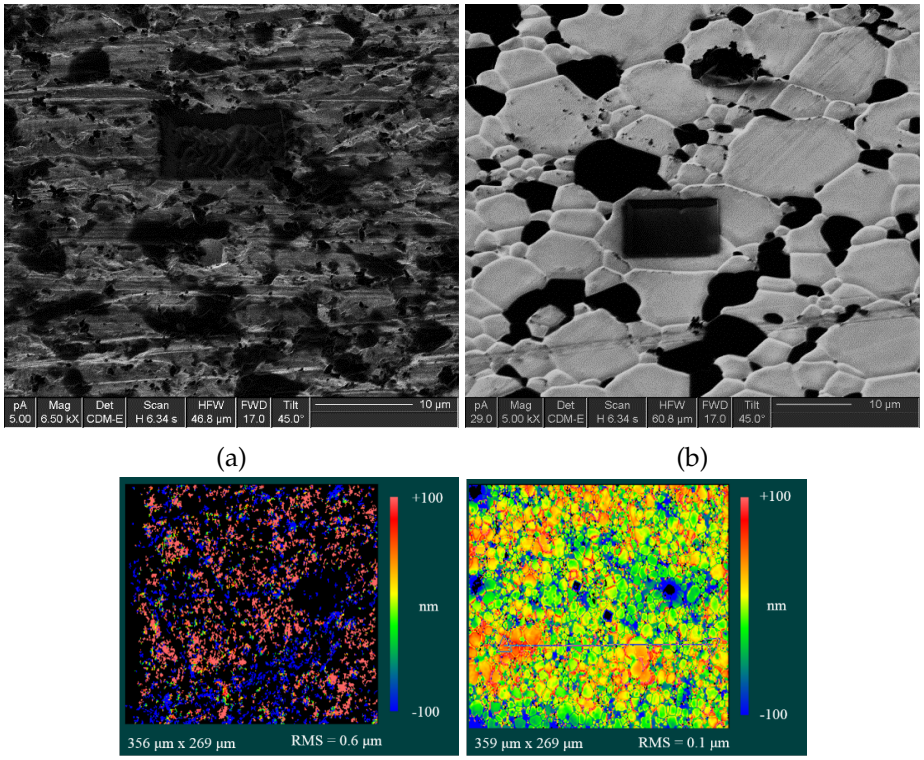


Figure A.9: Effect of surface roughness on a LLZO pellet. Rough-polished sample (left-hand column) is polished to 1200 grit SiC paper, polished pellet (right-hand column) is polished to 0.25 µm diamond paste and thermally etched at 900 °C. (a,b) Secondary electron images showing depth profile crater; (c,d) white light interferometry microscope images taken on Zygo New View 200.

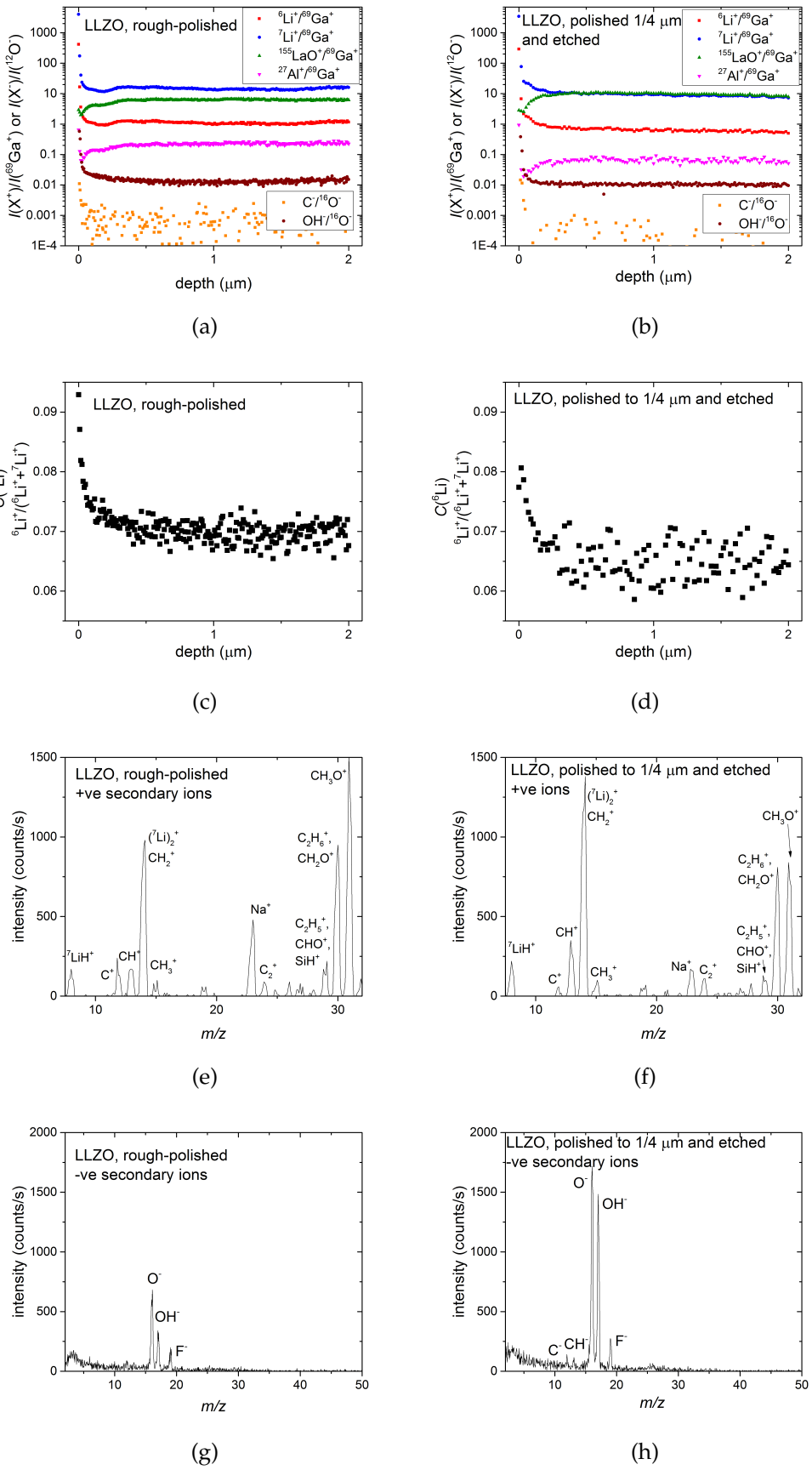


Figure A.10: Effect of surface roughness on a LLZO pellet. Rough-polished sample is polished to 1200 grit SiC paper, polished pellet is polished to 0.25 µm and thermally etched at 900 °C. (a,b) FIB-SIMS depth profiles over 10 µm by 10 µm area with with 1 nA primary ion beam current (giving a dose rate of 6.2×10^{15} ions cm^{-2} s^{-1}); (c,d) $C(^6Li)$ isotopic fractions; positive secondary ion (e,f) and negative secondary ion (g,h) mass spectra with 100 pA primary ion beam current rastered over 100 µm by 100 µm area (giving a dose rate of 6.2×10^{12} ions cm^{-2} s^{-1}).

A.7 Symmetric Cell Cycling Characterisation

Symmetric cells of Li/LLZO/Li for Ga0.15-LLZO and Al0.15-LLZO electrolyte compositions were cycled to correlate the role of dopant on the critical current for dendrite formation and short circuit (Chapter 8).

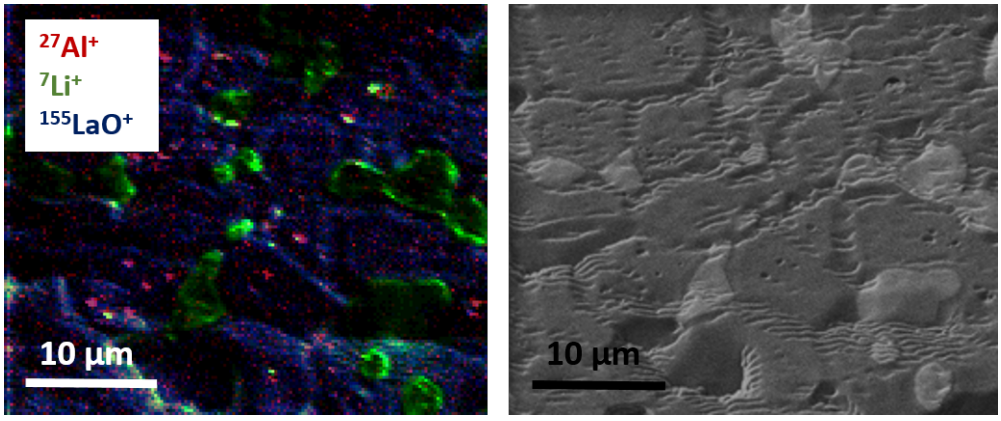


Figure A.11: Ga-LLZO pellet surface: FIB-SIMS map of $^{27}Al^+$, $^{7}Li^+$ and $^{155}(LaO)^+$ secondary ions overlayed with total positive ion image (shown alone, right) at 200 nm resolution, 1.95 nA primary ion beam current over 60.8 µm by 60.8 µm area, i.e. using a $3.3x10^{14}$ ions cm^{-2} s^{-1} dose rate. Li-rich regions are Li_2ZrO_3 grains (light contrast areas in secondary positive ion image). $^{69}Ga^+$ was not mapped in the here as it contains a major contribution from the primary beam.

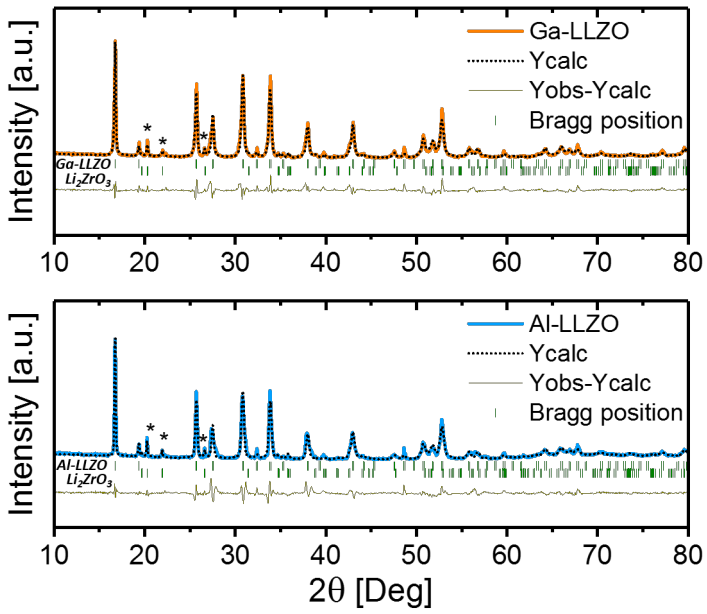
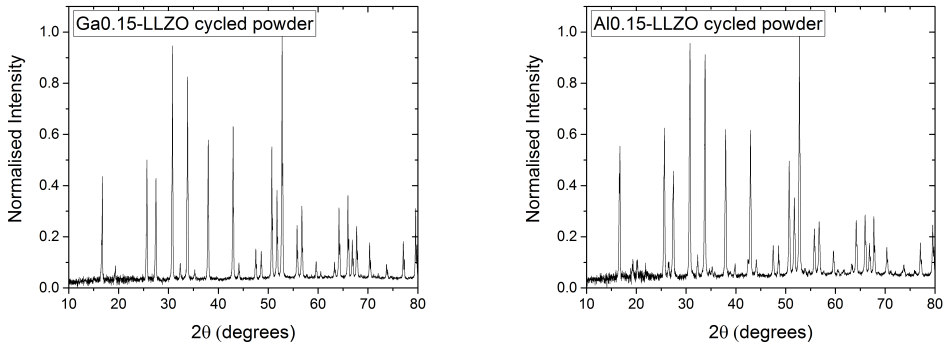


Figure A.12: X-ray powder diffraction patterns of Ga0.15-LLZO (top) and Al0.15-LLZO (bottom) before cell cycling, showing $Ia\bar{3}d$ space group cubic garnet and Li_2ZrO_3 impurity peaks (indicated by *).



(a) (b)

Figure A.13: X-ray powder diffraction patterns of (a) Ga0.15-LLZO and (b) Al0.15-LLZO following cell cycling and failure.

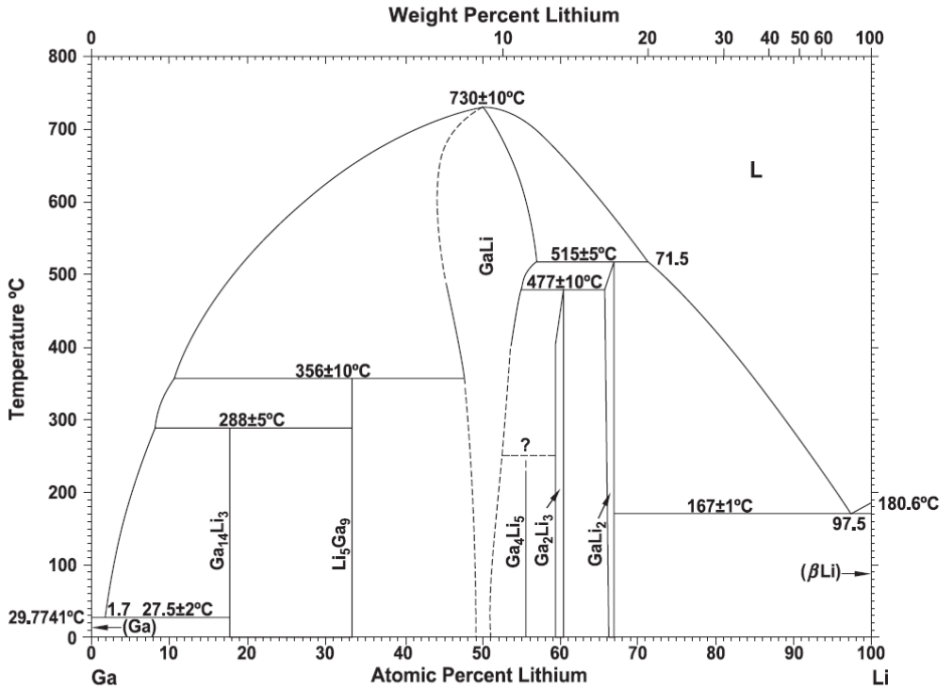


Figure A.14: Phase equilibrium diagram of the Li–Ga system at 1 atmosphere pressure. Figure from Saint [278].

Dissemination

Journal Publications from this Thesis

1. R. H. Brugge, A. K. Ola Hekselman, A. Cavallaro, F. M. Pesci, R. J. Chater, J. A. Kilner and A. Aguadero, “Garnet Electrolytes for Solid State Batteries: Visualisation of Moisture-Induced Chemical Degradation and Revealing its Impact on the Li-Ion Dynamics”, *Chemistry of Materials* 30, 3704-3713 (2018)

2. F. M. Pesci, R. H. Brugge, A. K. Ola Hekselman, A. Cavallaro, R. J. Chater and A. Aguadero, "Elucidating the Role of Dopants on the Critical Current Density for Dendrite Formation in Garnet Electrolytes", *Energy and Environmental Science*, *under review*

3. R. H. Brugge, J. A. Kilner and A. Aguadero, "Li Metal Isotopic Exchange for Probing Li Diffusion in Garnets: A Methodology", *in preparation*

4. R. H. Brugge and A. Aguadero, "Germanium as a Supervalent Dopant in Li-Conducting Garnet Electrolytes", *in preparation*

5. A.K. Ola Hekselman, F. M. Pesci, A. Cavallaro, R. H. Brugge and A. Aguadero, "The Dynamics at the Li Metal-Garnet Interface", *in preparation*

Conference Proceedings from this Thesis

1. R. H. Brugge, A. K. Ola Hekselman, F. M. Pesci, A. Cavallaro, R. J. Chater and A. Aguadero, "Local Chemical Degradation Processes and Ionic Transport in Garnet All-Solid-State Batteries", *Interfaces in Energy Materials*, Cambridge, U.K., 2018 (invited oral presentation)

2. R. H. Brugge, A. K. Ola Hekselman, A. Cavallaro, R. J. Chater, J. A. Kilner and A. Aguadero, “Proton Exchange and Transport Properties in Garnet Electrolytes”, *21st Solid State Ionics conference*, Padua, Italy, 2017 (oral presentation)

3. R. H. Brugge, A. K. Ola Hekselman, F. M. Pesci, A. Cavallaro, R. J. Chater and _A. Aguadero, “Degradation Processes and Ionic Transport in Garnet-Based Solid

Electrolytes", *21st Solid State Ionics conference*, Padua, Italy, 2017 (invited oral presentation)

4. R. H. Brugge, R. J. Chater, J. A. Kilner and A. Aguadero, "Isotopic Labelling and Diffusion in Garnet-Type Li Conductors", *SIMS Europe*, Münster, Germany, 2016 (poster presentation)

5. R. H. Brugge, W. Manalastas, J. A. Kilner and A. Aguadero, "Conductivity and Degradation in Garnet Electrolytes", *18th International Meeting on Lithium Batteries*, Chicago, U.S., 2016 (poster presentation)

6. R. H. Brugge, W. Manalastas, J. A. Kilner and A. Aguadero, "Conductivity and Degradation in Garnet Electrolytes", *Advances in Lithium Battery Research*, Bath, U.K., 2016 (poster presentation)

7. R. H. Brugge, W. Manalastas, J. A. Kilner and A. Aguadero, "Lithium-Rich Garnet Electrolytes: Ge-Doping and Moisture Degradation", *RSC UK-Korea Lithium Battery Symposium*, London, U.K., 2016 (poster presentation)

8. R. H. Brugge, R. J. Chater, W. Manalastas, J. A. Kilner and A. Aguadero, "Revealing the Optimum Li-Mobility in Garnet Electrolytes", *229th ECS Meeting*, San Diego, U.S., 2016 (invited oral presentation)

9. R. H. Brugge, J. A. Kilner and A. Aguadero, "Lithium-Rich Garnet Electrolytes: Moisture Control and Doping Methods for Understanding Conductivity", *2nd Energy Materials Symposium*, Bath, U.K., 2015 (poster presentation)

10. R. H. Brugge, J. A. Kilner and A. Aguadero, "Revealing Lithium Conduction Pathways in Lithium-Rich Garnets using Aliovalent Dopants", *ECS SOFC XIV*, Glasgow, U.K., 2015 (oral presentation)

11. R. H. Brugge, J. A. Kilner and A. Aguadero, "Revealing Lithium Conduction Pathways in Lithium-Rich Garnets using Aliovalent Dopants", *20th Solid State Ionics conference*, Colorado, U.S., 2015 (oral presentation)

12. R. H. Brugge, J. A. Kilner and A. Aguadero, "Revealing the Lithium Conduction Pathway using Dopants at the Li Sites in Stuffed Garnets", *227th ECS Meeting*, Chicago, U.S., 2015 (poster presentation, in absentia)

Other Journal Publications

1. W. Song, R. H. Brugge, I. G. Theodorou, A. Lim, Y. Yang, T. Zhao, C. H. Burgess, I. D. Johnson, A. Aguadero, P. R. Shearing, D. J. L. Brett, F. Xie and D. J. Riley, "Enhancing

Distorted Metal−Organic Framework-Derived ZnO as Anode Material for Lithium Storage by the Addition of Ag_2S Quantum Dots", *ACS Applied Materials & Interfaces* 9 (43), 37823-37831 (2017)

2. W. Manalastas, J. Rikarte, R. J. Chater, R. H. Brugge, A. Aguadero, L. Buannic, A. Llordes, F. Aguesse and J. A. Kilner, "Mechanical failure of garnet electrolytes during Li electrodeposition observed by in-operando microscopy", *ACS Applied Materials & Interfaces*, *submitted*